NASA/CR—1999-209401

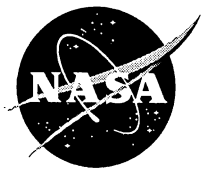

The Interactions of a Flame and Its Self-Induced Boundary Layer

James D. Ott and Elaine S. Oran
Naval Research Laboratory, Washington, DC

John D. Anderson
Univeristy of Maryland, College Park, Maryland

September 1999

The NASA STI Program Office . . . in Profile

Since its founding, NASA has been dedicated to the advancement of aeronautics and space science. The NASA Scientific and Technical Information (STI) Program Office plays a key part in helping NASA maintain this important role.

The NASA STI Program Office is operated by Langley Research Center, the Lead Center for NASA's scientific and technical information. The NASA STI Program Office provides access to the NASA STI Database, the largest collection of aeronautical and space science STI in the world. The Program Office is also NASA's institutional mechanism for disseminating the results of its research and development activities. These results are published by NASA in the NASA STI Report Series, which includes the following report types:

- TECHNICAL PUBLICATION. Reports of completed research or a major significant phase of research that present the results of NASA programs and include extensive data or theoretical analysis. Includes compilations of significant scientific and technical data and information deemed to be of continuing reference value. NASA's counterpart of peer-reviewed formal professional papers but has less stringent limitations on manuscript length and extent of graphic presentations.

- TECHNICAL MEMORANDUM. Scientific and technical findings that are preliminary or of specialized interest, e.g., quick release reports, working papers, and bibliographies that contain minimal annotation. Does not contain extensive analysis.

- CONTRACTOR REPORT. Scientific and technical findings by NASA-sponsored contractors and grantees.

- CONFERENCE PUBLICATION. Collected papers from scientific and technical conferences, symposia, seminars, or other meetings sponsored or cosponsored by NASA.

- SPECIAL PUBLICATION. Scientific, technical, or historical information from NASA programs, projects, and missions, often concerned with subjects having substantial public interest.

- TECHNICAL TRANSLATION. English-language translations of foreign scientific and technical material pertinent to NASA's mission.

Specialized services that complement the STI Program Office's diverse offerings include creating custom thesauri, building customized data bases, organizing and publishing research results . . . even providing videos.

For more information about the NASA STI Program Office, see the following:

- Access the NASA STI Program Home Page at ***http://www.sti.nasa.gov***

- E-mail your question via the Internet to help@sti.nasa.gov

- Fax your question to the NASA Access Help Desk at (301) 621-0134

- Telephone the NASA Access Help Desk at (301) 621-0390

- Write to:
  NASA Access Help Desk
  NASA Center for AeroSpace Information
  7121 Standard Drive
  Hanover, MD 21076

NASA/CR—1999-209401

The Interactions of a Flame and Its Self-Induced Boundary Layer

James D. Ott and Elaine S. Oran
Naval Research Laboratory, Washington, DC

John D. Anderson
Univeristy of Maryland, College Park, Maryland

Prepared under Cooperative Agreement C–78082–F

National Aeronautics and
Space Administration

Glenn Research Center

September 1999

Trade names or manufacturers' names are used in this report for identification only. This usage does not constitute an official endorsement, either expressed or implied, by the National Aeronautics and Space Administration.

Available from

NASA Center for Aerospace Information
7121 Standard Drive
Hanover, MD 21076
Price Code: A09

National Technical Information Service
5285 Port Royal Road
Springfield, VA 22100
Price Code: A09

The Interactions of a Flame and Its Self-Induced Boundary Layer

James D. Ott and Elaine S. Oran
Laboratory for Computational Physics and Fluid Dynamics
Naval Research Laboratory
Washington, DC

Dr. John D. Anderson, Jr.
Department of Aerospace Engineering
University of Maryland
College Park, MD

Work performed for NASA on
Inter-Agency Order, Request No. C-78082-F

Contents

List of Symbols

A_c = Channel Cross-sectional Area (cm)

A_f = Flame Surface Area (cm)

A_r = Constant in Arrhenius Rate Law

c = Speed of Sound (cm/s)

c_i = Mass Fraction of Species i

c_p = Specific Heat at Constant Pressure (ergs/g K)

D = Binary Diffusion Coefficient (cm^2/s)

d_q = Quenching Distance (cm)

E_c = Total Chemical Heat Release (ergs/s)

e_{s_i} = Sensible Internal Energy of Species i (ergs/g)

e_t = Total Internal Energy (ergs/g)

F = Unburned Fuel

h = Channel Height (cm)

h = Enthalpy (ergs/g)

k = Thermal Conductivity (ergs/cm-s-K)

k_b = Boltzmann Constant

k_f = Rate Constant

Le = Lewis-Semenov Number

l = Reference length (cm)

M = Mach Number

$\mathcal{M}$ = Molecular Weight (g/gmol)

Na = Avogadro's Number

n_i = Number density of Species i (particles/cm^3)

P = Mass Fraction of Burned Product

Pr = Prandtl Number

p = Pressure (dynes/cm^2)

Q_w = Total Heat Extracted (ergs/s)

q = Effective Zero Point Energy (ergs/g)

q = Heat Flux (ergs/s K cm^2)

Re = Reynolds Number

R_s = Specific Gas Constant (ergs/g K)

R_u = Universal Gas Constant (ergs/gmol K)

r = General Coordinate Direction

r_m = Minimun Spark Radius

S_F = Flame Speed Relative to Fixed Coordinates (cm/s)

S_l = Laminar Flame Speed (cm/s)

T = Temperature (K)

T_a = Activation Temperature (K)

T_b = Temperature in Burned Gas (K)

T_q = Quenching Temperature (K)

T_u = Temperature in Unburned Gas (K)

t = Time (s)

t_x = Local Time (s)

U_i = Diffusion Velocity (cm/s)

u = X-direction Velocity (cm/s)

v = Y-direction Velocity (cm/s)

Y = Mass Fraction of Unburned Fuel

Greek

α = Thermal Diffusivity

γ = Ratio of Specific Heats

ΔE_c= Local Chemical Energy Release (ergs/s cm^3)

Δh_{f_i}= Heat of Formation of Species i (erg/g)

δ^* = Boundary layer displacement thickness (cm)

δ_{99} = Boundary layer thickness (cm)

δ_t = laminar flame thickness (cm)

λ = Bulk Viscosity Coefficient

Ψ = Characteristic Wave Amplitude

ρ = Global Density (g/cm^3)

ρ_i = Density of Species i (g/cm^3)

τ = Stress ($dynes/cm^2$)

μ = Dynamic Viscosity Coefficient (g/cm s)

$\dot{\omega}_i$ = Chemical Source Term

ω = Vorticity (1/s)

subscripts

b = Burned conditions

i = Inflow Condition

o = Outflow condition

r = Reference condition

u = Unburned conditions

w = Wall conditions

x = X-Axis direction

y = Y-Axis direction

acronmyns

CMRFAST2D = Connection Machine, Reacting, FAST 2D code

FAST = Routine using LCPFCT for the convective terms

LCPFCT = Flux-Corrected Transport Algorithm

Chapter 1

Introduction

1.1 Problem Statement

The objective of this study is to numerically examine the interaction of a premixed laminar flame with its self-induced boundary layer in a channel. As a flame propagates down a channel, it creates pressure waves ahead of it.[1] If the flame is accelerating, the flame generates compression waves and if the flame is decelerating, expansion waves are formed. These waves cause motion of the gas ahead of the flame. If the channel has an open end toward which the flame propagates, the gas set in motion by the flame can exit the channel. This self-induced fluid motion ahead of the flame causes a boundary layer to form along the channel wall. The flame then propagates into this boundary layer created by its own motion.

A flame, or a deflagration wave, is a self-sustaining combustion zone moving at subsonic speeds. If the combustion zone moves at a supersonic speed, the wave is a detonation. Many factors influence the speed of the flame.[2] The effect of the fuel type is important, with different fuels propagating at different speeds. Another factor influencing flame speed is the mixture composition, whether the mixture is rich, lean, or stoichiometric. A stoichiometric reaction is one where all of the fuel and oxidizer is consumed. A rich mixture is one where there is more fuel present than the stoichiometric condition, and a lean mixture is one where there is less fuel than the stoichiometric conditions. The initial temperature and pressure also affect the flame speed. If the initial mixture is heated, the resulting flame speed will be faster. Pressure effects vary with the order of the reaction. The reaction order depends on the exponential powers of the reactants in the rate equation. For zero and first order reactions, the flame speed increases as the pressure decreases. For second order reactions, the flame speed is independent of the pressure, and for reaction orders greater then two, the flame speed decreases with decreasing pressure.

Two types of flames exist, premixed and diffusion. A premixed flame has the fuel and oxidizer mixed at the molecular level before the material is ignited. An example of this type of flame would be a Bunsen burner. The fuel and air enter at the bottom of the Bunsen tube and mix before they reach the top of the tube where the flame is located. In a diffusion flame, also called a non-premixed flame, the fuel and oxidizer are initially separated. The reaction occurs in the zone where the fuel and oxidizer come together and mix. A candle is an example of a diffusion flame. The wax of the candle is melted, evaporates, diffuses into the air, and burns in the diffusion zone.

The main purpose of this investigation is to examine the basic flow physics of the formation of the boundary layer ahead of the flame and the interaction with the flame as it propagates into the boundary layer. Flames in channels with an open end have applications to the flame spread in ducts and in mines. It also deals with the flame spread in an aircraft fuel tank. If the tank becomes ruptured and ignites, the gases can escape out from the tank through the rupture. The rate of the flame propagation through the tank will depend on where the rupture occurs, either ahead of the flame or behind it. In the study of the transition from a deflagration wave to a detonation wave, localized ignitions have occurred ahead of the flame in the boundary layer.[2-5] The study of micro-propulsion, the use of small thrusters on light-weight spacecraft, depends on the combustion in tiny chambers and channels to generate the high pressure and high temperature gas for use in the nozzle. The effects of the boundary layer on the flame structure is of interest in the micro-channel environment of these propulsion devices.

In this study, the two-dimensional Navier-Stokes equations are used to simulate the propagation of a flame in a channel. A single step, two species chemistry model is used which simulates the reaction of an acetylene-air mixture. The boundary condition for the temperature at the wall is examined for adiabatic and isothermal conditions to study its effect on the flame propagation. The flame ignition method is varied from a planar ignition to a spark ignition to examine what effects ignition has on the flame structure.

1.2 Previous Work

There are three channel configurations that are used for the numerical and experimental work dealing with flames in tube. The different configurations depend on the conditions at the ends of the tube. Using the notation that the ignition occurs on the left side of the channel, and that the channel is described by defining the left and then the right hand sides, the three channel configurations are closed-closed, open-closed, and closed-open.

1.2.1 Closed - Closed

Figure 1.1 shows the channel configuration for the closed-closed geometry. The ignition occurs at the left closed end and the flame propagates toward the right closed end. A great amount

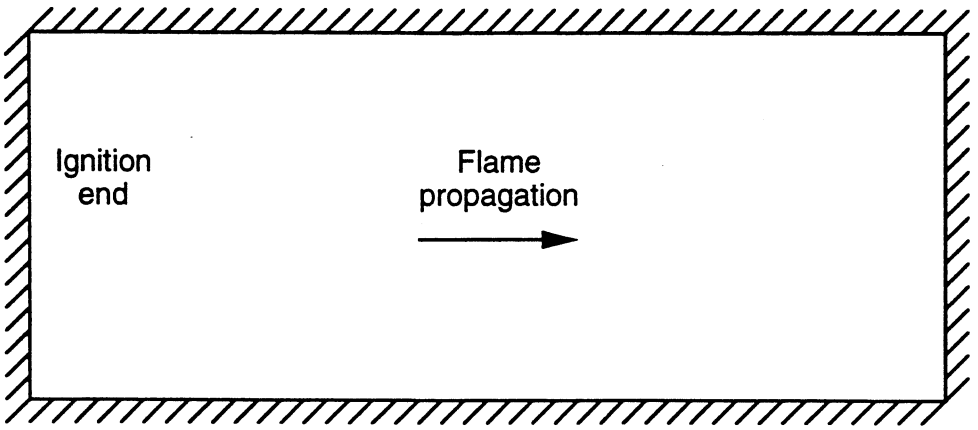

Figure 1.1: Closed-Closed Channel Configuration.

of experimental work[6–12] and numerical work[13–23] has been done on tubes with a closed-closed configuration. Figure 1.2 shows the experimental stroboscopic flame record of Ellis[6] for the flame propagation in tubes with the same diameter but varying the tube length. For all the tubes, the flame was ignited using a spark on the left end. After the sparked ignition, the flame expands spherically until it approaches the top and bottom walls. The flame then takes on an elliptical shape as the portions that are nearing the top and bottom walls slow down. When the flame reaches these walls, the flame is quenched (extinguished) and the flame surface area decreases. This causes the flame to slow, since a lower flame area results in less burning, and therefore less hot, expanding gas.

After the flame slows, one of two possibilities can happen, depending on the length to diameter ratio, L/D, of the tube. For tubes with a large L/D ratio, the portions of the flame close to the walls begin to move faster than the flame near the centerline. The flame develops a rearward cusp near the centerline as the flame at the centerline lags behind the flame closer to the top and bottom walls. Salamandra et al.[8] called this a 'tulip' flame. For tubes with an $L/D < 2$, no tulip flame appears.[6,9] This is seen in figure 1.2 as photograph (d). Photographs (a), (b), and (c) all develop the tulip flame.

The reason for the formation of the tulip is not yet clearly understood. It is known that the formation depends on the tube aspect ratio, L/D, the mixture composition, and the initial mixture pressure.[9] An earlier explanation by Guenoche[9] theorizes that the tulip is caused by the interaction of pressure waves that have reflected off the end wall. During the initial expansion of the flame due

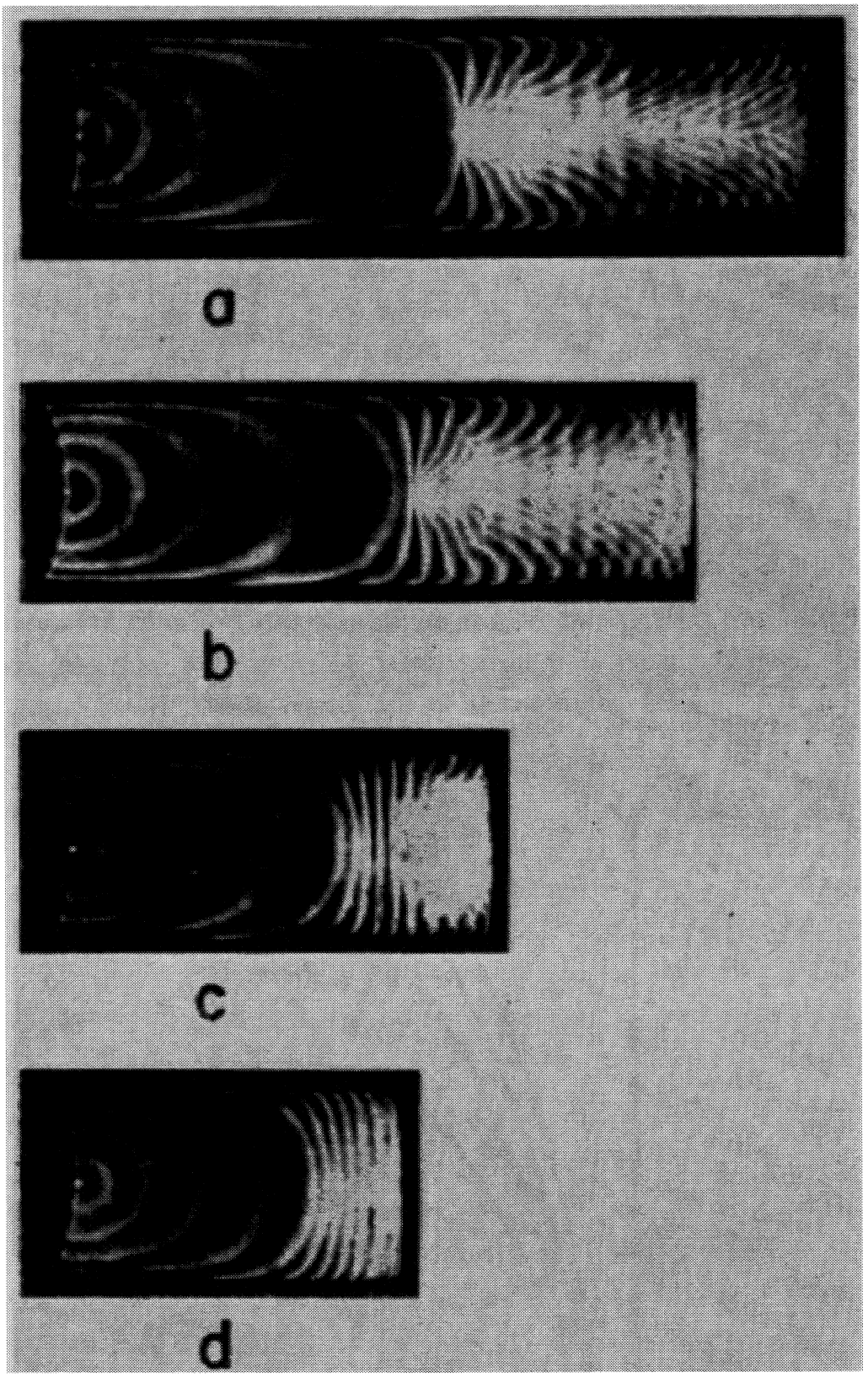

Figure 1.2: Flame propagation in a tube closed at both ends, from Ellis.[6] (a) 19.5 cm, (b) 17 cm, (c) 12 cm, (d) 9.5 cm

to the spark, the flame emits pressure waves.[1] These waves reflect off of the closed end of the tube and intersect the flame. This explanation is dismissed since numerical studies have been performed using low Mach number approximations that negate pressure waves and these studies have still seen the formation of the tulip flame phenomena.[12,15,18] Dunn-Rankin et al.[12] determined that the presence of vorticity is not required for the tulip formation. It has also been determined that viscosity is not required since much numerical work has been done using the inviscid formulation and has still generated a tulip flame.[12,16,18,19] The work of Marra and Continillo[23] disagrees with this conclusion. They show that when the wall boundary is the slip condition, no tulip forms, but if viscosity is included and the condition is the no-slip wall, a tulip forms in the same tube. The most recent theory is that the tulip is formed from the Darrieus-Landau[24,25] instability caused by the flow through a curved flame front.[12,18,19,26]

1.2.2 Open - Closed

Figure 1.3 shows the channel configuration for the open-closed geometry. The ignition is on the left hand side and the flame propagates to the right toward the closed end of the tube. The hot expanding gases are allowed to escape from the open end of the channel, providing a nearly stagnant gas into which the flame moves.

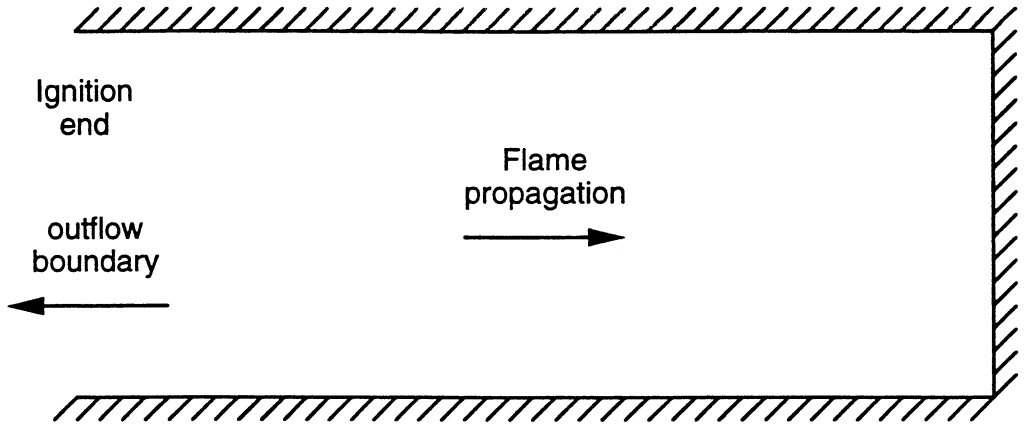

Figure 1.3: Open-Closed Channel Configuration.

This open-closed configuration has been studied both experimentally[7,27–31] and recently numerically.[16,26,32–34] Mallard and Le Chatelier[27] discovered that for this configuration, the flame travels for some distance at a constant speed. Coward and Hartwell[28] found that below a minimum diameter, the flame speed is not constant. As the diameter is increased, the flame speed becomes constant over some distance. As the diameter increases, this constant flame speed also increases.[28]

Table 1.1: Experimental tubes for the open-closed configuration. [29]

tube number	1	2	3	4
Length (cm)	56	57	98	100
diameter ψ (cm)	2.9	2.9	4.0	2.0
ignition source	flame	spark	spark	spark

Figure 1.4, taken from Guenoche and Jouy,[29] shows the flame propagation in various tubes for acetylene-air mixtures. Table 1.1 gives the tube parameters for the four tubes used in the experiment. In the figure, the flames move from the right to the left. The 'h' and 'v' on the right side of the figure refer to the plane that the photographs were taken in, 'h' in the horizontal plane and 'v' in the vertical. The variables d_i and d_f in the original caption refer to the size of the openings on the ignition and opposite ends of the tube. The flames are ignited using either a spark or using an already developed flame that enters the tube on the open end. The time between photographs is given by Δt.

The flames in the figure 1.4 take on a variety of shapes.[29] The hook-shaped flame, as seen in the third tube from the top, is due to buoyancy effects. A tulip flame can appear in this type of tube as well, as seen in the second and twelveth tubes, but it is not always present. The existence of the tulip in this configuration was also shown numerically.[16] The flame can also take on a 'mushroom' or parabolic shape.

Lee and Tsai[33] and Hackert et al.[34] performed numerical studies on the effects of the wall boundary condition on the flame shapes, with the objective of determining whether a tulip or a mushroom flame is formed. For insulated tubes, both shapes appeared in tubes with a large diameter. As the diameter decreases, only the tulip flame shape develops.[33] The tulip flames also propagate at a faster speed then the mushroom shaped flames.[33] For an isothermal wall, both flame shapes exist, but as the diameter decreases, only the mushroom shape occurs.[33,34] For this boundary condition, the mushroom-shaped flame propagates the fastest.[33] If the walls are convectively cooled, both flame shapes appear.[34]

1.2.3 Closed - Open

Figure 1.5 shows the channel configuration for the closed-open geometry. Here, ignition occurs at the closed end, and then the flame forms and propagates toward the open end, where the gas escapes the channel. Since the gas is allowed to escape, there is a flow formed ahead of the flame. This flow is caused by the expansion of the gas as it burns and pushes the flow ahead of the flame,

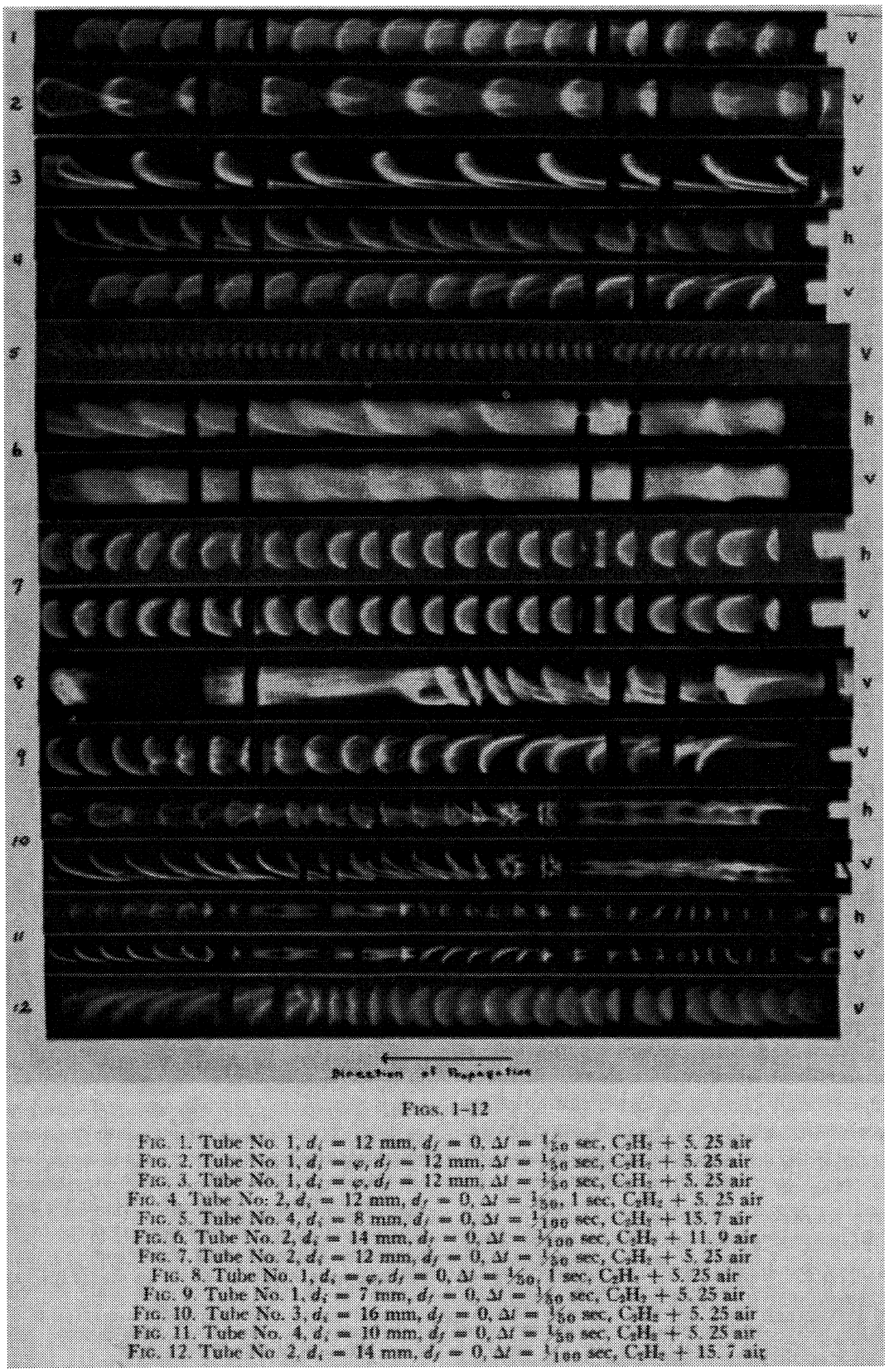

FIGS. 1–12

FIG. 1. Tube No. 1, d_t = 12 mm, d_f = 0, Δl = $\frac{1}{50}$ sec, C_2H_2 + 5. 25 air
FIG. 2. Tube No. 1, d_t = φ, d_f = 12 mm, Δl = $\frac{1}{50}$ sec, C_2H_2 + 5. 25 air
FIG. 3. Tube No. 1, d_t = φ, d_f = 12 mm, Δl = $\frac{1}{50}$ sec, C_2H_2 + 5. 25 air
FIG. 4. Tube No. 2, d_t = 12 mm, d_f = 0, Δl = $\frac{1}{50}$, 1 sec, C_2H_2 + 5. 25 air
FIG. 5. Tube No. 4, d_t = 8 mm, d_f = 0, Δl = $\frac{1}{100}$ sec, C_2H_2 + 15. 7 air
FIG. 6. Tube No. 2, d_t = 14 mm, d_f = 0, Δl = $\frac{1}{100}$ sec, C_2H_2 + 11. 0 air
FIG. 7. Tube No. 2, d_t = 12 mm, d_f = 0, Δl = $\frac{1}{50}$ sec, C_2H_2 + 5. 25 air
FIG. 8. Tube No. 1, d_t = φ, d_f = 0, Δl = $\frac{1}{50}$, 1 sec, C_2H_2 + 5. 25 air
FIG. 9. Tube No. 1, d_t = 7 mm, d_f = 0, Δl = $\frac{1}{50}$ sec, C_2H_2 + 5. 25 air
FIG. 10. Tube No. 3, d_t = 16 mm, d_f = 0, Δl = $\frac{1}{50}$ sec, C_2H_2 + 5. 25 air
FIG. 11. Tube No. 4, d_t = 10 mm, d_f = 0, Δl = $\frac{1}{50}$ sec, C_2H_2 + 5. 25 air
FIG. 12. Tube No. 2, d_t = 14 mm, d_f = 0, Δl = $\frac{1}{100}$ sec, C_2H_2 + 15. 7 air

Figure 1.4: Flame propagation in tube opened at the ignition end. Taken from Guenoche and Jouy[29]

similar to a piston. Due to the motion ahead of the flame, the flame propagates at a greater speed then it did for the previous two channel configurations.[9]

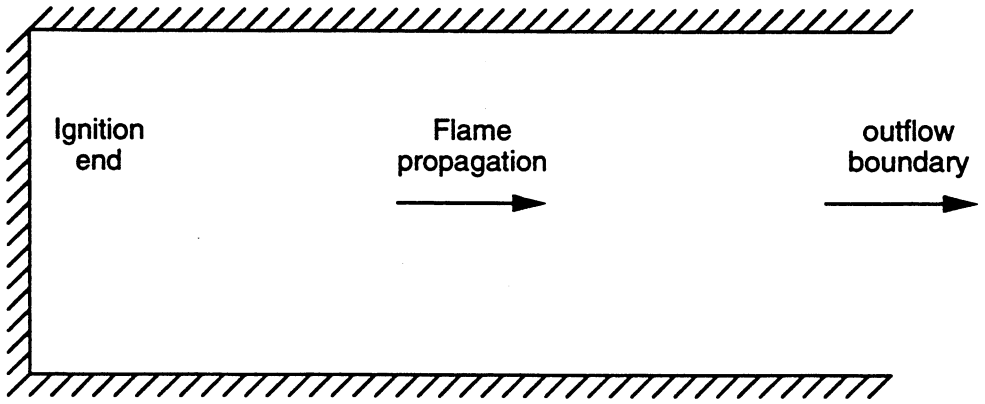

Figure 1.5: Closed-Open Channel Configuration.

Little experimental work[7,9,27] has been done on the closed-open configuration and no references to numerical work were found. Figures 1.6, 1.7, and 1.8 show schlieren photographs for flames in fuel lean, stoichiometric, and fuel rich conditions.[7] On the top of figure 1.6, the experimental tube is seen with its four windows. The schlieren photographs are shown below the window from which they were taken. The times on the right between the photographs represent the time intervals between photographs. The flame was ignited with a spark.

After the flame induced by the spark has reached the side wall, the flames in all three mixtures keep their rounded shapes, no tulips forms. Guenoche reported that tulips have formed in closed-open channel configurations.[9] As the flames continued to propagate down the tube, they underwent a transition from laminar to turbulent. When this happens, the flame speed greatly increases due the increased burning area of the flame. The transition occurs sooner the closer that the mixture is to stoichiometric conditions.[7] Figure 1.8, a rich fuel mixture, shows that the flame oscillates, and even reverses direction for a time before resuming movement toward the open end of the tube. Mallard and Le Chatelier called this the 'movement saccade' or 'jerky motion'.[27]

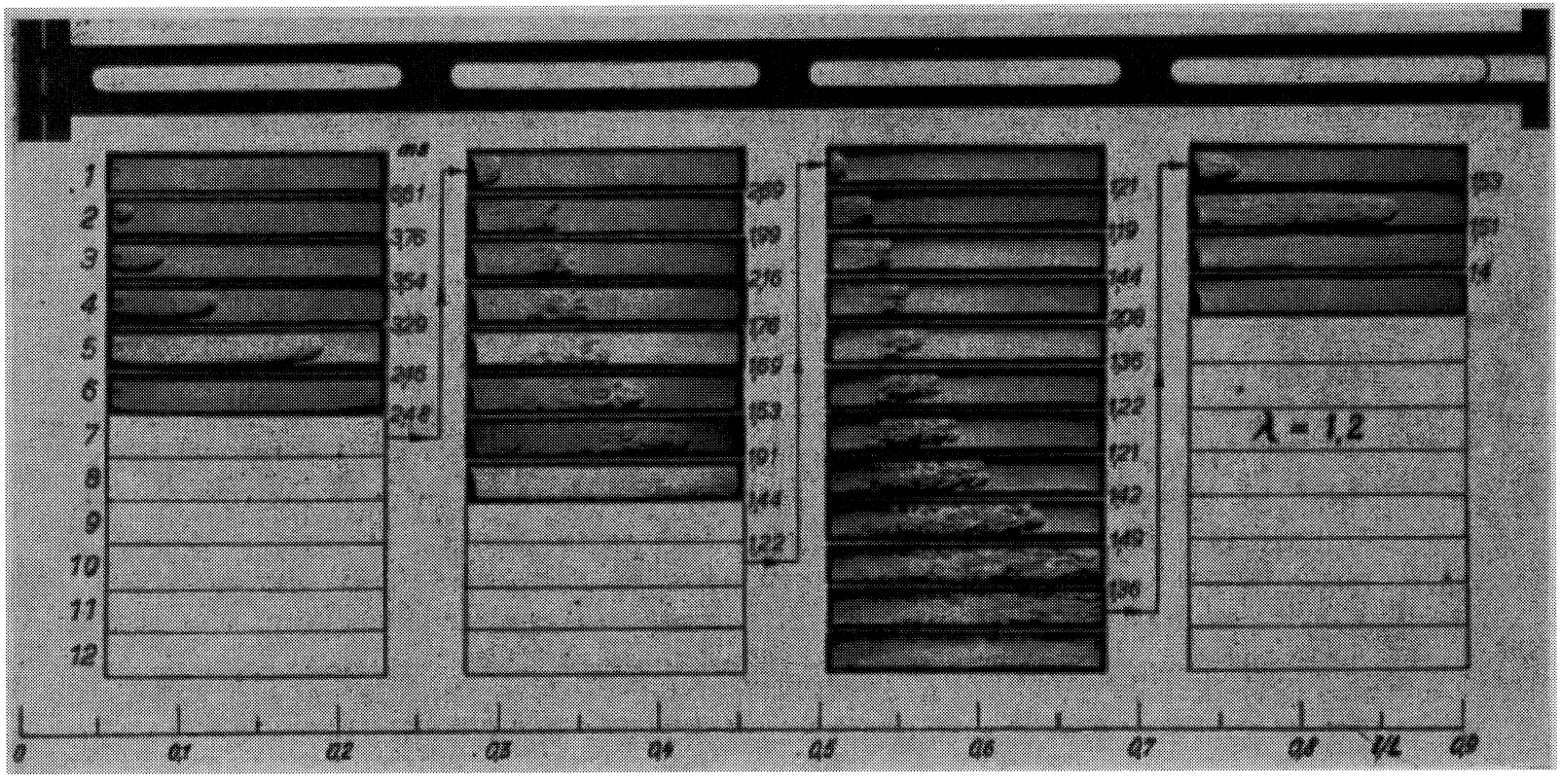

Figure 1.6: Flame propagation in a tube closed at the ignition end and open at the other, fuel lean, from Schmidt et al.[7]

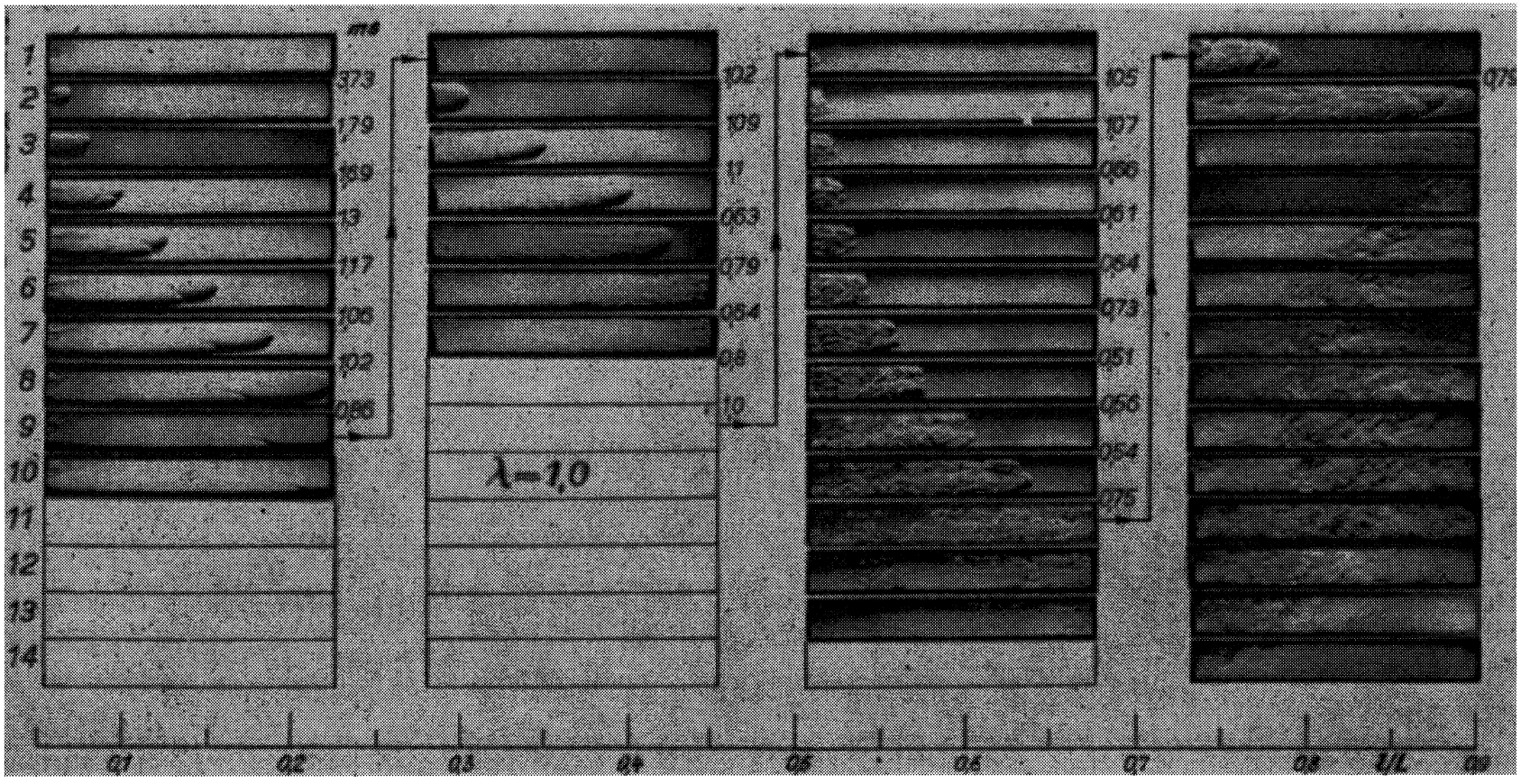

Figure 1.7: Flame propagation in a tube closed at the ignition end and open at the other, stoichiometric, from Schmidt et al. [7]

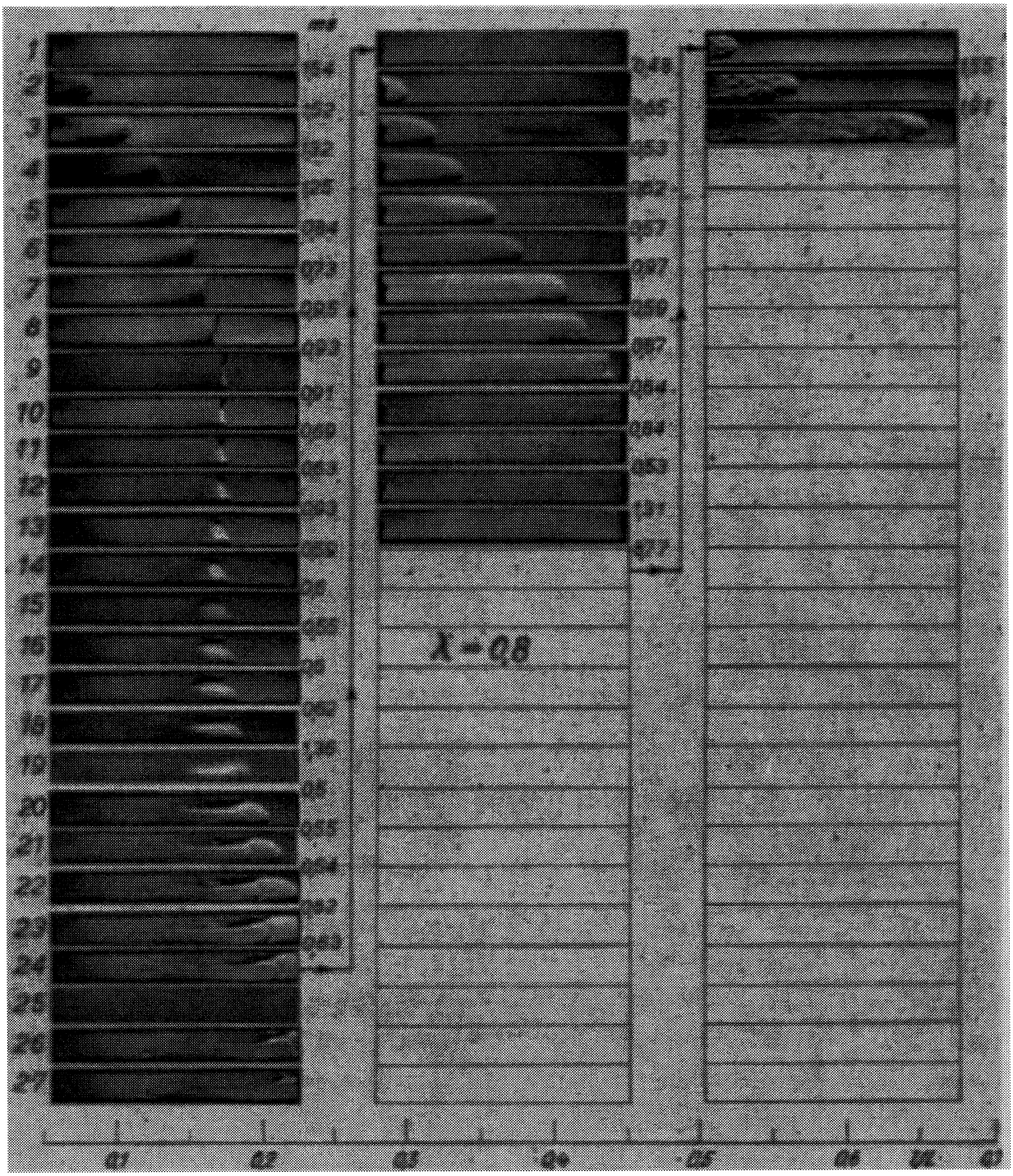

Figure 1.8: Flame propagation in a tube closed at the ignition end and open at the other, fuel rich, from Schmidt et al.[7]

Chapter 2

Governing Equations and Numerical Procedure

This chapter details the governing equations, chemistry model, integration technique, and boundary conditions.

2.1 Navier-Stokes Equations

The unsteady, two-dimensional, compressible, chemically reacting, Navier-Stokes equations in conservation form were solved. These equations model the conservation of total mass density, species mass in terms of number densities, momentum, and energy. In differential form, they may be written:[35]

- Conservation of Total Mass

$$\frac{\partial \rho}{\partial t} + \frac{\partial \rho u}{\partial x} + \frac{\partial \rho v}{\partial y} = 0 \tag{2.1}$$

- Conservation of x-Momentum

$$\frac{\partial(\rho u)}{\partial t} + \frac{\partial(\rho u u)}{\partial x} + \frac{\partial(\rho u v)}{\partial y} = -\frac{\partial p}{\partial x} + \frac{\partial \tau_{xx}}{\partial x} + \frac{\partial \tau_{xy}}{\partial y} \tag{2.2}$$

- Conservation of y-Momentum

$$\frac{\partial(\rho v)}{\partial t} + \frac{\partial(\rho v u)}{\partial x} + \frac{\partial(\rho v v)}{\partial y} = -\frac{\partial p}{\partial y} + \frac{\partial \tau_{yx}}{\partial x} + \frac{\partial \tau_{yy}}{\partial y} \tag{2.3}$$

- Conservation of Total Energy

$$\begin{aligned} \frac{\partial(\rho e_t)}{\partial t} + \frac{\partial(\rho e_t u)}{\partial x} + \frac{\partial(\rho e_t v)}{\partial y} &= -\frac{\partial(pu)}{\partial x} - \frac{\partial(pv)}{\partial y} - \frac{\partial q_x}{\partial x} - \frac{\partial q_y}{\partial y} \\ &+ \frac{\partial(u\tau_{xx} + v\tau_{xy})}{\partial x} + \frac{\partial(u\tau_{yx} + v\tau_{yy})}{\partial y} \end{aligned} \tag{2.4}$$

• Conservation of Species Mass Density

$$\frac{\partial n_i}{\partial t} + \frac{\partial (n_i u)}{\partial x} + \frac{\partial (n_i v)}{\partial y} = -\frac{\partial (n_i U_{x_i})}{\partial x} - \frac{\partial (n_i U_{y_i})}{\partial y} + \dot{\omega}_i \tag{2.5}$$

The total internal energy is the sum of the individual species sensible internal energies plus zero point energies, as represented by the heats of formation, and the kinetic energy. The total internal energy density can be written as

$$\rho e_t = \sum_{i=1}^{ns} \rho_i \left(e_{s_i} + \Delta h_{f_i} \right) + \frac{1}{2} \rho \left(u^2 + v^2 \right) \tag{2.6}$$

where ns is the number of species. The viscous stress terms, τ_{xx}, $\tau_{xy} = \tau_{yx}$, and τ_{yy}, are written as

$$\tau_{xx} = \lambda \left(\frac{\partial u}{\partial x} + \frac{\partial v}{\partial y} \right) + 2\mu \frac{\partial u}{\partial x} \tag{2.7}$$

$$\tau_{xy} = \mu \left(\frac{\partial u}{\partial y} + \frac{\partial v}{\partial x} \right) \tag{2.8}$$

$$\tau_{yy} = \lambda \left(\frac{\partial u}{\partial x} + \frac{\partial v}{\partial y} \right) + 2\mu \frac{\partial v}{\partial y} \tag{2.9}$$

Stokes Hypothesis is used to relate the bulk viscosity to the dynamic viscosity, $\lambda = -\frac{2}{3}\mu$. The heat flux terms, q_x and q_y, contain contributions due to conduction and heat flux due to the diffusion of the species,

$$q_x = -k \frac{\partial T}{\partial x} + \sum_{i=1}^{ns} \rho_i U_{x_i} \left(h_{s_i} + \Delta h_{f_i} \right) \tag{2.10}$$

$$q_y = -k \frac{\partial T}{\partial y} + \sum_{i=1}^{ns} \rho_i U_{y_i} \left(h_{s_i} + \Delta h_{f_i} \right) \tag{2.11}$$

The diffusion velocities, U_{x_i} and U_{y_i} are calculated using a modified form of Fick's Law,[36]

$$\rho_i U_{x_i} = -\rho D_i \frac{\partial c_i}{\partial x} + \rho_i \sum_{j=1}^{ns} D_j \frac{\partial c_j}{\partial x} \tag{2.12}$$

$$\rho_i U_{y_i} = -\rho D_i \frac{\partial c_i}{\partial y} + \rho_i \sum_{j=1}^{ns} D_j \frac{\partial c_j}{\partial y} \tag{2.13}$$

To complete the system of equations, the individual gases are assumed to be thermally perfect, and the perfect gas equation of state is used,

$$p = \rho R_s T \tag{2.14}$$

$$e_{s_i} = e_{s_i}(T) \tag{2.15}$$

The exact formulation of the species sensible internal energy will be given in the next section. The species densities are constrained such that the sum of the species densities must equal the total density.

2.2 Chemistry Model

A single-step chemistry model consisting of two species was implemented. The model was developed by Khokhlov et al.[37] to simulate a stoichiometric acetylene-air reaction at 100 torr (100 torr = 1/7.6 atm).

$$C_2H_2 + \frac{5}{2}(O_2 + 3.76N_2) \rightarrow 2CO_2 + H_2O + 9.4N_2 \tag{2.16}$$

The model consists of a unimolecular reaction that consumes a fuel, F, representing the acetylene and air mixture, producing a product, P, representing the carbon dioxide, water, and nitrogen.

$$F \rightarrow P \tag{2.17}$$

The rate equation is written in terms of the mass fraction of fuel, Y. It is first order with the rate constant given by an Arrhenius Law,

$$\frac{dY}{dt} = -\rho Y k_f \tag{2.18}$$

$$k_f = A_r e^{(-T_a/T)} \tag{2.19}$$

The energy release due to the combustion is a constant given by

$$q = 35 R_s T_r \tag{2.20}$$

This represents an effective zero-point energy or heat of formation of the fuel species, F. The heat of formation of the product species, P, is zero. The use of a simplified one-step chemistry model, as opposed to a multi-reaction, multi-species model, is done to reduce the chemical integration time while still maintaining an accurate representation of the chemistry in the problem. A multi-species, multi-reaction model can lead to significant increases in the computational time. In some situations, the chemistry integration time can be of the same order of magnitude or greater then the fluid dynamic integration time.[38]

Table 2.1 gives the values of the chemical and gas properties. The molecular weights of the fuel and product are equal and constant. The value of 29.0 was chosen as the average of the molecule weights of the acetylene and air mixture and of the carbon-dioxide, water and nitrogen mixture. The specific heats, c_p and c_v, of both species are equal and constant. The actual values of the specific heats increase as the temperature increases. Since one of the goals of this research is to investigate the basic flow physics, the use of a constant specific heat assists in the formation of constant flow parameters, such as Prandtl number and Lewis number. Also, the use of a constant

Table 2.1: Chemical and Fluid Properties

Property	Value
$\mathcal{M}$	29.0 (g/mol)
R_s	2.8670×10^6 (erg/g-K)
γ	1.250
c_p	1.4335×10^7 (erg/g-K)
c_v	1.1468×10^7 (erg/g-K)
A_r	1.0×10^{12} (cm^3/g-s)
T_r	293 (K)
T_a	$29.3T_r$ (K)
μ_r	2.439×10^{-8} (g/cm-s)
k_r	2.439×10^{-8} (g/cm-s)
D_r	2.439×10^{-8} (g/cm-s)

specific heat reduces the cost of the computation by simplifying the calculation of the temperature. If a function of temperature was implemented, the temperature calculation would be an iterative procedure, increasing the computational time. These parameters were chosen by Khokhlov et al.[37] to fit the measured values of the laminar flame speed, laminar flame thickness, Chapman-Jouget detonation velocity, and the detonation thickness of an acetylene-air mixture for a pressure range of 0.1 to 1.0 atmospheres.

With the specific heats constant, the sensible internal energy of both species becomes c_vT. It is now possible to define the equations for the species internal energies and enthalpies. Both contain the sensible part and the heat of formation.

$$e_Y = c_vT + q \tag{2.21}$$

$$e_P = c_vT \tag{2.22}$$

$$h_Y = c_pT + q \tag{2.23}$$

$$h_P = c_pT \tag{2.24}$$

Taking the above equations and substituting them into equation (2.6) gives the equation for the total internal energy as

$$\rho e_t = \rho c_vT + \frac{1}{2}\rho\left(u^2 + v^2\right) + \rho Yq \tag{2.25}$$

2.3 Transport Properties

2.3.1 Dynamic Viscosity and Thermal Conductivity

The dynamic viscosity, μ, and the thermal conductivity, k, are calculated from power-law functions of temperature,[37]

$$\mu = \mu_r \left(\frac{T}{T_r}\right)^n \tag{2.26}$$

$$k = k_r c_p \left(\frac{T}{T_r}\right)^n \tag{2.27}$$

where $n = 0.7$. These forms of the equations give a Prandtl Number of

$$Pr = \frac{\mu c_p}{k} = \frac{\mu_r}{k_r} \tag{2.28}$$

This allows parametric studies to be done by changing the reference coefficients, μ_r and k_r, to get the desired Prandtl Number.

2.3.2 Mass Diffusion Coefficient

Since in this model the gas contains two species, the binary diffusion coefficients for the two species are equal,[39] $D_Y = D_P$. These coefficients are calculated as power-law functions of temperature and density,[37]

$$D = \frac{D_r}{\rho}\left(\frac{T}{T_r}\right)^n \tag{2.29}$$

With the binary diffusion coefficient in this form the Lewis-Semenov number can be written as

$$Le = \frac{\rho c_p D}{k} = \frac{D_r}{k_r} \tag{2.30}$$

This definition of the Lewis number is the standard way it is defined in aerodynamic texts. Some texts on combustion define the Lewis Number as the reciprocal, so that Le would be equal to k_r/D_r.

For a binary gas, Fick's Law as given by equation (2.12) reduces to

$$\rho_i U_{x_i} = -\rho D \frac{\partial c_i}{\partial x} \tag{2.31}$$

$$\rho_i U_{y_i} = -\rho D \frac{\partial c_i}{\partial y} \tag{2.32}$$

Using this form of Fick's Law, the definitions of the enthalpies as given in equation (2.21), and the fact that the sum of the mass fluxes must be zero, ($\rho_Y U_Y = -\rho_P U_P$), the heat flux terms from

equation (2.10) can be written as

$$q_x = -k\frac{\partial T}{\partial x} - \rho D q \frac{\partial Y}{\partial x} \tag{2.33}$$

$$q_y = -k\frac{\partial T}{\partial y} - \rho D q \frac{\partial Y}{\partial y} \tag{2.34}$$

2.4 Numerical Procedure - LCPFCT

The convective terms of the Navier-Stokes equations are integrated in time using a parallel version of the Flux Corrected Transport model, LCPFCT.[40] The viscous, conductive, and mass diffusion terms can be treated as either source terms or can be added in separately after the convective terms are integrated. The pressure terms are always included as source terms for the LCPFCT routine. The species production term, $\dot{\omega}_i$, is integrated separately.

The LCPFCT routine is a cell centered, finite volume convection routine which is second-order in time and fourth-order in space. The evaluation of the source terms, the viscous, conduction, and mass diffusion fluxes, are second order, which reduces the entire scheme to second order in space. LCPFCT is a nonlinear, monotone method designed to calculate sharp gradients with minimal numerical diffusion. The flux quantity, for example ρ, is convected to an intermediate value in a predictor step. Diffusion is added to guarantee that the new density is monotonic. This value is then corrected by an anti-diffusion term to remove the added diffusion and advance the density to the new time. The amount of anti-diffusion that is added depends on the local values of the flux term making the method nonlinear. The amount of anti-diffusion added also ensures that no new minima or maxima are generated, or adds to those that already exist.

The LCPFCT routine solves the general, one-dimensional, continuity equation as given by :

$$\frac{\partial \psi}{\partial t} = -\frac{1}{r^{\alpha-1}}\frac{\partial (r^{\alpha-1}\psi u)}{\partial r} - \frac{1}{r^{\alpha-1}}\frac{\partial (r^{\alpha-1}B_1)}{\partial r} + C_2\frac{\partial B_2}{\partial r} + B_3 \tag{2.35}$$

The density flux terms in the Navier-Stokes equations, ρ, ρu, ρv, and ρe_t, are represented by ψ. The α represents the coordinate system used, 1 for Cartesian, 2 for cylindrical, and 3 for spherical, with r being a generalized coordinate direction. The terms B_1, B_2, and B_3 represent source terms, such as viscous stress terms or heat flux terms. The C_2 is a constant.

LCPFCT first convects the the above general continuity equation to get a temporary term ψ_i^*

$$\Lambda_i^o \psi_i^* = \Lambda_i^o \psi_i^o - \Delta t \psi_{i+\frac{1}{2}}^o A_{i+\frac{1}{2}} \Delta u_{i+\frac{1}{2}} + \Delta t \psi_{i-\frac{1}{2}}^o A_{i-\frac{1}{2}} \Delta u_{i-\frac{1}{2}} \tag{2.36}$$

where Λ is the cell volume per unit depth, A is the cell interface area per unit depth, and Δu is the difference between the flow velocity and the grid motion for a moving grid. For the stationary

Cartesian grid that was used for this study, $A = 1$, $\Lambda_i = r_{i+\frac{1}{2}} - r_{i-\frac{1}{2}}$, and Δu is equal to the fluid velocity. Since LCPFCT is a cell centered algorithm, the subscript i refers to the cell centers. The subscripts $i \pm 1/2$ refer to points on the cell interfaces. These cell interface values are calculated as average values of the cell centered values that they are located between. The source terms are then added in to calculate a transported density, ψ_i^T.

$$\begin{aligned} \Lambda_i^o \psi_i^T = \Lambda_i^o \psi_i^* &+ \frac{1}{2}\Delta t A_{i+\frac{1}{2}} \left(B_{1,i+1} + B_{1,i}\right) - \frac{1}{2}\Delta t A_{i-\frac{1}{2}} \left(B_{1,i} + B_{1,i-1}\right) \\ &+ \frac{1}{4}\Delta t C_{2,i} \left(A_{i+\frac{1}{2}} + A_{i-\frac{1}{2}}\right) \left(B_{2,i+1} - B_{2,i-1}\right) \\ &+ \Delta t \Lambda_i^o B_{3,i} \end{aligned} \tag{2.37}$$

The diffusion is now added to obtain the transported-diffused density, $\tilde{\psi}_i$.

$$\Lambda_i^n \tilde{\psi}_i = \Lambda_i^o \psi_i^T + \nu_{i+\frac{1}{2}} \Lambda_{i+\frac{1}{2}} \left(\psi_{i+1}^o - \psi_i^o\right) - \nu_{i-\frac{1}{2}} \Lambda_{i-\frac{1}{2}} \left(\psi_i^o - \psi_{i-1}^o\right) \tag{2.38}$$

where the diffusion term, ν, is given by

$$\nu_{i+\frac{1}{2}} = \frac{1}{6} + \frac{1}{3}\epsilon_{i+\frac{1}{2}}^2 \tag{2.39}$$

$$\epsilon_{i+\frac{1}{2}} = A_{i+\frac{1}{2}} \Delta u_{i+\frac{1}{2}} \frac{\Delta t}{2} \left(\frac{1}{\Lambda_i^n} + \frac{1}{\Lambda_{i+1}^n}\right) \tag{2.40}$$

The anti-diffusion flux, $f_{i+\frac{1}{2}}^{ad}$, is calculated from the transported density, ψ^T, from equation (2.37). This density is used so that there is no residual diffusion for the case when the fluid velocity is equal to the grid velocity ($\Delta u_{i+\frac{1}{2}} = 0$). This would be the case if the transported-diffusion density, $\tilde{\psi}$, was used instead.

$$f_{i+\frac{1}{2}}^{ad} = \mu_{i+\frac{1}{2}} \Lambda_{i+\frac{1}{2}} \left(\psi_{i+1}^T - \psi_i^T\right) \tag{2.41}$$

where the anti-diffusion term, μ, is given by

$$\mu_{i+\frac{1}{2}} = \frac{1}{6} - \frac{1}{6}\epsilon_{i+\frac{1}{2}}^2 \tag{2.42}$$

The diffusion term, ν, and the anti-diffusion term, μ, were chosen by Boris and Book[41] to reduce the phase errors for the convection to be fourth order accurate. The anti-diffusion flux must now be corrected to ensure that no new minima or maxima are created. This is accomplished by applying a flux limiter to obtain the corrected anti-diffusion flux, $f_{i+\frac{1}{2}}^c$.

$$\begin{aligned} f_{i+\frac{1}{2}}' &= \min\left[|f_{i+\frac{1}{2}}^{ad}|, S_{i+\frac{1}{2}} \Lambda_{i+1}^n \left(\tilde{\psi}_{i+2} - \tilde{\psi}_{i+1}\right), S_{i+\frac{1}{2}} \Lambda_i^n \left(\tilde{\psi}_i - \tilde{\psi_{i-1}}\right)\right] \\ f_{i+\frac{1}{2}}^c &= S_{i+\frac{1}{2}} \max\left\{0, f_{i+\frac{1}{2}}'\right\} \end{aligned} \tag{2.43}$$

where $S_{i+\frac{1}{2}}$ is given by

$$S_{i+\frac{1}{2}} = \bar{S} \times sgn\left(\tilde{\psi_{i+1}} - \tilde{\psi_i}\right) \tag{2.44}$$

In theory $\bar{S}$ should be equal to one. In practice the value used is slightly less then one, around 0.999 to 0.997, to provide residual diffusion to be retained by the solution. Then, from the corrected anti-diffusion flux, the new density, ψ_i^n, is calculated by

$$\psi_i^n = \tilde{\psi_i} - \frac{1}{\Lambda_i^n}\left(f_{i+\frac{1}{2}}^c - f_{i-\frac{1}{2}}^c\right) \tag{2.45}$$

To obtain second order accuracy in time, the density flux terms from the Navier-Stokes equation, ρ, ρu, ρv, ρe_t, and n_i are convected to the half time-step, $t^{\frac{1}{2}} = t^o + \frac{1}{2}\Delta t$. These new half-step values are used to evaluate the density fluxes for the entire time step, $t^n = t^o + \Delta t$.

To use the one-dimensional LCPFCT on the two-dimensional Navier-Stokes equations, the equations are split into two sets of equations, one for the x direction and the other for the y direction. Each direction is then integrated separately. To avoid biasing one direction over the other, the integration for each time step is switched. For one time step the x direction is done first and then the y, for the next time step the y is integrated first then the x. To perform this direction splitting, the time step must be small enough so that the cell values do not change rapidly over the time step.[40]

2.5 Time Step Determination

The time step for explicit methods, such as LCPFCT, are restricted due to stability requirements. These can be derived as in Hoffman[42] for the linear stability of parabolic equations. The time step is restricted to be the minimum value of the convective, viscous, conductive, and diffusive time steps.

$$\Delta t = (CFL)\min\left(\Delta t_{conv}, \Delta t_{visc}, \Delta t_{cond}, \Delta t_{diff}\right) \tag{2.46}$$

where CFL represents the Courant-Friedrichs and Lewy number. For each new time step, the above equation is evaluated over the entire grid. For positivity of the LCPFCT routine, the CFL number is limited to be less then one-half.[40] It was determined that for the flame calculations, the CFL number needed to be less then 0.25 for stability. A value of 0.2 was used for all calculations.

The convective time step is determined by

$$\Delta t_{conv} = min\left(\frac{\Delta x_{i,j}}{|u_{i,j}| + c_{i,j}}, \frac{\Delta y_{i,j}}{|v_{i,j}| + c_{i,j}}\right) \tag{2.47}$$

The viscous time step is determined by

$$\Delta t_{visc} = min\left(\frac{\Delta x_{i,j}^2}{2\nu_{i,j}}, \frac{\Delta y_{i,j}^2}{2\nu_{i,j}}\right) \tag{2.48}$$

where ν is the kinematic viscosity coefficient. The thermal conduction time step is determined by

$$\Delta t_{cond} = min\left(\frac{\Delta x_{i,j}^2}{2\alpha_{i,j}}, \frac{\Delta y_{i,j}^2}{2\alpha_{i,j}}\right) \tag{2.49}$$

where α is the thermal diffusivity. The time step due to the mass diffusion is given by

$$\Delta t_{diff} = min\left(\frac{\Delta x_{i,j}^2}{2D_{i,j}}, \frac{\Delta y_{i,j}^2}{2D_{i,j}}\right) \tag{2.50}$$

where D is the binary mass diffusion coefficient. The limiting time scale was determined to be the convective time-step in the burned region.

2.6 Chemistry Integration

After LCPFCT has solved the convective part of the Navier-Stokes equations the chemistry part is integrated. The chemical source term, $\dot{\omega}_i$ appears only in the species continuity equation (2.5). The other conserved quantities, ρ, ρu, ρv, and ρe_t, are held constant during the chemistry integration. The chemical reactions do not change the total internal energy, ρe_t, as given by equation (2.25) but only convert the chemical energy, $\rho Y q$, into sensible energy, $\rho c_v T$.

From the chemical rate equation, (2.18), the rate constant defined in equation (2.19) is evaluated at the current temperature. The resulting ordinary differential equation is then integrated in time to give the new species fuel mass fraction as

$$Y_i^n = Y_i^o exp\left(-\rho k_f \Delta t\right) \tag{2.51}$$

With the new fuel mass fraction found from the above equation, the product mass fraction is found from $P = 1 - Y$ since the sum of the mass fractions must equal one. The new number densities are calculated from the mass fraction of fuel as

$$n_Y = \frac{\rho Y N_a}{\mathcal{M}} \tag{2.52}$$

$$n_P = \frac{\rho(1-Y)N_a}{\mathcal{M}} \tag{2.53}$$

The temperature and pressure are updated due to the reaction. From the equation for the definition of the total internal energy (2.6) the temperature can be found as

$$T^n = \frac{\rho e_t - \frac{1}{2}\rho\left(u^2 + v^2\right) - \rho Y^n q}{\rho c_v} \tag{2.54}$$

The pressure can be found from the equation of state (2.14).

2.7 Boundary Conditions

The Navier-Stokes equations control the fluid dynamics of the system. The boundary conditions are what defines the system. These conditions tell the equations where there are walls, inflows, outflows, etc. The boundary conditions control the solution to the problem.

The boundary conditions for subsonic inflows, subsonic outflows and walls were calculated using the characteristic method of Poinsot and Lele[43] developed for a three-dimensional calorically perfect gas. Their method for boundary conditions of the Navier-Stokes equations is an extension on the Euler method of Thompson.[44,45] This method uses the Navier-Stokes equations to solve for the boundary variables that are not specified. It does this by calculating the characteristic waves that are leaving and entering the system and using these waves to calculate the variables that are not known.

Using the characteristic analysis in Thompson,[44] the Navier Stokes equations are written for a two-dimensional system as[43] :

$$\frac{\partial \rho}{\partial t} + d_1 + \frac{\partial(\rho v)}{\partial y} = 0 \tag{2.55}$$

$$\frac{\partial(\rho u)}{\partial t} + u d_1 + \rho d_3 + \frac{\partial(\rho u v)}{\partial y} = \frac{\partial \tau_{xx}}{\partial x} + \frac{\partial \tau_{xy}}{\partial y} \tag{2.56}$$

$$\frac{\partial(\rho v)}{\partial t} + v d_1 + \rho d_4 + \frac{\partial(\rho v v)}{\partial y} = -\frac{\partial p}{\partial y} + \frac{\partial \tau_{yx}}{\partial x} + \frac{\partial \tau_{yy}}{\partial y} \tag{2.57}$$

$$\begin{aligned} \frac{\partial(\rho e_t)}{\partial t} &+ \frac{1}{2}\left(u^2 + v^2\right) d_1 + \frac{d_2}{\gamma - 1} + \rho u d_3 + \rho v d_4 \\ &+ \frac{\partial(\rho e_t v)}{\partial y} = -\frac{\partial(pv)}{\partial y} - \frac{\partial q_x}{\partial x} - \frac{\partial q_y}{\partial y} \\ &+ \frac{\partial(u\tau_{xx} + v\tau_{xy})}{\partial x} + \frac{\partial(u\tau_{yx} + v\tau_{yy})}{\partial y} \end{aligned} \tag{2.58}$$

It is assumed that the x-direction is normal to the boundaries. The d_i terms contain the values for the derivatives in the x direction. They are given by:[44]

$$d_1 = \frac{1}{c^2}\left[\Psi_2 + \frac{1}{2}\left(\Psi_1 + \Psi_4\right)\right] \tag{2.59}$$

$$d_2 = \frac{1}{2}\left(\Psi_1 + \Psi_4\right) \tag{2.60}$$

$$d_3 = \frac{1}{2\rho c}\left(\Psi_4 - \Psi_1\right) \tag{2.61}$$

$$d_4 = \Psi_3 \tag{2.62}$$

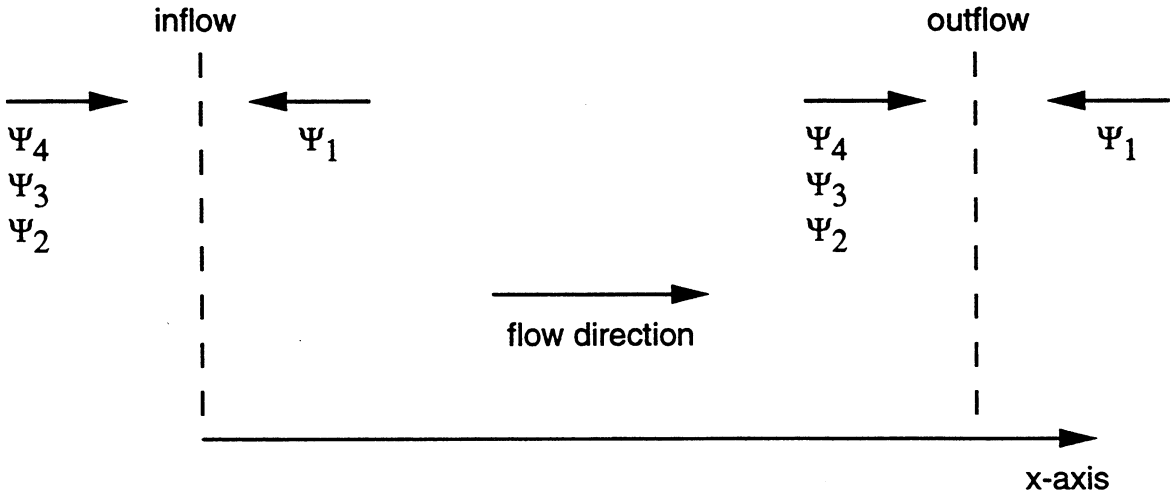

Figure 2.1: Characteristic Wave Configuration

The Ψ_i terms are the amplitudes of the characteristic waves. These waves are shown in Figure 2.1 for an the inflow and outflow configuration. The waves Ψ_2 , Ψ_3, and Ψ_4 move in the positive x direction. The wave Ψ_1 moves in the negative x direction. These terms are given by :

$$\Psi_1 = (u-c)\left(\frac{\partial p}{\partial x} - \rho c \frac{\partial u}{\partial x}\right) \tag{2.63}$$

$$\Psi_2 = u\left(c^2 \frac{\partial \rho}{\partial x} - \frac{\partial p}{\partial x}\right) \tag{2.64}$$

$$\Psi_3 = u\left(\frac{\partial v}{\partial x}\right) \tag{2.65}$$

$$\Psi_4 = (u+c)\left(\frac{\partial p}{\partial x} + \rho c \frac{\partial u}{\partial x}\right) \tag{2.66}$$

The waves propagating from the inside of the domain out of the boundaries are calculated using one sided finite differencing. To calculate the waves moving into the system from the outside, Poinsot and Lele[43] used a one-dimensional analysis to estimate their values. In terms of the primitive variables, ρ, u, v, p, and T, these equations are written as[44] :

$$\frac{\partial \rho}{\partial t} + d_1 = 0 \tag{2.67}$$

$$\frac{\partial u}{\partial t} + d_3 = 0 \tag{2.68}$$

$$\frac{\partial v}{\partial t} + d_4 = 0 \tag{2.69}$$

$$\frac{\partial p}{\partial t} + d_2 = 0 \tag{2.70}$$

$$\frac{\partial T}{\partial t} + \frac{T}{\rho c^2}\left[-\Psi_2 + \frac{1}{2}(\gamma-1)(\Psi_1+\Psi_4)\right] = 0 \tag{2.71}$$

From these equation, relations between the incoming and outgoing waves can be established based

on the set values at the boundaries.

Saint-Martin-Tillet[46] implemented these boundary conditions for nonreacting flow in a two-dimensional channel. He modeled the boundary conditions by considering the one-dimensional Euler equations alone as given by equations (2.67 - 2.71). This worked for the wall boundary and for the inflow if it consisted of parallel flow, $v = 0$. It also worked well for the outflow in an inviscid region of the flow, such as near the centerline of a channel. Problems arose for inflows that were not parallel, such as flow at a stagnation point, and for the outflow of a viscous region, such as a boundary layer. These problems were corrected by expanding the boundary conditions to two dimensions and solving equations (2.55 - 2.58), including all the viscous terms.

2.7.1 Subsonic Inflow Boundary Condition

For an inflow boundary, it is common to define the velocities and a thermodynamic variable, such as temperature. For a reacting case, the inflow mass fractions are also specified. With the primitive variables u, v, and T specified the boundary equations (2.56), (2.57), and (2.58) do not need to be solved, only the equation of the global mass density, (2.55) needs to be solved.

For an inflow, the wave Ψ_1 is leaving the domain and the other waves are entering, therefore Ψ_1 is the only wave that can be calculated. To obtain values for the waves that are entering the domain through the boundary, the one-dimensional equations (2.67 - 2.71) are used to define the incoming waves in terms of the outgoing wave. Imposing the velocities (u and v are set) gives $d_3 = 0$ and $d_4 = 0$. Using equations (2.61) and (2.62), these conditions define the the wave amplitudes Ψ_3 and Ψ_4 as

$$\Psi_3 = 0 \tag{2.72}$$

$$\Psi_4 = \Psi_1 \tag{2.73}$$

From equation (2.71), imposing the temperature and making use of the above equations gives the expression for Ψ_2 as

$$\Psi_2 = (\gamma - 1)\Psi_1 \tag{2.74}$$

These values are used to calculate d_1 which is used in the calculation of the new inflow density. Once the new global density is determined the pressure is obtained from the equation of state. The inflow number densities are calculated from the specified inflow mass fraction and the new global density. The total energy density is calculated from equation (2.25).

2.7.2 Wall Boundary Conditions

For the case of a solid wall, the no-slip condition applies. This means that the two components of velocity are zero at the wall, $u = v = 0$. Using $u = 0$ in equations (2.63) and (2.65) gives the waves Ψ_2 and Ψ_3 as

$$\Psi_2 = \Psi_3 = 0 \tag{2.75}$$

From the one-dimensional equation for u, (2.68), $d_3 = 0$ which provides a relationship from the remaining two waves as

$$\Psi_1 = \Psi_4 \tag{2.76}$$

From Figure 2.1, if the inflow is replaced by a wall, then the wave Ψ_1 is calculated from the computational system. If the outflow is replaced by a wall then the wave Ψ_4 is calculated.

For the wall temperature, there are three possible numerical boundary conditions. The first is the isothermal wall where the wall temperature is held constant. The second is the adiabatic wall where the heat flux to the wall is zero. The third possible numerical boundary condition for the temperature at the wall is the convectively cooled or heated wall. The wall temperature is calculated based on an energy balance between the wall heat flux and the convective heat flux. If the wall has a non-zero thickness, then modeling of the heat conduction through the wall is required. This third type will not be discussed here.

For the mass fraction at the wall there are three possibilities. The first is an equilibrium wall where the mass fractions are calculated based on their chemical equilibrium value at the wall temperature. The second is a non-catalytic wall, where the mass flux to the wall, as given by Fick's' Law, is zero. For the binary gas system this condition reduces to a zero mass fraction gradient at the wall. The third condition, lying in between the first two conditions, is for a catalytic wall. For this boundary condition the species mass fractions are calculated based on a combination of the wall material properties and mass diffusion flux from the fluid. This third type will not be discussed here. For an excellent explanation of catalytic wall boundary conditions see Grumet.[47]

Using the first two temperature and mass fractions boundary conditions, four sets of wall conditions can be formed.

- For an isothermal, non-catalytic wall, the temperature is specified and the species mass fractions are found by setting the mass fraction gradients at the wall to zero.
- For an isothermal equilibrium wall, the temperature is specified. The species mass fractions are calculated based on the wall temperature.

- For an adiabatic, non-catalytic wall, the mass fraction is found by setting the gradient at the wall to zero. The temperature is found by setting the temperature gradient at the wall to zero. This has the effect of making the heat flux to the wall zero.

- For an adiabatic, equilibrium wall, the wall conditions need to be calculated based on the condition of zero heat flux from equation (2.33). Assuming the wall is normal to the x direction this gives

$$-k_w \left(\frac{\partial T}{\partial x}\right)_w - \rho_w D_{wq} \left(\frac{\partial Y}{\partial x}\right)_w = 0 \tag{2.77}$$

  As a first estimate, the the old values of the wall mass fraction are used to calculate the species gradient. The above equation can then be used to iterate on the new wall temperature. An iteration method is required since the species mass fraction is a function of the wall temperature.

With the wall temperature, mass fraction, and velocities known, only equation (2.55) for the density at the wall needs to be solved. With the new wall density, the equation of state is used to calculate the wall pressure. The definition of mass fraction is used to calculate the new number densities. The total energy density at the wall is calculated from equation (2.25).

2.7.3 Subsonic Outflow Boundary Conditions

For the subsonic outflow, pressure waves can both enter and leave the computational domain through the boundary. The wave, Ψ_1, that is entering the domain carries information into the domain from the downstream conditions. The other waves, Ψ_2, Ψ_3, and Ψ_4, are leaving the system and can be calculated from the interior grid points. The wave entering the system needs to be estimated. Poinsot and Lele did this by specifying a constant pressure at infinity and calculating the entering wave as[43]

$$\Psi_1 = K(p - p_\infty) \tag{2.78}$$

The constant, K, taken from Rudy and Strikwerde,[48] is given by

$$K = \frac{\sigma c(1 - \overline{M}^2)}{L} \tag{2.79}$$

where $\overline{M}$ is the maximum Mach number in the flow, L is a characteristic length such as channel height or plate length, and σ is a constant equal to 0.25.[43]

For a viscous problem, there are additional viscous boundary conditions that are required.[43] These viscous boundary conditions for a two-dimensional flow are that the derivative normal to the

boundary of the tangential shear stress, τ_{xy} and the normal heat flux, q_x, are zero. These conditions are implemented directly into equations (2.55 - 2.58) when they are solved to get the outflow fluxes. The boundary condition for the species are obtained from simple extrapolation of the mass fractions for the interior.

Calculating the outflow boundary conditions using the above methods works for single and multispecies nonreacting flows. When the chemistry was turned on and the flow allowed to react the outflow boundary conditions became unstable when the flow was treated as two-dimensional. For the one-dimensional reacting case the boundary conditions described above were stable. To alleviate the unstable problem the energy density and mass density were extrapolated at the outflow boundary. The velocities were calculated using equations (2.56) and (2.57) so that the characteristic waves could be accounted for. The species mass fractions were also extrapolated. One possible reason for the instability is that the boundary condition model was developed for a non-reacting, calorically perfect gas.

2.8 Initial Conditions

The initial channel configuration is shown in figure 2.2. The channel is 8.2 cm in length and 0.127 cm in width. The left and bottom sides are solid walls. The top of the domain is a symmetry condition and the right side is an outflow. This simulates a rectangular channel that is closed on one end and open at the other. The symmetry condition is used here since the gravitational terms have been neglected. If the gravitational terms were included, then the orientation of the channel would be important. If the tube was horizontal, buoyancy effect would distort the flame and a symmetry condition could not be used. If the channel was vertical, then a symmetry could be used.

Starting at the closed end, the first 0.3 cm is set to the adiabatically burned conditions. These conditions come from laminar flame theory that will be discussed in section 4.2. From 0.3 cm to the end of the channel, the gas is at the unburned conditions. The values of the properties in the burned and unburned region are given in Table 2.2.

Table 2.2: Initial Conditions

Value	Unburned	Burned
T (K)	293	2344
p (dynes)	133322	133322
ρ (g/cm^3)	1.587×10^{-4}	1.984×10^{-5}
Y	1	0
u (cm/s)	0	0
v (cm/s)	0	0

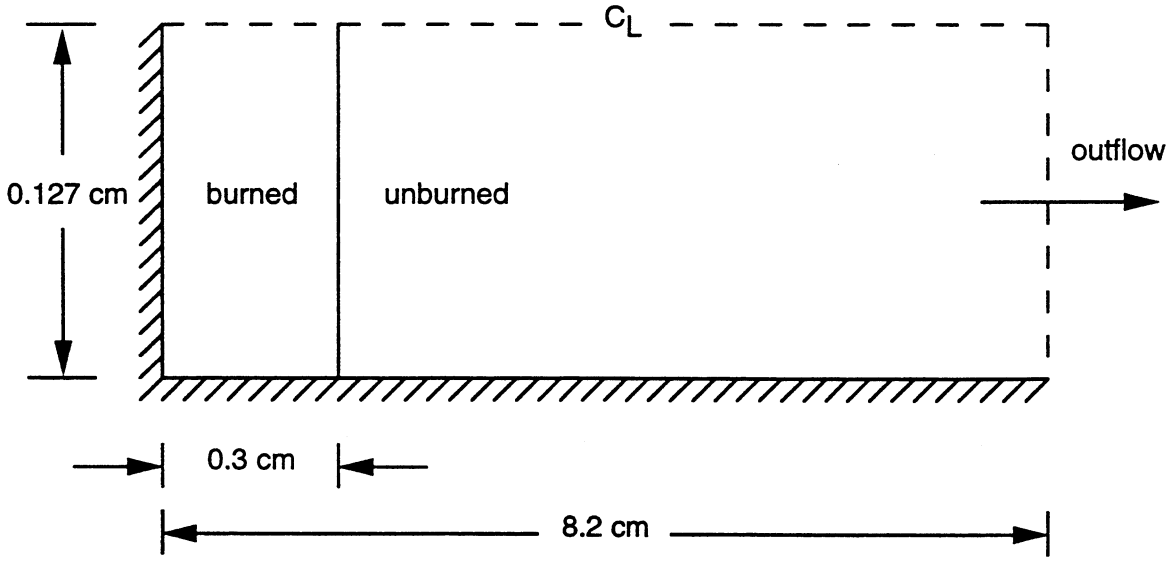

Figure 2.2: Two-Dimensional Channel Configuration

Chapter 3

Code Validation

The present chapter consists of three sections, each with various subsections. The first section describes previous uses of the parallel code. The second section contains results for a non-reacting flow. The third section incorporates the chemistry with the fluid dynamics.

3.1 Past Code Work

CMRFAST2D was used successfully in previous works. J. Weber[38] parallelized an Euler code and added chemical reaction to study the two dimensional detonation wave problem using a hydrogen-air chemistry. Y. Weber[49] added viscosity and thermal conductivity to the Euler code and calculated the interaction of a reflected shock with a boundary layer in a shock tube. Piana[50] added the effects of mass diffusion to create a fully reactive Navier-Stokes code. Nguyen et al.[51] used a non-reacting version to study the interaction of a vortex with a boundary layer in a channel containing ribs.

3.2 Non-Reaction Code Validation

The non-reacting parts of the code were tested to ensure that they are working properly. These parts consist of the viscous, thermal conduction, mass diffusion, and Euler convection routines.

3.2.1 Gaussian Profile - Mass Diffusion

The convection, viscosity, and thermal conductivity are turned off. The pressure and temperature are held constant at 100 torr and 293 K respectively, which fixes the mass diffusion coefficient and global density. This reduces the governing equations to just the two species continuity equations.

Table 3.1: Gaussian Profile Parameters

Parameter	Value
ρ	1.723×10^{-5} (g/cm^3)
D	0.402 (cm^2/s)
t_1	0.15 (s)
n_1	7.876×10^{17} (1/cm^3)

Making use of Fick's Law and reducing to one dimension, equation (2.5) becomes :

$$\frac{\partial n_i}{\partial t} = D\frac{\partial^2 n_i}{\partial x^2} \tag{3.1}$$

Initially, species 1 is deposited along the x axis from -0.1 to 0.1 at a value equal to the global density, and is set to zero everywhere else. This species density spreads out due to the diffusion and becomes Gaussian over time. The theoretical solution for the density profiles in time and space for the Gaussian diffusion problem is given by:[52]

$$n(x,t) = n_1 \left(\frac{-t}{t_1}\right)^{\frac{1}{2}} e^{\left(\frac{-x^2}{4Dt}\right)} \tag{3.2}$$

In this equation, t_1 and n_1 refer to a reference state that occurs after the initial start of the diffusion process. For this problem, the reference state was chosen at 0.15 s. The number density for the reference state at $x = 0$ is $n_1 = n(0, t_1)$. Table 3.1 gives the values of the parameters used for this calculation. Figure 3.1 shows the numerically generated Gaussian profiles versus the theoretical values at 0.3 s and 0.5 s for the first species. The symbols represent numerical values and the lines represent theoretical values. The cell size is constant at 0.02 cm. The code and theory agree well.

3.2.2 Heat Flow Problem - Thermal Conductivity

For this problem the viscosity, convection, and mass diffusion are turned off. The gas used was air with a constant density of 1.548×10^{-4} g/cm^3 which is based on a pressure of 100 torr and a temperature of 300 K. The thermal conductivity was also set constant, at 2650 erg/cm-s-K, which was calculated from Sutherland's Law[53] at 300 K. With these assumptions, the energy equation (2.4) in one dimension reduces to :

$$\frac{\partial T}{\partial t} = \left(\frac{\lambda}{\rho c_v}\right)\frac{\partial^2 T}{\partial x^2} \tag{3.3}$$

This is the classical form of the heat conduction equation.

Initially, the temperature of the domain was constant at 300 K. Then the side at x = 0 was increased impulsively to 600 K and held at that temperature. The classical solution of the conduction

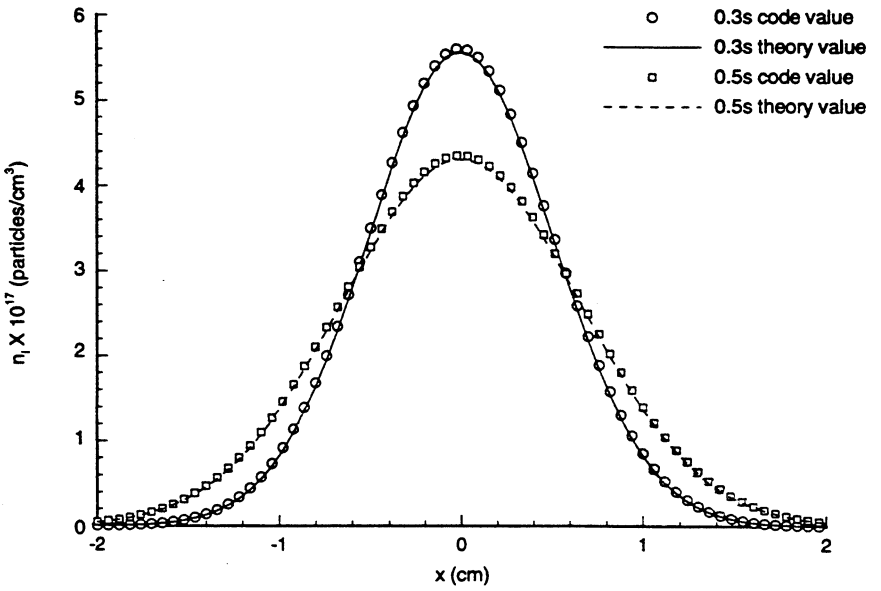

Figure 3.1: Gaussian Profiles for times 0.3 s and 0.5 s.

equation from Hildebrand[54] for these conditions reduces to :

$$\begin{aligned} T(x,t) &= [T_1 + (T_2 + T_1)\frac{x}{L}] \\ &\times [\sum_{n=1}^{\infty} \frac{2}{n\pi}(T_2 - T_1)\sin\frac{n\pi x}{L} e^{-n^2 kt}] \end{aligned} \tag{3.4}$$

where $T_1 = 600$ K, $T_2 = 300$ K, $L = 1.0$ cm, and k is given by :

$$k = \left(\frac{\pi\lambda}{\rho c_v L}\right)^2$$

Figure 3.2 shows the result of the integration for a time of 12.2 ms. The grid cell size is 0.016 cm. The solid line is the theoretical value and the symbols are the numerical values. The summation in the theoretical equation was taken to n = 600. The plot shows an excellent agreement between the theoretical and numerical temperatures.

3.2.3 Stokes' First Problem - Viscosity

For this case, the convection, thermal diffusion, and mass diffusion are turned off. The density, pressure, and temperature are all held constant. The viscosity coefficient is also held constant at 1.846×10^{-4} g/cm-s, which is the value at 300 K from Sutherland's Law.[53] The density is 1.548×10^{-4}

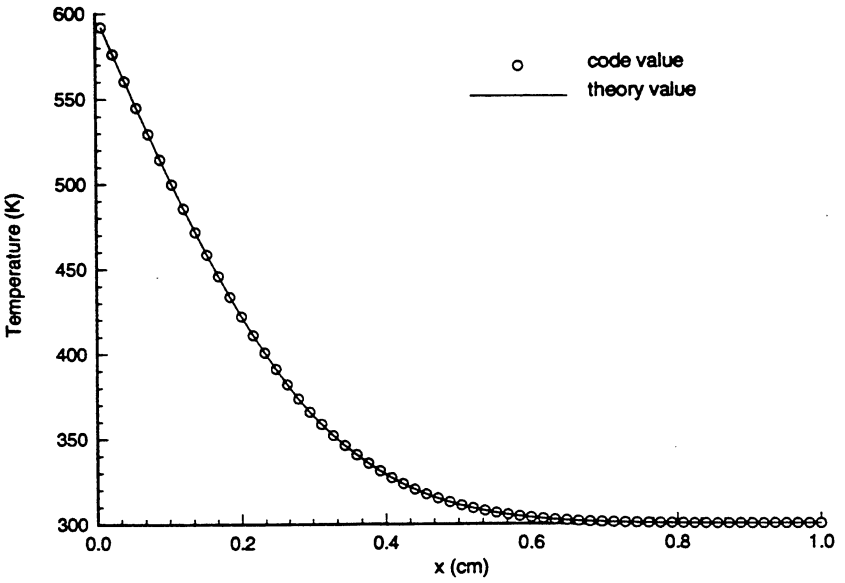

Figure 3.2: Temperature Profile for the One-Dimensional Thermal Conduction Equation.

g/cm^3. In one dimension, the momentum equation reduces to

$$\frac{\partial u}{\partial t} = \frac{4}{3}\nu\frac{\partial^2 u}{\partial y^2} \tag{3.5}$$

Initially the air in the domain was at rest. Then at y = 0, the velocity was impulsively increased to 600 cm/s and held at this speed. The classical solution to this problem is given by Schlichting[55] as

$$\frac{u}{U_o} = \frac{2}{\sqrt{\pi}}\int_{\eta}^{\infty} exp(-\eta^2)d\eta \tag{3.6}$$

where $U_o = 600$ cm/s, and η is the normalized length scale given by

$$\eta = \frac{y}{2\sqrt{\nu t}} \tag{3.7}$$

Figure 3.3 shows the normalized calculated values as compared to the classical solution. The agreement is excellent. The grid resolution for this problem is 0.006 cm. An interesting result of this problem is that the boundary layer thickness is proportional to the square root of the product of the kinematic viscosity and time, $\delta \propto \sqrt{\nu t}$. This result, and the results for varying edge flow velocity in Appendix A, will be useful in the discussion of the formations of the boundary layer in the channel.

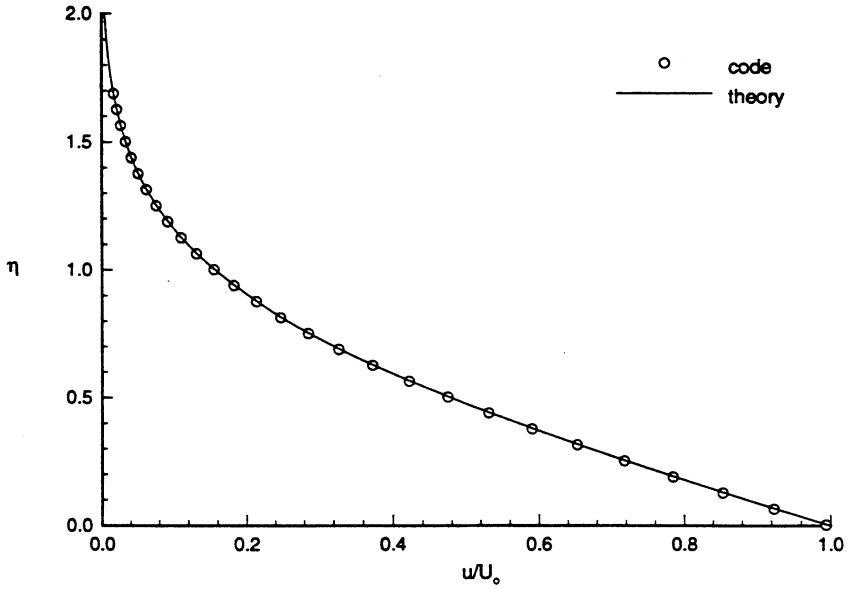

Figure 3.3: Normalized velocity profile for Stokes' first problem.

3.2.4 One Dimensional Shock Wave - Convection

For this case, the viscosity, thermal conduction, and mass diffusion are turned off. This reduces the Navier-Stokes equations to the Euler equations. A one dimensional shock tube problem for air was set up with an initial diaphragm pressure ratio, p_4/p_1, of 120. The initial temperature was uniform at 300 K. The theoretical solution to this problem can be found in Anderson.[56] From the diaphragm pressure ratio, the pressure ratio across the shock, p_2/p_1, can be calculated from

$$\frac{p_4}{p_1} = \frac{p_2}{p_1}\left\{1 - \frac{(\gamma-1)((p_2/p_1)-1)}{\sqrt{2\gamma\left[2\gamma+(\gamma+1)((p_2/p_1)-1)\right]}}\right\}^{-\frac{2\gamma}{\gamma-1}} \tag{3.8}$$

where the conditions in region 2 are behind the wave and the conditions in region 1 are ahead of the wave. Once the pressure ratio is calculated, the density and temperature ratios across the shock are calculated from

$$\frac{\rho_2}{\rho_1} = \left[1+\frac{\gamma+1}{\gamma-1}\left(\frac{p_2}{p_1}\right)\right] / \left[\frac{\gamma+1}{\gamma-1}+\frac{p_2}{p_1}\right] \tag{3.9}$$

$$\frac{T_2}{T_1} = \frac{p_2}{p_1}/\frac{\rho_2}{\rho_1} \tag{3.10}$$

Table 3.2: One-Dimension Shock Properties

Value	Code	Theory
p_2/p_1	6.75	6.75
ρ_2/ρ_1	3.26	3.25
T_2/T_1	2.07	2.07
u_p	585.1 m/s	584.0 m/s

The piston velocity, u_p, is the velocity that the shock wave induces into the flow behind it. It is calculated from

$$u_p = a_1 \left(1 - \frac{\rho_1}{\rho_2}\right) \sqrt{\frac{\gamma+1}{2\gamma}\left(\frac{p_2}{p_1} - 1\right) + 1} \tag{3.11}$$

Figure 3.4 shows the shock pressure ratio, density ratio and piston velocity. Table 3.2 gives the calculated shock properties versus the theoretical calculated values. The grid resolution for the numerical solution is 0.03 cm. As can be seen, all the code values compare to well with 1% of the theoretical values.

3.3 Reacting Code Validation

For these tests the chemistry routine was active in the integration. The chemistry routine was tested for a constant volume combustion and a one-dimensional detonation wave. The results for a one-dimensional laminar flame will be presented in the next chapter.

3.3.1 Constant Volume Combustion - Chemistry Alone

For this case, the convection is turned off along with all the transport properties. The mass density, ρ, and the total energy density, ρe_t, are constants. The energy equation then reduces to

$$c_v T_f + q Y_f = c_v T_i + q Y_i \tag{3.12}$$

The initial conditions for temperature and pressure were 500 K and 100 torr respectively. The initial mass fraction, Y_i, was set to 1. Assuming that the reaction goes to completion, $Y_f = 0$, the above equation gives a final temperature of 3063.75 K. By using the perfect gas law, and the fact that density is constant, the final pressure becomes 8.17×10^5 torr.

Figure 3.5 shows plots of the temperature and pressure versus time. The code generated final values of temperature and pressure are 3063.75 K and 8.17×10^5 torr. These match the expected values exactly. This test shows that the chemistry integration routine is working properly.

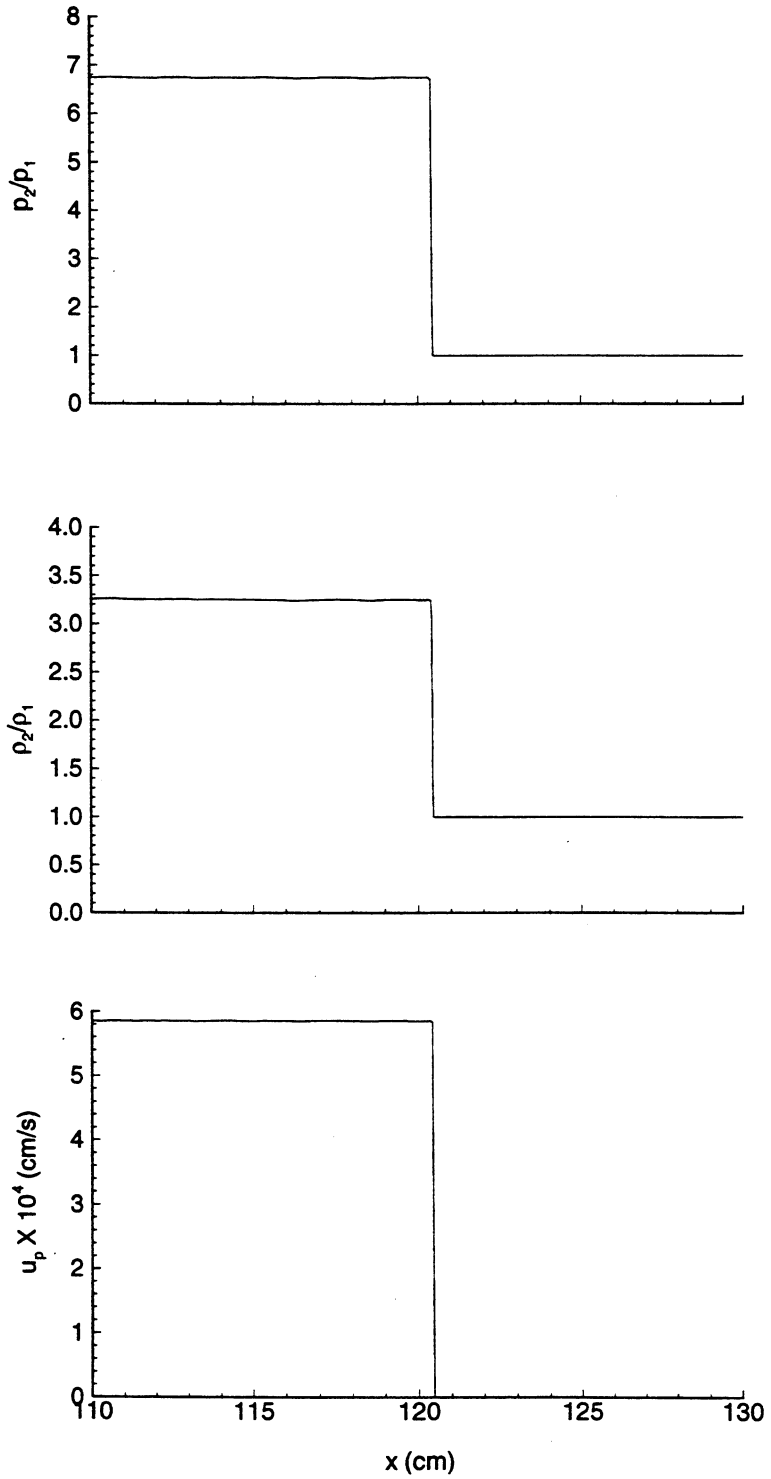

Figure 3.4: Shock wave profiles for air in a shock tube with initial pressure ratio of 120.

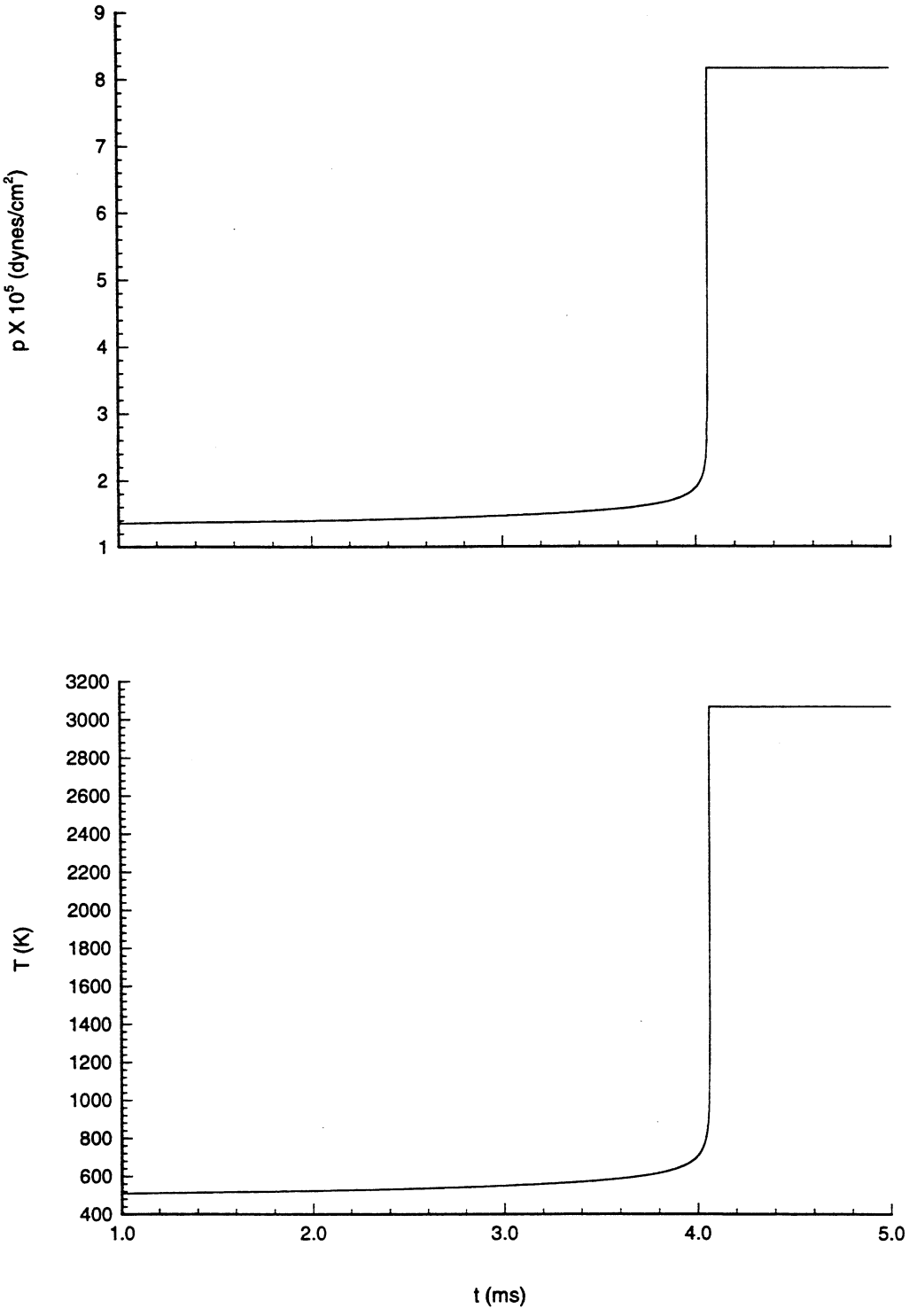

Figure 3.5: Temperature and pressure for a constant volume combustion.

Table 3.3: One-Dimensional Detonation Wave Properties

Values	Theory	Code	% Difference
p_2/p_1	19.04	18.30	3.89
ρ_2/ρ_1	1.76	1.71	2.84
T_2/T_1	10.83	10.70	1.20
u_p (m/s)	808.3	775.0	4.12

3.3.2 Detonation Wave - Chemistry and Convection

This case is similar to the 1-D shock wave done above except now the chemistry integration routine is active. The viscous, thermal conductivity, and mass diffusion are all deactivated, leaving active just the chemistry and convection routines, and reducing the equations to the reacting Euler equations. The initial conditions were set up similarly to the shock tube problem. A diaphragm was placed at x = 6 cm with a pressure ratio across the diaphragm of 150 and a temperature ratio of 4. Burned gas, $Y = 0$, was placed from 0 cm to 6 cm. Unburned fuel, $Y = 1$, was placed from 6 cm to the end of the tube. The solution to the detonation wave problem can be found in numerous combustion textbooks.[2,5,57,58]

The governing equations in one dimension for the flow across a detonation wave are given as

$$\rho_1 u_1 = \rho_2 u_2 \tag{3.13}$$

$$p_1 + \frac{1}{2}\rho_1 u_1^2 = p_2 + \frac{1}{2}\rho_2 u_2^2 \tag{3.14}$$

$$c_p T_1 + \frac{1}{2}u_1^2 + q = c_p T_2 + \frac{1}{2}u_2^2 \tag{3.15}$$

The equation of state also holds on both sides of the wave.

$$p = \rho R_s T \tag{3.16}$$

The condition for a Chapman-Jouget detonation is that the velocity of the burned gas, region 2, be at the local speed of sound.

$$u_2 = a_2 = \sqrt{\gamma R_s T_2} \tag{3.17}$$

This equation (3.17) provides the closing relationship. Equations (3.13)-(3.17) provide five equations for the five unknowns, p_2, T_2, ρ_2, u_1, and u_2. The known values in the problem are the conditions in region 1, p_1, T_1, ρ_1, the chemical energy release, q, which is defined in equation (2.20), the specific gas constant, R_s, and the ratio of specific heats, γ.

Figure 3.6 shows the computed pressure ratio, temperature ratio, and velocity of the detonation wave at one time. The grid resolution for this case is 0.001 cm. Table 3.3 lists the calculated

detonation properties, the theoretical values, and the percent difference between the two. All the numerically calculated values are within 5% of the theoretical values. The plot of pressure shows an initial spike before it relaxes to the value of 18.30. At the time shown, the spike has a pressure ratio of 43.9 and corresponds to the von Neumann spike as discussed in Kuo[2] and Williams.[58] The calculated value of the von Neumann spike, determined as discussed in Williams,[58] is found to be 37. The numerical value of this spike is 18% greater than the theoretical value. The magnitude of the spike changes in time but is always greater then the theoretical value. The longitudinal waves seen in the solutions are a property of "galloping" detonations.[38] For one-dimensional detonations, the shock front oscillates as a result of the detonation propagating into unreacted gas. The oscillations in shock strength caused the properties behind the shock to oscillate as well, causing the longitudinal waves.

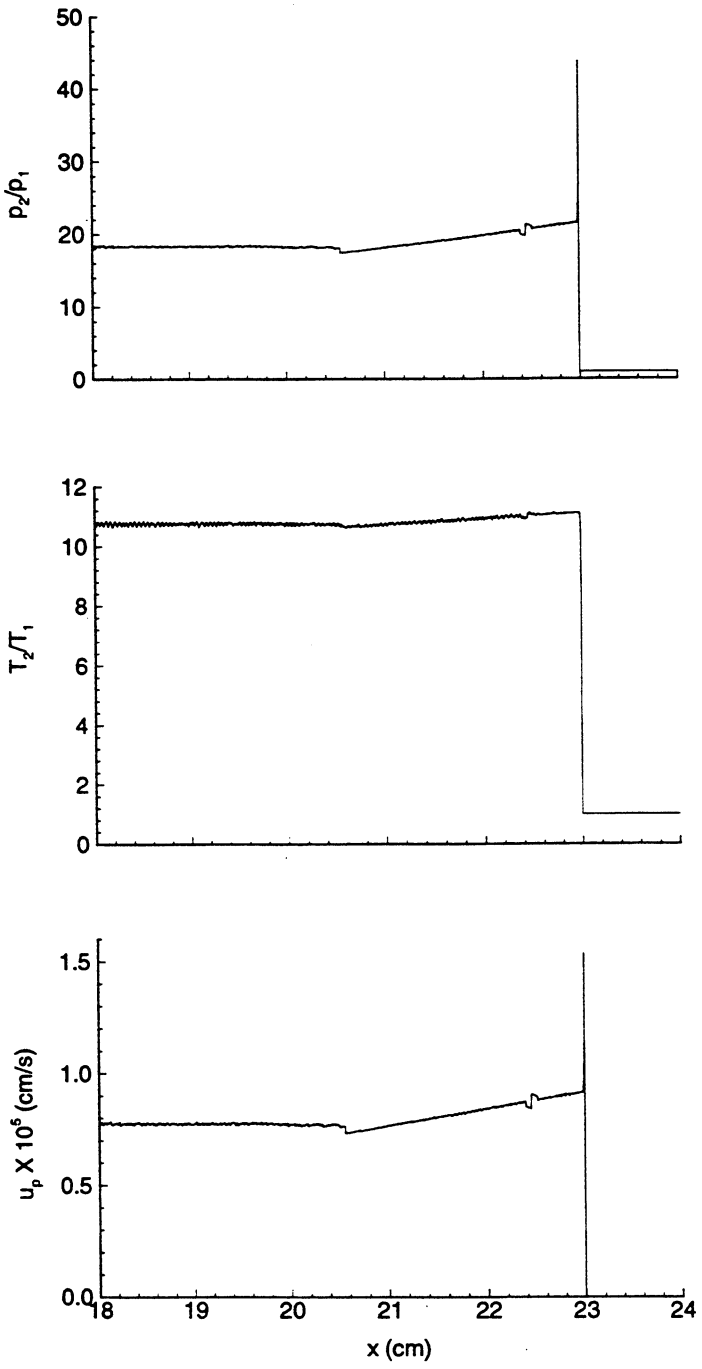

Figure 3.6: Pressure ratio, temperature ratio, and velocity for a 1-D detonation wave.

Chapter 4

One-Dimensional Flame Results

4.1 Overview

A series of one dimensional flame simulations were performed to evaluate the chemistry model with the convective and all the transport properties active. A comparison of the calculations with the laminar flame theory is shown. This theory is described in the next section. A grid study was performed to evaluate the dependence of the gridding on the flame speed and flame thickness. The transport properties were varied to compare the results to the general trends as provided by theory. The initial conditions are the same as the initial conditions described for the two-dimensional channel in section 2.8. For this case though, a symmetry condition is applied at the bottom boundary to create a one-dimensional configuration. The initial conditions are provided in table 2.2.

The general trends for the flow properties through a one-dimensional flame are shown in Figure 4.1 from Kanury.[59] In the figure, the flame is moving to the right into a stagnant gas. As the flame propagates into the unburned stagnant gas, the temperature increases and the density decreases. The pressure slightly decreases, which is the basis for may numerical flame studies occurring at an assumed constant pressure.

4.2 Laminar Flame Theory

Laminar flame theory provides a means to estimate the flame speed, which is defined as the speed of the flame relative to the flow ahead of it. It also allows the estimation of the flame thickness. The detailed theory of Zeldovich and Frank-Kamenetskii[60–62] and Semenov[63] is described in Appendix C.

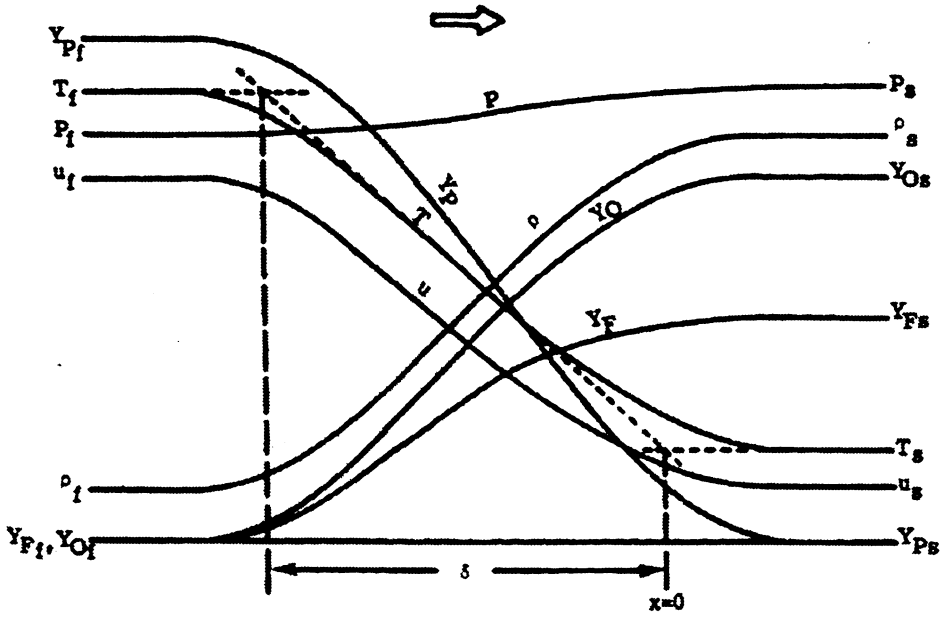

Figure 4.1: General trends across a 1-D flame, from Kanury[59]

From the theory, the resulting equation for the laminar flame speed is

$$S_l = \sqrt{\left(\frac{k}{\rho_u c_p}\right)\left(\frac{1}{\rho_u}\right)\left(\frac{2}{T_b - T_u}\right) I} \tag{4.1}$$

where I is the reaction rate given as

$$I = \int_{T_u}^{T_b} \omega dT \tag{4.2}$$

According to Kuo,[2] this formula doesn't give very accurate results, but it does predict the trends well. One of these trends is that the flame speed is proportional to the square root of the thermal conductivity, $S_l \propto \sqrt{k}$. Another result from the theory is that for an adiabatic flame, the enthalpy across the flame is constant. This can be used to relate the temperature in the burned region to the temperature in the unburned region.

$$c_p T_b = c_p T_u + q \tag{4.3}$$

$$c_p T_u + q = c_p T + qY \tag{4.4}$$

Turns[64] outlines a method from Spalding[65] to calculate the laminar flame thickness, defined by

$$\delta_t = \frac{T_b - T_u}{\left(\frac{dT}{dx}\right)_{max}} \tag{4.5}$$

From this method, the flame thickness can be estimated from the laminar flame speed as

$$\delta_t = \frac{2}{S_l}\left(\frac{k}{\rho_u c_p}\right) \tag{4.6}$$

Since the flame speed is proportional to the square root of the thermal conductivity, this equation shows that the thickness is also proportional to the square root of the thermal conductivity, $\delta_t \propto \sqrt{k}$.

4.3 Standard Case

For the first case the computational cell size was set at a constant 0.001 cm, which will be shown later to give about 20 cells in the 1D planar flame thickness. The transport properties had all the reference coefficients equal, as given by Table 2.1, so that Le = Pr = 1. The actual Lewis number for a stoichiometric acetylene and air mixture is 1.02 at 298 K and 100 torr. The actual Prandtl number under those same conditions is 0.75. Figure 4.2 shows the computed temperature, velocity, and fuel mass fraction profiles through the flame. Figure 4.3 shows the density, chemical energy release, and pressure through the flame. The trends show by these figures for the one-dimensional flame match the general trends as shown in Figure 4.1 from Kanury.[59] As the flame propagates, it induces flow ahead of it. The flow ahead of the flame reaches a steady condition at a velocity of 913 cm/s, relative to fixed coordinates. The pressure curve slightly increases ahead of the flame, on an order of 0.05% which is consistent with the assumption that is made in laminar flame theory of constant pressure.

From the temperature profile, the ratio of the temperature of the burned to unburned material is 8.01. From theory, the enthalpy across the flame is conserved and is given by equation (4.3). The right hand side of the equation is evaluated in the unburned gas, where $Y = Y_u = 1$, and $T = T_u = 293K$. Using the definition of the chemical heat release (2.20), and noting that the reference temperature is equal to the unburned gas temperature, $T_r = T_u$, the theoretical temperature ratio across the flame is

$$\frac{T_b}{T_u} = 8 \tag{4.7}$$

This theoretical value is very close to the 8.01 obtained numerically.

Figures 4.4 and 4.5 show the flame position and velocity in the laboratory or fixed frame of reference. The flame velocity, S_F, approaches 1044 cm/s relative to fixed coordinates. The laminar flame speed is defined as the speed of the flame relative to the flow ahead of the flame

$$S_L = S_F - u_u \tag{4.8}$$

This gives a laminar flame speed of $1044 - 913 = 131$ cm/s.

An alternate method of finding the laminar flame speed is to apply conservation of mass to a control volume containing the flame. Transforming the moving flame to stationary coordinates by

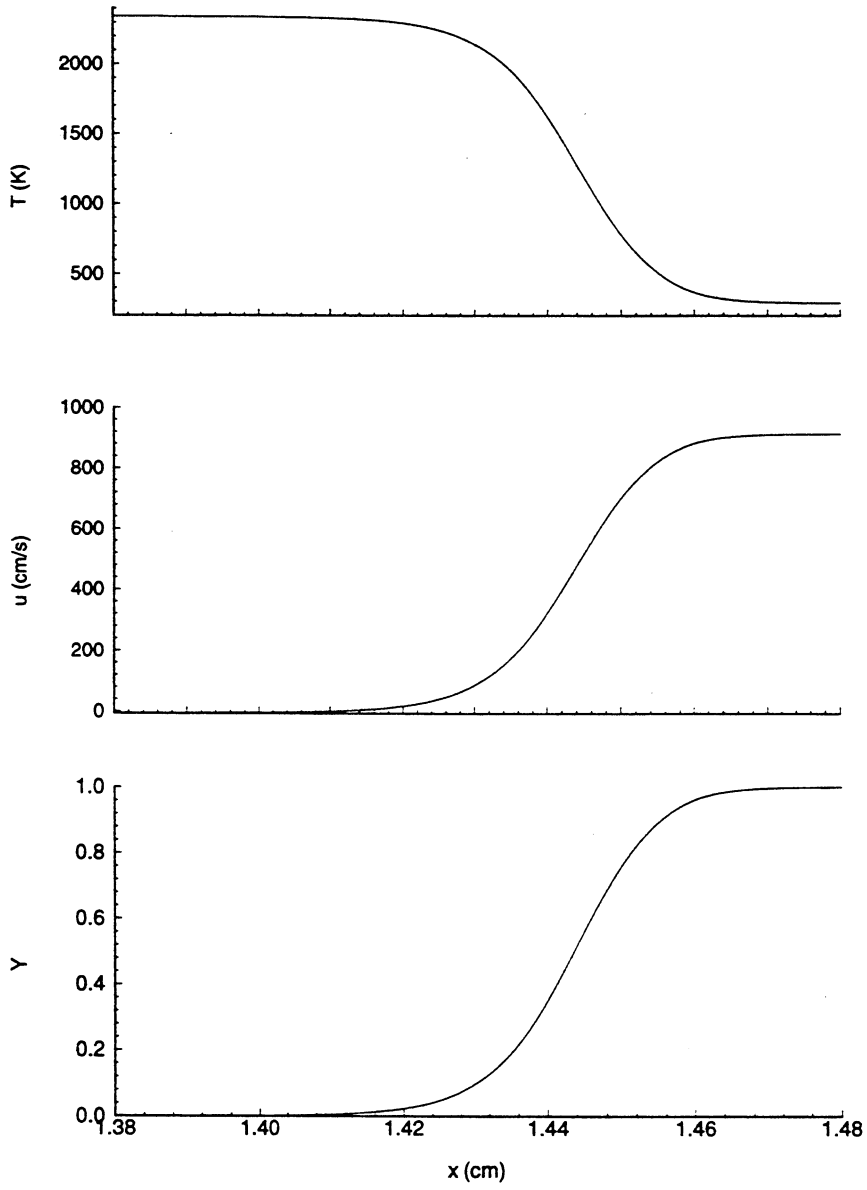

Figure 4.2: Temperature, velocity, and fuel mass fraction for a one-dimension flame

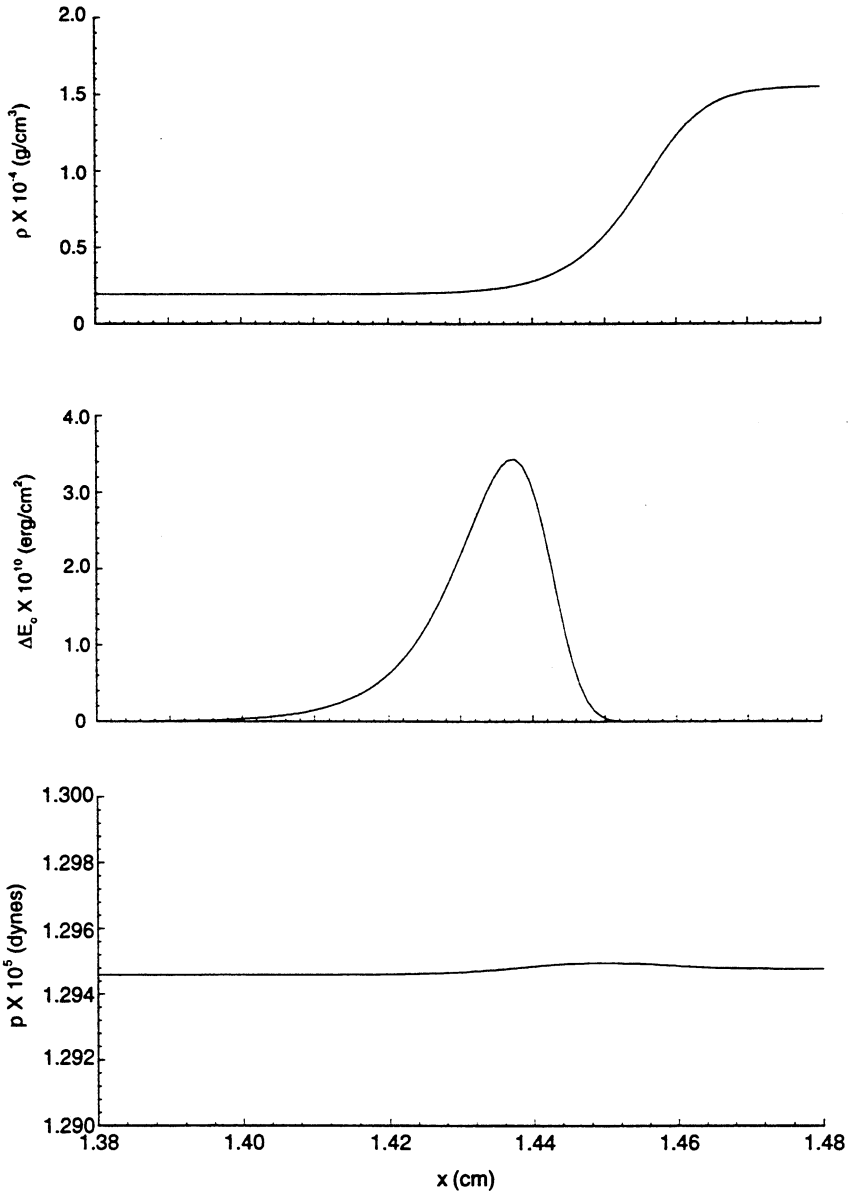

Figure 4.3: Density profile, chemical energy release, and pressure across a one-dimension flame

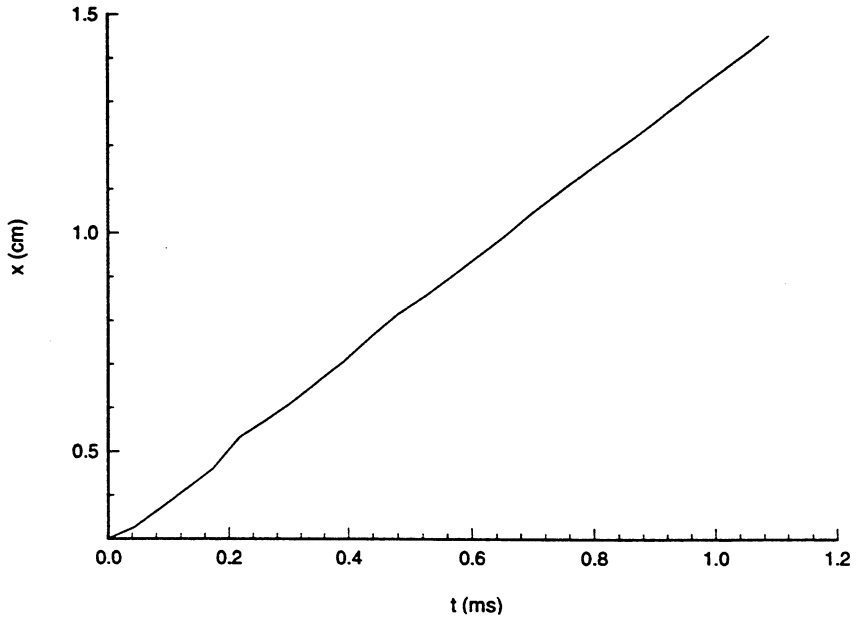

Figure 4.4: Position as a function of time for the one-dimensional flame.

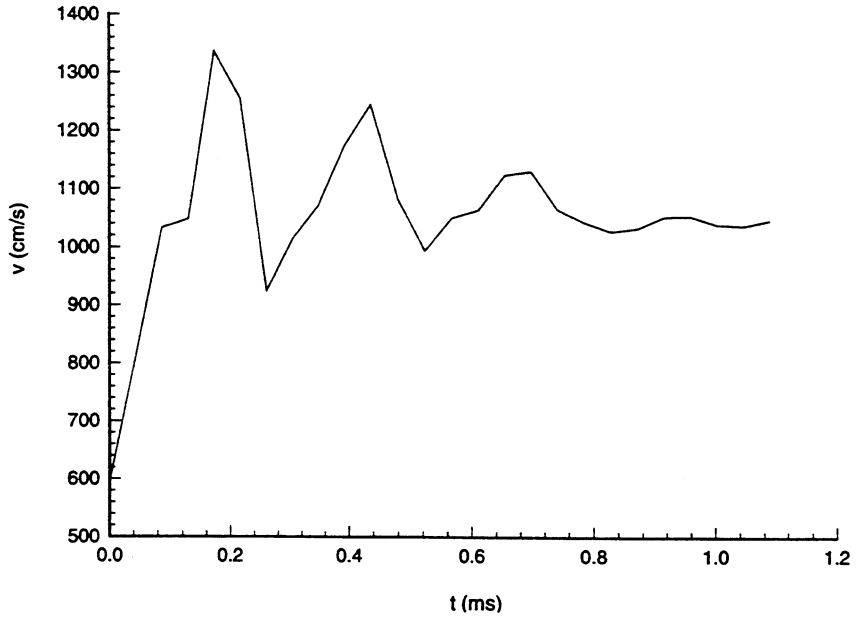

Figure 4.5: Velocity relative to the laboratory for a one-dimension flame.

subtracting the flame velocity, the continuity equation becomes

$$\rho_b(S_F - u_b) = \rho_u(S_F - u_u) \tag{4.9}$$

Using equation (4.8) to replace S_F as $S_L + u_u$, solving for the laminar flame speed, S_L, gives

$$S_L = \frac{u_u - u_b}{(\rho_u/\rho_b) - 1} \tag{4.10}$$

Since the pressure is nearly constant, and the temperature ratio across the flame is 8.01, the density ratio ρ_u/ρ_b, is also 8.01 from the equation of state (2.14). Then from equation (4.10), the laminar flame speed is calculated as 130.2 cm/s, a value very close to the computational value of 131 cm/s.

The laminar flame theory, described in the previous section, provides an equation to calculate the laminar flame speed. This equation is reproduced below.

$$S_l = \sqrt{\left(\frac{k}{\rho_u c_p}\right)\left(\frac{2}{T_b - T_u}\right)\left(\frac{1}{\rho_u}\right) I} \tag{4.11}$$

The I term is found from equations (C.4) and (4.2). After substituting the density from the equation of state, (2.14), and the mass fraction from equation (4.4), the integral becomes

$$I = \left(\frac{p}{R_s}\right)^2 \frac{c_p}{q} A_r \int_{T_u}^{T_b} \frac{T_b - T}{T^2} exp(-T_a/T) dT \tag{4.12}$$

The theory assumes a constant value of the thermal conductivity. The present computation allows the thermal conductivity to be a function of temperature, as given by equation (2.27). To evaluate equation (4.11) for the laminar flame speed, an average value of temperature was used to determine the thermal conductivity. Using an unburned gas temperature of 293 K, the theoretical value of the burned gas temperature is 2344 K, as determined from equation (4.7). This results in an average temperature of 1319 K, which is used to calculate the thermal conductivity. Evaluating the integral, I, numerically using a pressure of 100 torr, the theory gives a laminar flame speed of 103 cm/s. This value is 27% off from the value determined computationally. Kuo[2] states that the theory does not give very accurate results, but does predict the general trends that flame speed is proportional to the square root of the thermal conductivity.

The laminar flame thickness is another important property of the flame, defined in equation (4.5) and shown again as

$$\delta_t = \frac{T_b - T_u}{(dT/dx)_{max}} \tag{4.13}$$

Evaluating this expression from the temperature plot gives a flame thickness of 0.023 cm. For the cell size of 0.001 cm, this gives 23 cells in the flame thickness. From laminar flame theory, equation (4.6) provides a formula for calculating the thickness. This formula relates the flame thickness to

Table 4.1: One-dimensional Flame Properties

	S_l (cm/sec)	δ_t (cm)	T_b/T_o
CMRFAST2D	131	0.023	8.01
Khokhlov et al.[37]	144	0.022	8.00
Theory[67]	103	0.024	8.00
Experimental[37,66]	150	~0.020	NA

the thermal conductivity and the flame speed. Using the values from the calculation of the flame speed, the theoretical value of the flame thickness is 0.024 cm, a 4.2% difference from the computed value.

Table 4.1 compares the values of the flame speed, thickness, and temperature ratio obtained from the computed results using CMRFAST2D, separately computed results of Khokhlov et al.,[37] the experimental values[37,66] which the chemistry model was based on, and the theoretical results. The two computed results agree well with each other and with the experimental results. The theoretical results are the furthest from the three other results, but as stated above from Kuo,[2] the theory provides the trends, but is not very accurate.

4.4 Transport Property Test

These tests compare computations of the laminar flame with the transport properties, μ_r, k_r, and D_r, halved and doubled, so that the Lewis and Prandtl numbers were always unity. The goal of these tests is to show the response of the flame to a change in the thermal conductivity. Figure 4.6 shows the temperature, velocity, and mass fraction profiles for the two cases. Shown for comparison is the results for the standard case flame. The x axis was repositioned so that all three cases could be plotted in the same figure. This was done by defining x = 0 as the point where the maximum value of the temperature derivative, $(dT/dx)_{max}$ occurred.

The temperature profiles shows that the ratio of burned to unburned gas temperature is essentially unaffected by the thermal conductivity. This is because the ratio is a function of chemical parameters, as shown in equation (4.3). The ratio is independent of the thermal conductivity. This is also true of the mass fraction profiles.

The velocity profiles show that when the thermal conductivity is doubled the velocity increases and when the thermal conductivity is halved the velocity decreases as compared to the standard case described in the previous section. To obtain the flame speed, the continuity method as given by equation (4.10) can be used. These values along with the flame thickness as determined by equation

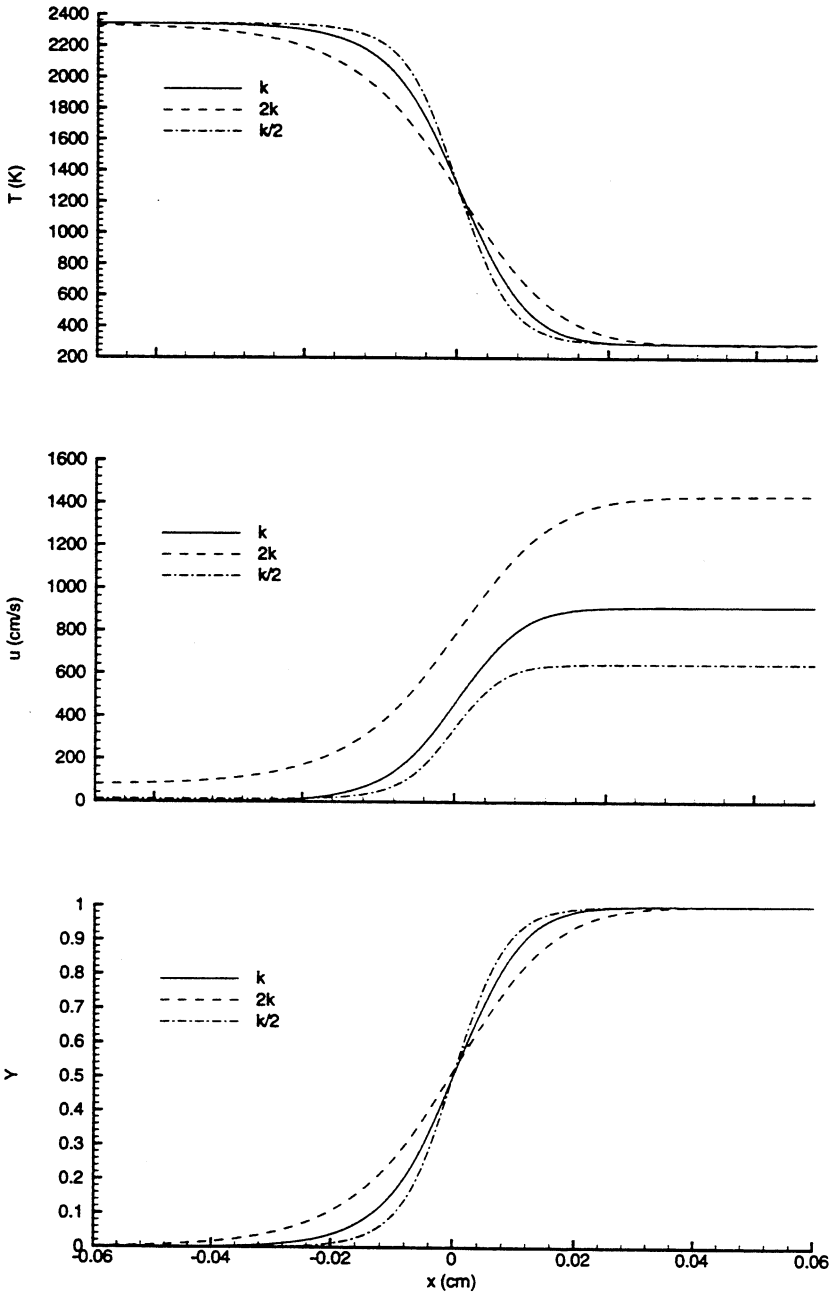

Figure 4.6: Temperature, velocity, and fuel mass fraction for the cases of the thermal conductivity halved, k/2, and doubled, 2k.

Table 4.2: Laminar Flame Speed and Thickness Variations with Thermal Conductivity

	k	2k	$\sqrt{2}$(k value)	k/2	(k value)/$\sqrt{2}$
S_l (cm/s)	131	194.4	185.3	90.7	92.6
δ_t (cm)	0.023	0.032	0.033	0.016	0.016

Table 4.3: Grid Study Flame Thickness and Velocity

cell size (cm)	S_l (cm/s)	δ_t (cm)
0.0010	131	0.023
0.0015	131	0.023
0.0020	128	0.025
0.0030	125	0.030
0.0040	125	0.036

(4.5) are shown in Table 4.2.

The laminar flame theory described in the previous section shows that the flame thickness and speed are directly proportional to the square root of the thermal conductivity. From equations (4.1) and (4.6), this is shown as

$$S_l \propto \sqrt{k} \tag{4.14}$$

$$\delta_t \propto \sqrt{k} \tag{4.15}$$

If the thermal conductivity is doubled, 2k, the laminar flame speed should increase by $(\sqrt{2})(131) = 185.3$, which is within 4.9% of the calculated value. Similarly, when the thermal conductivity is halved,k/2, the flame speed should decrease to $(131)/(\sqrt{2}) = 92.6$, which is within 2.1% of the calculated value. The same trends are true for the flame thickness which for both cases are nearly identical to the calculated values.

4.5 Grid Study

For these test cases the cell size was increased to study the effect of the gridding on the results obtained above. Figure 4.7 shows the temperature, velocity, and mass fraction for five cell sizes ranging from 0.001 cm to 0.004 cm. Table 4.3 gives the calculated flame thicknesses and the laminar flame speed. The maximum error in flame speed is 4.6%. The errors for the flame thickness range from 8.7% at 0.002 cm to 56% at 0.004 cm.

The simulations for the two-dimensional channel flame use a cell size of 0.002 cm in the lengthwise direction. This allowed about 13 cells in the flame thickness area. The decreased accuracy for this

cell size, 2.3% in flame speed and 8.7% in thickness, is offset by the increased step sized and domain size increases for the same number of cells.

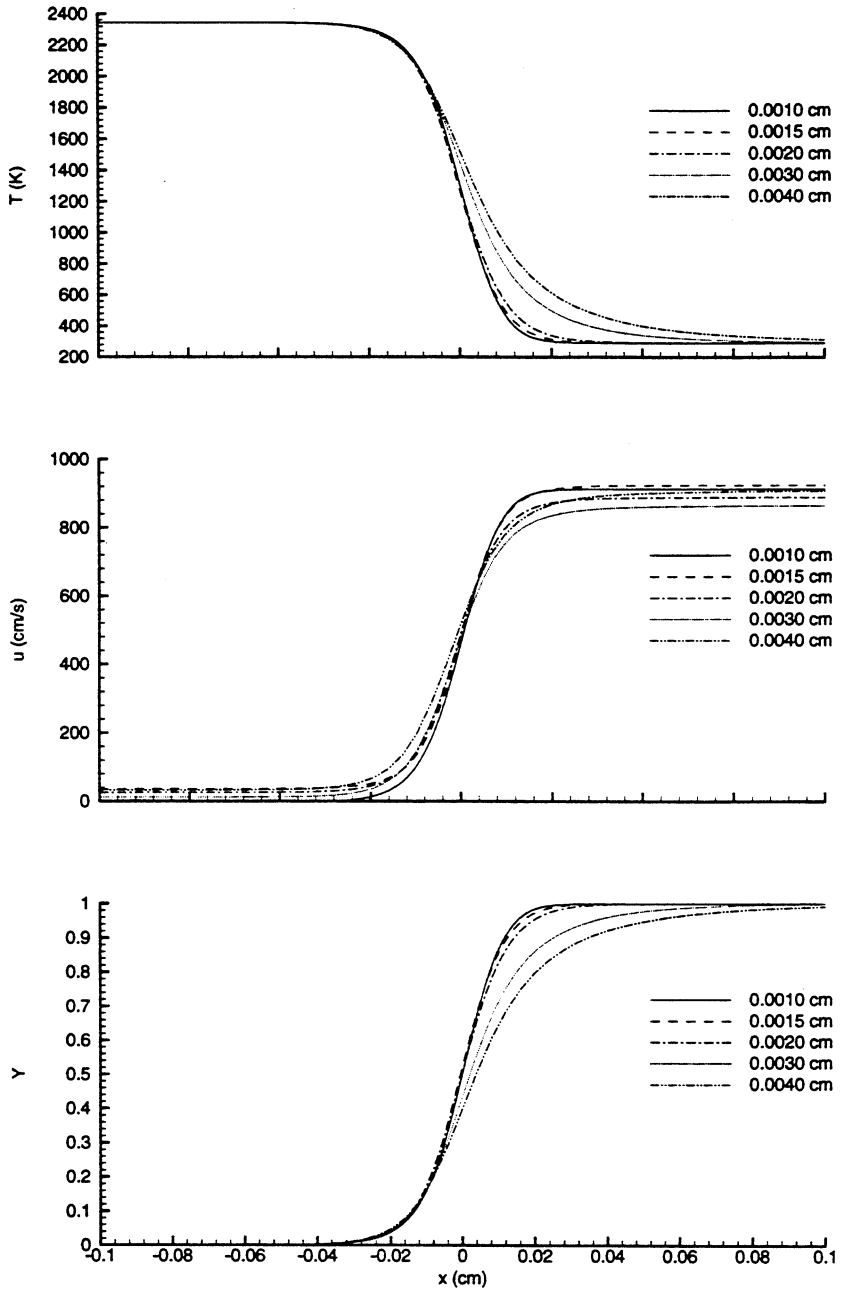

Figure 4.7: Temperature, velocity, and fuel mass fraction varying grid resolutions

Chapter 5

Two-Dimensional Channel Results

This chapter describes the results for the two-dimension channel configuration. The wall boundary conditions for both an adiabatic and an isothermal wall will be discussed. For all cases, the boundary condition for the species at the wall is noncatalytic.

5.1 Adiabatic Wall : Planar Ignition

For these studies, the boundary condition for the temperature at the wall is adiabatic. The ignition method is described in section 2.8 : a discontinuity in temperature, species mass fraction, and density located 0.3 cm from the end wall of the tube. Table 5.1 lists the flame simulations that were performed. In the table, h is the channel height, μ_r and D_r are the reference values for the transport properties from equations 2.26 and 2.29, Re is the Reynolds number, and Le is the Lewis number. The reference Reynolds number is based on the laminar flame speed, channel height, and kinematic viscosity in the unburned gas. For all the simulations the reference value for the thermal conductivity, k_r, is kept constant.

Table 5.1: Adiabatic Wall Studies : Planar Ignition

Case	h (cm)	$\mu_r \times 10^{-8}$	$D_r \times 10^{-8}$	Re	Le
AD1	0.254	2.439	2.439	76.2	1.0
AD2	0.254	4.878	2.439	38.1	1.0
AD3	0.508	2.439	2.439	152.4	1.0
AD4	0.254	2.439	1.951	85.2	0.8
AD5	0.254	2.439	2.927	69.6	1.2

5.1.1 Case AD1 : Baseline

This first case is the baseline case that will be used for comparisons. The channel aspect ratio, length to height, is 32.2. Figure 5.1 shows the temperature profiles for the first 0.6 ms. The initial condition is a discontinuity of temperature, density, and mass fraction, as described in section 2.8. From this discontinuity in temperature, a flame develops. As the flame forms and begins to propagate down the channel, the wall inhibits the flame motion. The result is that the flame at the centerline of the channel moves faster than near the wall, resulting in the structure shown in Figure 5.1. In time, the curved portion of the flame near the wall grows longer. By 0.607 ms, this curved portion is about 0.3 cm long.

Figure 5.2 shows the flame position as a function of time at two positions in the tube: the centerline and the wall. The position of the one-dimensional flame (shown in Figure 4.4) is also shown for comparison. The flame position is defined as the location in the flame front where the temperature is 1000 K. The flame position at the centerline closely follows the position for the one-dimensional flame for approximately 0.3 ms and then it becomes larger. The position of the flame at the wall is initially less then the one-dimensional result, but by about 0.55 ms it also is greater than the one-dimensional location. Figure 5.3 shows the flame velocity relative to the laboratory for the flame at the centerline and the wall, and these are compared to the velocity for the one-dimensional flame (also given in Figure 4.5). The flame speed has greatly increased over that of the one-dimensional flame. The one-dimensional flame reaches a constant velocity, but both the two-dimensional centerline and wall flames are still increasing at the end of the channel.

Figures 5.4 - 5.11 show the temperature (T), density (ρ), vorticity (ω), pressure (p), velocity in the x direction (u), velocity in the y direction (v), velocity vectors, and instantaneous streamline pattern superimposed on the temperature contours at times of 0.433 ms, 0.758 ms, 1.104 ms, and 1.450 ms. The vorticity is defined as twice the angular velocity and is given by

$$\omega = \frac{\partial v}{\partial x} - \frac{\partial u}{\partial y} \tag{5.1}$$

These results are shown on the same scale to facilitate comparisons at the different times.

The temperature profiles maintain the curved shape shown in Figure 5.1. By 1.450 ms, the curved flame has grown to be nearly 1.5 cm long. The flame thickness in the curved region and near the centerline are approximately the same, they only appear different due to the different scaling of the x and y axes. The shape of the density contours closely follows the shape of the temperature contours, because the pressure is nearly constant through the flame. The mass fraction profiles are not shown since, for adiabatic conditions, those profiles also resemble the the temperature profiles.

This can be shown by solving equation (4.4) for the mass fraction Y, and substituting in equation (4.3) to find

$$Y = \frac{T_b - T}{T_b - T_u} \tag{5.2}$$

On Figure 5.4, the pressure slightly increases near 2.5 cm and this extends to about 3 cm. This is due to a reflected wave caused by the initial pressure wave reaching the outflow boundary and reflecting back into the domain.

The u velocity shows that the speed of the gas in the unburned region increases in time. The v velocity shows that there is an upwelling at the wall in the curved-flame region. The maximum v velocity in this upwelling region remains essentially constant as the flame moves down the entire channel. The explanation for this upwelling lies in the observation that the material expands as it burns. The burned material cannot move downward because of the solid wall, and it cannot move backward, as it is being blocked by the previous burned material. The only direction for the material to expand is forward toward the outflow end of the channel. The burned material near the lower wall is restricted in moving forward because of the boundary layer ahead of the flame. The material that burned near the lower wall that is unable to move forward must then expand upwards toward the centerline. The material flows upwards behind the the flame, turns at the centerline, and provides additional momentum to the center of the flame.

The instantaneous streamlines, or fluid paths, are plotted with the temperature contours to show the streamlines relative to the flame location. These figures show the flow upwelling and then turning toward the outflow boundary. The highest values of vorticity occur in the boundary layer. There is relatively little vorticity behind the flame and near the centerline of the channel, most of the vorticity occurs in the boundary layer and along the curved flame surface.

Figure 5.12 shows the evolution of the boundary-layer thickness along the channel in front of the flame. The times in the figure are about 0.2 ms apart. The boundary layer thickness, δ_{99}, is defined as the vertical height above the wall where the u velocity reaches 99% of the centerline value. At a given location, the boundary-layer grows in time until the flame reaches that location. As the flame moves over that location it destroys the boundary layer. Initially the boundary-layer thickness grows rapidly and then this growth rate slows. The centerline velocity, Figure 5.14, shows that the fluid velocity in the unburned gas accelerates as the flame moves down the channel. At 0.217 ms the centerline velocity drops to zero at about 7 cm. This is because this is the furthest point that the initial pressure wave, traveling at the local sound speed, has reached. Ahead of this location, at this time, the gas is unaware of the developing flame.

Figure 5.13 shows the displacement thickness in front of the flame for various times. The displacement thickness represents the distance that the inviscid freestream is displaced from the wall

due to the decrease in velocity in the boundary layer. It is defined as

$$\delta^* = \int_0^{h/2} \left[1 - \frac{\rho u}{(\rho u)_{h/2}}\right] dy \tag{5.3}$$

This plot is similar to the boundary layer thickness but it shows that the displacement thickness levels off more quickly, to a value close to 0.017 cm. The small displacements in the profiles at 0.433 ms and 0.650 ms represent the reflection of the initial pressure wave from the outflow boundary and the reflection of the reflected wave from the flame front. This is also seen in the centerline velocity discussed in the previous paragraph.

Figures 5.15 and 5.16 show the boundary layer growth at different channel locations. The time, t_x, is the local time at a channel location, x. This is defined as the time starting from when the initial pressure wave, traveling at the local speed of sound in the unburned gas, has reached that point. The local time, t_x, is calculated from the global time ,t, as

$$t_x = t - \frac{(x - 0.3)}{\sqrt{\gamma R_s T_u}} \tag{5.4}$$

The 0.3 is needed since the initial high temperature region used to initialize the flame was located up to 0.3 cm, so this is where the initial pressure wave is formed.

Examining these figures, the boundary layer growth curves at different channel locations collapse onto the same curve for times greater than about 0.3 ms, becoming self-similar. The solid line in both figures gives the theoretical results from Stokes' First Problem discussed in section 3.2.3. From White,[53] the boundary layer thickness for this problem is given by

$$\delta_{99} = 3.64\sqrt{\nu_u t_x} \tag{5.5}$$

In the theory, it was assumed that the freestream velocity and kinematic viscosity, ν_u, are constant. Using equation 2.26, the kinematic viscosity is given as

$$\nu = \frac{\mu}{\rho} = \frac{\mu_r}{\rho}\left(\frac{T}{T_r}\right)^{0.7} \tag{5.6}$$

The theoretical value of the boundary layer thickness was calculated with the kinematic viscosity held constant at a value based on the unburned gas conditions.

The boundary layer growth initially follows the theory, but it then slows its growth. This is due to two effects acting together. The primary cause for the deviation is that the centerline velocity is not constant (Figure 5.14), but increases in time for all channel locations ahead of the flame. Figure 5.17 gives the centerline velocity ahead of the flame for the local time at selected channel locations. After about 0.2 ms, the curves for the centerline velocity have a similar shape, which gives similar accelerations at a given channel location at the same local time. The acceleration of the flow

causes the boundary layer thickness to decrease from that predicted by Stokes' First Problem. This is shown in Appendix A for three different accelerations. It is the acceleration of the centerline velocity that is the primary cause of the slower boundary layer growth.

The secondary cause of the slower growth is due to the change in the kinematic viscosity in the unburned gas. For the theory, it was assumed that the kinematic viscosity was constant at the initial conditions of the unburned gas. The pressure waves that are generated as the flame propagates down the channel cause a decrease in the value of the kinematic viscosity in the unburned gas. The pressure wave increases the temperature and density above the initial values. The relative increase in density is greater than the relative increase in temperature (shown in Appendix B). By equation 5.6, the greater rise in density lowers the kinematic viscosity. Since the boundary layer growth is proportional the square root of the kinematic viscosity, a lower value gives a slower boundary layer growth.

5.1.2 Case AD2 : Effects of Increased Viscosity

This second case has initial conditions identical to case AD1 described in the previous subsection. The aspect ratio of the channel is the same, 32.2. The reference coefficient for the viscosity is doubled, since the viscosity controls the growth rate of the boundary layer. By doubling the reference coefficient, the Reynolds number based on laminar flame speed is halved.

The development of the flame from the initial conditions is similar to the development in the first case, Figure 5.1. The flame forms from the discontinuity in temperature and starts to propagate down the channel. The wall inhibits this motion and a curved flame develops.

Figure 5.18 shows the flame position as a function of time for the channel centerline and wall. Figure 5.19 shows the velocity of the flame relative to laboratory coordinates. From these two figures it can be seen that the flame is faster then in the case AD1 and therefore exits the channel earlier. By 1 ms, the flame has reached 1 cm further down the channel and is moving 3000 cm/s faster than the first case.

Figures 5.21 and 5.22 show the temperature, density, pressure, vorticity, velocities, and instantaneous streamlines at a time of 1.100 ms. This time is very close to the time of 1.104 ms in figures 5.8 and 5.9 for case AD1. Both sets of figures are also in the same scale to facilitate comparisons. Examining these two sets of figures shows that the flame has moved further down the channel then in the first case. Comparing the temperature plots, the length of the curved region of the flame near the wall has increased for the second case. Figure 5.20 shows the length of this curved region for the two cases, Δx_f. This length increases faster for the doubled viscosity case. The added length provides more burned material in the fountain effect, which in turn gives a greater push to the flame. This is what accelerates the flame faster then in the first case which has less of

a curved flame region at the wall.

Figure 5.23 shows the evolution of the boundary layer thickness in front of the flame. The times shown are similar to the times in Figure 5.12 for comparisons. Comparing these two figures it can be seen that the boundary growth is greater for the higher viscosity case, as is to be expected. Figure 5.24 shows the time history of the displacement thickness along the channel. The plot is qualitatively similar to Figure 5.13 in case AD1, but the magnitudes are greater. Both the displacement and boundary layer thicknesses have grown thicker in less time, providing a greater blockage to the flame induced flow, which also adds to the increased fluid velocity ahead of the flame.

Figure 5.25 and Figure 5.26 show the boundary layer growth at different channel locations at the local time, t_x. The boundary layer growth is again seen to become self-similar in local time but the deviation from theory is greater then was shown for case AD1. This greater deviation is caused by the greater acceleration of the flow. Figure 5.27 shows the velocity in the channel for different times. Comparing this to case AD1, Figure 5.14, the velocity is seen to be faster at a given time. Figure 5.28 shows the velocity at different channel locations for local time. The velocity curves are similar in shape after about 0.2 ms, which leads to similar accelerations at a given channel location for the same local time.

5.1.3 Case AD3 : Effects of Increased Channel Height

For this case, the channel height is doubled, to 0.508 cm. This has the effect of doubling the Reynolds number, to 152.4, and halving the channel aspect ratio, to 16.1. The initial conditions are identical to case AD1, described in section 5.1.1. The reference coefficients for the transport properties are the same as case AD1.

Figure 5.29 shows the temperature profiles for the first 0.6 ms from a flame forming at the initial temperature discontinuity located at 0.3 cm. The times shown are similar to the times in figure 5.1 for the first case. Comparing the two figure shows that the flame in AD3 has not moved as far down the channel in the same amount of time. Figure 5.30 shows the position of the flame versus time. The flame position is defined as the location of the 1000 K isotherm. Now the flame takes about 2.6 ms to move out the end of the channel, as opposed to about 1.5 ms for the first case. Figure 5.31 shows the velocity of the flame relative to laboratory coordinates. The flame is slower moving than case AD1, which accounts for the longer time to reach the end of the channel.

A second interesting feature shown in figure 5.29 is the formation of a bulge at the flame front that begins near the lower wall and moves upward towards the channel centerline in time. The vertical location of the furthest downstream point of the flame front is shown in figure 5.32. By the end of the channel, the vertical height of the bulge has moved to about 0.165 cm, or a little over half

the distance to the centerline. This bulge creates a flame that bends back at the centerline, forming a cusp. Since the bulge is moving upwards, the cusp forms, grows, and then begins to disappear. This is shown in figure 5.33, which gives the horizontal distances between the position of the flame front at the centerline to the position of the flame front at the wall, the position at the the bulge to the wall, and the position at the bulge to the centerline. For comparison purposes, the distance from the centerline to the wall for the first case, AD1, is also shown. The cusp, or the bulge to centerline distance, forms, grows to a maximum at about 1 ms, and then begins to disappear. This figure also shows that the curved flame front near the wall (bulge to wall distance) is not as long as in case AD1. Since this region is where the upwelling originates from, a smaller region provides less upwelling which provides less additional momentum to the flame.

Figures 5.34 - 5.41 show the flowfield properties at times of 0.541 ms, 1.061 ms, 1.601 ms, and 2.121 ms. All the figures are plotted in the same scale for comparison purposes. Due to the increase domain height though, the scale is not the same as the related figure from case AD1. The temperature and the density plots show the formation of the bulge and of the cusp at the centerline. The bulge moves upwards in time as the cusp grows and then shrinks in size. The pressure plots show the initial waves moving out from the flame. The pressure change at later times is about 0.1%. The vorticity shows that the highest values occur in the boundary layer and along the flame surface, which is where the flow curvature is the highest.

The velocity plots show how the bulge forms. In figure 5.35 the curved flame front near the wall is short. There is therefore a small amount of upwelling. This small amount of upwelling provides additional momentum to the flame that is closer to the wall then near the centerline. The flame at the centerline receives less additional momentum and moves more slowly then the flame closer to the wall, producing a bulge. As the flame propagates, the curved flame region near the wall grows longer and it produces more upwelling which is distributed over more of the flame surface. The bulge moves upwards as the push is felt over a greater area of the flame surface. The cusp at the centerline begins to shrink. As time increases, the upwelling reaches the centerline and is distributed over the entire flame surface. By the end of the channel, the bulge is about 0.035 cm ahead of the centerline, about $1\frac{1}{2}$ laminar flame thicknesses.

Figure 5.42 shows the time evolution of the boundary layer thickness along the channel ahead of the flame. Figure 5.43 shows the displacement thickness along the channel. Compared to the thicknesses in case AD1 (figures 5.12, 5.13), the boundary layer has grown thicker for a given time. Figure 5.44 shows the centerline velocity profiles. Compared to case AD1, (figure 5.14), the velocity is less. The smaller foot causes less of an upwelling which gets distributed over the larger flame area. This results in less of a momentum push to the flame which gives a lower acceleration and therefore

a slower velocity. With the lower acceleration, the boundary layer can grow thicker compared to the first case. A secondary effect which acts to lower the acceleration comes from the blockage effect of the boundary layer. As the boundary layer grows, the effective channel height decreases. Even though the boundary layer is thicker, the relative decrease in the channel height is less due the increased channel height.

Figures 5.45 and 5.46 shows the boundary layer growth related to the local time. The local time was defined in equation 5.4 as the time starting from when the initial pressure wave first reaches that point of the channel. As with the previous two cases, the boundary layer growth becomes self-similar in local time. The comparison to the solution of Stokes' First Problem, $\delta_{99} = 3.64\sqrt{\nu_u t_x}$, is better then the previous cases. This is due again to the lower acceleration. Stokes' solution assumed zero acceleration. This case has an acceleration that was lower then the previous two cases, so the comparison is better.

5.1.4 Case AD4 : Effects of Decreased Mass Diffusion

This case has a channel geometry the same as case AD1. The channel aspect ratio is 32.2. This case has the reference coefficient for the mass diffusion decreased so that the Lewis number decreases to 0.8. The Lewis number was defined as the ratio of the mass diffusivity to the thermal diffusivity, and was given in equation 2.30. The Lewis number was decreased, since according to Glassman,[57] flames instabilities may occur for Lewis number not equal to unity. From laminar flame theory, the laminar flame speed is related to the Lewis number by

$$S_l \propto \sqrt{\frac{1}{Le}} \tag{5.7}$$

Compared to the laminar flame speed from the first case, AD1, this flame will have a higher flame speed, about $1.12(S_l)_{AD1}$. For this case no flame instabilities were present even though the Lewis number was less then one.

The initial development of this flame from the planar discontinuity is very similar to the first case, as shown in figure 5.1. As with the first case, no cusp forms at the centerline as occurred in case AD3. Figures 5.47 and 5.48 shows the flame position and velocity relative to laboratory coordinates. The flame exits the channel at a slightly earlier time as compared to the first case, about 0.02 ms earlier, and has accelerated to a slightly higher speed, about 160 cm/s higher.

Figures 5.49 and 5.50 show the temperature, density, pressure, vorticity, velocity components, and instantaneous streamlines at a time of 1.172 ms. The figures show that the flame resembles the basic structure that was seen in all the previous cases. The flame is curved near the lower wall which produces the upwelling, which drives the flame faster down the channel. The pressure waves that

are generated by the flame are planar and move out ahead of the flame toward the outflow. The vorticity is concentrated in the boundary layer and along the flame surface, since these are where there is flow curvature.

Figure 5.51 shows the evolution of the displacement thickness along the channel. The times are similar to the times in figure 5.13 for comparisons. Figure 5.52 shows the boundary layer thickness along the channel and figure 5.53 shows the how the centerline velocity increases in time as the flame accelerates down the channel. These three figures are all qualitatively similar to the boundary layer profile plots of the first case. Figures 5.54 and 5.55 give the boundary layer growth at different x locations for varying local time. As with the other cases, the results are self-similar due to the similar slopes of the centerline velocities in local time as shown in figure 5.56. Due to the acceleration, the boundary layer growth is less than predicted by Stoke's First Problem.

5.1.5 Case AD5 : Effects of Increased Mass Diffusion

This case again has a channel geometry the same as case AD1, with a channel aspect ratio of 32.2. The reference coefficient for the mass diffusion was increased so that the Lewis number increased, $Le > 1$. Compared to the laminar flame speed from the first case, this flame will have a lower speed, about $0.91(S_l)_{AD1}$. The initial development of the flame from the planar discontinuity is very similar to the first case, AD1. As with the case in the previous section, no centerline cusp appears in the flame. Figure 5.57 shows the flame position in time. Figure 5.58 gives the flame speed relative to laboratory coordinates. The flame exits the channel at a slightly lesser time then the first case and is traveling at a slightly lower speed.

Figure 5.59 and 5.60 show the flowfield properties for this flame at 1.284 ms. The basic structure of the flame resembles the flame in the previous section and for case AD1. The upwelling at the wall provides the added momentum push to the flame at the centerline which accelerates it down the channel. Figure 5.61 and 5.62 show the displacement thickness and boundary layer thickness growth in time along the channel. Again the results are similar in shape to the first case. Figure 5.63 and 5.64 show the growth of the boundary in local time at selected channel locations. The curves for the different channel locations are self similar in local time and fall below Stokes' First Problem due to the flow acceleration.

5.1.6 Comparisons of the Planar Ignition Cases

Figure 5.65 shows the evolution of the relative flame area in time for the five planar ignition cases. The relative flame area is the flame surface area, defined as the length of the 1000 K isotherm, divided

by the channel cross-sectional area. Since the simulations were two-dimensional, a unit length into the page was assumed. Figure 5.66 shows the evolution of the flame speed relative to laboratory coordinates. Figure 5.67 gives the evolution of the boundary layer thickness at the 8 cm location. Also shown on this figure is the theoretical solution of Stokes' First Problem. Comparisons will made relative to the first case, AD1.

The second case, AD2, has the viscosity doubled. The increased viscosity causes the boundary layer to grow thicker for a given amount of time. This thicker boundary layer causes the curved area near the wall to be longer which leads to a larger flame area. The larger flame area burns more material which provides greater additional momentum. The greater additional momentum accelerates the flame faster which causes the boundary layer to grow slower then predicted by Stokes' First Problem.

The third case, AD3, has the channel height doubled. The relative burn area is lower at a given time then for any of the other cases. This lower burn area provides less of a push from the expanding burned material. This lower momentum push causes the flame to move slower. Since the flame has less acceleration, the boundary layer growth more closely matches that from Stokes' Problem. Even though the boundary layer growth is greater in time then the first case, it has less of an effect on the flow due to the increased channel height.

The fourth and fifth planar ignition cases, AD4 and AD5, have the channel height and viscosity the same as case AD1 but the Lewis number has been changed. The fourth case has the Lewis number lowered and the fifth case has the Lewis number raised. For both of these cases, the burn area and flame speed are close to the first case, with AD4 being slightly higher and AD5 being, for the most part, slightly lower. The higher flame speed for case AD4 leads to a higher acceleration which leads to it being slightly below the curve for AD1 in figure 5.67. Case AD5, which has a lower acceleration is slightly above case AD1 in that figure. Due to the acceleration though, both are below the curve for Stokes' Problem.

Figure 5.68 shows the flame speed plotted against the relative flame area. The relative burn area is defined as the ratio of the surface area of the flame front, A_f, to the channel cross-sectional area, A_c. The curves for all cases fall nearly on top of each other. Using a control volume fixed to the moving flame, the continuity equation reduces to

$$\rho_b(S_F - u_b)A_c = \rho_u(S_F - u_u)A_f \tag{5.8}$$

Assuming that the burned gas velocity is zero, using equation (4.8) for the definition of the laminar flame speed and the equation of state (2.14), equation (5.8) becomes[67]

$$S_F = \left[S_l\left(\frac{T_b}{T_u}\right)\right]\left(\frac{A_f}{A_c}\right) \tag{5.9}$$

Table 5.2: Adiabatic Wall Studies : Spark Ignition

Case	h (cm)	Re	Le
AS1	0.254	76.2	1.0
AS2	0.508	152.4	1.0

This equation states that the flame speed, relative to the laboratory, is directly related to the ratio of the flame area to channel cross-sectional area. In the above equation, both the temperature ratio and laminar flame speed are functions of the Lewis number. The relationship between the laminar flame speed and Lewis number was given by equation (5.7). According to Zel'dolvich,[67] an increase in Lewis number causes an increase in the temperature ratio and a decrease causes a drop in the ratio.

For cases AD1 - AD3, the Lewis number was unity. The temperature ratio is found from equation (4.7) to be 8 from theory. Using the laminar flame speed of 128 cm/s from table 4.3, the theoretical slope for the first three cases is 1024. Performing a least squares fit,[68] assuming a zero intercept, gives a slope of 1083, a 5.8% difference from the theoretical value. Part of the difference could come from the error associated with the calculation of the speed from the position data. Also the theory assumes an inviscid flow, but for all these cases the viscosity was non-zero.

For case AD4 the Lewis number was decreased to 0.8. This has the effect of increasing the laminar flame speed and decreasing the temperature ratio. Using an estimation of the laminar flame speed of 143 cm/s, $1.12(S_l)_{AD1}$, and a temperature ratio of 7.8, the slope is 1116. Curve fitting the data, a slope is 1101, a difference of 1.4%. For case AD5 the Lewis number was raised to 1.2 and the effect was reversed, the laminar flame speed was increased and the temperature ratio was lowered. Using a laminar flame speed of 117 cm/s and a temperature ratio of 8.4, the theoretical slope is 982. From the curve fit the slope is 1069, a difference of 8.1%.

5.2 Adiabatic Wall : Spark Ignition

For all of these studies, the wall boundary condition is adiabatic. The difference from the previously described cases is the ignition method. For these cases, the ignition is done with a simulated spark. A quarter-circular, high temperature region is placed at the center of the channel along the end wall. The reference coefficients for the transport properties, μ_r, k_r, D_r, are all given in Table 2.1, so that the Lewis and Prandtl number for the all cases is unity. Table 5.2 lists the flame channel simulations that were performed.

To ignite a flame from a spark, a minimum amount of energy, E_i, must be supplied from the

spark. From Turns,[64] this is the amount of energy required to raise the temperature of the spherical spark to the adiabatic flame temperature.

$$E_i = \frac{4}{3}\pi r_m^3 \rho_b c_p (T_b - T_u) \tag{5.10}$$

This requires knowledge of the minimum spark radius, r_m. Turns[64] outlines an approach that equates the rate of chemical heat release in the spark volume to the rate of heat loss due to conduction over the spark surface and estimates the minimum radius to be

$$r_m \doteq 1.22\delta_t \tag{5.11}$$

Using a different approach, Glassman[57] equates the chemical reaction time to the conduction time and estimates the minimum radius to be

$$r_m \doteq 1.85\delta_t \tag{5.12}$$

Using the laminar flame thickness of 0.023 cm from chapter 4, the above two equation give a minimum radius of 0.028 cm and 0.043 cm, respectively. The radius used for the spark simulations was 0.05 cm. Also the temperature of the initial burned material inside the spark was raised to 2930 K. This was done to ensure that there was enough energy to initiate flame propagation.

5.2.1 Case AS1 : Baseline

This case has a channel geometry the same as the first planar ignition case, AD1. The channel aspect ratio, length to height ratio, is 32.2. Figure 5.69 shows the temperature profiles for the first 0.39 ms of the simulation. From the initial temperature discontinuity, the flame develops and spreads outwards in a radial fashion. The flame traveling down the end wall toward the bottom of the channel is slowed down and the flame develops a non-circular shape. By the time the end wall flame has reached the bottom of the channel, a distance of about 0.077 cm from the initial temperature discontinuity at the centerline, the centerline flame has moved out a distance of about 0.473 cm. In time, the flame assumes the shape similar to the first case, AD1.

The final time in Figure 5.69, 0.391 ms, corresponds to the fourth time, t_4, in Figure 5.1. In the same amount of time, the present flame has traveled further down the channel and has developed a greater flame area then the first case. This is shown in Figures 5.70, 5.71, and 5.72 which show the flame position, velocity, and area ratio in time. As shown in Figure 5.72, the relative flame area to the channel cross-sectional area is greater for this case, AS1, as compared to the first case, AD1. The greater flame area results in more burned material which in turn provides greater additional momentum to accelerate the flame. Figure 5.72 shows a constant relative flame area from about

0.3 ms to 0.5 ms. During this time, the flame receives a constant push and moves at a constant speed. When the flame area begins to grow again, the flame accelerates due to the increase in burned material.

Figures 5.73 - 5.78 show the flowfield properties at 0.102 ms, 0.209 ms, and 0.305 ms. Figures 5.73 and 5.74 show the flowfield for the flame still traveling down the end wall of the channel. The velocity field induced by the flame shows that the expanding burned gas flows both behind the flame, up to the centerline, and then out, as well as down and along the bottom wall. The streamline patterns in the last plot show this. The vorticity plot shows a boundary layer that starts to grow from the end corner of the channel due to the initial expanding gas flowing down along the end wall. Figures 5.75 and 5.76 show the flowfield when the end wall flame has reached the bottom of the channel. The expanding burned material is then forced to flow up and out along the centerline due to the bottom wall boundary layer, as in the planar cases. By 0.305 ms, the flowfield has become qualitatively similar to the flowfield that developed in the planar ignition cases.

The pressure plots show a difference from the planar ignition cases. Since the flame is initialized as a circular discontinuity, the initial pressure wave is circular and not planar. This circular waves moves outward and is repeatedly reflected off of the channel side walls. The reflected waves also interact with each other inside of the channel. Figure 5.79 shows the pressure ahead of the flame normalized by the initial pressure at a time of 0.166 ms, a time about half way between the first two flowfield times. This plot shows that at a given channel location, the pressure varies across the channel. This is due to the the pattern of the reflected waves in the channel. Figure 5.74 shows that the streamline pattern oscillates due to the pressure oscillations. As the flame approaches a profile similar to case AD1, the pressure waves straighten out and this oscillating pattern flows out of the system.

Figure 5.80 and 5.81 show the evolution of the boundary layer thicknesses. At earlier times, both boundary layer thicknesses oscillate, which is caused by the fluctuating velocities due to the pressure wave interactions in the channel. As time increases, these waves leave the system and the thicknesses smooth. Figure 5.82 shows the velocity along the channel centerline for various times. At earlier times, the velocity is constant for a distance ahead of the flame, followed by a decrease in velocity to the end of the channel. The first time plotted corresponds to when the relative flame area was nearly constant. As time increases, the area ratio increases, and the flame velocity increases.

Figures 5.83 and 5.84 show the boundary layer growth in local time. Since the initial pressure wave is curved, the starting point for the local time calculation is when the pressure wave along the wall first reaches a given location. As can be seen in both figures, the boundary layer growth is less then Stoke's First Problem, due to the flow acceleration. Also seen is the fluctuations in the

boundary layer thickness at early times due to the pressure wave reflections. By about 0.25 ms local time, these waves have passed by all locations and the thickness smooth and become self-similar.

5.2.2 Case AS2 : Effects of Increased Channel Height

This case has the same channel geometry as the third planar ignition case, AD3, in that the channel height is doubled, making the channel aspect ratio 16.1. Figure 5.85 shows the initial flame development for the first 0.672 ms. The circular spark deforms greatly in time. The end wall of the channel acts like the side wall for the portion of the flame that is moving along it. As seen at time t_3, the portion of the flame moving along the end wall has obtained a shape similar to the flame that moves along the channel side wall for later times, for example t_5. As the end wall flame approaches the side wall, the portion of the flame traveling along the end wall overtakes the flame a short distance from the end wall. This creates a flame remnant, as seen at time t_5. This remnant becomes detached from the main body of the flame which propagates down the channel. In time, the remnant burns itself out.

The reason that the remnant was not seen for the first spark case is that there was not enough time, or distance traveled along the end wall, for it to develop. As seen in figure 5.69 for the first spark case, the flame moving down the end wall reaches the side wall by about 0.230 ms. For case AS1, the flame moving along the end wall is nearly straight, as opposed to the highly curved flame that exists in the present case. When the straight flame nears the end wall, the flame along the wall accelerates to the corner as seen at time t_3 in figure 5.69, so that no remnant forms.

Figures 5.86 and 5.87 show the flame position and velocity. Compared to the third planar ignition case, AD3, which has the same channel height, this case exits the channel sooner and reaches a higher flame speed. This is caused by a higher burn area, as shown in figure 5.88. This figure compares the relative burn area for the two cases. The higher burn area for the spark case leads to a higher flame speed. Also, comparing figures 5.87 and 5.88, the flame speed has the same general shape as the area ratio.

Figures 5.89 - 5.96 show the flowfield properties at 0.348 ms, 0.500 ms, 0.650 ms, and 0.801 ms. Figure 5.89 and 5.90 show the flame when it is still moving down the end wall. The end wall flame has the same shape as the side wall flame seen in the previous cases. The velocity vectors and instantaneous streamlines show that the burned material from the end wall flame expands both ahead of and behind the flame. The flow that expands ahead of the flame turns the corner and proceeds out the channel. The material that expands upwards along the end wall then turns and provides an extra push to the flame near the centerline. This flow pattern is similar to the flowfield reported by Gonzalez[16] for the flow induced during a spark ignition. The vorticity plot shows that

the boundary layer for this case begins at the corner of the channel. The pressure plot shows that, like the first spark case AS1, the pressure contours are not straight. This is due to the initially circular pressure wave reflecting off of the side walls.

Figures 5.91 and 5.92 shows the end wall flame as it nears the side wall. The expanding gas that was pushed ahead of the flame and around the corner is now pushed either along the flame surface or is expanded behind the flame. With the gas flow ahead of the end wall flame stopped, the flame traveling adjacent to the wall moves into a nearly stagnant gas. The boundary layer along the end wall formed by the expanding gas disappears when the velocity goes to zero.

Figures 5.93 and 5.94 show how the remnant flame forms. The flame has reached the side wall of the channel. The velocity vectors show that the remnant is drawing material upwards towards it. This upward flow provides an added momentum push from the remnant flame towards the centerline of the channel. Due to the presence of the end wall, the additional push on the flame attached to the end wall is less due to the no-slip boundary condition bringing the velocity to zero. This allows the attached flame to overtake the flame in the center of the remnant. This is similar to what happens to a flame in a closed channel when it reaches the wall opposite from the ignition source. The flame that reaches the side wall is quenched, and a remnant is left behind by the main flame as it propagates down the channel. Figures 5.95 and 5.96 show the flame after the remnant has burned out. The flame assumes a shape similar to the shape in case AD1. Unlike case AD3, no cusp forms at the centerline. This is because the centerline flame always has an additional momentum push and can remain ahead of the rest of the flame body.

The evolution of the displacement thickness and boundary layer thickness is shown in figures 5.98 and 5.97. The oscillations at the earliest time shown are due to the pressure oscillations caused by the reflecting waves from the initial circular pressure wave. This is the same thing that happened in the first spark case, AS1. By later times the fluctuations have exited the channel and the thicknesses smooth out. Both thicknesses are greater than the first spark case due to the lower velocity. They are thinner though than the third planar case, AD3, because compared to that case this case has greater acceleration. The greater acceleration thins out the boundary layer.

Figure 5.99 and 5.100 give the growth of the boundary layer in local time. Due to the acceleration of the flow, the boundary layer growth is less than Stokes' First Problem until about a local time of 1.2 ms when the growth becomes greater. This corresponds to the deceleration of the flame as shown in figure 5.87. The oscillations that occur in the beginning of the plots are from the pressure reflections as described in the preceding paragraph.

5.2.3 Comparison of the Spark Ignition Cases

Figure 5.101 show the evolution of the area ratio for the two spark ignition cases. Figure 5.102 shows the time history of the flame speed. On both figures, the related case from the planar ignition simulations with the same channel height is also shown. For the first spark case, AS1, the area starts out less then the area for the planar ignition, due to the smaller spark size, but very rapidly surpasses the area from the first planar ignition case. Since the burn area is increased, the speed of the flame is increased. The second spark case, AS2, also starts out with less flame area, but quickly surpasses the burn area from the third planar case. It always remains above the area for the third planar case. Figure 5.103 shows the growth of the boundary layer at the 8 cm location for both spark cases. Both are seen to be less then the solution to Stokes' First Problem, except for the later part of AS2 which starts to grow faster. This is due to the deceleration of the flame as shown in figure 5.102.

Figure 5.104 shows the flame speed and burn area plotted on the same graph. The curve for the flame speed is seen to follow the curve for the burn area. Figure 5.105 shows the flame speed plotted against the burn area. In both cases, for the initial expansion of the spark, the curves are nearly linear and lie almost on top of each other. The relationship between the flame speed and burn area was given in equation 5.9, and is repeated here.

$$S_F = \left[S_l \left(\frac{T_b}{T_u}\right)\right] \left(\frac{A_f}{A_c}\right) \tag{5.13}$$

Using a laminar flame speed of 128 cm/s and a temperature ratio of 8, the theoretical value for the slope is 1024. For the initially linear portion of both curves, the slopes are 991 for AS1 and 970 for AS2, differences from theory of 3.2% and 5.3% respectively. The curve for AS1, after the initial expansion of the spark, the burn area curve flattens out, as does the flame speed. Since the two curves are slightly out of phase with each other this accounts for the notch back at an area ratio of about 5. After this constant region the flame area begins to increase again with a slope of 1096, 7.0% from the theoretical value. After the spark expansion, the burn area decreases, then slightly increases again. Since there is a lag time in the response of the flame speed, this accounts for the wandering of the curve in figure 5.105 after the initial straight section.

5.3 Isothermal Wall

This case has a channel geometry the same as the first adiabatic wall case, AD1. The channel is 0.254 cm in height and 8.2 cm in length. The ignition method is a planar high temperature region

located at the closed end of the channel from 0 cm to 0.3 cm. This is the same ignition method as in the first adiabatic wall case. The wall temperature boundary condition from 0.3 cm to the outflow end of the channel is isothermal, with a wall temperature of 293 K, which is equal to the initial unburned gas temperature. The species boundary condition is non-catalytic. The reference coefficients for the transport properties, μ_r, k_r, and D_r, are given in Table 2.1, so that the Lewis and Prandtl numbers are unity.

Figure 5.106 shows the flame position in time at the centerline of the channel. Shown for comparison is the flame position for the first adiabatic wall case and the 1-D flame. Figure 5.107 gives the isothermal flame speed in time. Compared to case AD1, the isothermal flame takes a longer time to exit the channel. The flame speed also shows that the flame accelerates and decelerates as it propagates down the channel. This is consistent with the "jerky" motion of a flame,[9,27] where the motion oscillates. It is also interesting to note that the mean propagation location and velocity is close to the 1-D flame results.

Figure 5.108 shows the flowfield temperature, T, fuel mass fraction, Y, chemical energy release, ΔE_c, and pressure, p, at 0.217 ms. The chemical energy release is the amount of energy that is transferred from the zero point energy term, $\rho q Y$, to the sensible energy term, $\rho c_v T$ in the energy equation, (2.25), during the chemical reaction.

$$\Delta E_c = \rho q \frac{dY}{dt} \tag{5.14}$$

The pressure waves that emanate from the initial planar discontinuity are nearly planar, as with the first adiabatic wall case. As seen in the temperature plot, the cold wall cools the hot burned product behind the flame. The mass fraction profiles do not follow the temperature profiles as they did for all of the adiabatic wall cases. This is due to the mass diffusion effects. The energy release shows that the flame is quenched, or extinguished, due to the cold wall. This is evident by the energy release not touching the lower wall. The quenching distance for a flame traveling between parallel plates is derived in Appendix C and is repeated here.

$$d_q = \delta_t \sqrt{2 \left(\frac{k_w}{k} \right) \left(\frac{T_q - T_u}{T_b - T_u} \right)} \tag{5.15}$$

where d_q is the quenching distance, and T_q is a quenching temperature. Using a value of 1000 K for the quenching temperature, and evaluating the thermal conductivity, k, at the average flame temperature of 1319 K, the theoretical quenching distance is 0.011 cm. Again using the 1000 K isotherm as a reference, the average separation distance over the entire calculation between the wall and the nearest position of the isotherm to the wall is 0.005 cm. Since this value represents quenching for half of the flame, due to the symmetry condition at the centerline, the total quenching distance is 0.010 cm, about a 10% difference from the theoretical value.

Figure 5.109 shows the velocities and instantaneous streamlines for this time. The expanding burned gas induces a flow ahead of the flame in the unburned material toward the open end of the channel. A flow also develops behind the flame in the burned region. This is due to the cooling of the hot burned product by the cold wall. This cooling of the gas by the wall causes the density to decrease. This decrease in density provides space into which the burned material can expand.

Figures 5.110 and 5.111 show the flame properties at 1.304 ms. By this time in the adiabatic wall cases, the flame is nearly at or has exited the channel. For this case, the flame has reached about 1.5 cm down the channel from the initial planar discontinuity. The temperature plots shows that the cooling is more pronounced, with a large cool region existing behind the flame. This large cool region behind the flame allows the burned material to expand back toward the end wall. Examining the u velocity plot, there is a greater magnitude of reverse flow then there is for flow out of the channel ahead of the flame. The streamlines show a region of reversed flow has developed ahead of the flame close to the lower wall and extends to the exit of the channel. The flow in the center of the channel is still directed out of the channel. The pressure plots shows that there is an adverse pressure gradient in the channel.

Figures 5.112 and 5.113 show the flame properties at 1.760 ms. The streamlines show that the reversed flow region near the lower wall is gone. The flow ahead of the flame is entirely moving toward the exit of the channel. The velocity at the centerline ahead of the flame has accelerated to a faster speed. The pressure gradient ahead of the flame has also reversed itself into a favorable one. Figures 5.114 and 5.115 give the flame properties at 2.519 ms. The reversed flow region near the lower wall has returned. The pressure gradient is again adverse. Re-examining figure 5.107, the regions of flow reversal roughly correspond to the regions where the flame is decelerating. When the flow reversal ahead of the flame is not present the flame is accelerating. The pressure gradient reversing is directly related to the flame motion. When the flame motion is decelerating, expansion waves are generated, causing an adverse pressure gradient to form ahead of the flame.[1]

The centerline velocity at different times is shown in figure 5.116. The velocity at various channel locations ahead of the flame in the unburned gas is given in figure 5.117. Both figures show that the flow at the centerline of the channel ahead of the flame always remains positive, that is the flow is always directed toward the outflow of the channel. The centerline flow behind the flame is directed backwards toward the end wall, and can be greater in magnitude then the outward directed flow.

Figure 5.118 gives the variation in the flame area in time. Shown for comparison is the flame area for case AD1. The flame area is defined for this case as the length of the 1000 K isotherm from the channel centerline to the closest point that it reaches from the lower wall. Comparing the variation of the flame area with the flame speed from figure 5.107, the area ratio follows the flame

speed. When the speed decreases, the area decrease, and vice-versa.

The total chemical energy release and the total heat extracted by the cold wall are shown in figure 5.119. The total chemical energy release is defined as the integration of the local chemical energy release, as defined in equation (5.14), over the entire flame volume. Assuming a unit depth, the total chemical energy release can be calculated as

$$E_c = \int\int (-\rho q \frac{dY}{dt}) dx dy \tag{5.16}$$

This gives the total amount of energy at each time that is released in the chemical reaction. The total heat extracted from the flow is due to the cooling of the flow by the lower wall. Again assuming a unit depth, the total heat extracted from the flow is given by

$$Q_w = \int_{0.3}^{L} (-k \frac{dT}{dy})_w dx \tag{5.17}$$

where equation (2.33) has been used to evaluate the local heat flux to the lower wall. Due to the noncatalytic wall boundary condition, the term $(dY/dy)_w$ is identically zero. Examining figure 5.119, the total chemical energy release follows the general shape of the flame area and speed variation. As flame area increases, there is more burning so the total energy release increases. The total heat removed by the cold wall is always increasing in time. This is due to the propagation of the flame constantly providing a longer heated zone behind the flame.

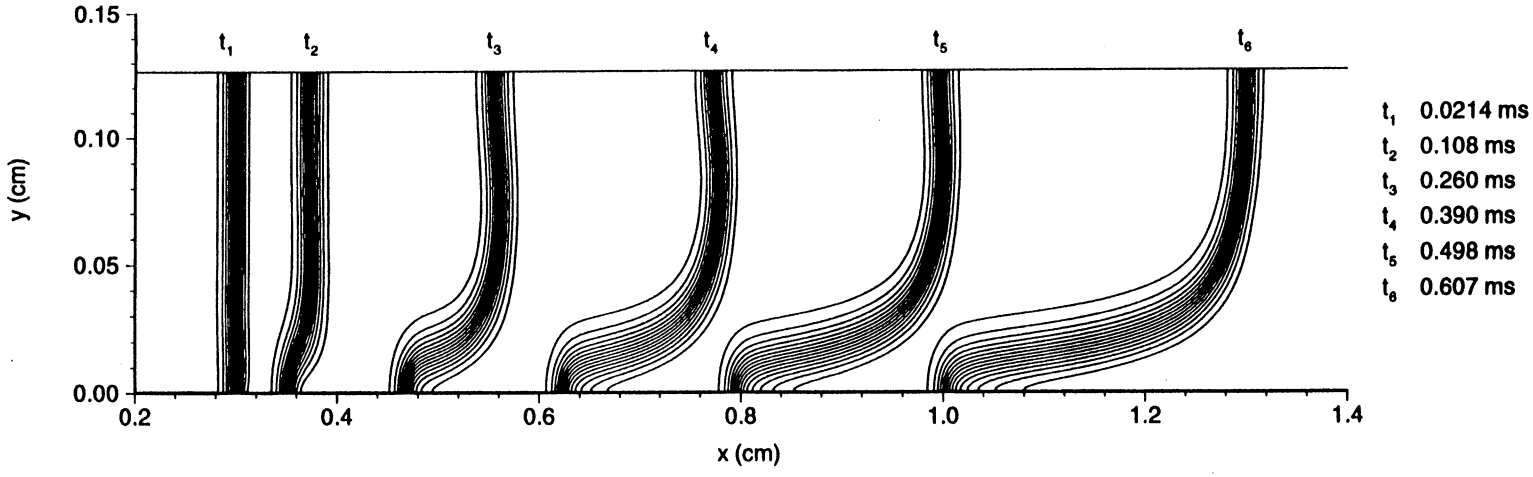

Figure 5.1: Temperature profiles showing the initial flame development, AD1.

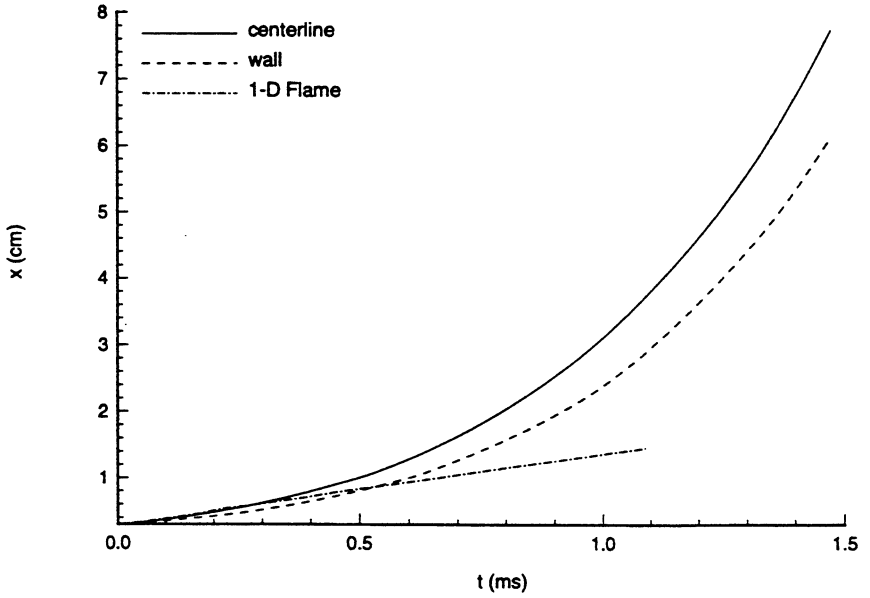

Figure 5.2: Position of the flame at the centerline and wall, AD1.

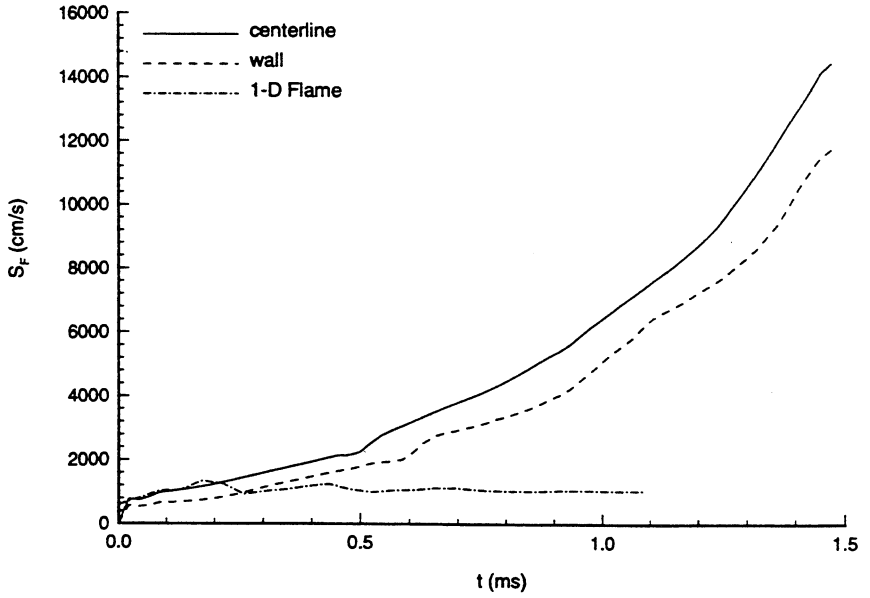

Figure 5.3: Flame velocity relative to laboratory coordinates for the centerline and wall, AD1.

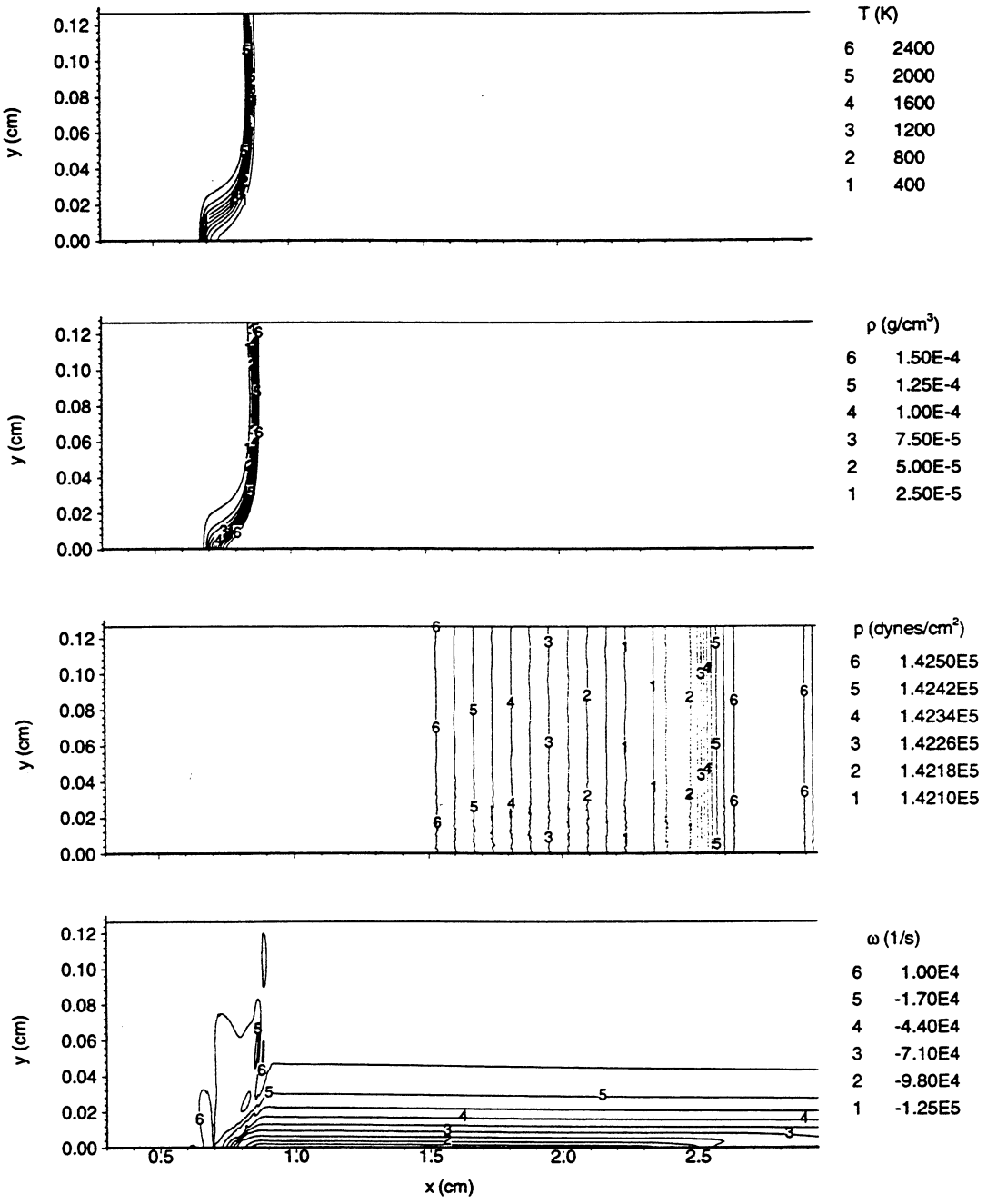

Figure 5.4: Temperature, density, pressure, and vorticity contours, 0.433 ms, AD1.

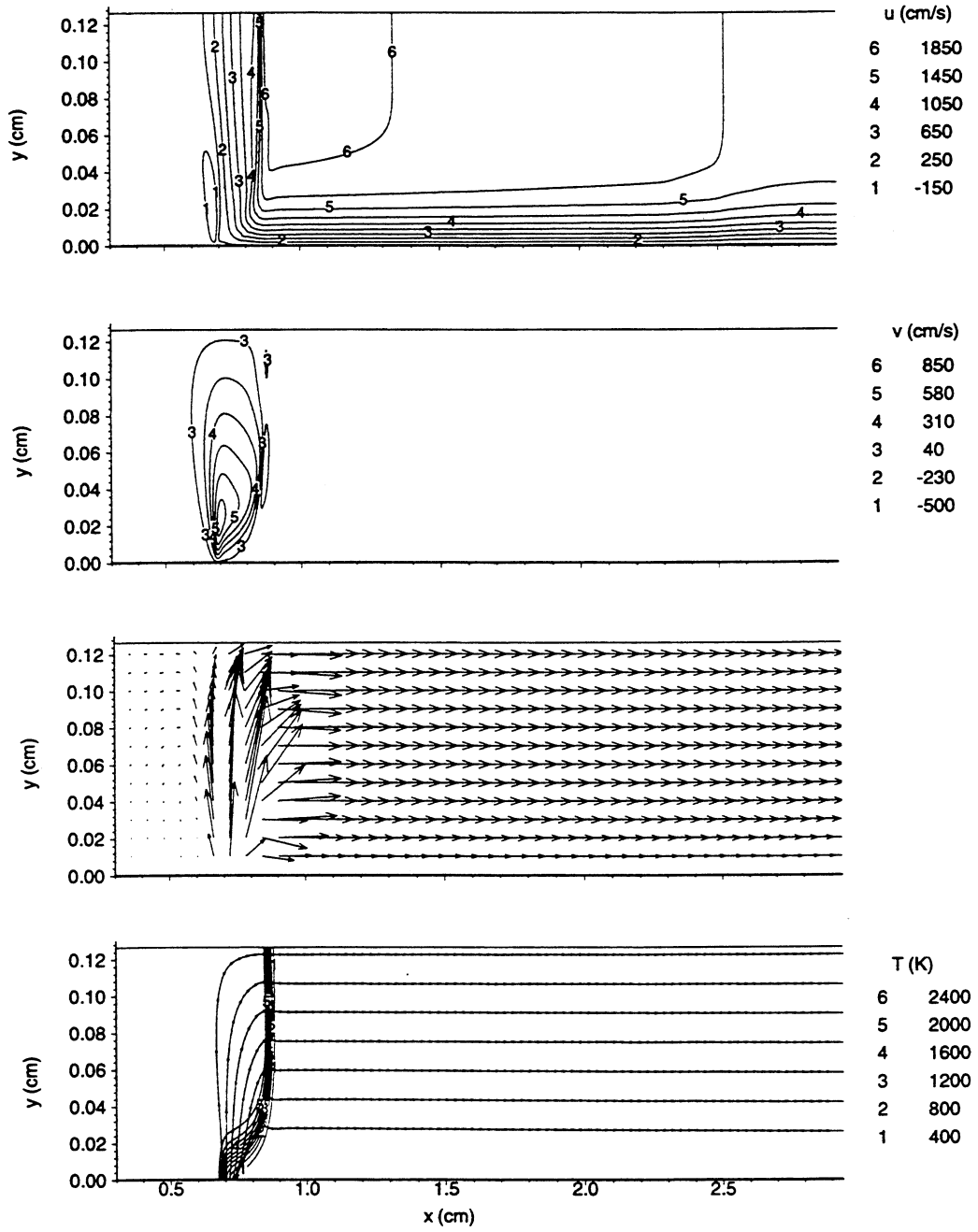

Figure 5.5: Velocity contours, velocity vectors and instantaneous streamlines, 0.433 ms, AD1.

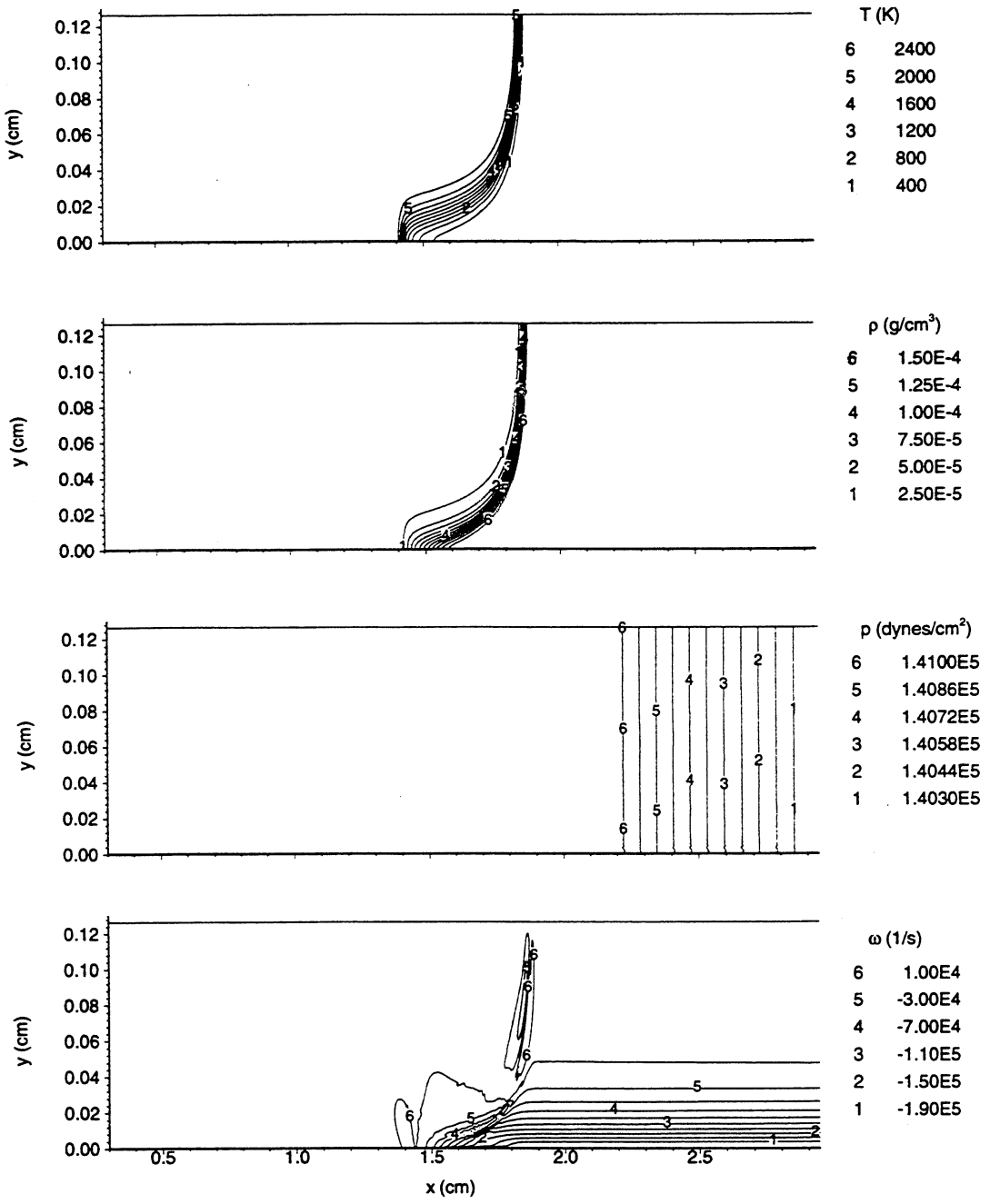

Figure 5.6: Temperature, density, pressure, and vorticity contours, 0.758 ms, AD1.

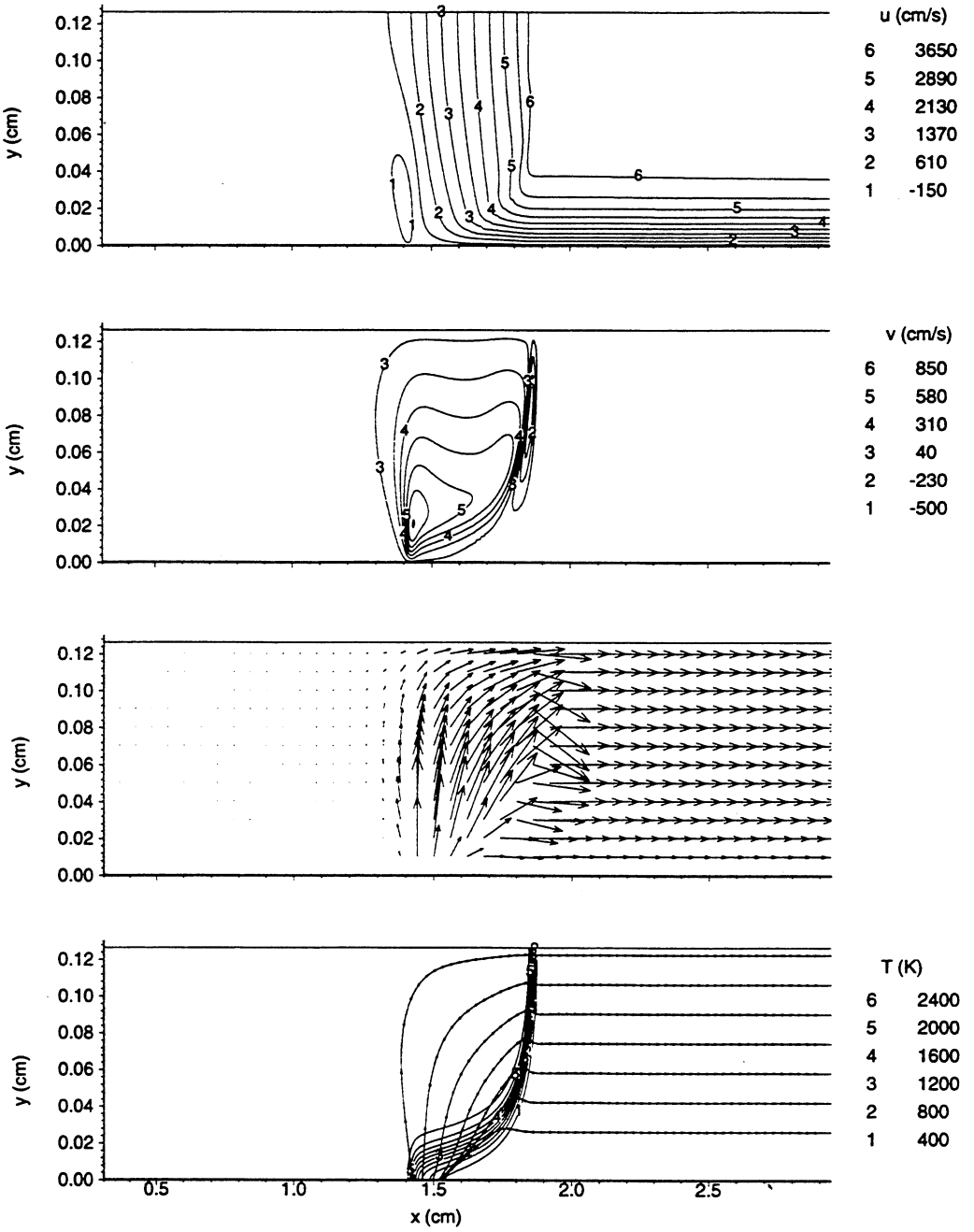

Figure 5.7: Velocity contours, velocity vectors and instantaneous streamlines, 0.758 ms, AD1.

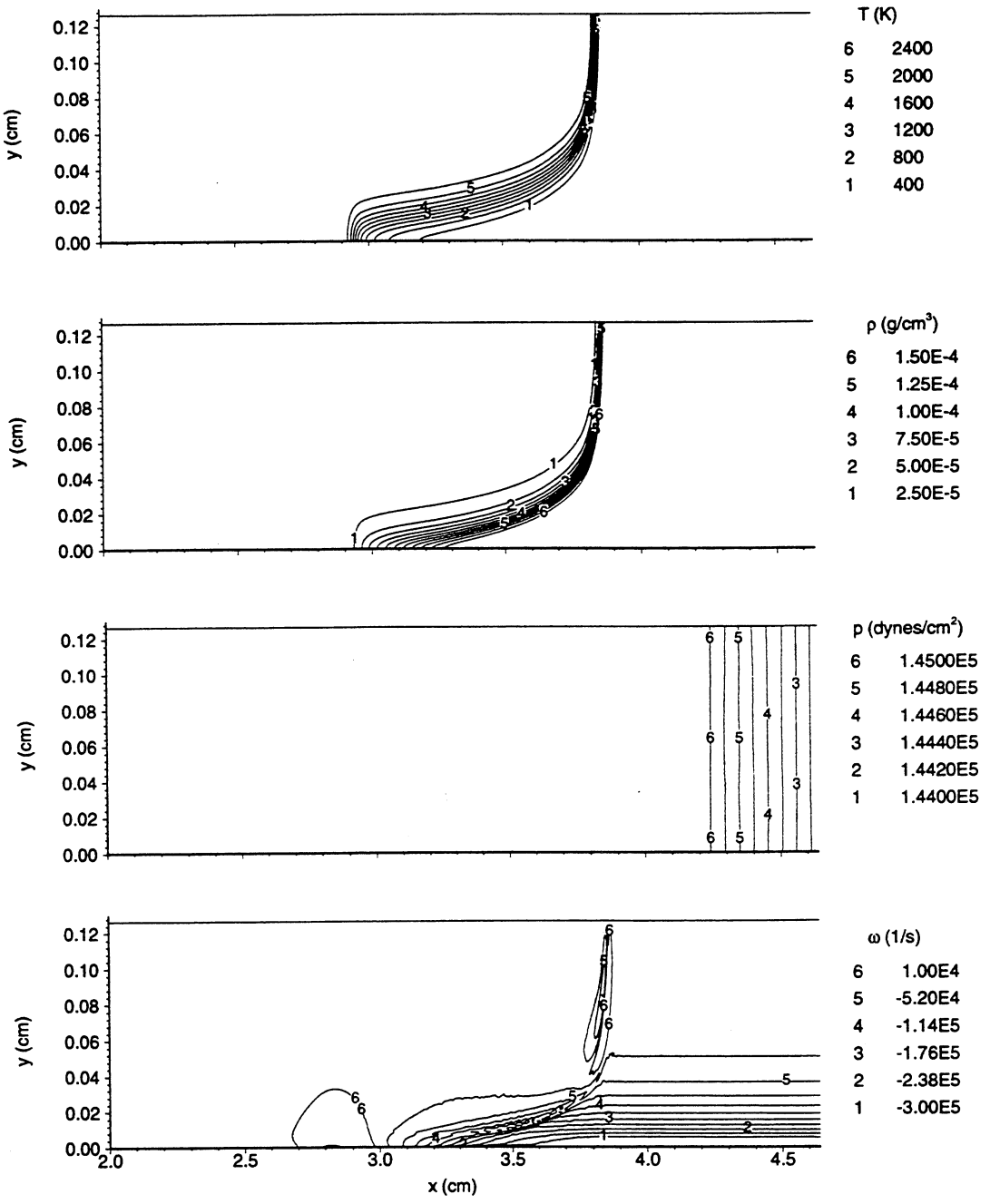

Figure 5.8: Temperature, density, pressure, and vorticity contours, 1.104 ms, AD1.

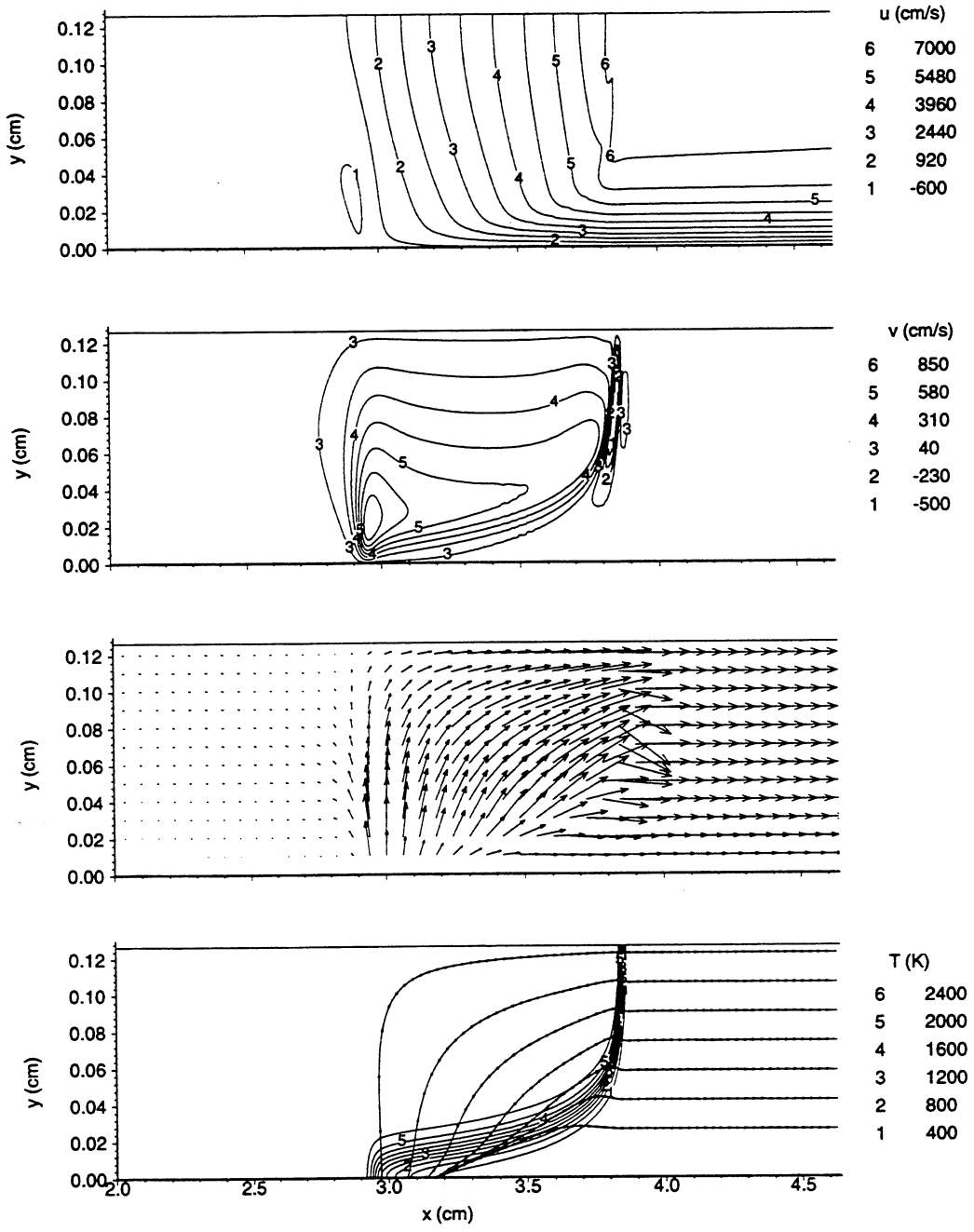

Figure 5.9: Velocity contours, velocity vectors and instantaneous streamlines, 1.104 ms, AD1.

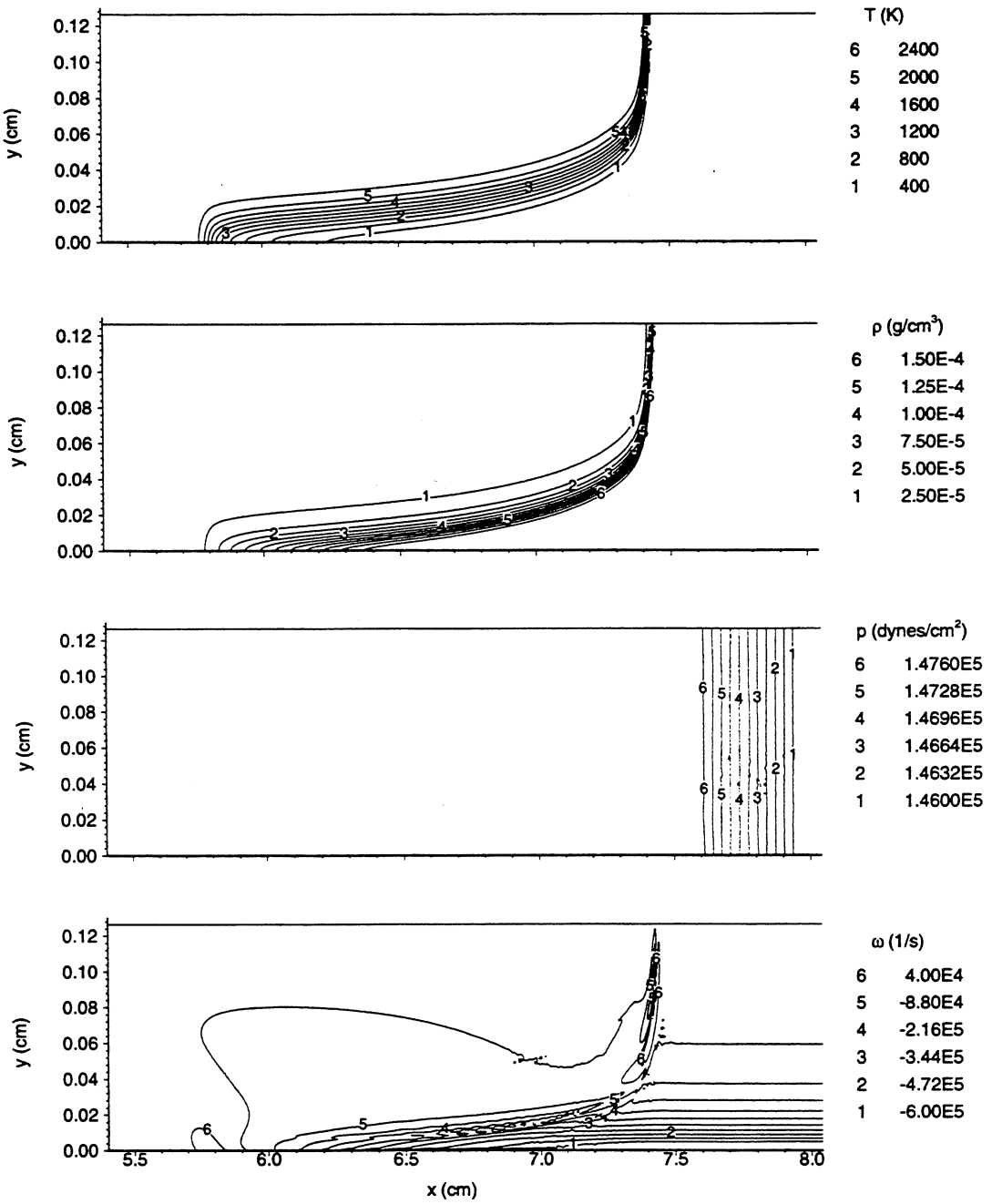

Figure 5.10: Temperature, density, pressure, and vorticity contours, 1.450 ms, AD1.

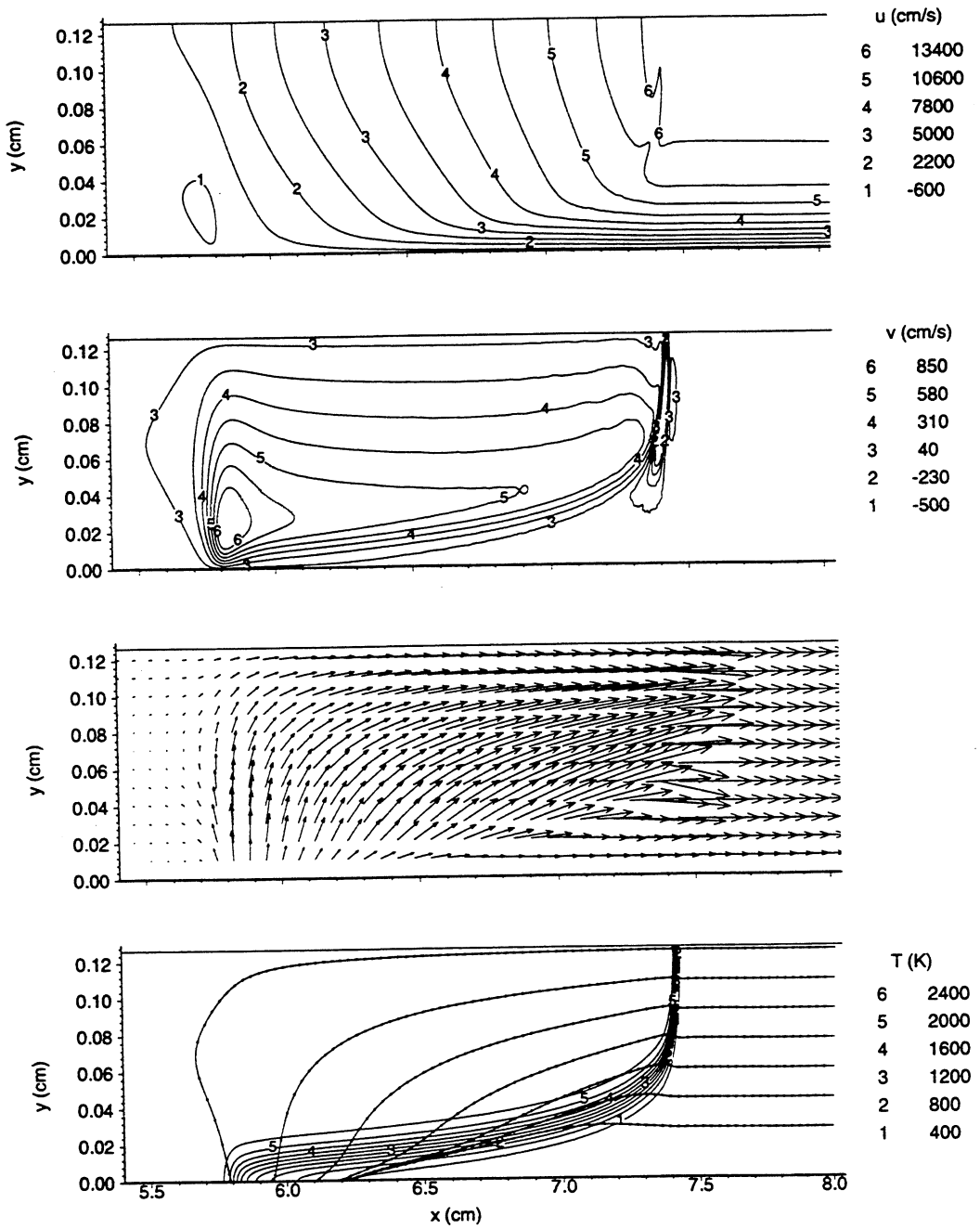

Figure 5.11: Velocity contours, velocity vectors and instantaneous streamlines, 1.450 ms, AD1.

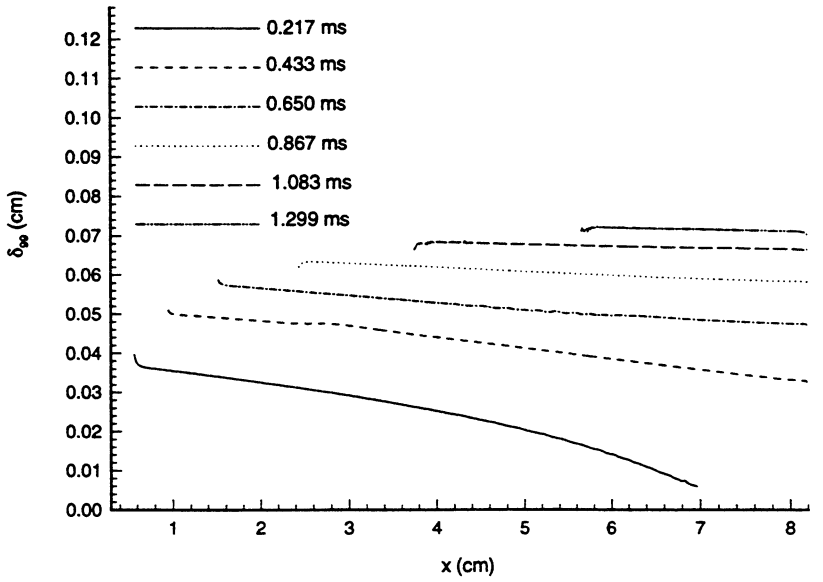

Figure 5.12: Boundary layer thickness for varying time, AD1.

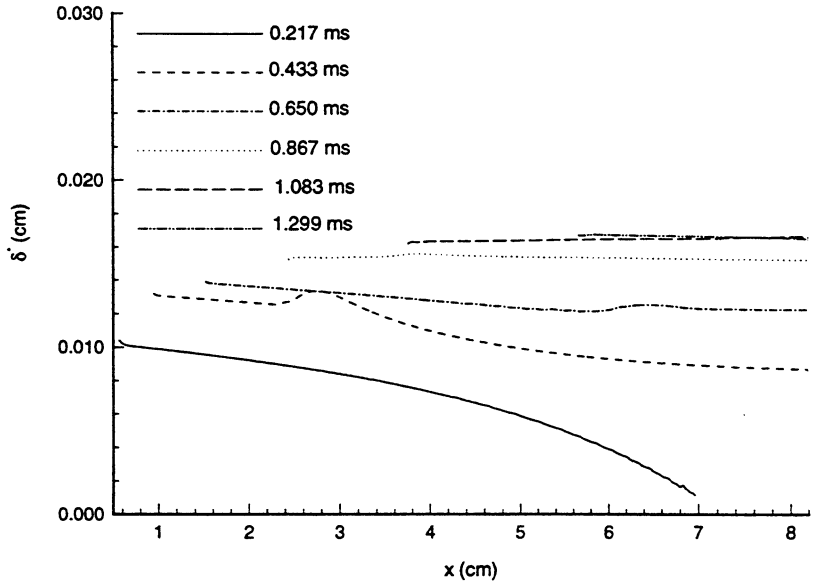

Figure 5.13: Displacement thickness for varying times, AD1.

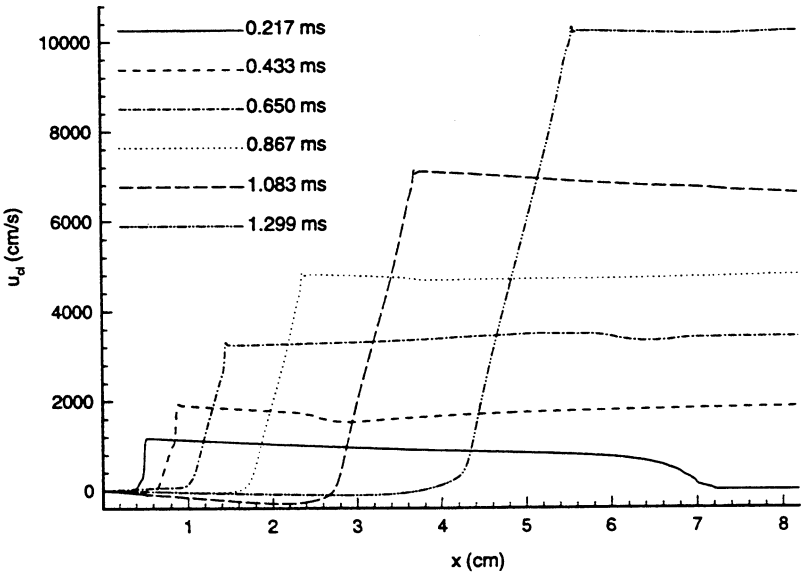

Figure 5.14: Centerline u velocity profiles for varying times, AD1.

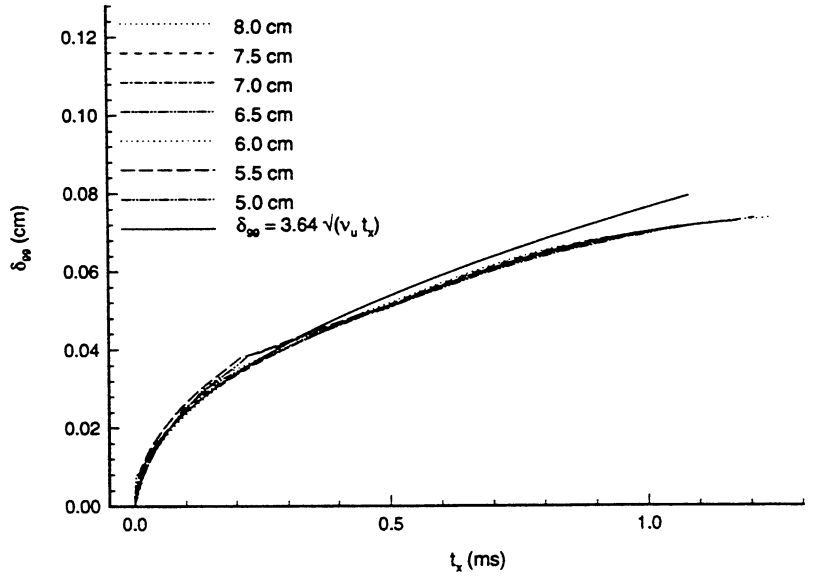

Figure 5.15: Boundary layer height for different x locations as a function of local time, AD1.

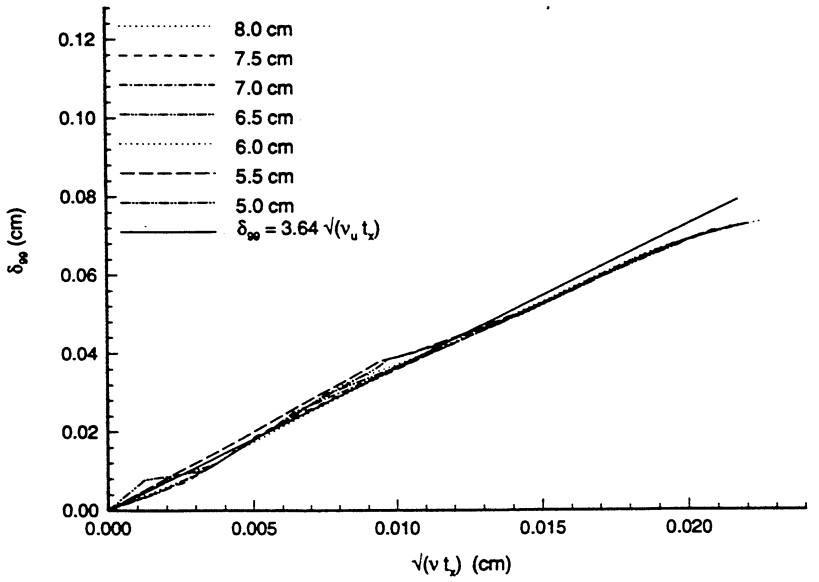

Figure 5.16: Boundary layer height for different x locations as a function of the square root of the product of the local time and edge kinematic viscosity, AD1.

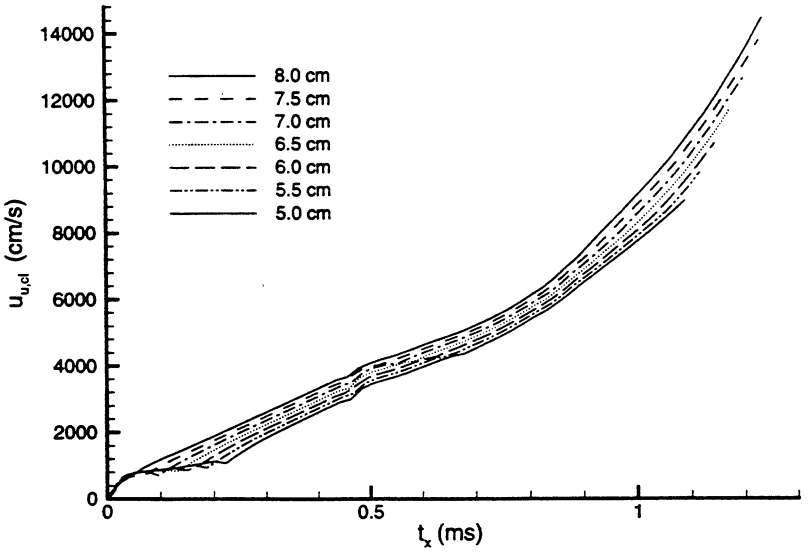

Figure 5.17: Centerline velocity for different channel locations at the local time, AD1.

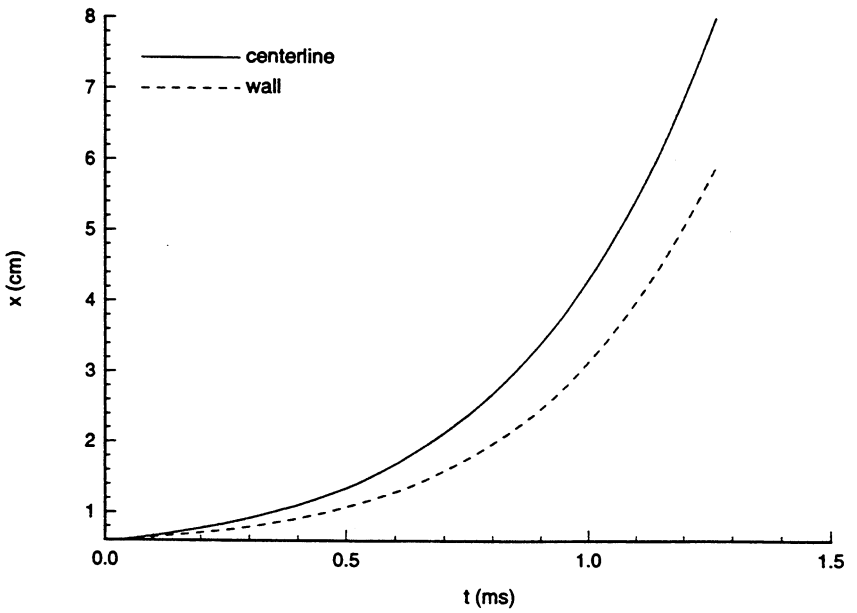

Figure 5.18: Position of the flame at the centerline and wall, AD2.

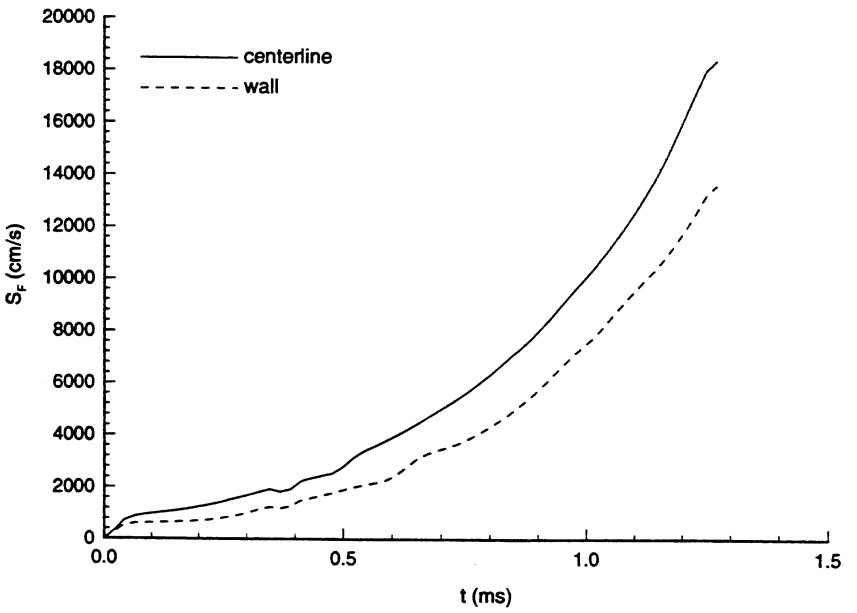

Figure 5.19: Flame velocity relative to laboratory coordinates for the centerline and wall, AD2.

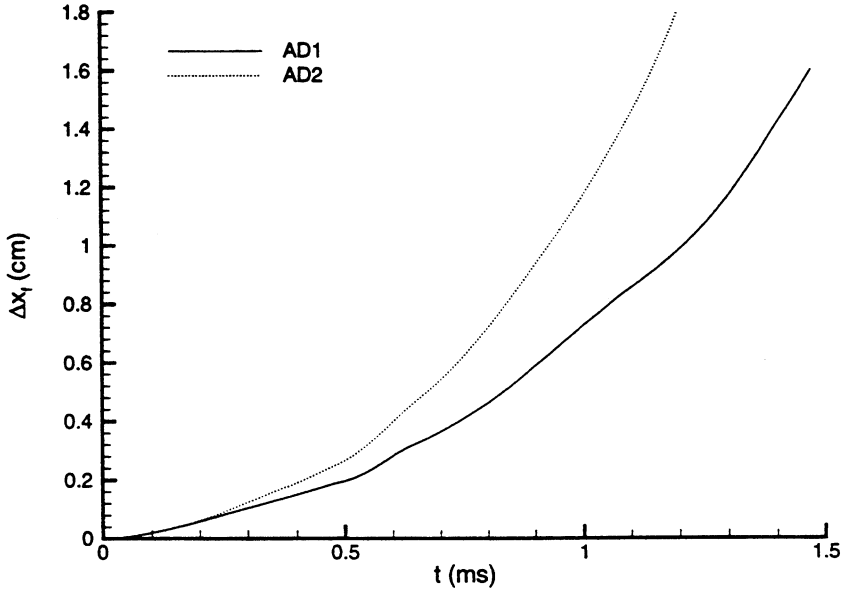

Figure 5.20: Comparison of the length of the curved flame near the wall between cases AD1 and AD2.

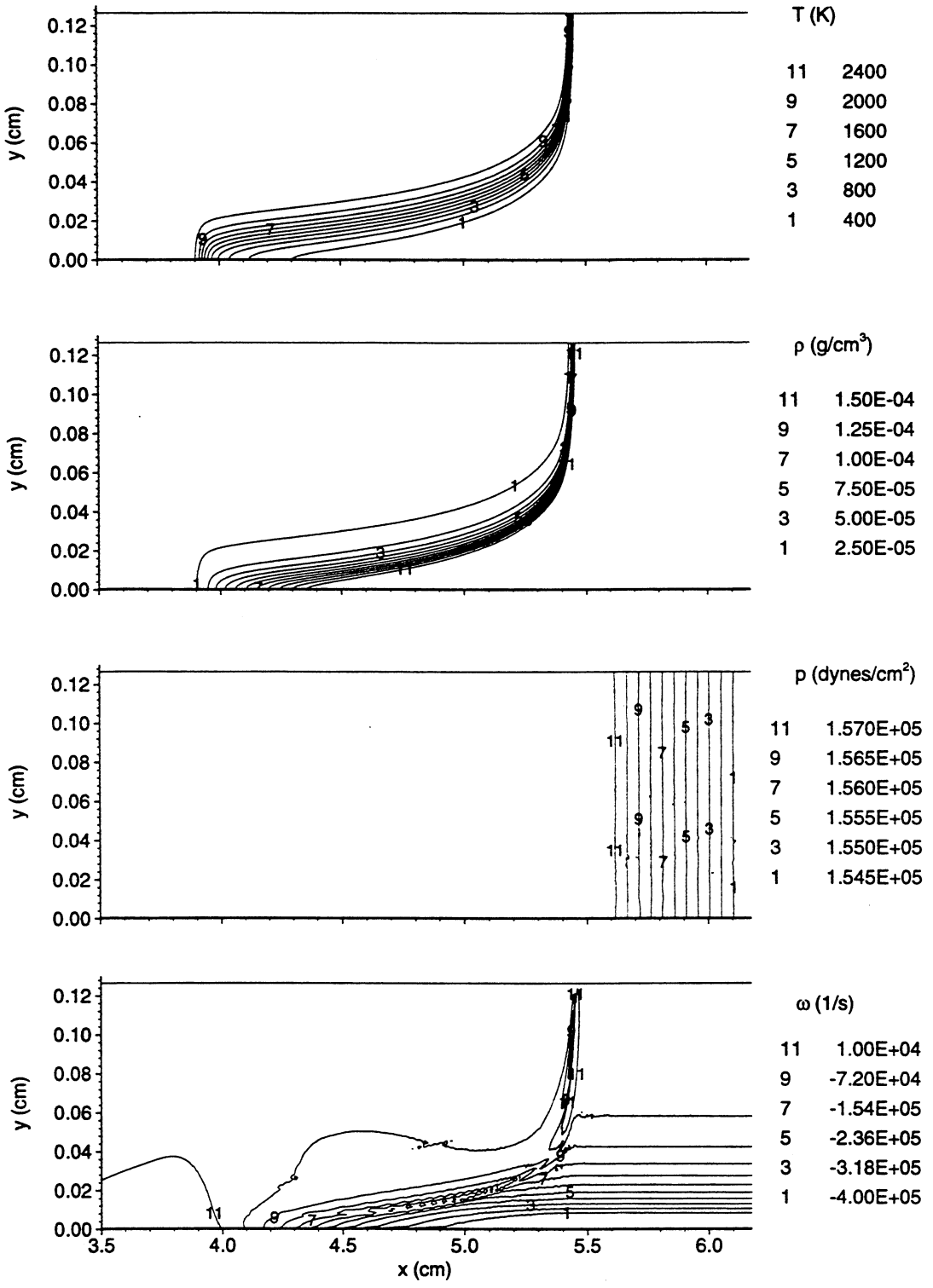

Figure 5.21: Temperature,density,pressure, and vorticity contours, 1.100 ms, AD2.

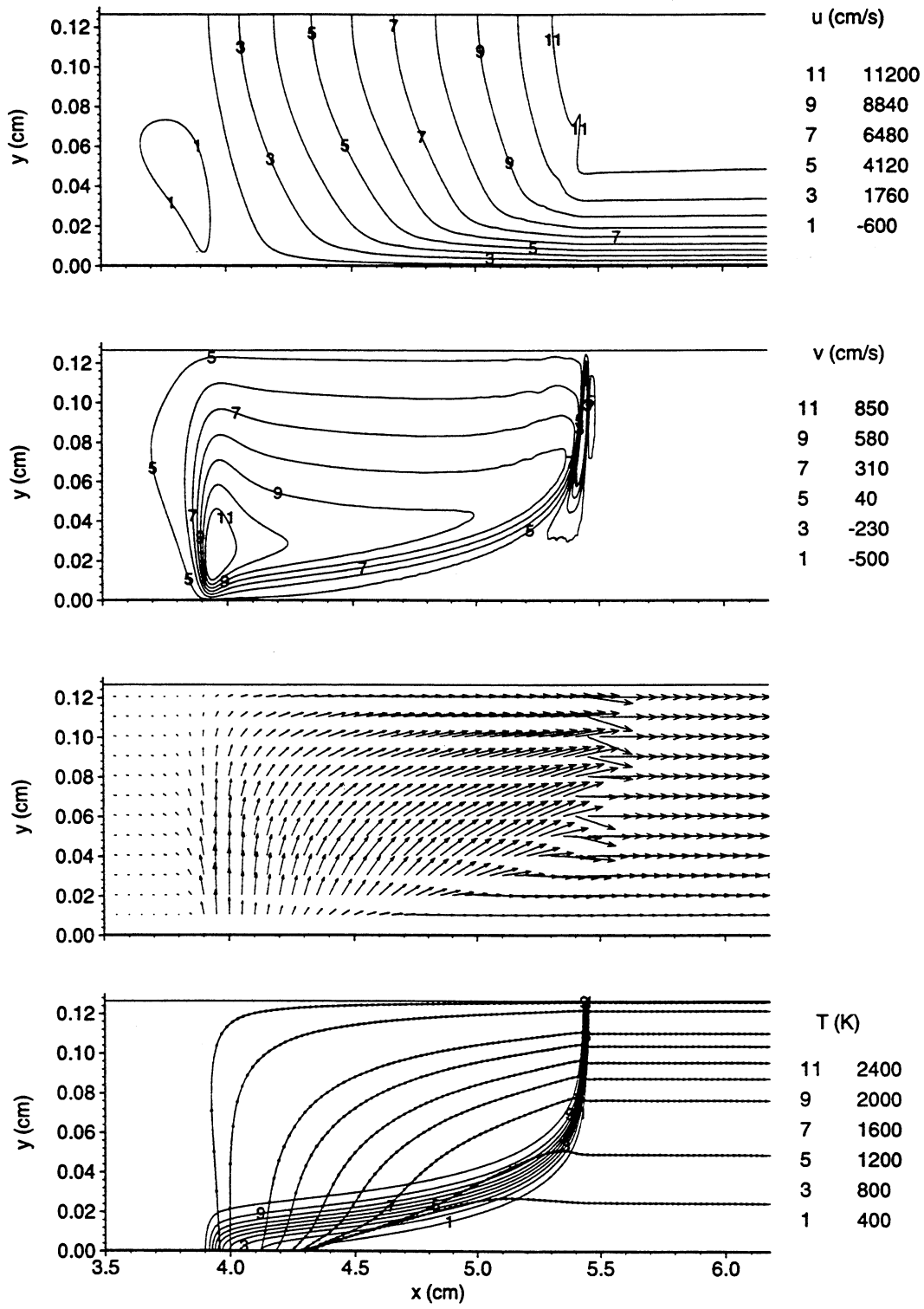

Figure 5.22: Velocity contours, velocity vectors and instantaneous streamlines, 1.100 ms, AD2.

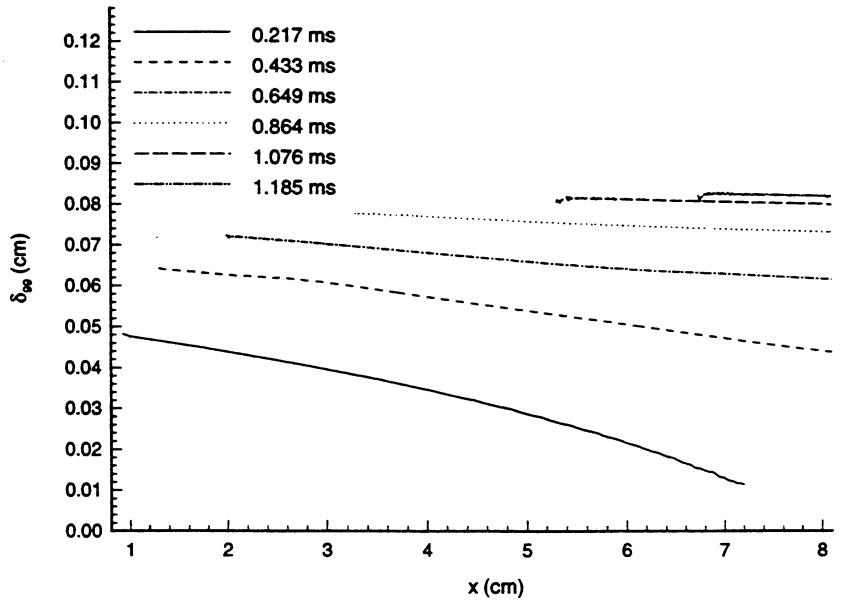

Figure 5.23: Boundary layer thickness for varying time, AD2.

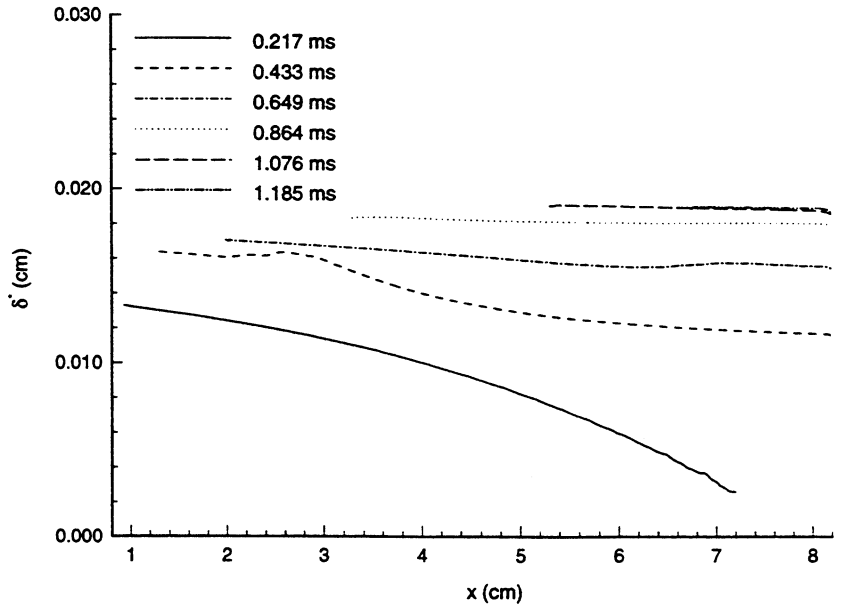

Figure 5.24: Displacement thickness for varying times, AD2.

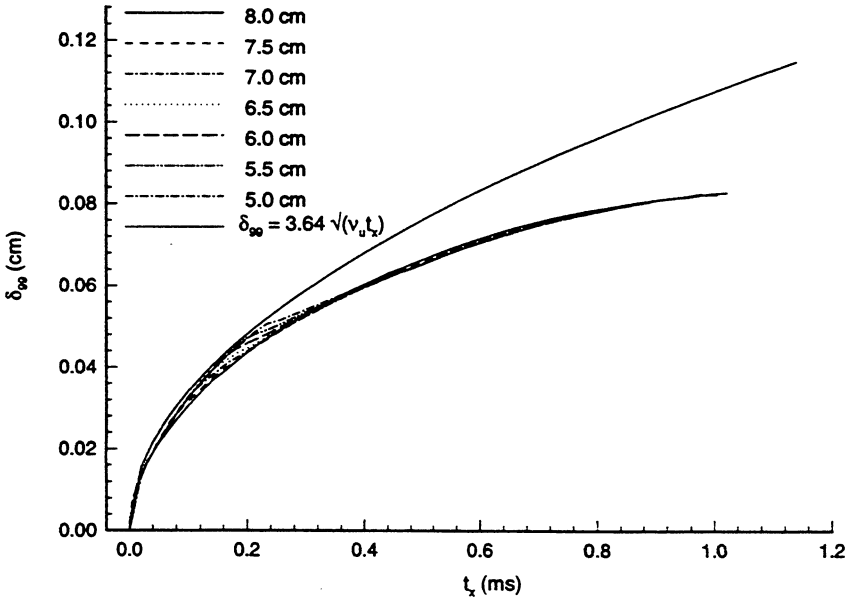

Figure 5.25: Boundary layer height for different x locations as a function of local time, AD2.

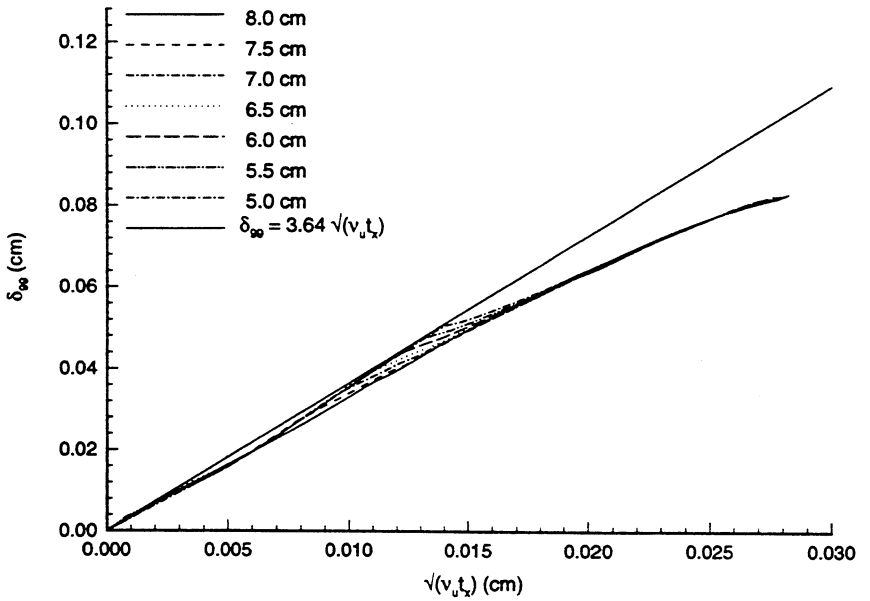

Figure 5.26: Boundary layer height as a function of the square root of the product of the local time and edge kinematic viscosity, AD2.

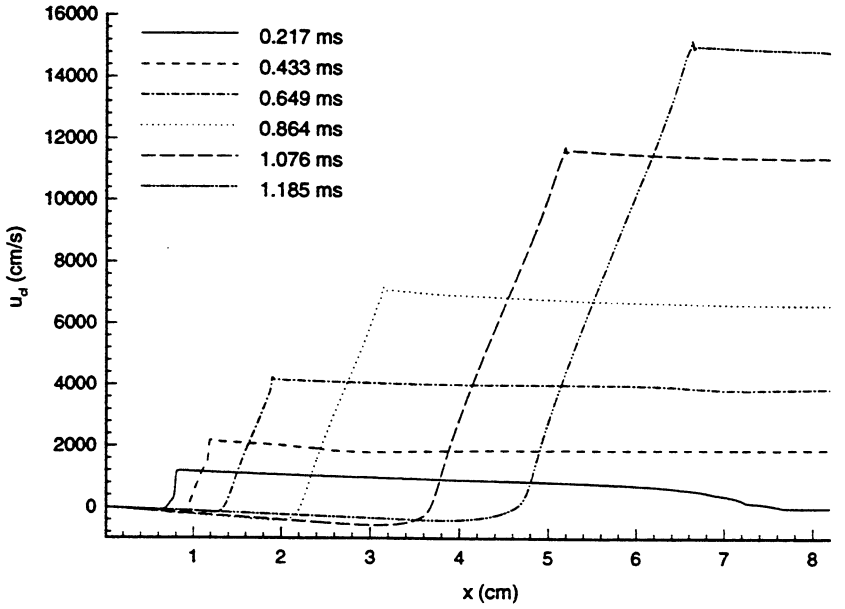

Figure 5.27: Centerline velocity profiles for varying times, AD2.

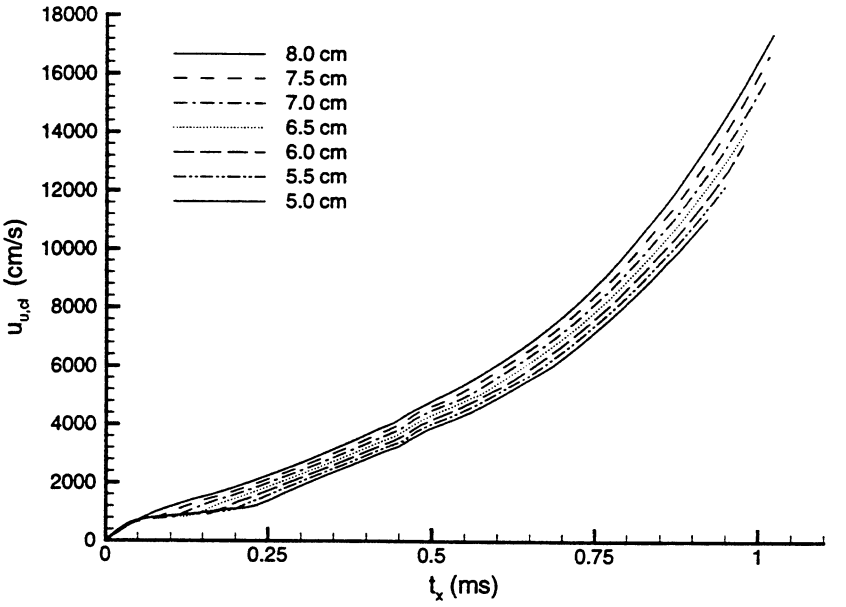

Figure 5.28: Centerline velocity profiles at different channel locations, AD2.

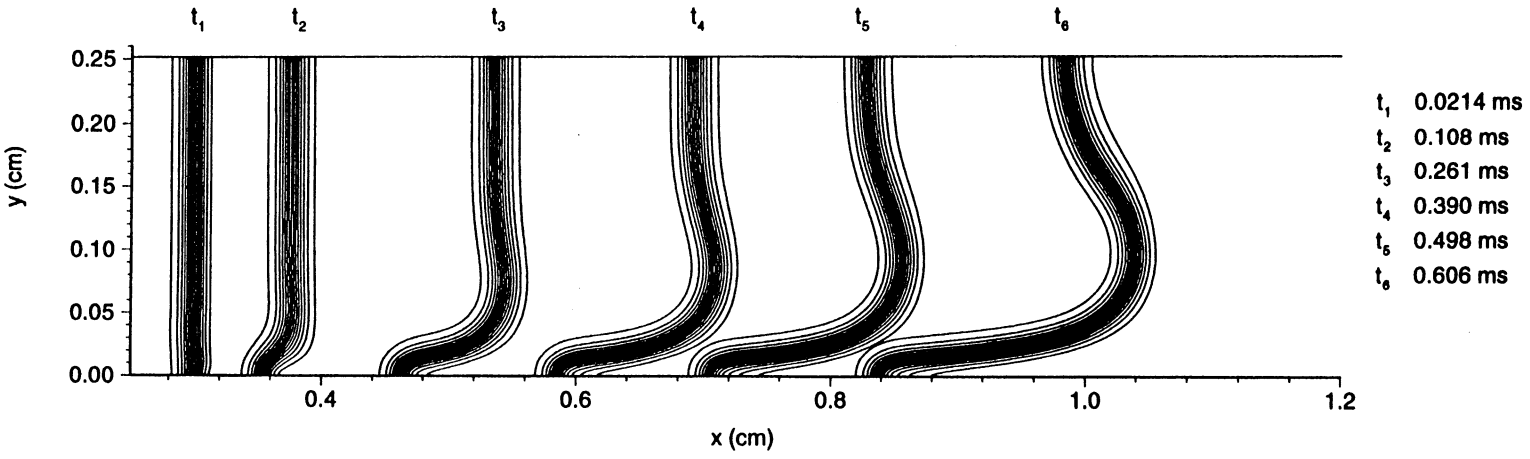

Figure 5.29: Temperature profiles showing the initial flame development, AD3.

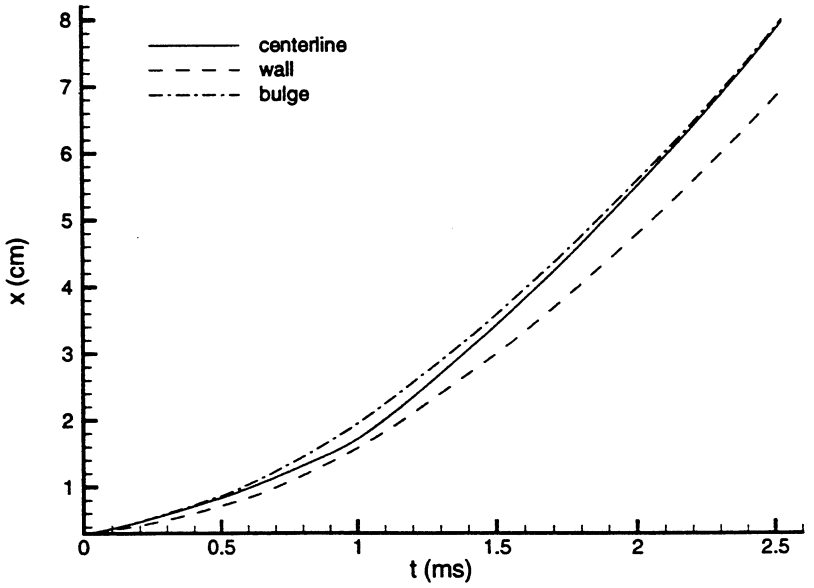

Figure 5.30: Flame position at the centerline, bulge, and wall, AD3.

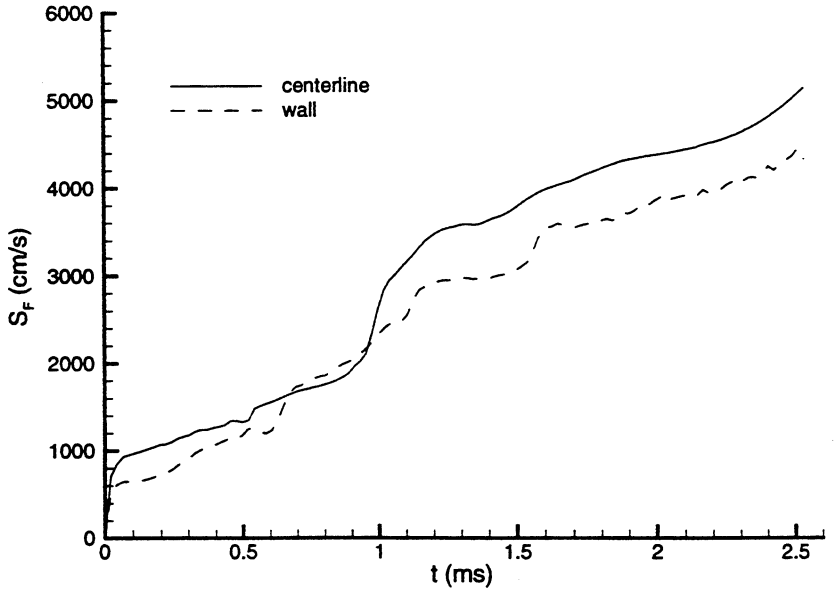

Figure 5.31: Flame velocity relative to laboratory coordinates for the centerline and wall, AD3.

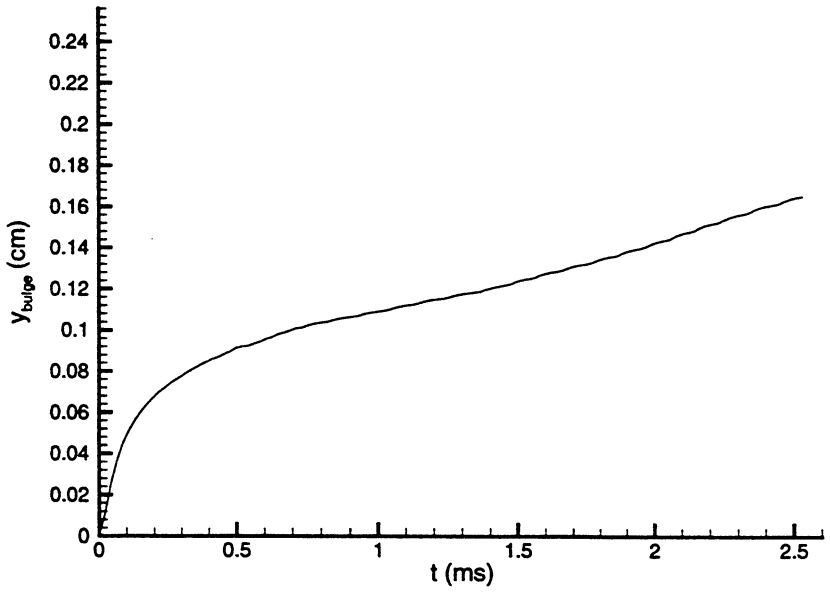

Figure 5.32: Vertical position of the bulge in time, AD3.

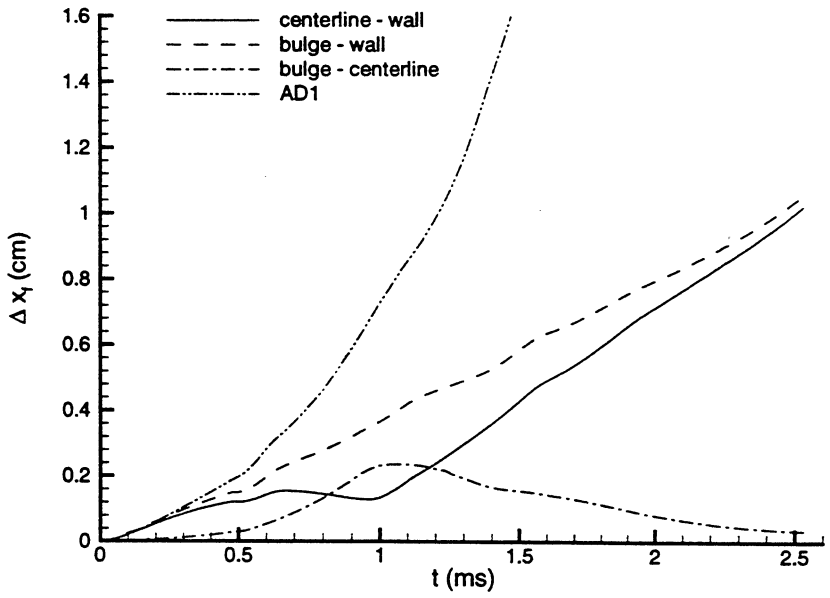

Figure 5.33: Length comparisons between flame points.

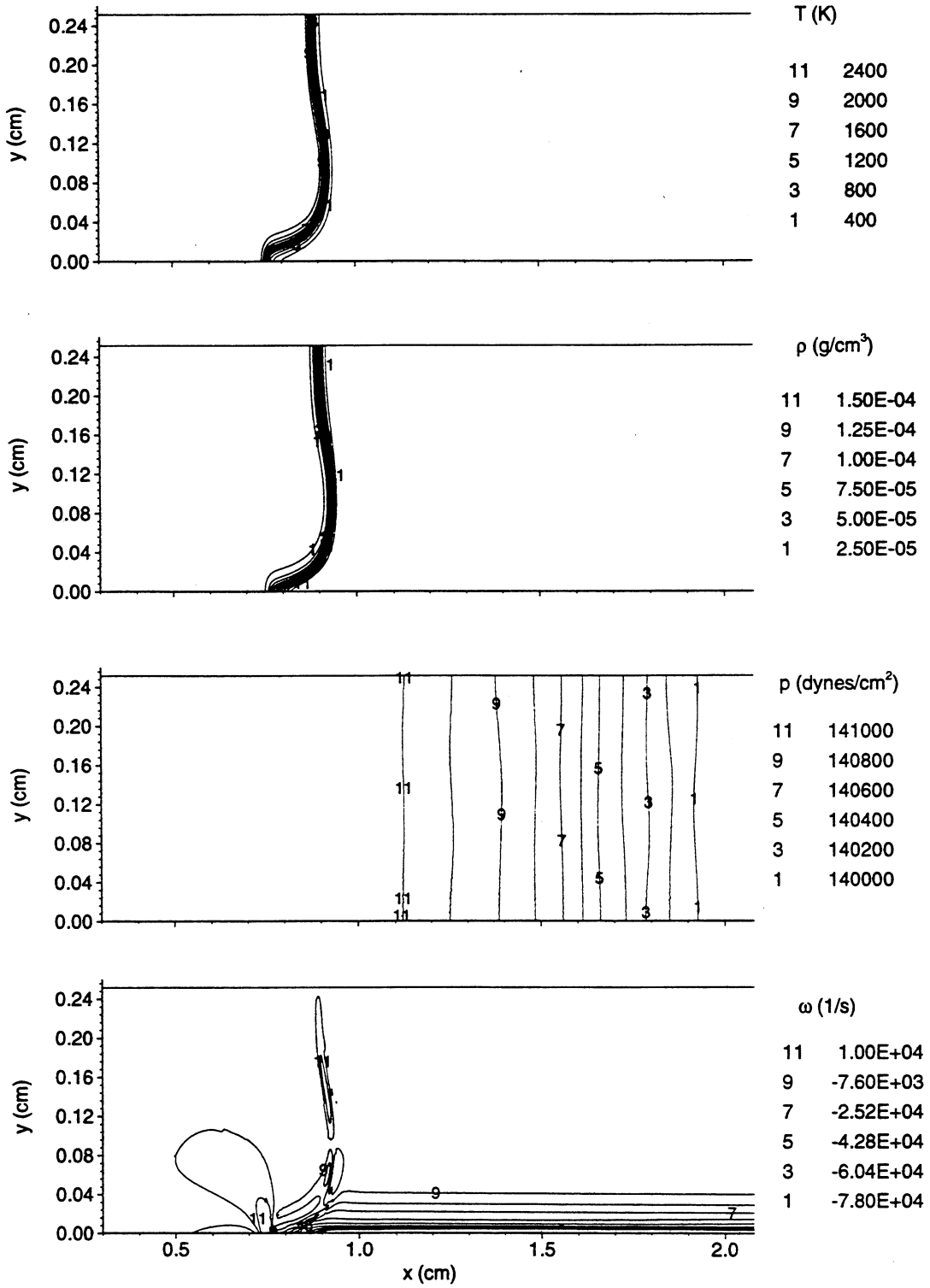

Figure 5.34: Temperature,density,pressure, and vorticity contours, 0.541 ms, AD3.

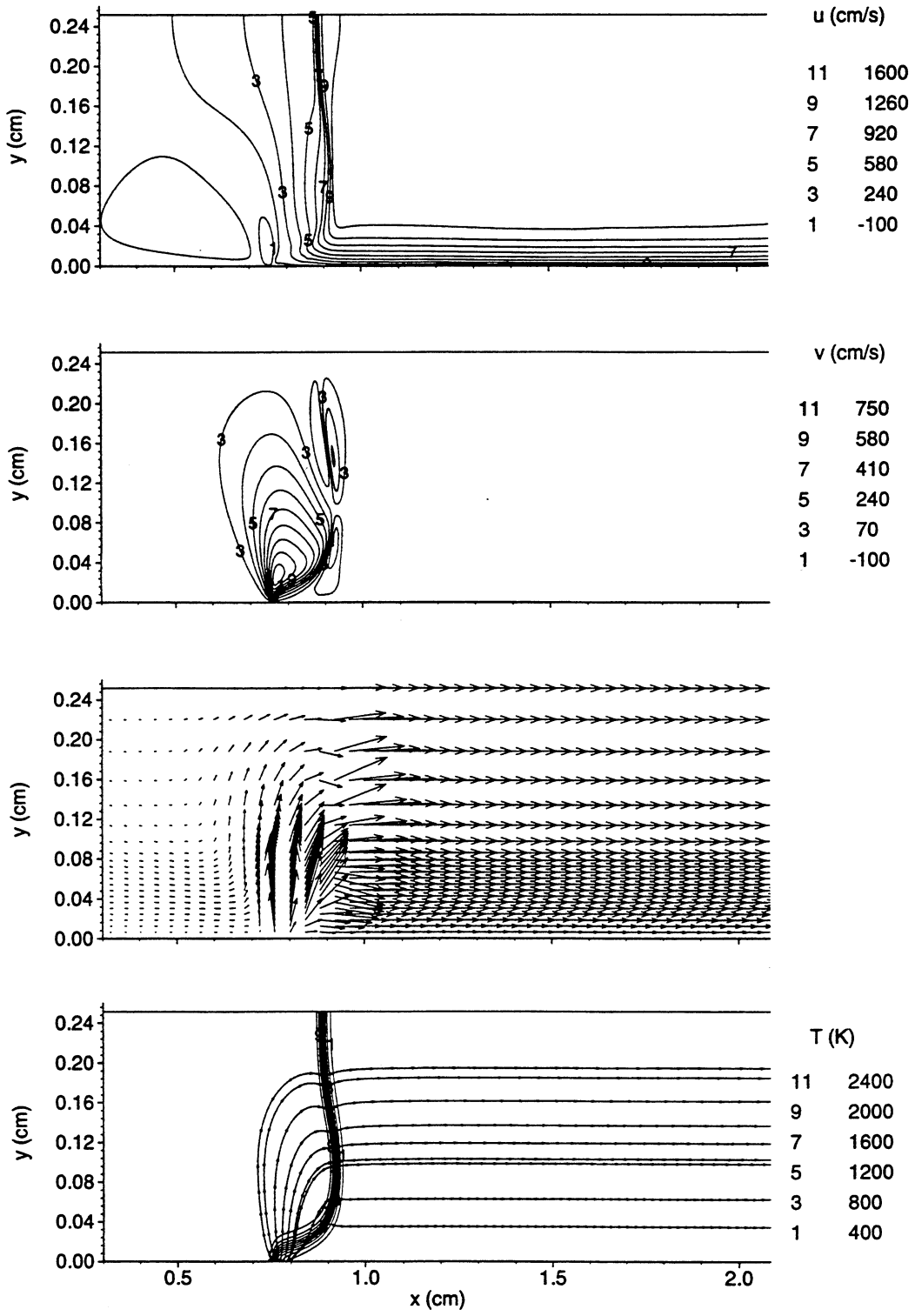

Figure 5.35: Velocity contours, velocity vectors and instantaneous streamlines, 0.541 ms, AD3.

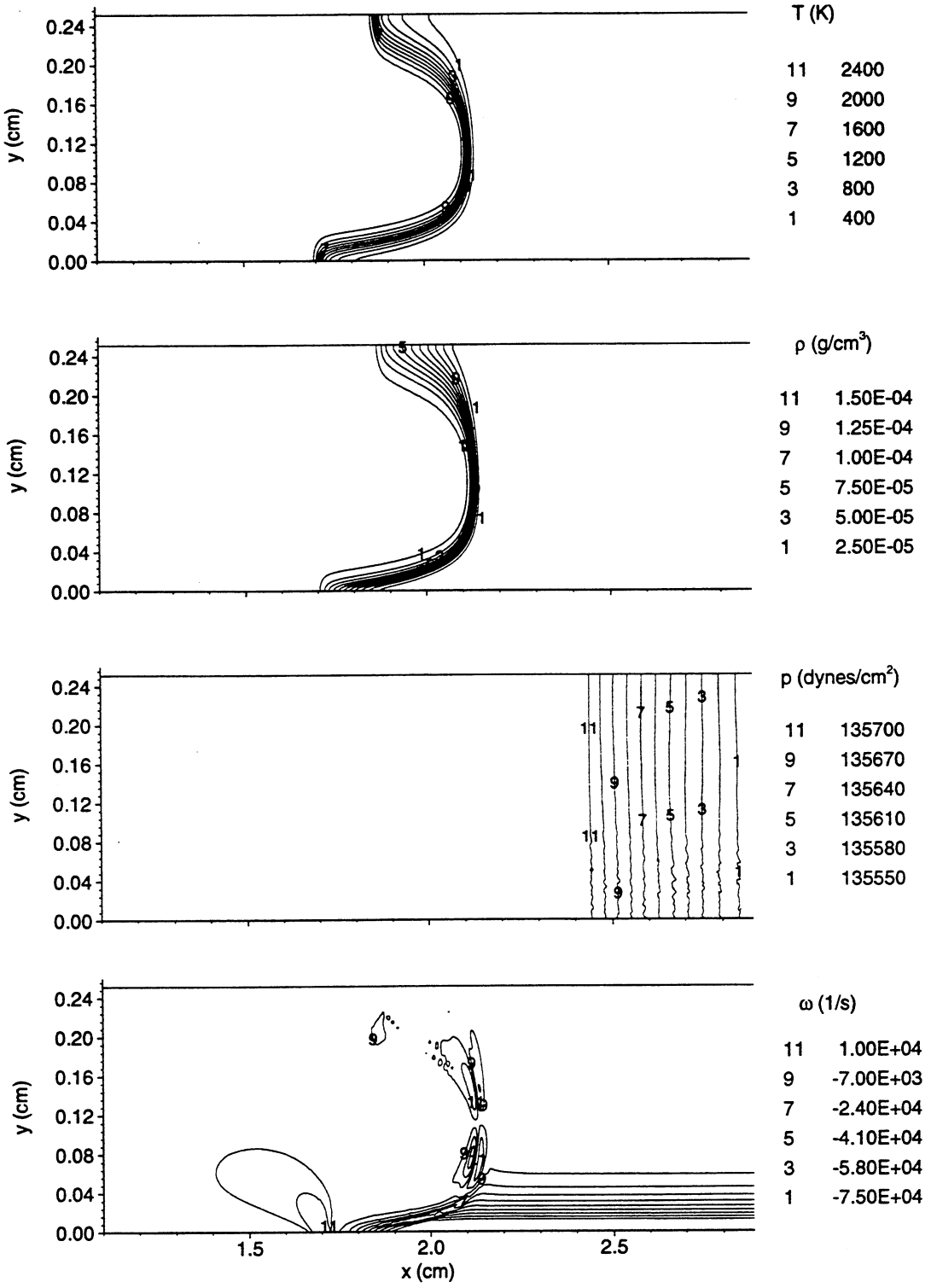

Figure 5.36: Temperature,density,pressure, and vorticity contours, 1.061 ms, AD3.

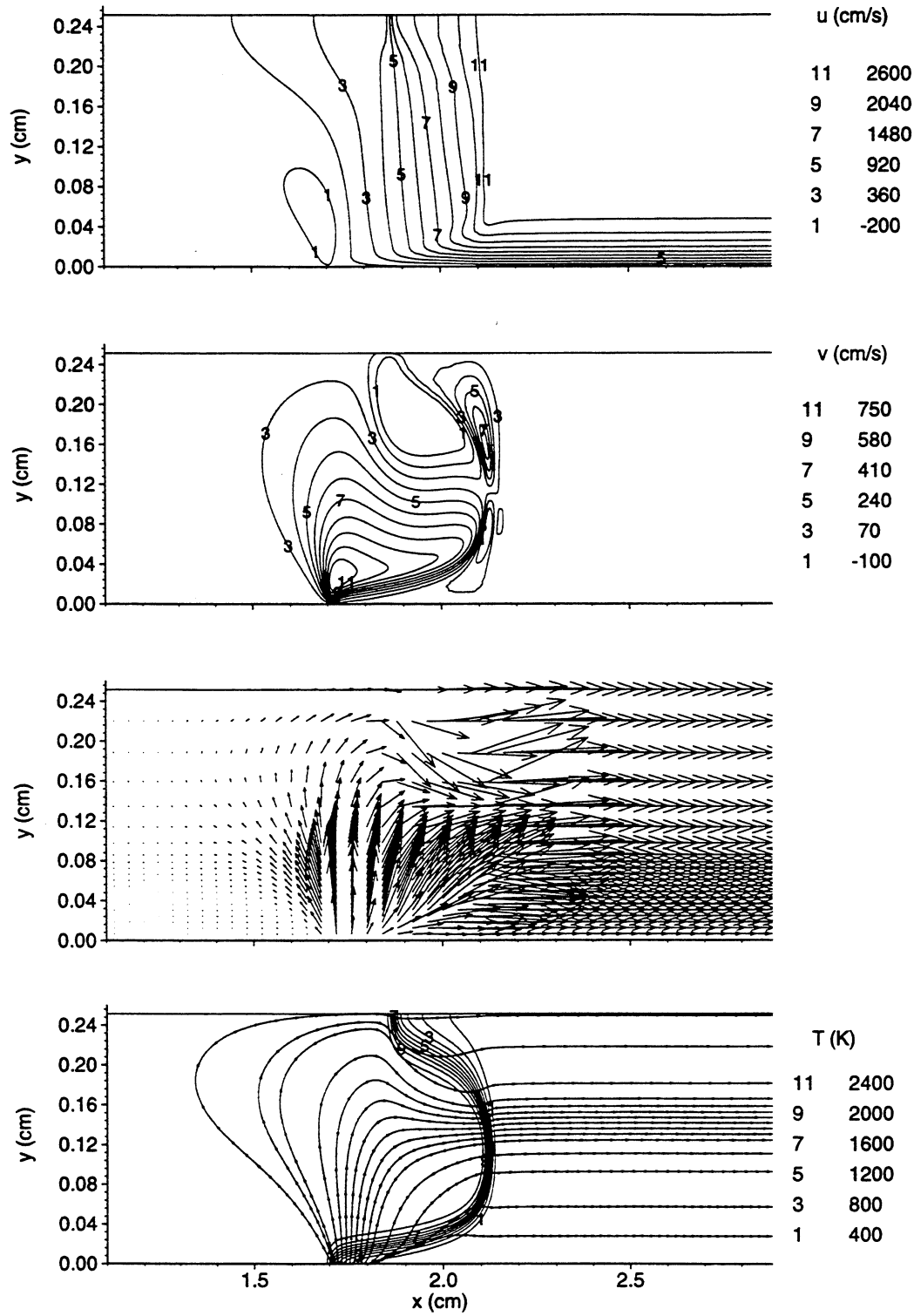

Figure 5.37: Velocity contours, velocity vectors and instantaneous streamlines, 1.061 ms, AD3.

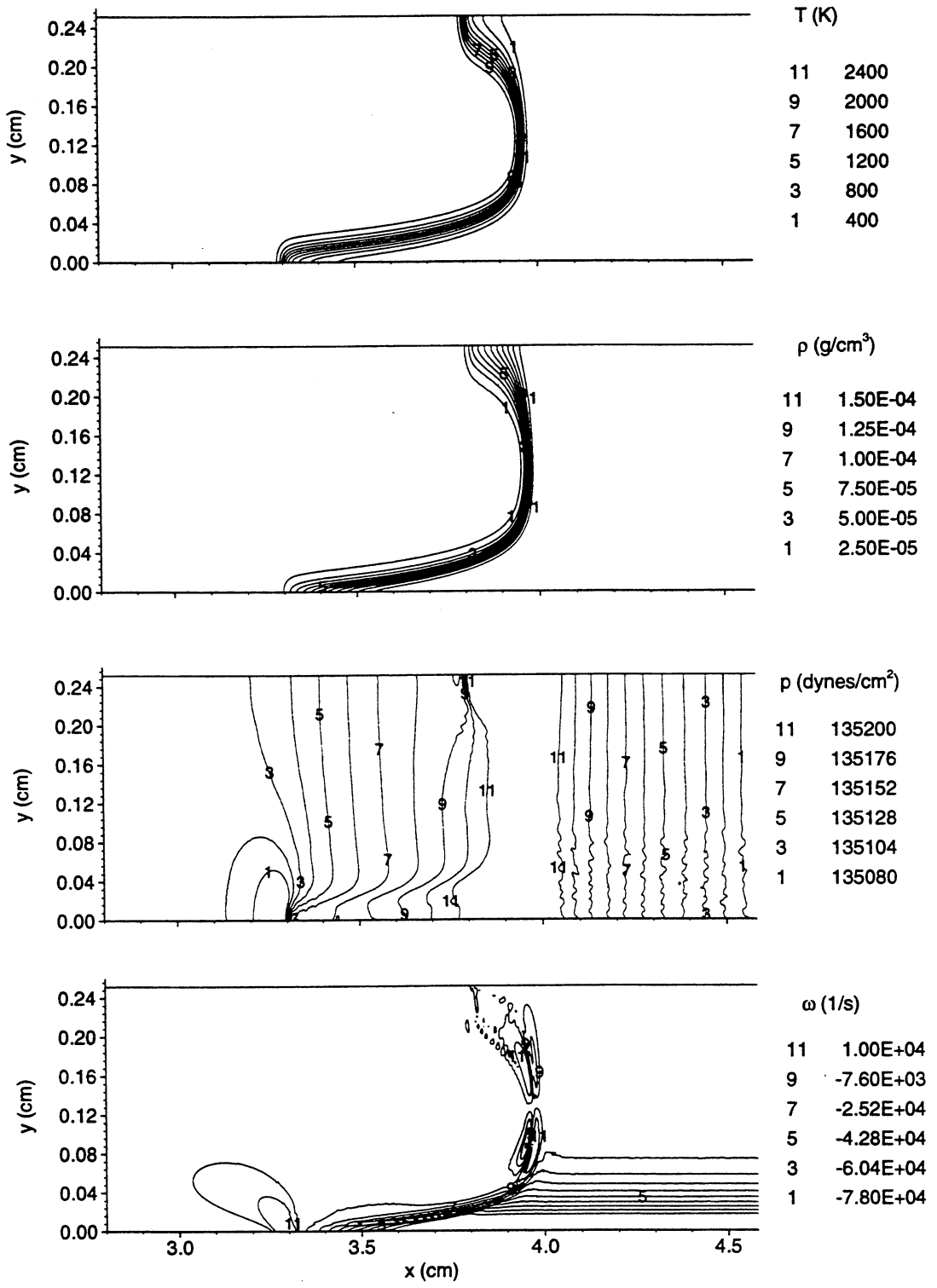

Figure 5.38: Temperature,density,pressure, and vorticity contours,1.601 ms, AD3.

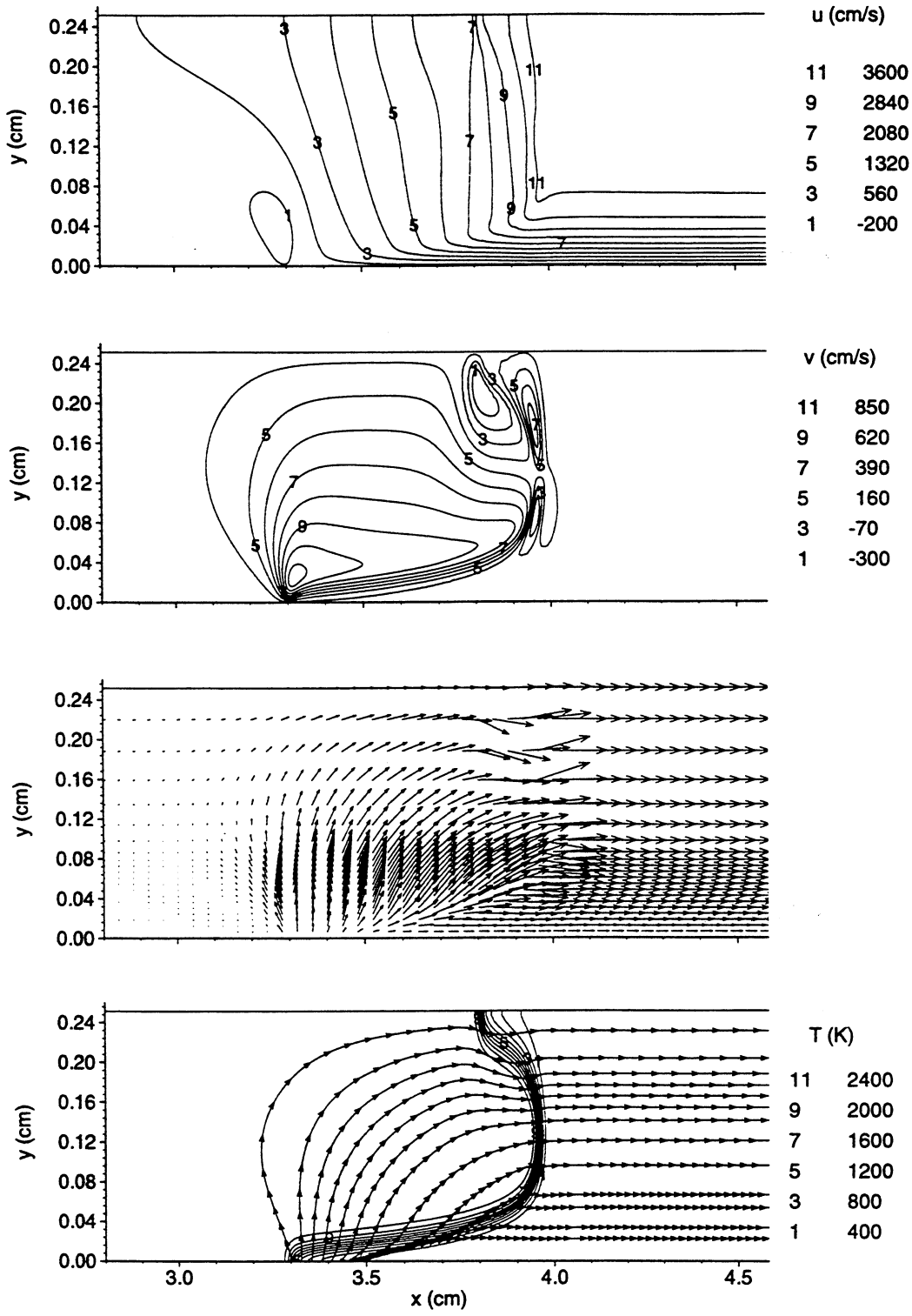

Figure 5.39: Velocity contours, velocity vectors and instantaneous streamlines, 1.601 ms, AD3.

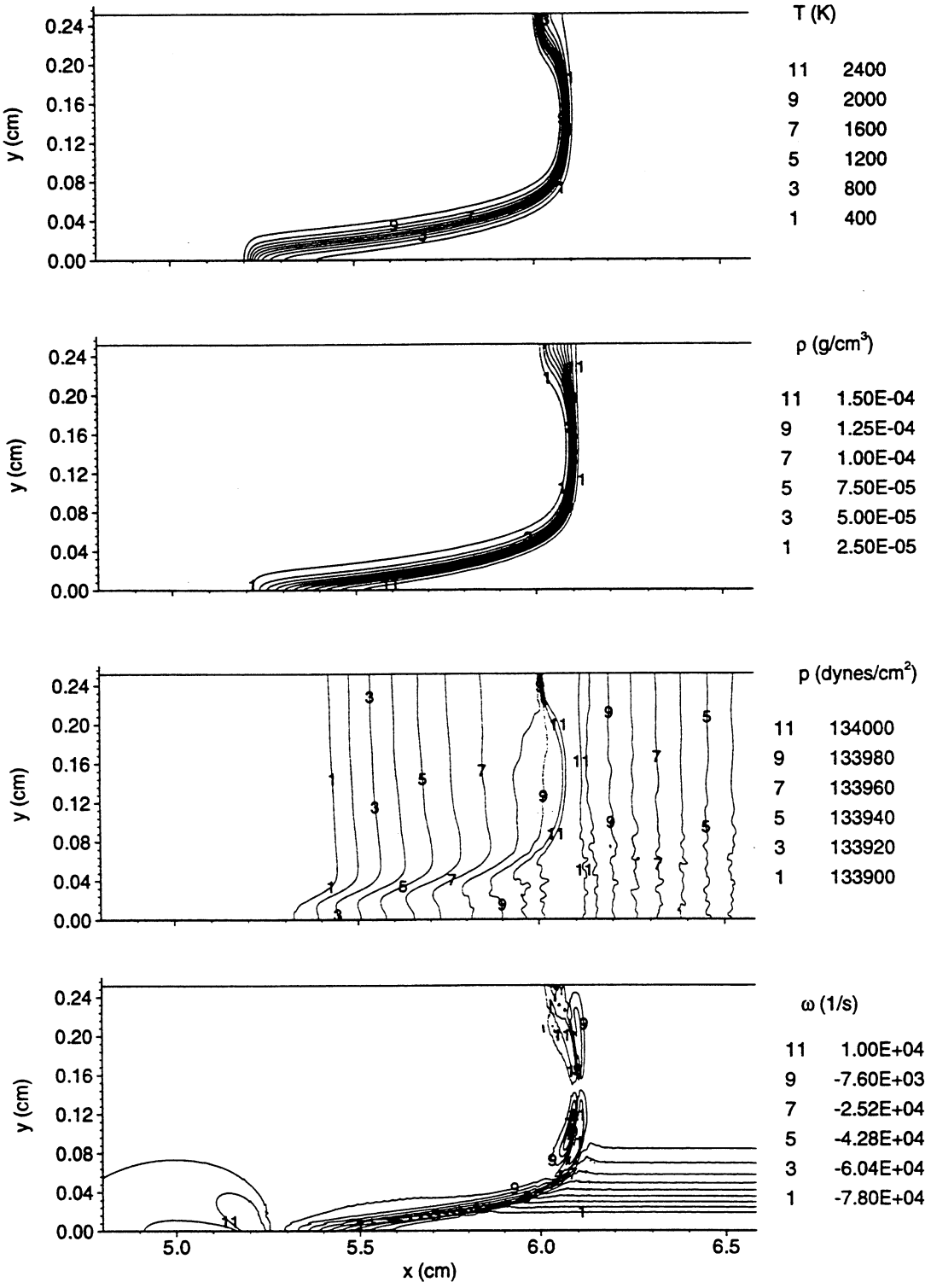

Figure 5.40: Temperature,density,pressure, and vorticity contours, 2.121 ms, AD3.

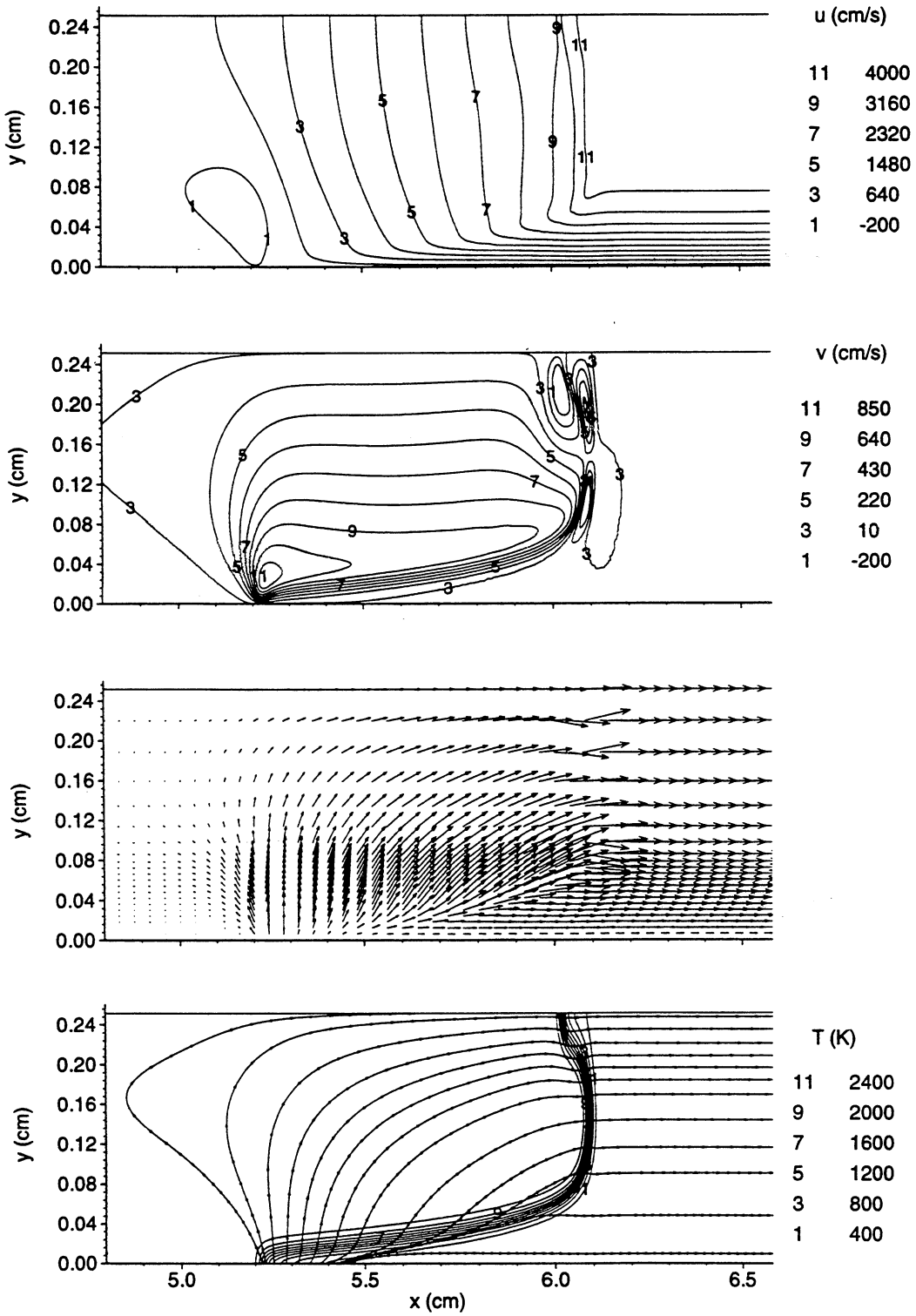

Figure 5.41: Velocity contours, velocity vectors and instantaneous streamlines, 2.121 ms, AD3.

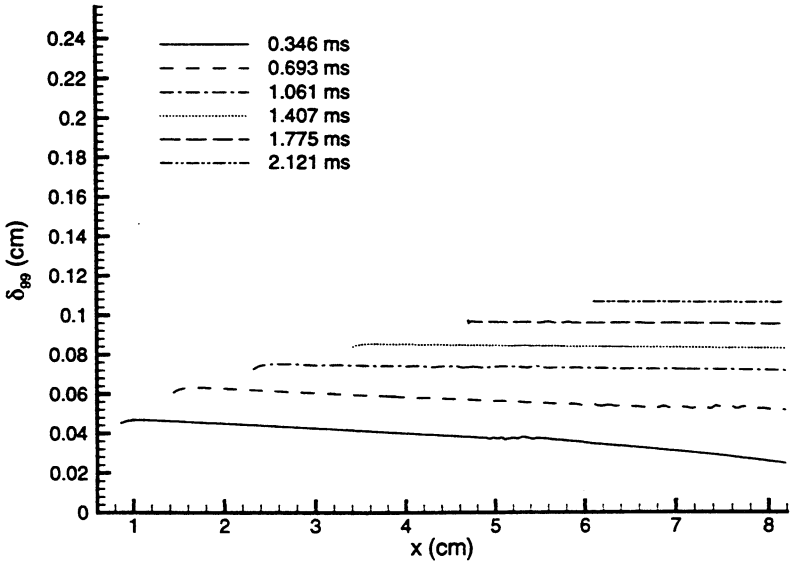

Figure 5.42: Boundary layer thickness for varying time. AD3.

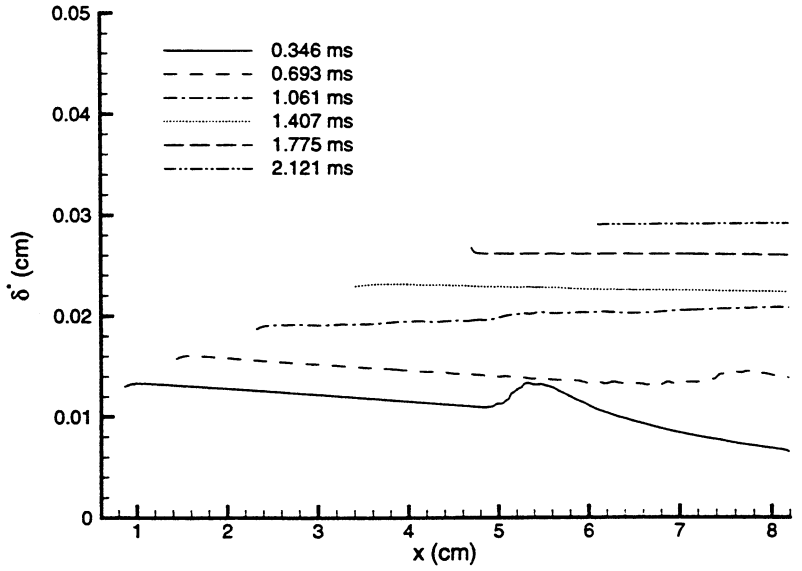

Figure 5.43: Displacement thickness for varying times, AD3.

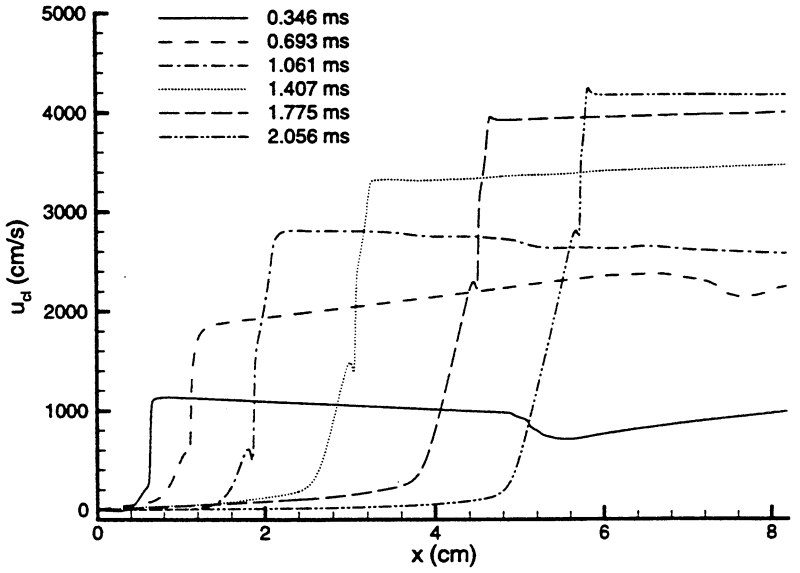

Figure 5.44: Centerline u velocity profiles for varying times, AD3.

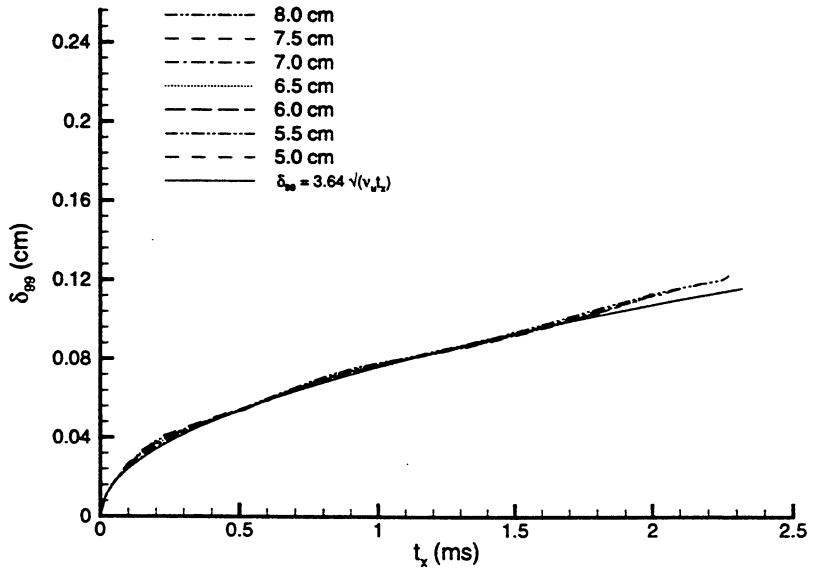

Figure 5.45: Boundary layer height for different x locations as a function of local time, AD3.

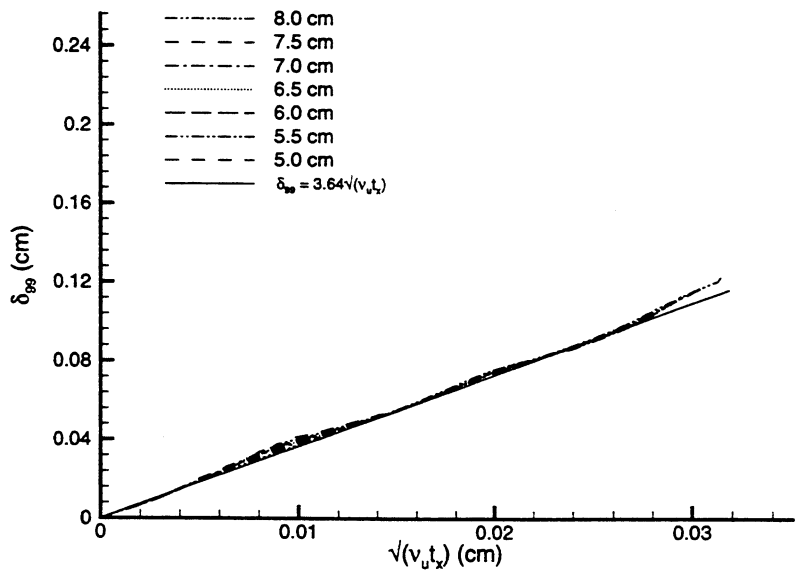

Figure 5.46: Boundary layer height as a function of the square root of the product of the local time and edge kinematic viscosity, AD3.

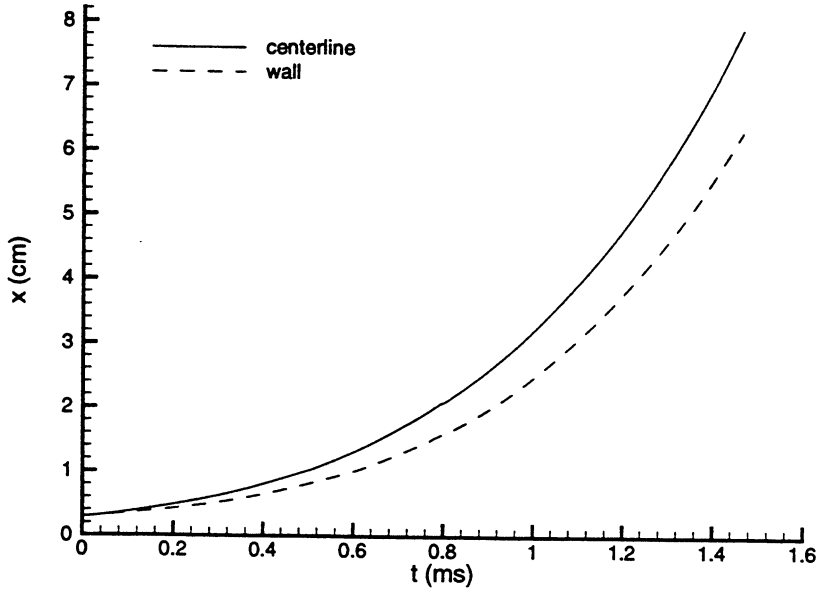

Figure 5.47: Flame position at the centerline and wall, AD4.

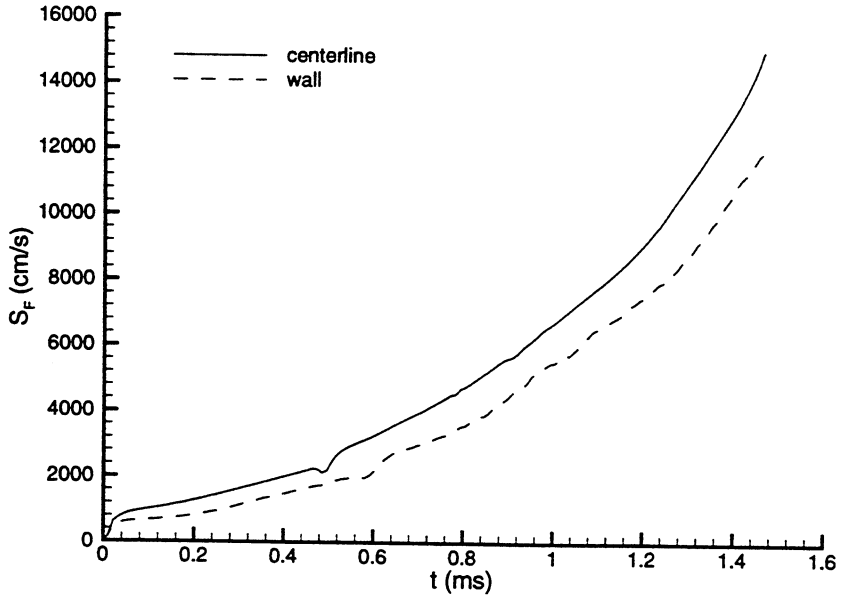

Figure 5.48: Flame velocity relative to laboratory coordinates for the centerline and wall, AD4.

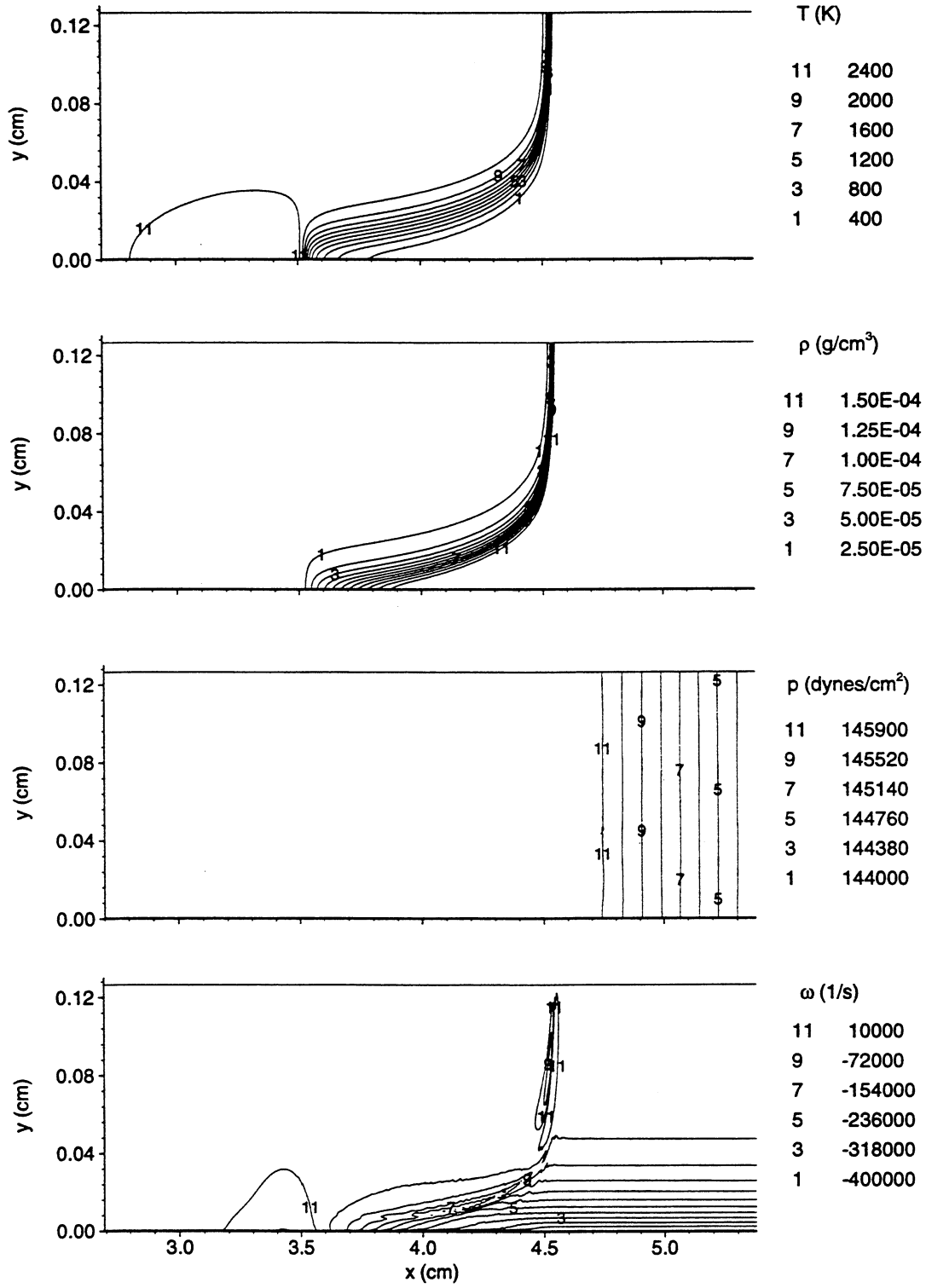

Figure 5.49: Temperature,density,pressure, and vorticity contours, 1.172 ms, AD4.

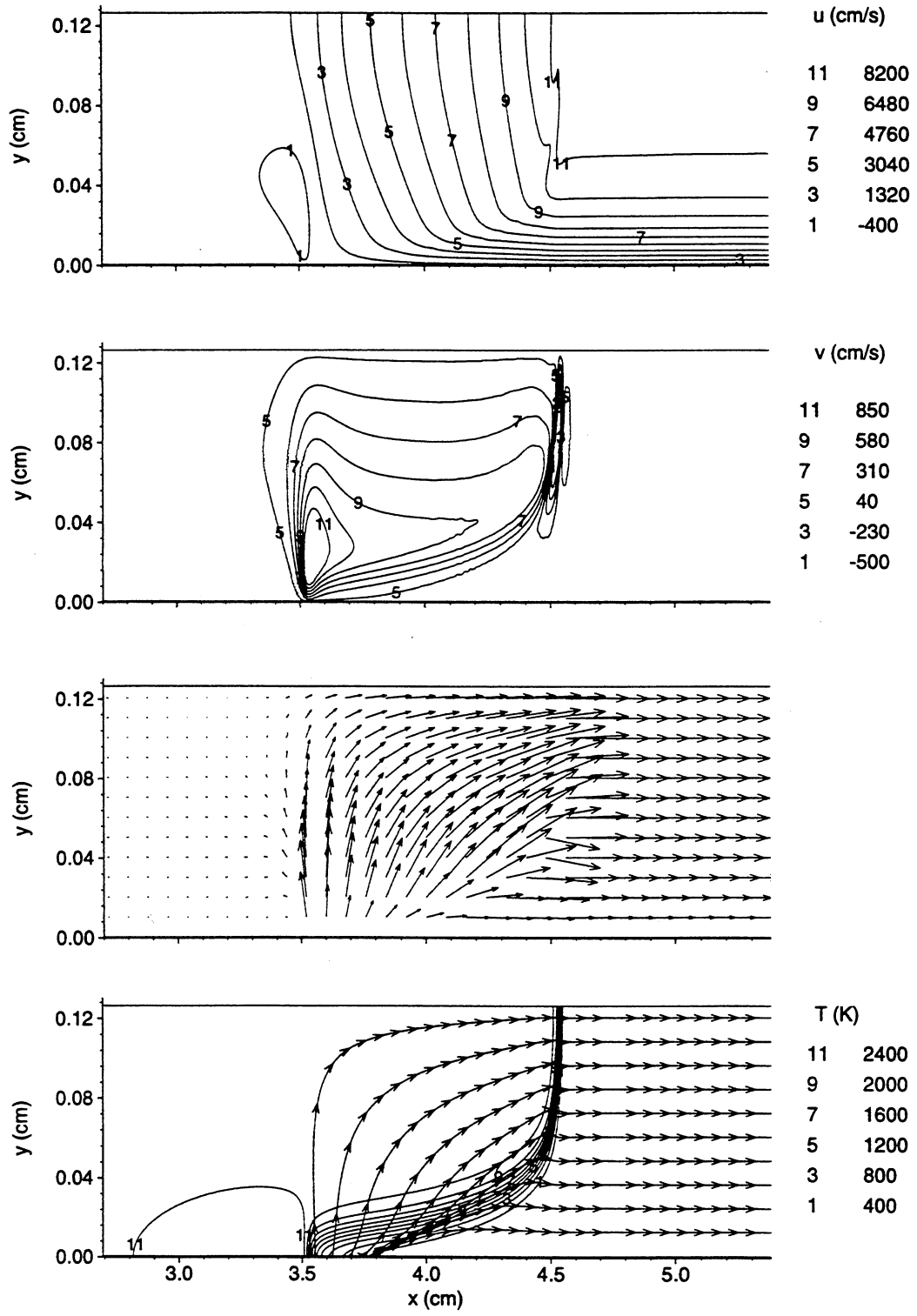

Figure 5.50: Velocity contours, velocity vectors and instantaneous streamlines, 1.172 ms, AD4.

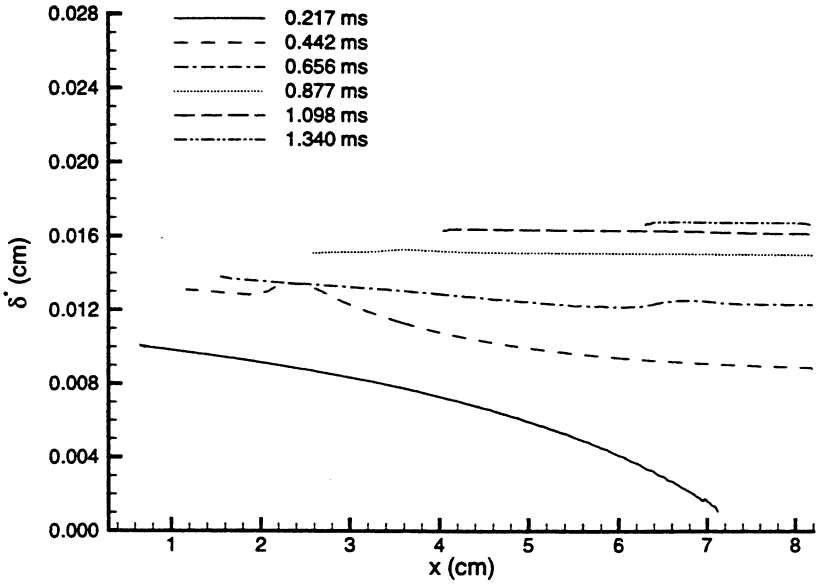

Figure 5.51: Displacement thickness at varying times, AD4.

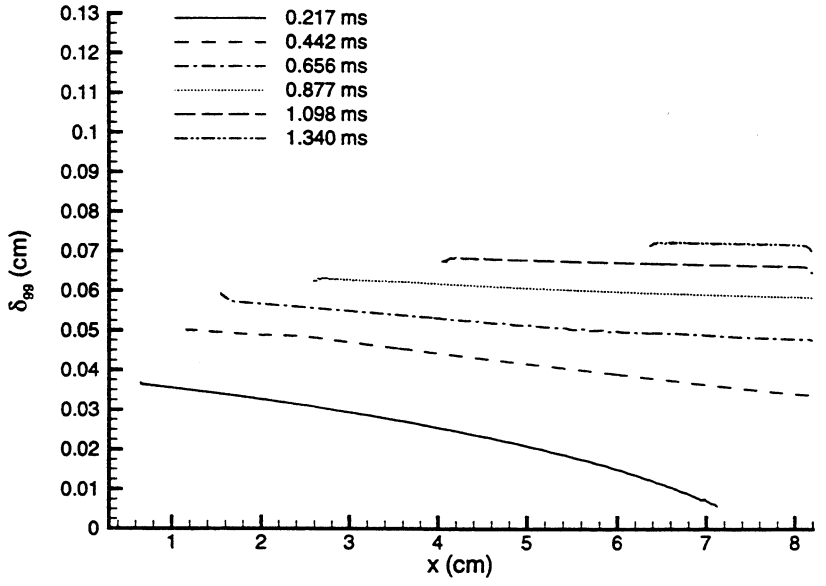

Figure 5.52: Boundary layer thickness at varying times, AD4.

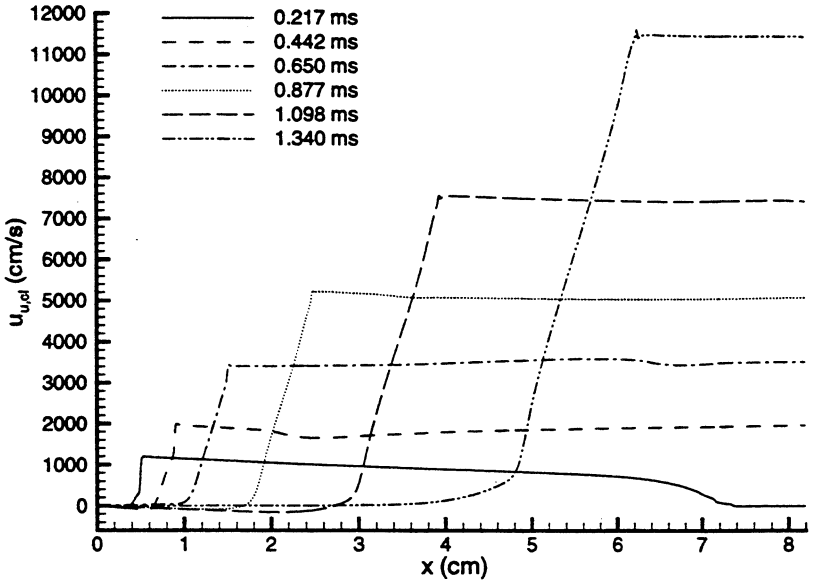

Figure 5.53: Centerline velocity for varying times, AD4.

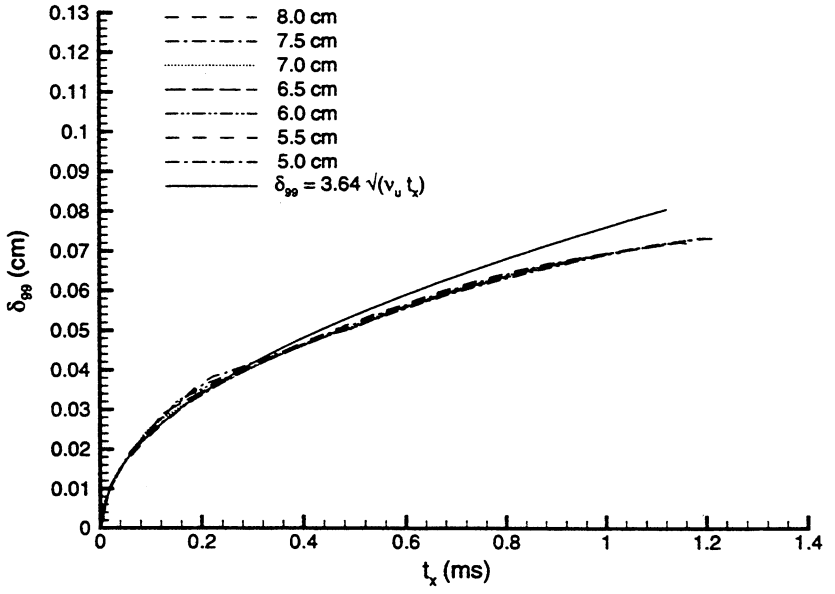

Figure 5.54: Boundary layer thickness in local time, AD4.

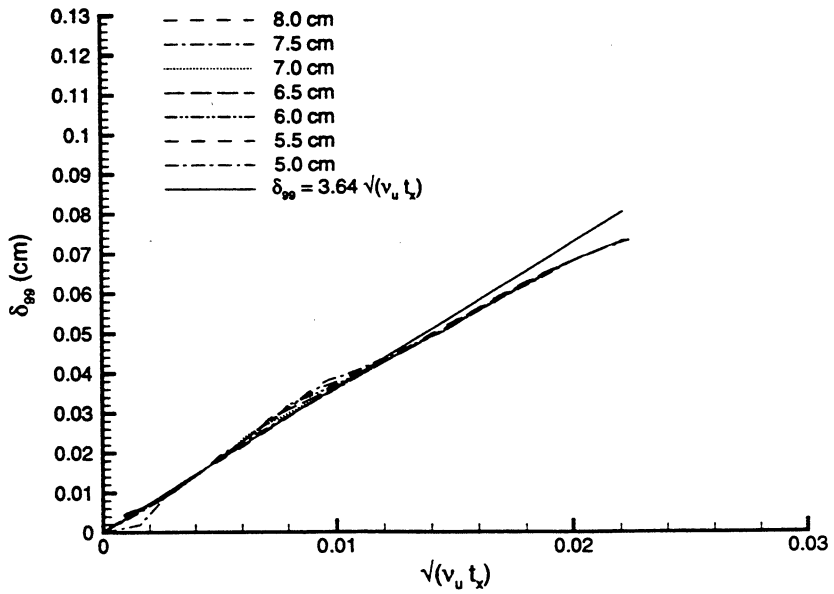

Figure 5.55: Boundary layer thickness versus the square root of local time, AD4.

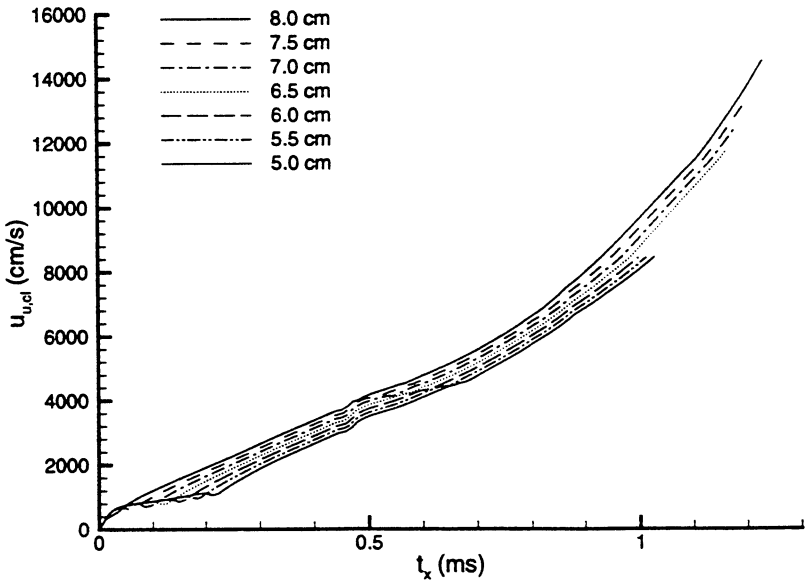

Figure 5.56: Centerline velocity at varying x locations, AD4.

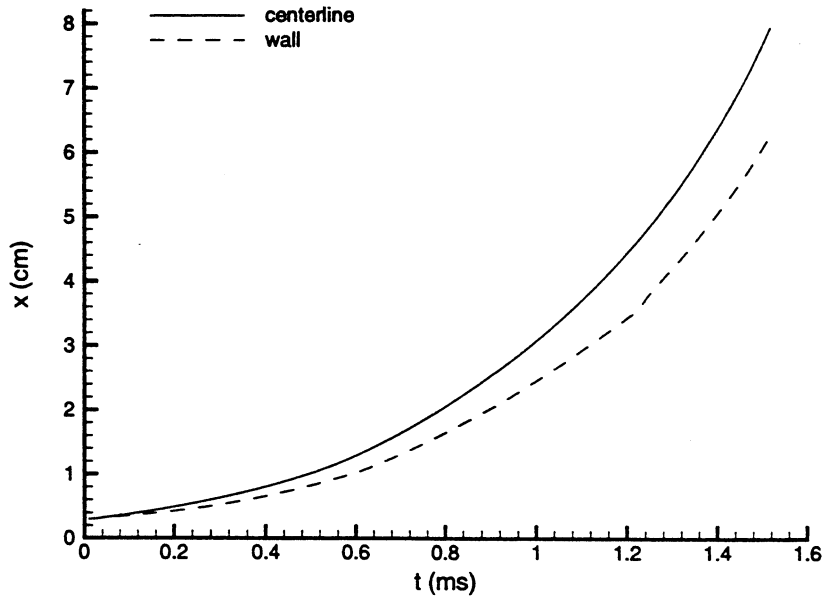

Figure 5.57: Flame position at the centerline and wall, AD5.

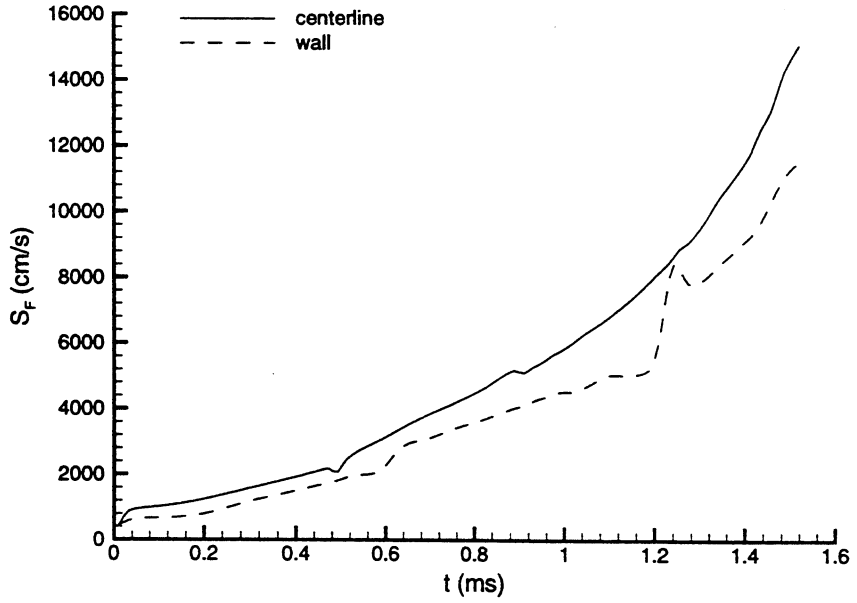

Figure 5.58: Flame velocity relative to laboratory coordinates at the centerline and wall. AD5.

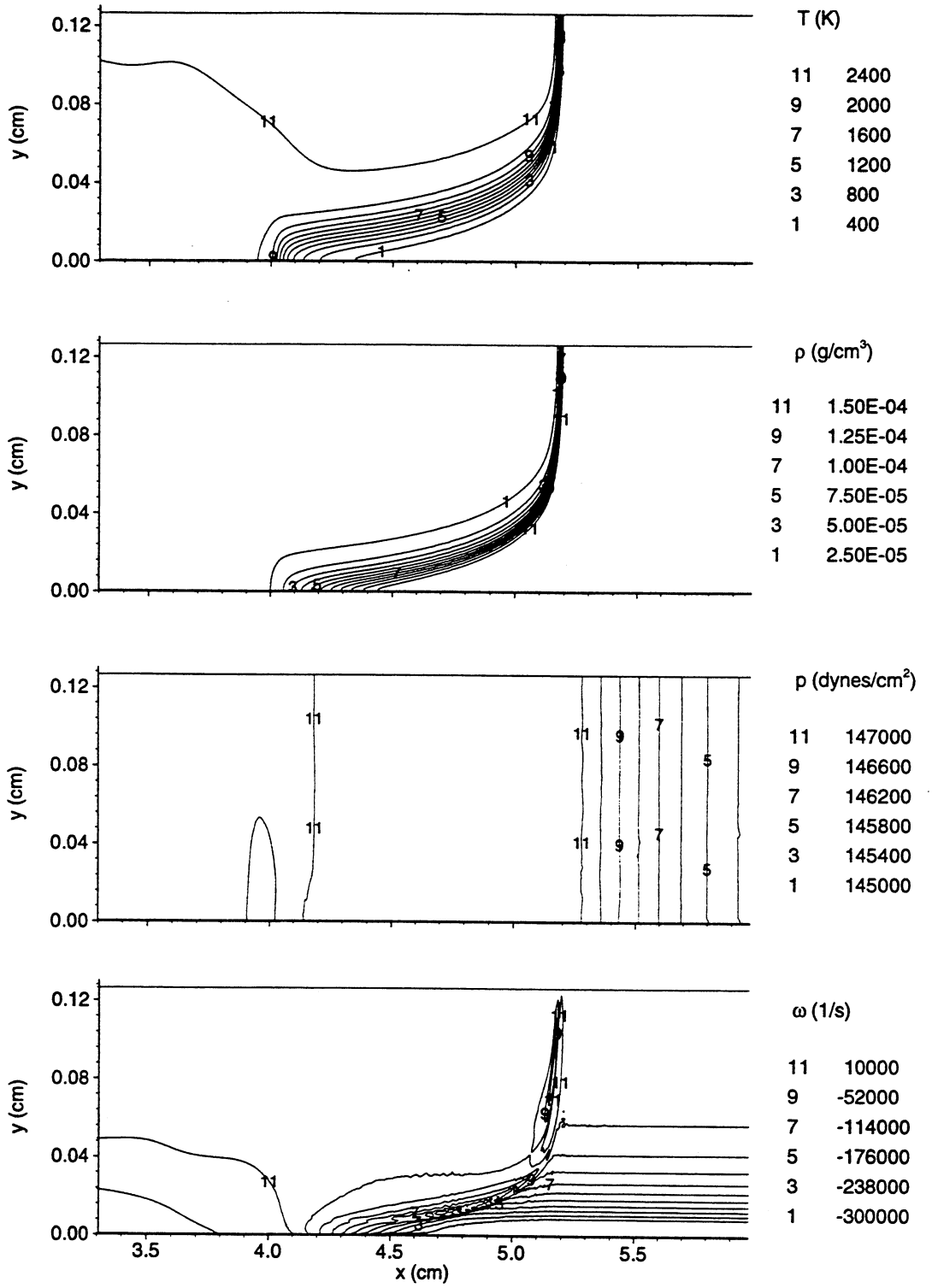

Figure 5.59: Temperature,density,pressure, and vorticity contours, 1.284 ms, AD5.

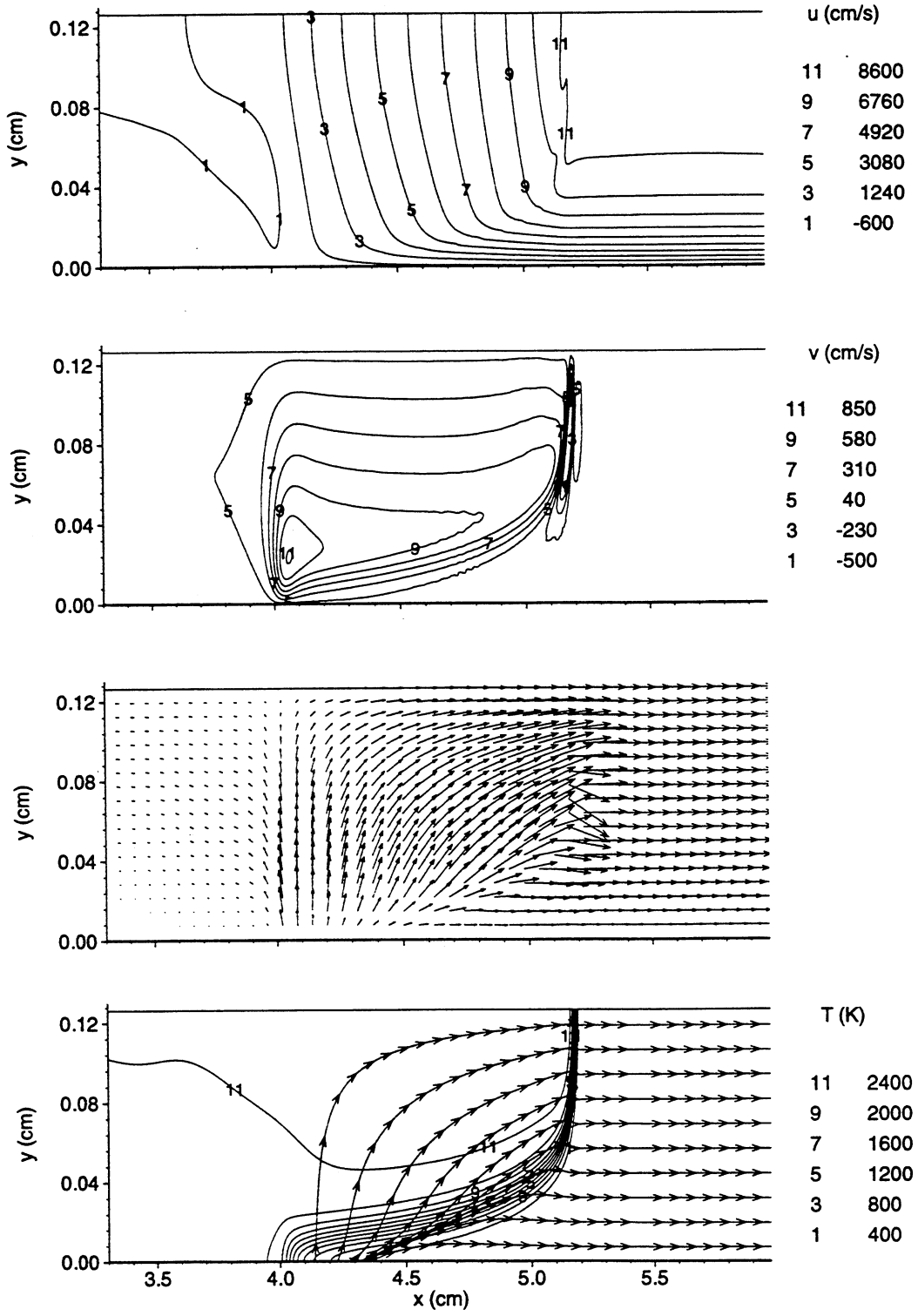

Figure 5.60: Velocity contours, velocity vectors and instantaneous streamlines, 1.284 ms, AD5.

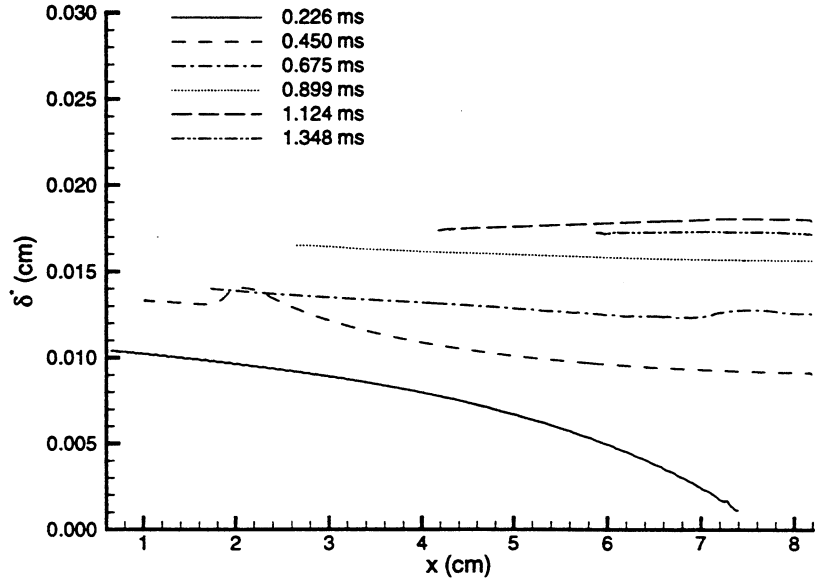

Figure 5.61: Displacement thickness at varying times, AD5.

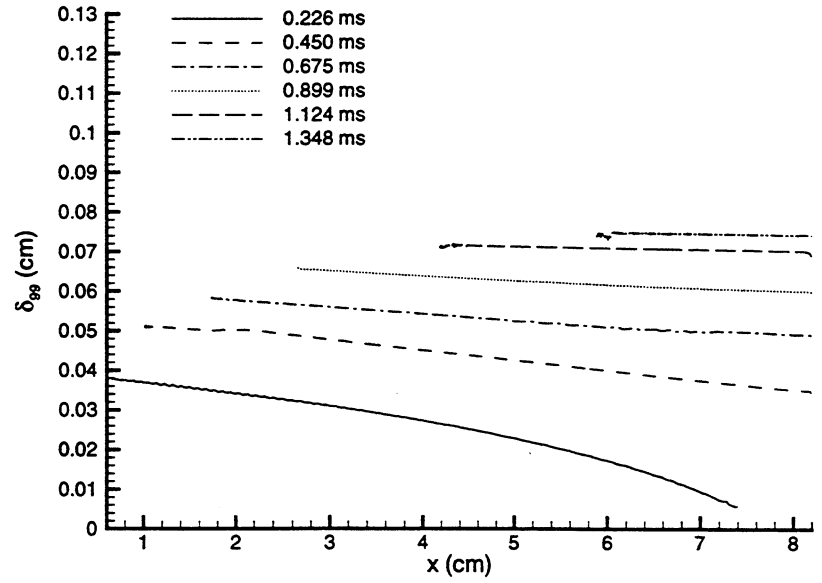

Figure 5.62: Boundary layer thickness at varying times, AD5.

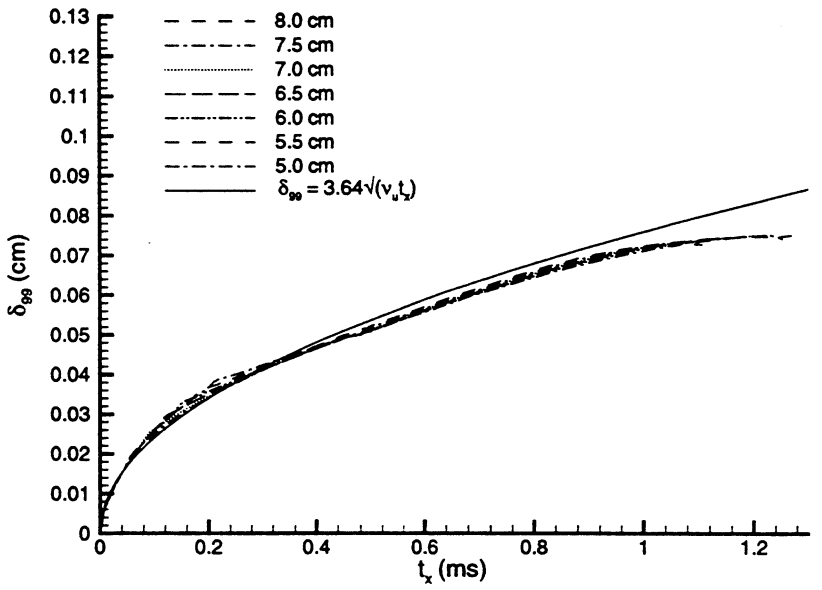

Figure 5.63: Boundary layer thickness in local time, AD5.

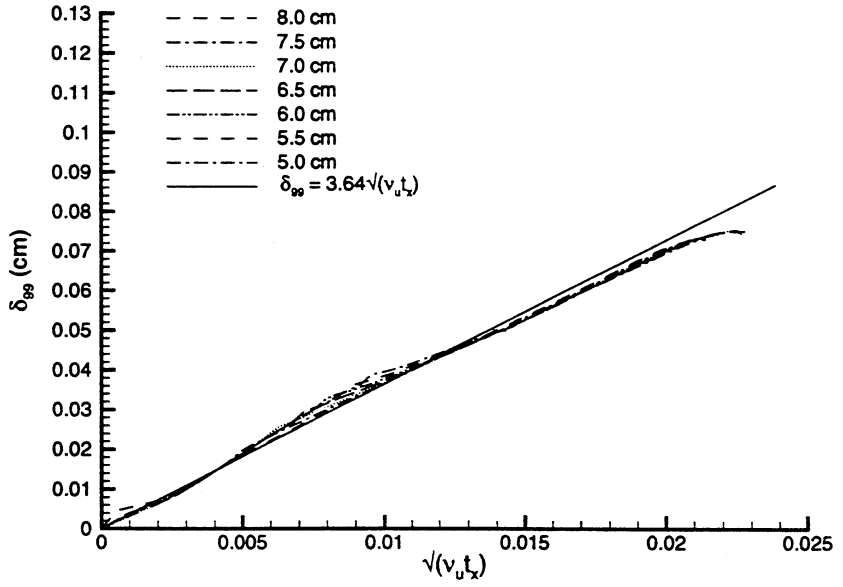

Figure 5.64: Boundary layer thickness versus the square root of local time, AD5.

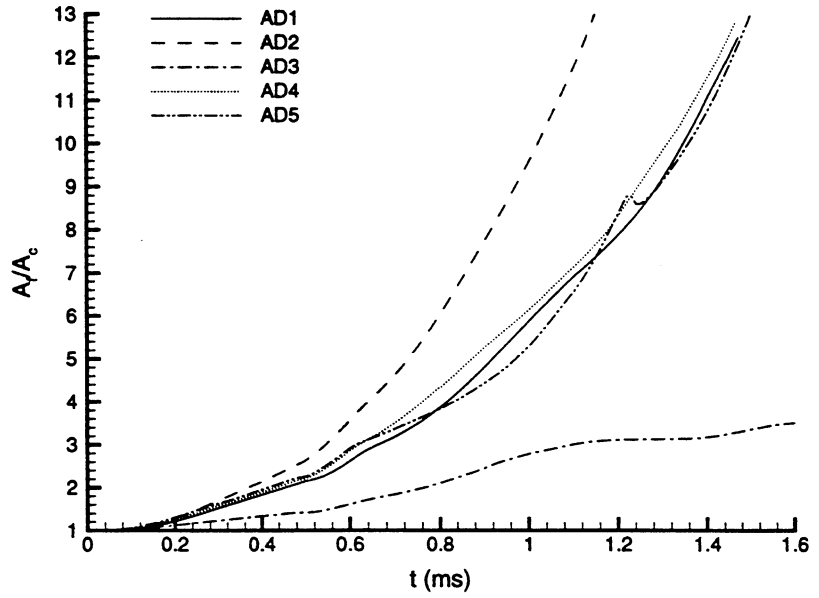

Figure 5.65: Comparison of the relative flame area in time for the planar ignition cases.

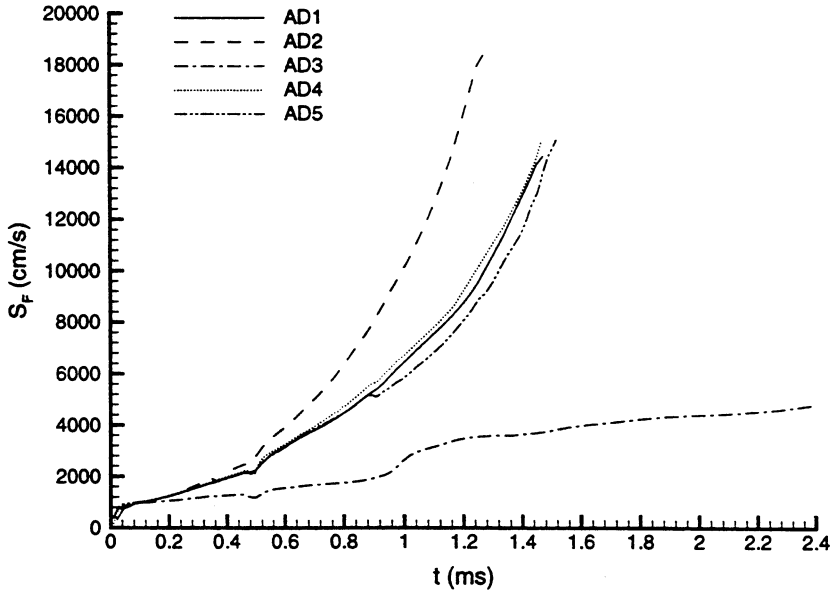

Figure 5.66: Comparison of the flame speed for the planar ignition cases.

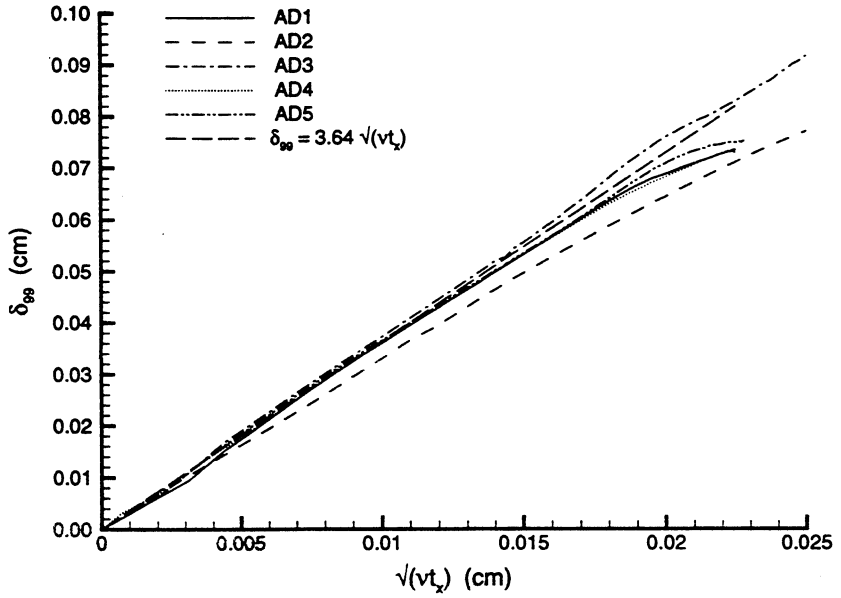

Figure 5.67: Comparison of the boundary layer thicknesses for the planar ignition cases.

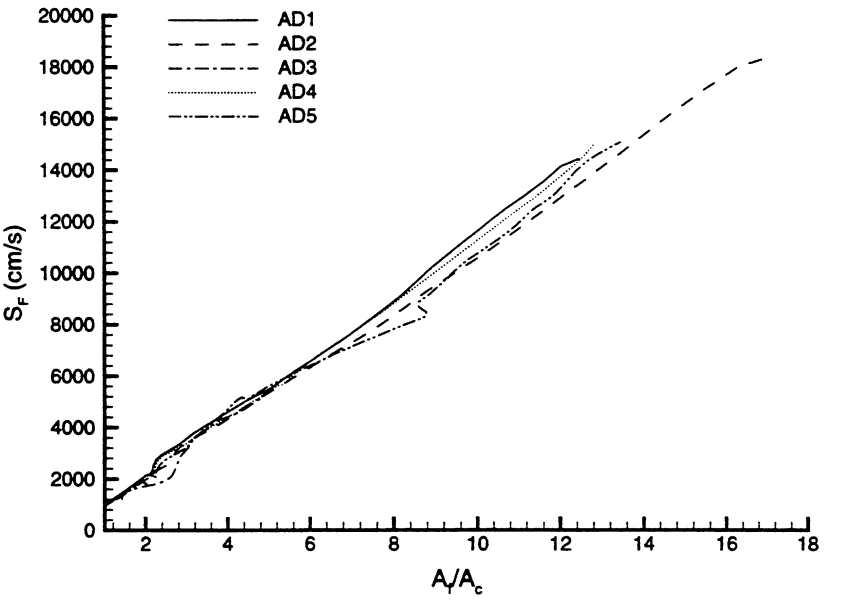

Figure 5.68: The relation of flame speed to relative flame area.

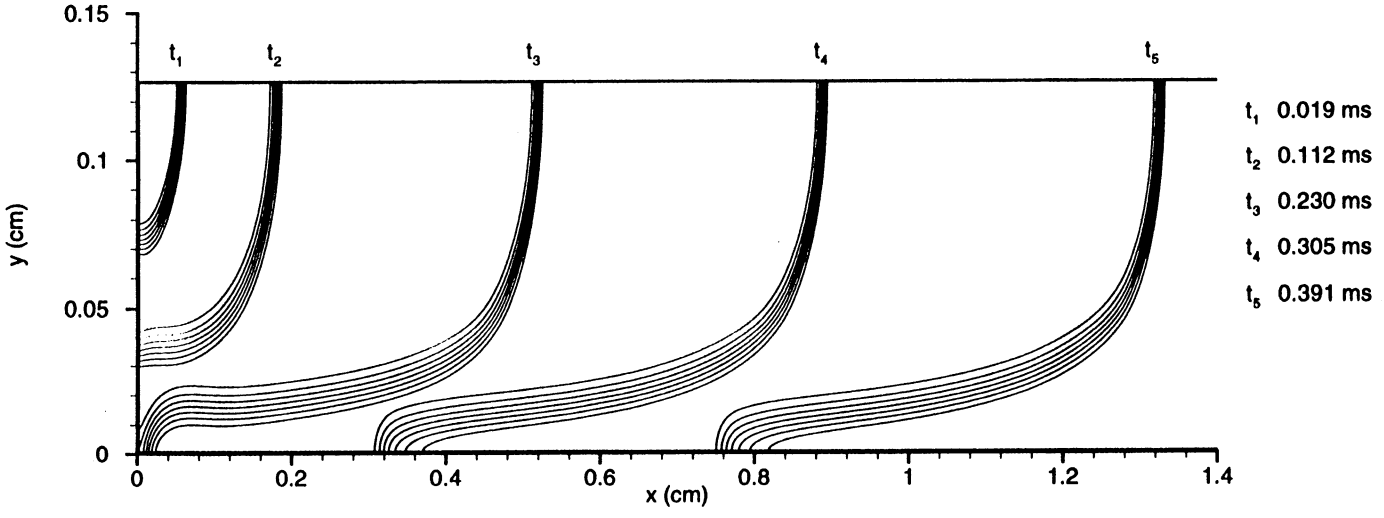

Figure 5.69: Temperature profiles showing the initial flame development, AS1.

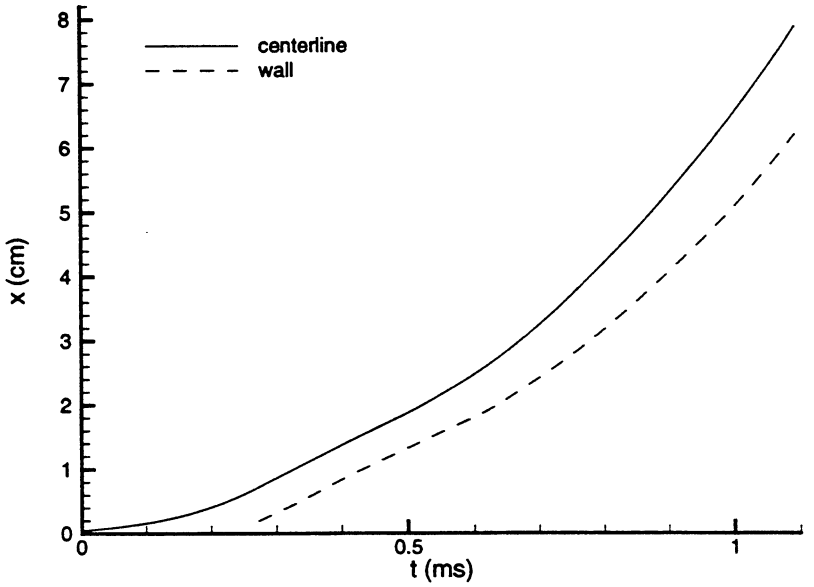

Figure 5.70: Position of the flame at the centerline and wall, AS1.

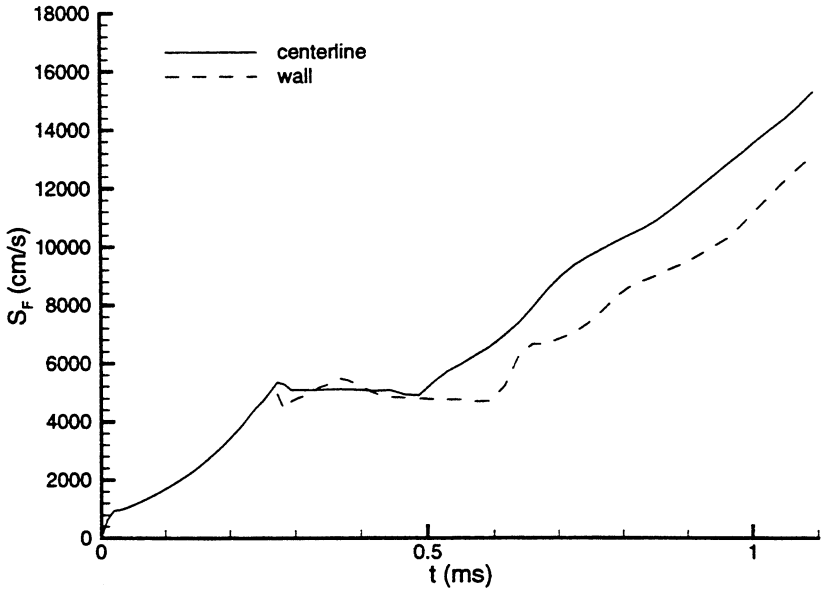

Figure 5.71: Flame velocity relative to laboratory coordinates for the centerline and wall, AS1.

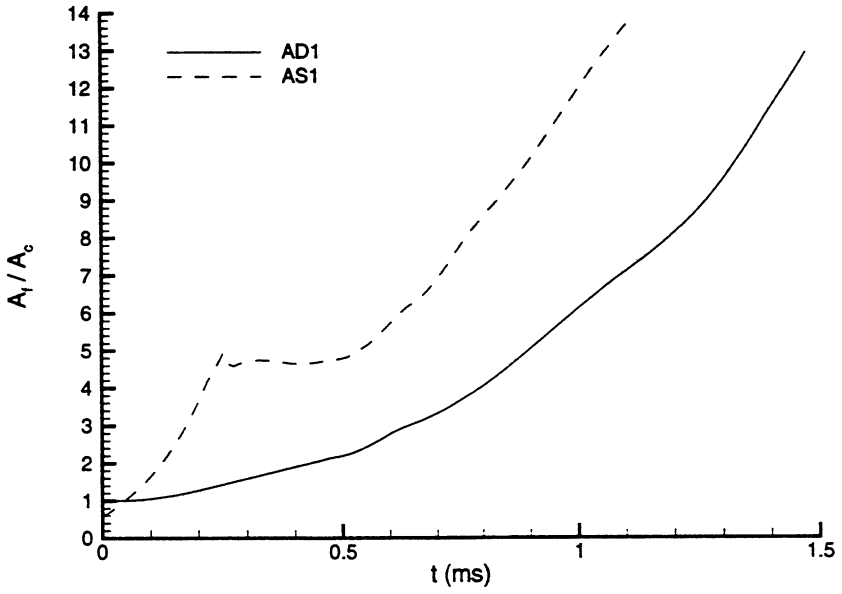

Figure 5.72: Relative flame area versus time, AS1.

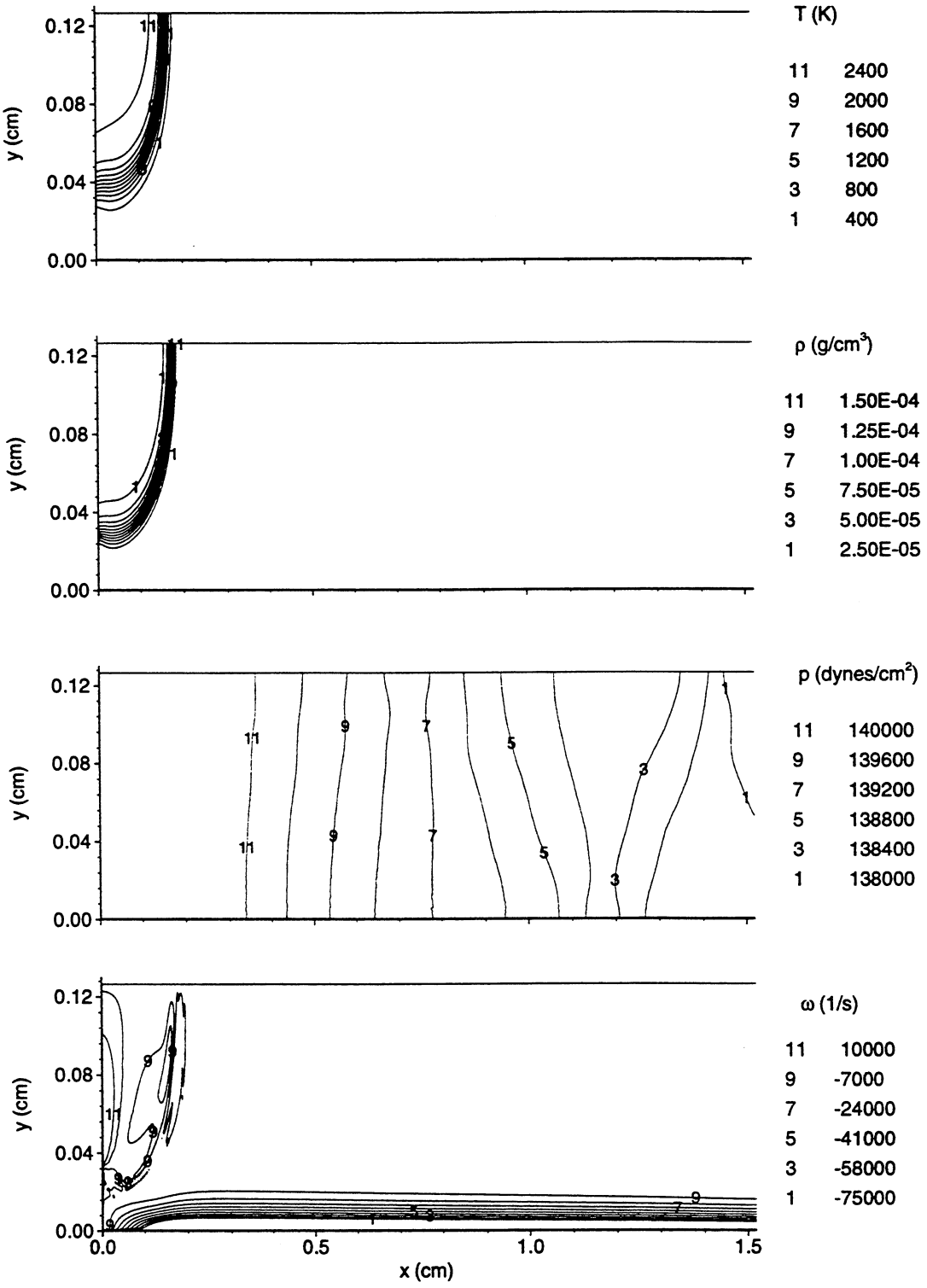

Figure 5.73: Temperature, density, pressure, and vorticity contours, 0.102 ms, AS1.

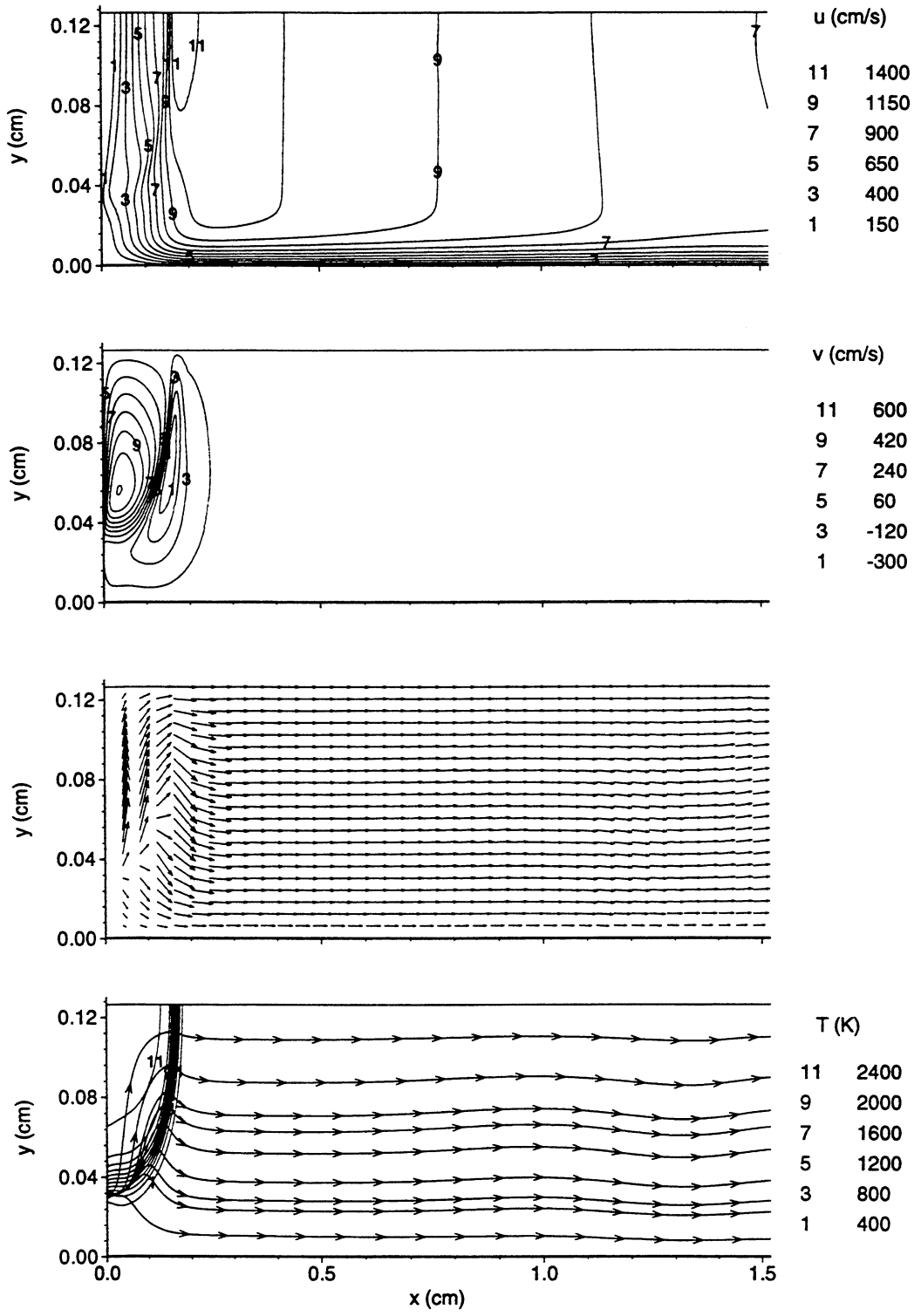

Figure 5.74: Velocity contours, velocity vectors and instantaneous streamlines, 0.102 ms, AS1.

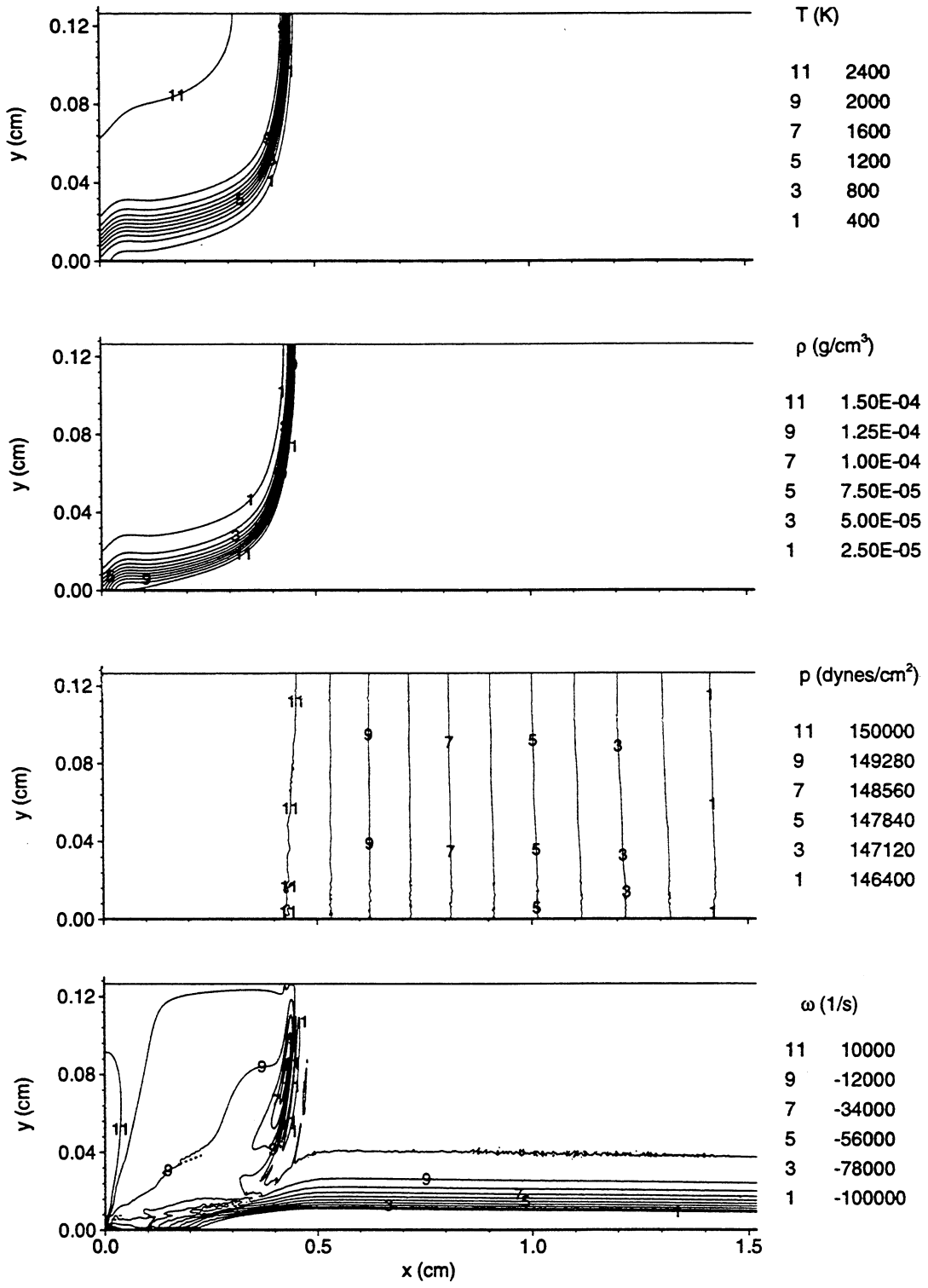

Figure 5.75: Temperature, density, pressure, and vorticity contours,0.209 ms, AS1.

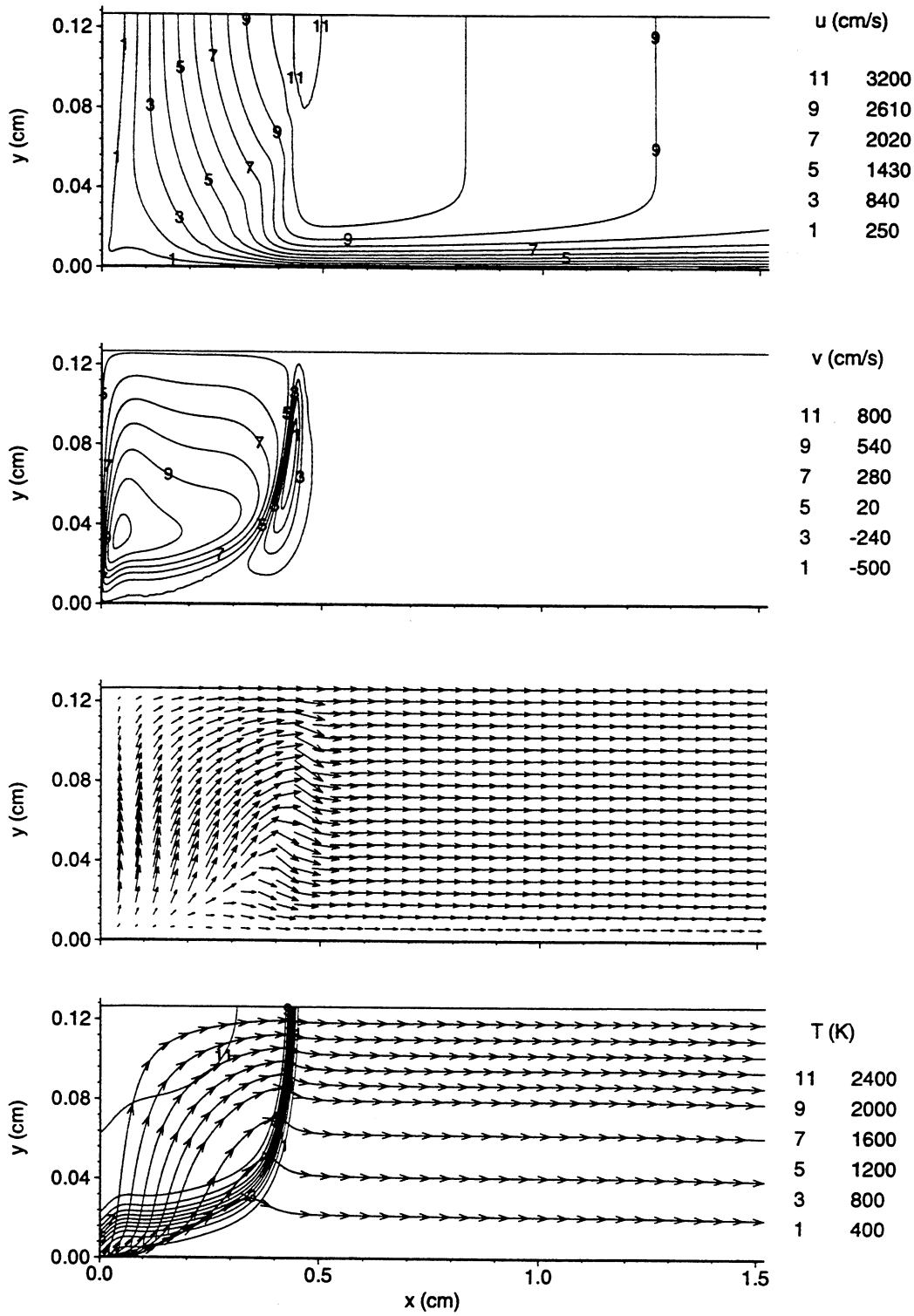

Figure 5.76: Velocity contours, velocity vectors and instantaneous streamlines, 0.209 ms, AS1.

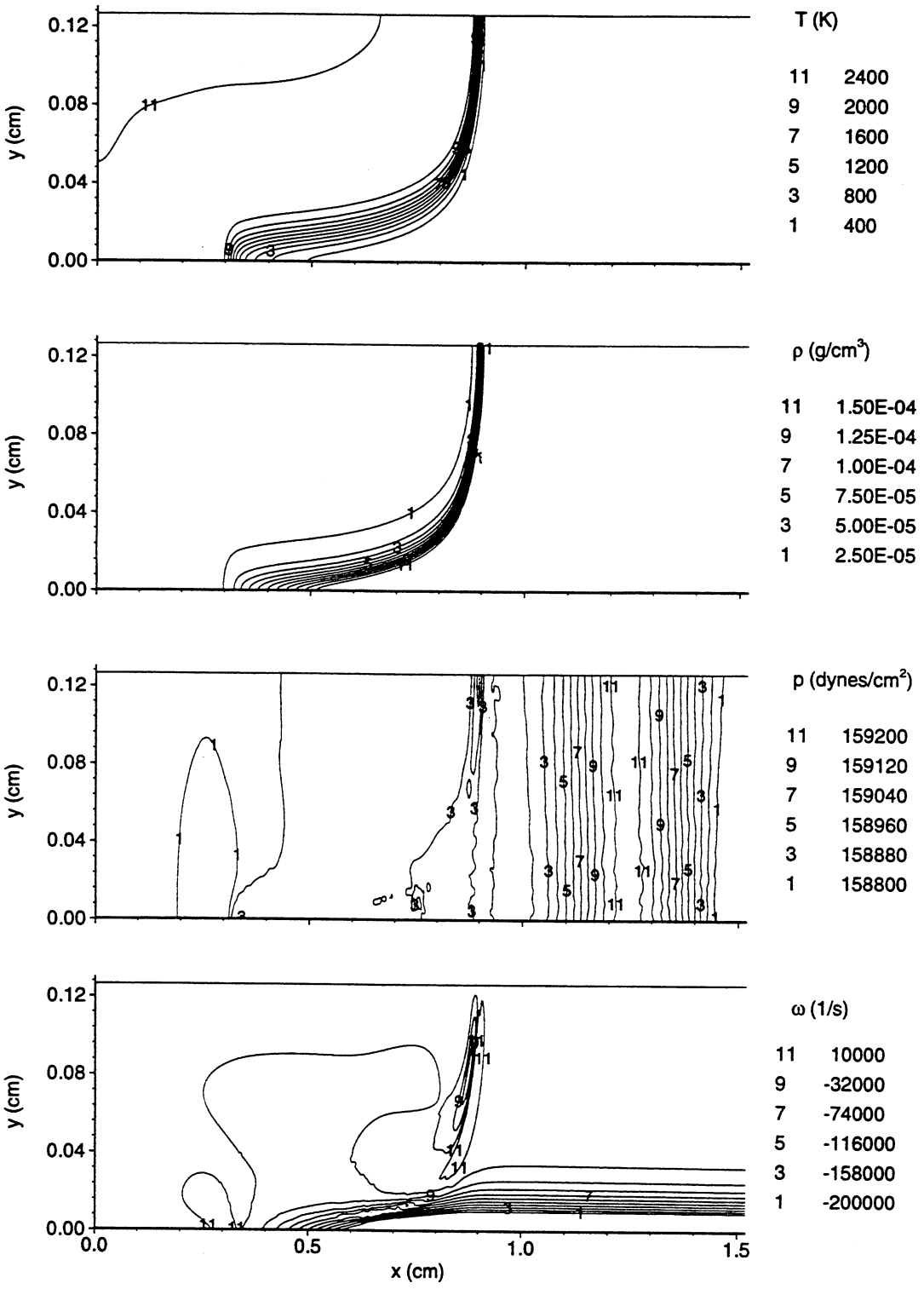

Figure 5.77: Temperature, density, pressure, and vorticity contours, 0.305 ms, AS1.

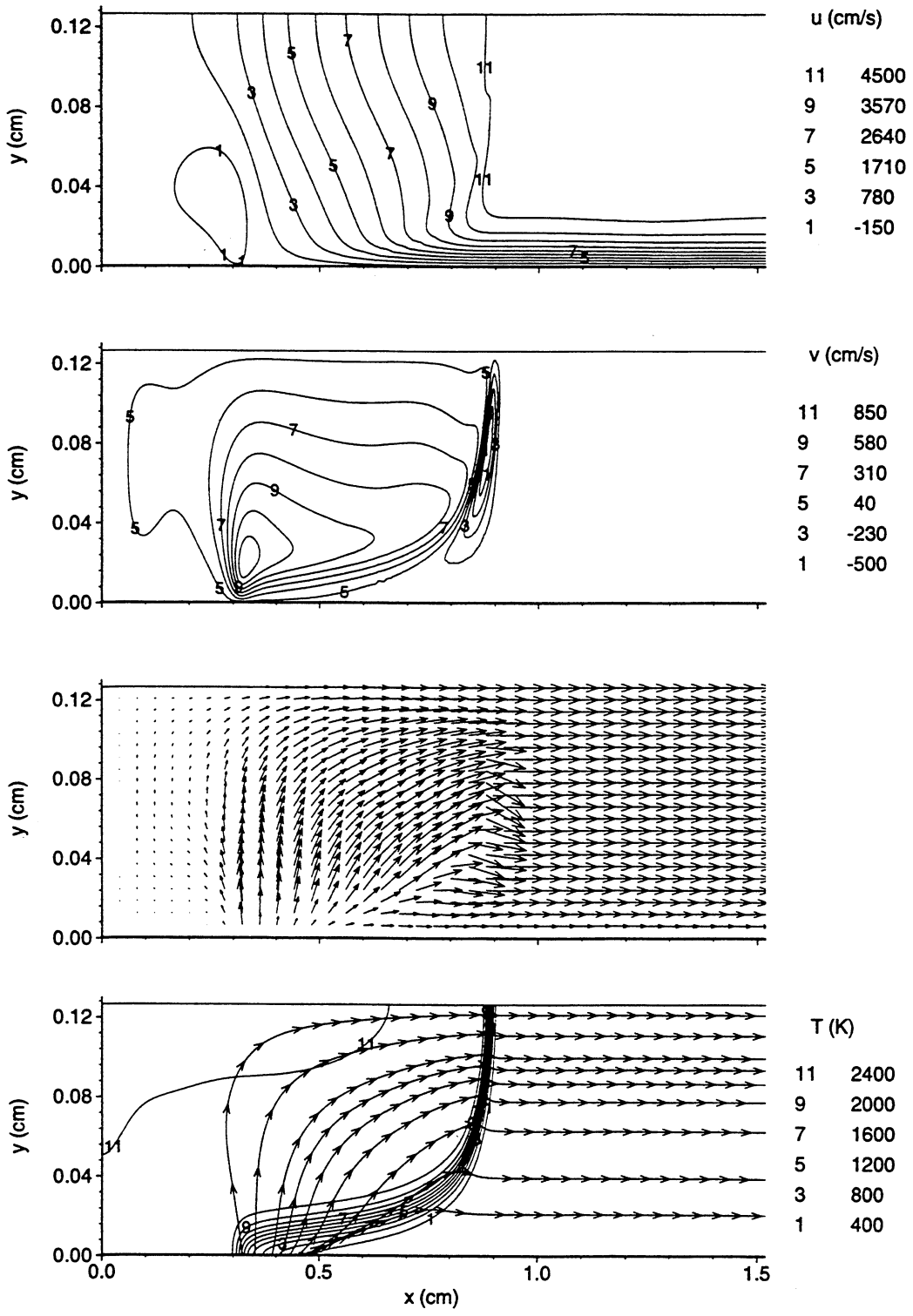

Figure 5.78: Velocity contours, velocity vectors and instantaneous streamlines, 0.305 ms, AS1.

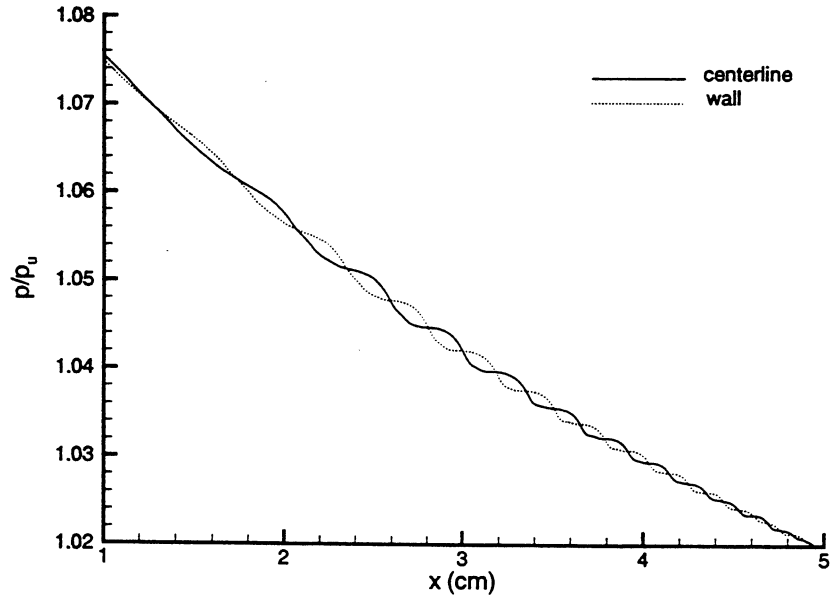

Figure 5.79: Normalized pressure ahead of the flame at 0.166 ms, AS1.

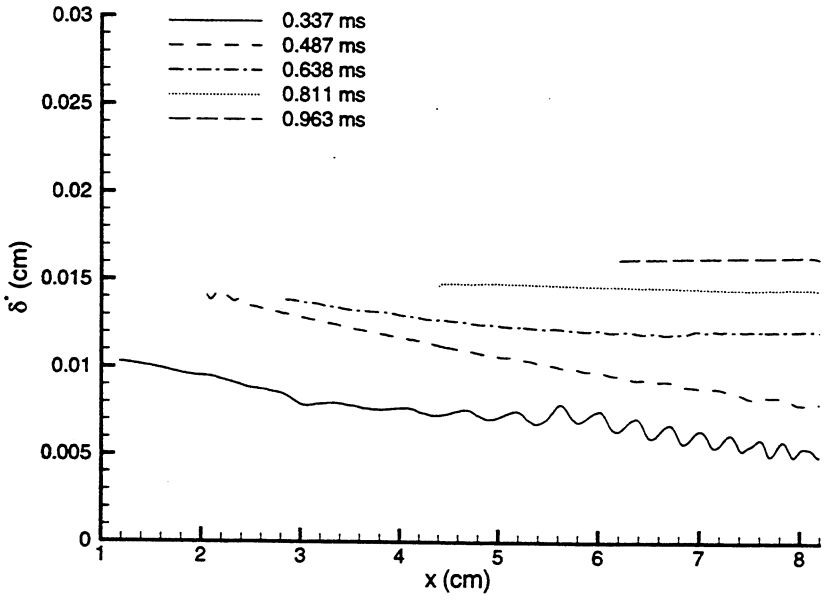

Figure 5.80: Displacement thickness for varying times, AS1.

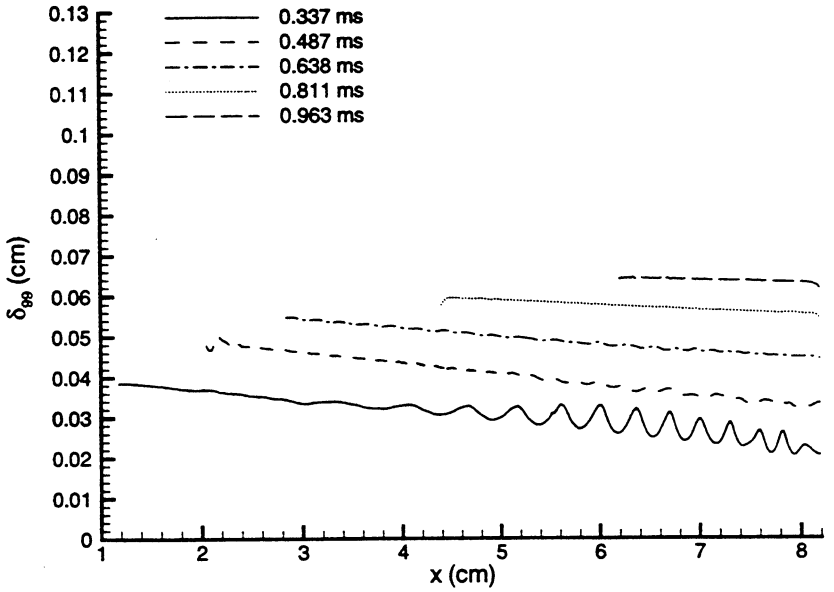

Figure 5.81: Boundary layer thickness at varying times, AS1.

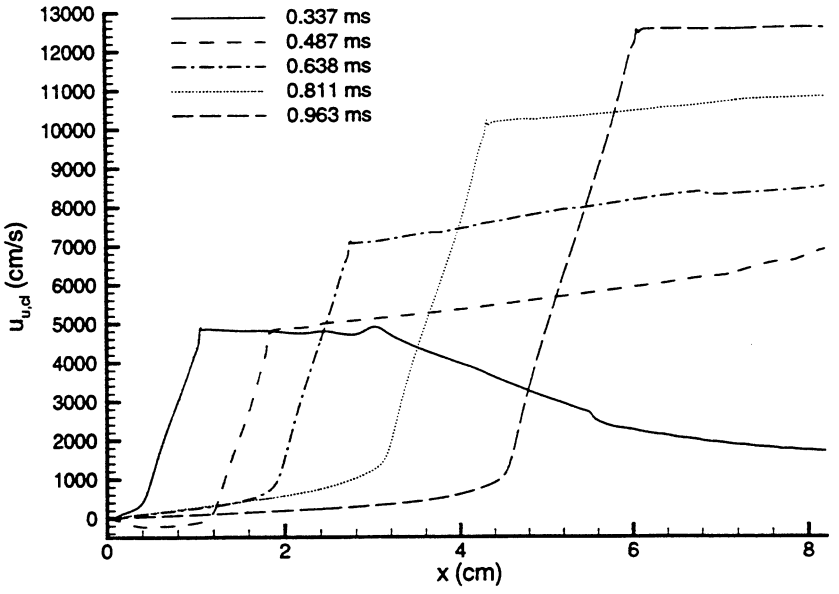

Figure 5.82: Centerline velocity at selected times, AS1.

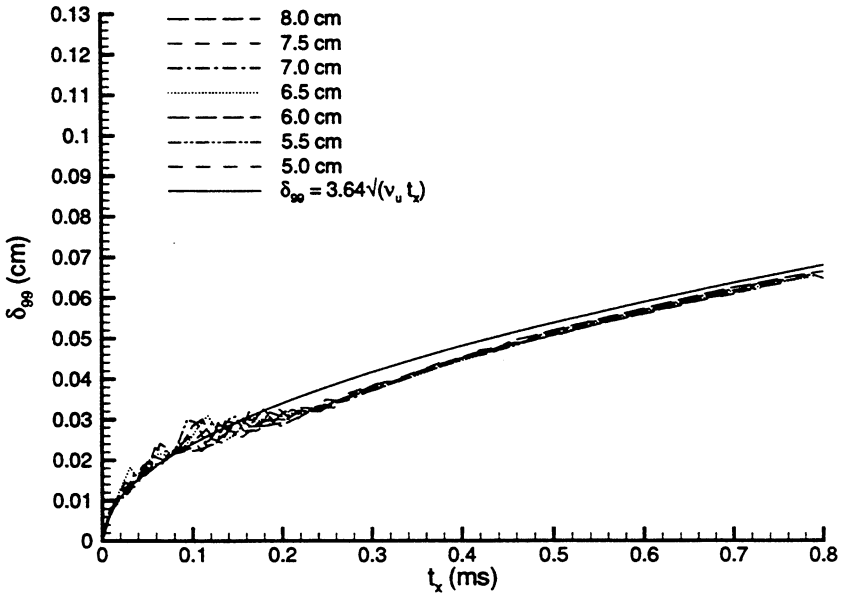

Figure 5.83: Boundary layer thickness at local times, AS1

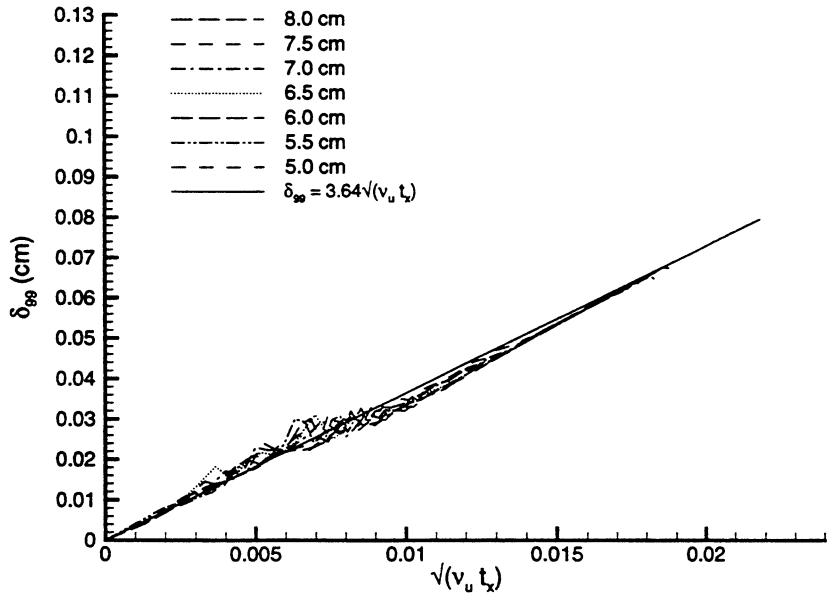

Figure 5.84: Boundary layer thickness for local times, AS1.

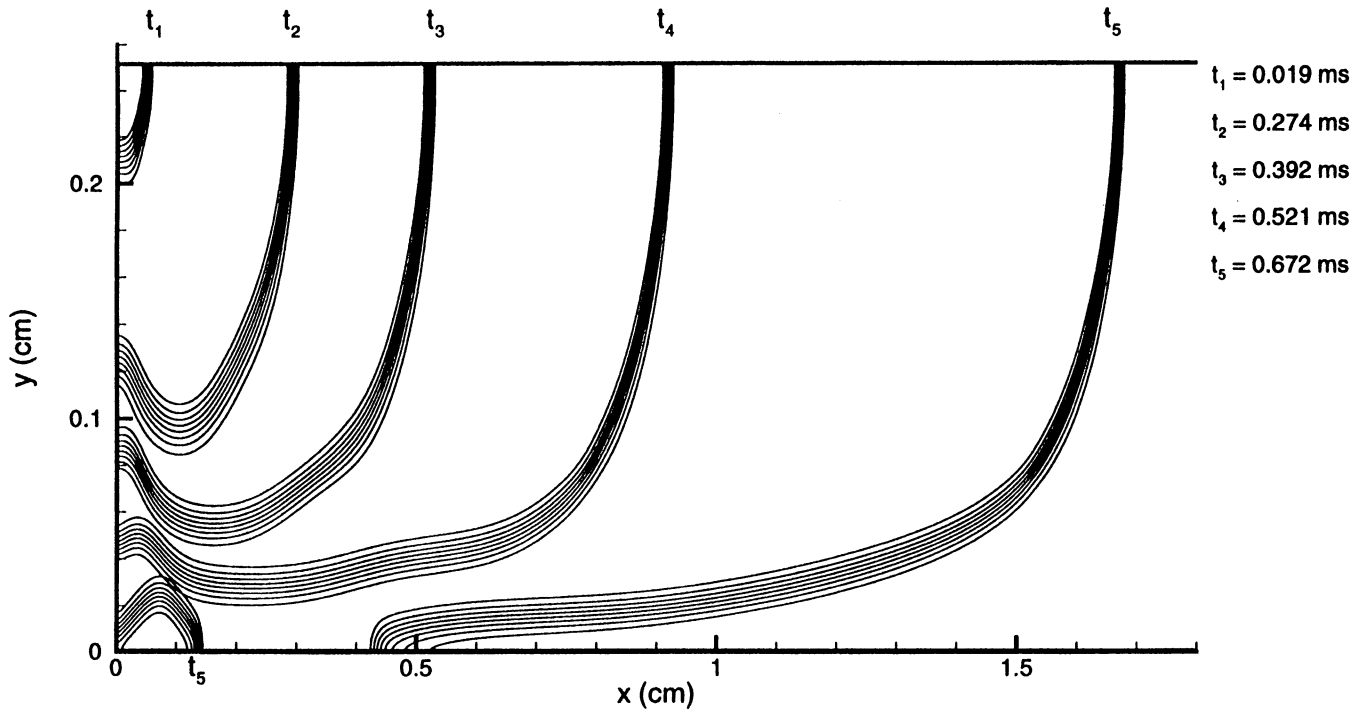

Figure 5.85: Temperature profiles showing the initial flame development, AS2.

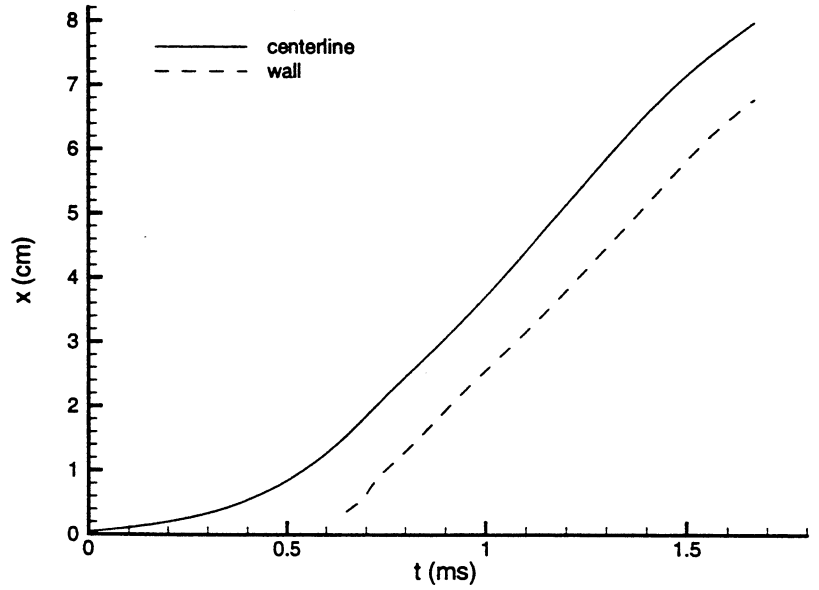

Figure 5.86: Position of the flame at the centerline and wall, AS2.

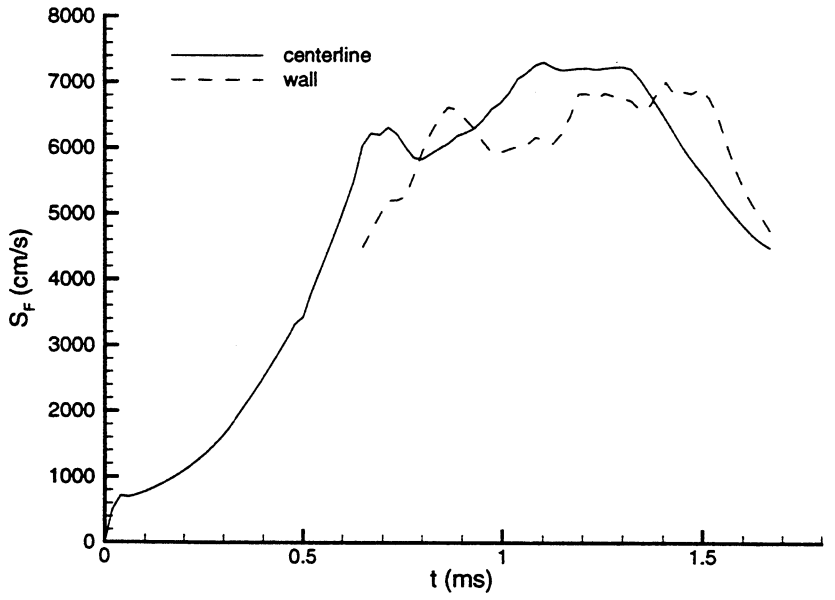

Figure 5.87: Flame velocity relative to laboratory coordinates for the centerline and wall, AS2.

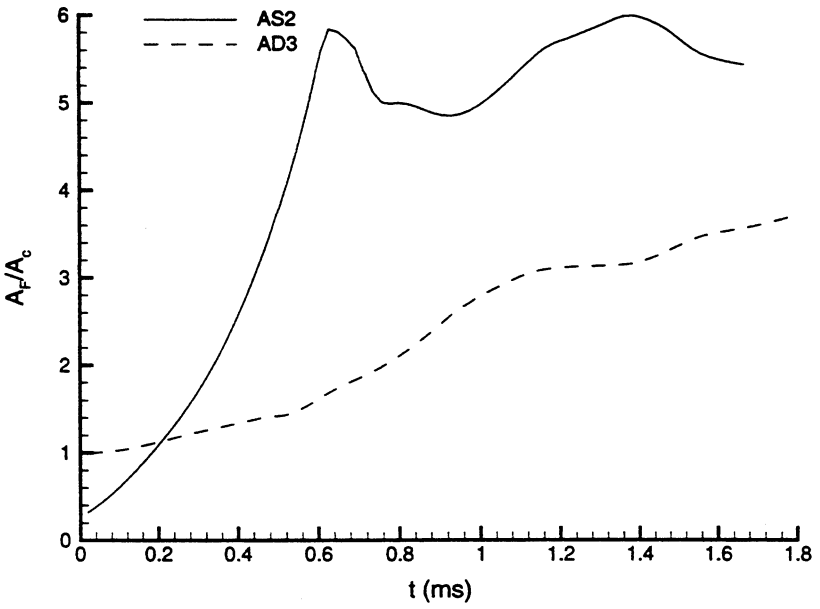

Figure 5.88: Relative flame area versus time, AS2.

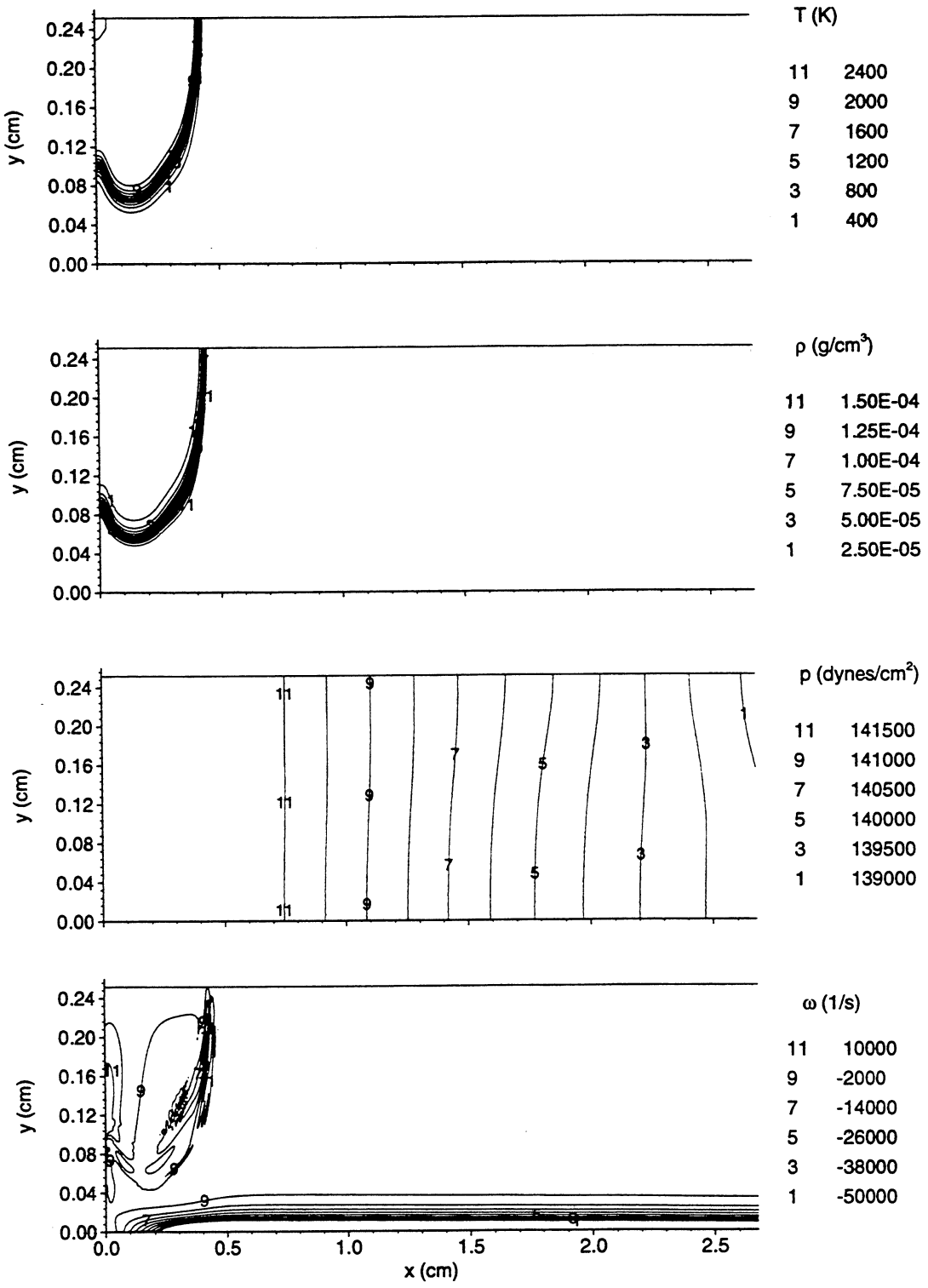

Figure 5.89: Temperature, density, pressure, and vorticity contours, 0.348 ms, AS2.

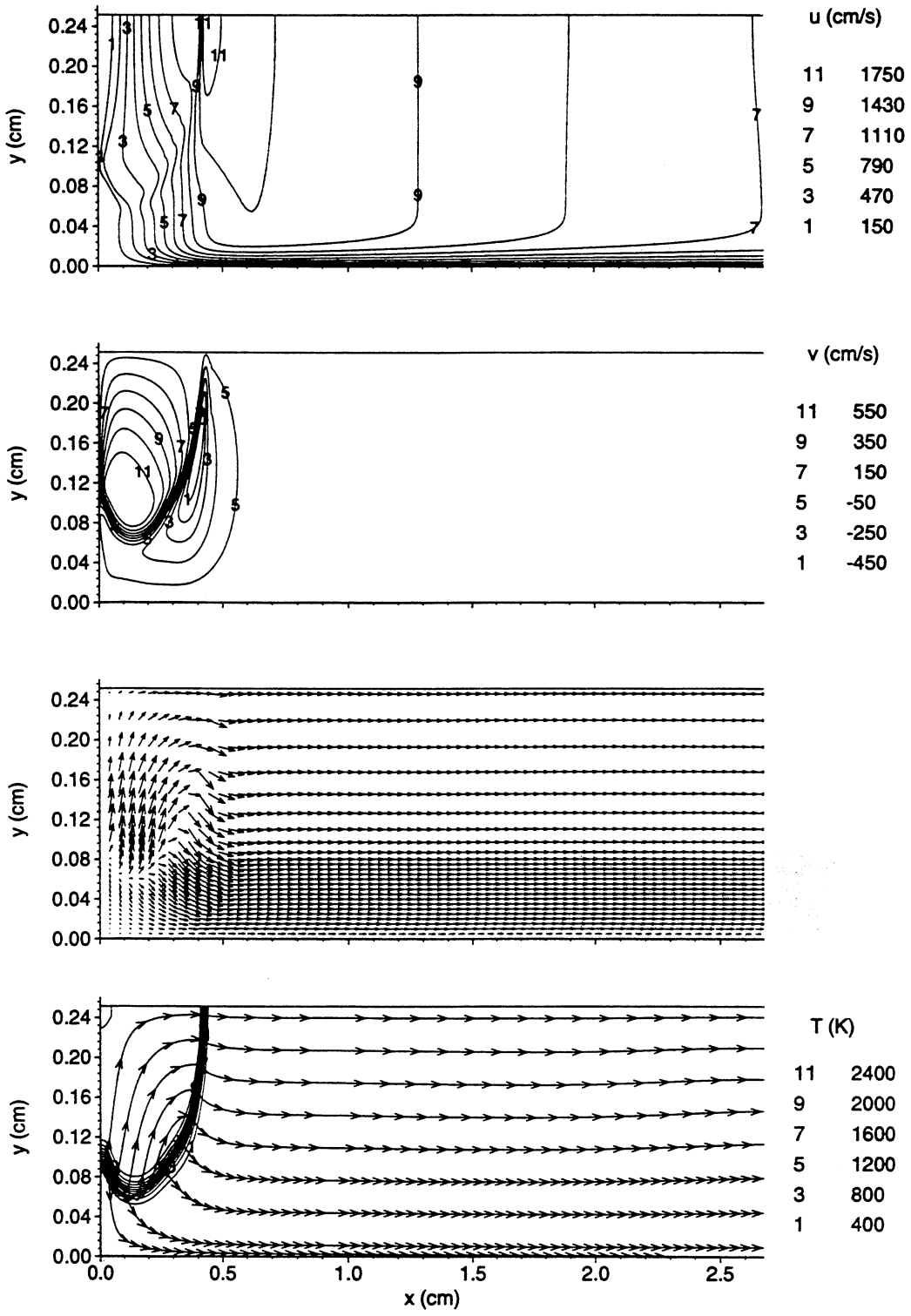

Figure 5.90: Velocity contours, velocity vectors and instantaneous streamlines, 0.348 ms, AS2.

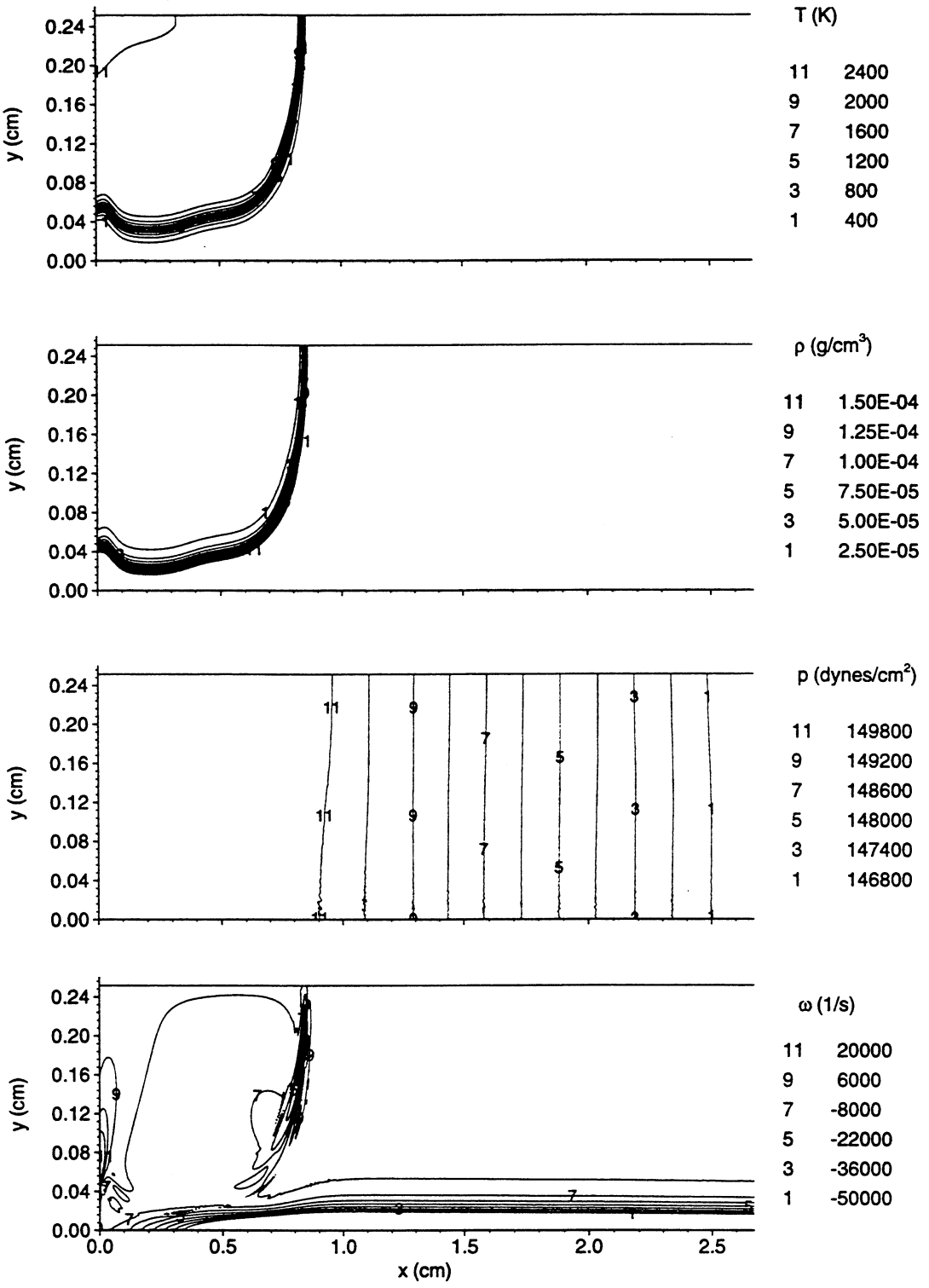

Figure 5.91: Temperature, density, pressure, and vorticity contours, 0.500 ms, AS2.

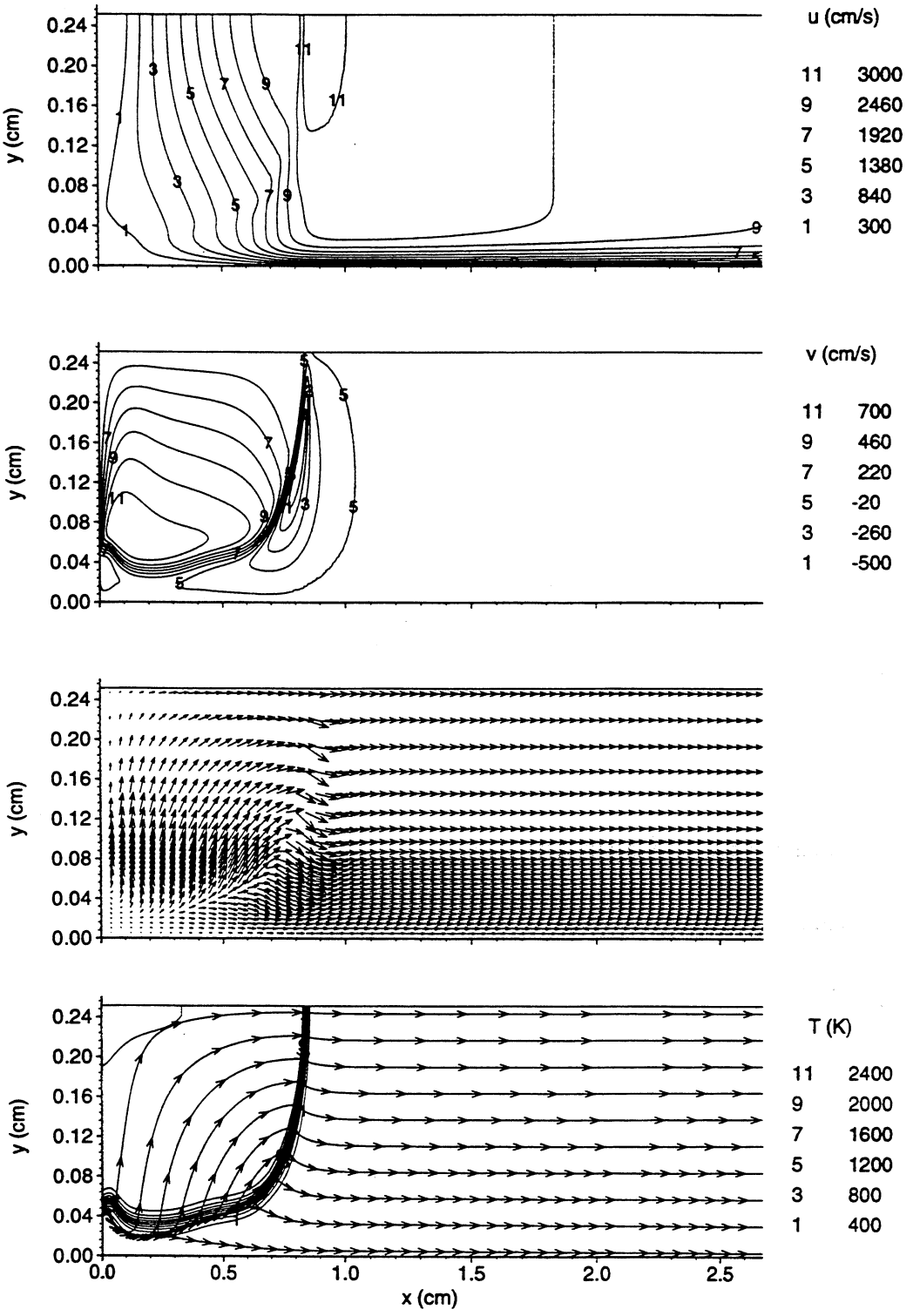

Figure 5.92: Velocity contours, velocity vectors and instantaneous streamlines, 0.500 ms, AS2.

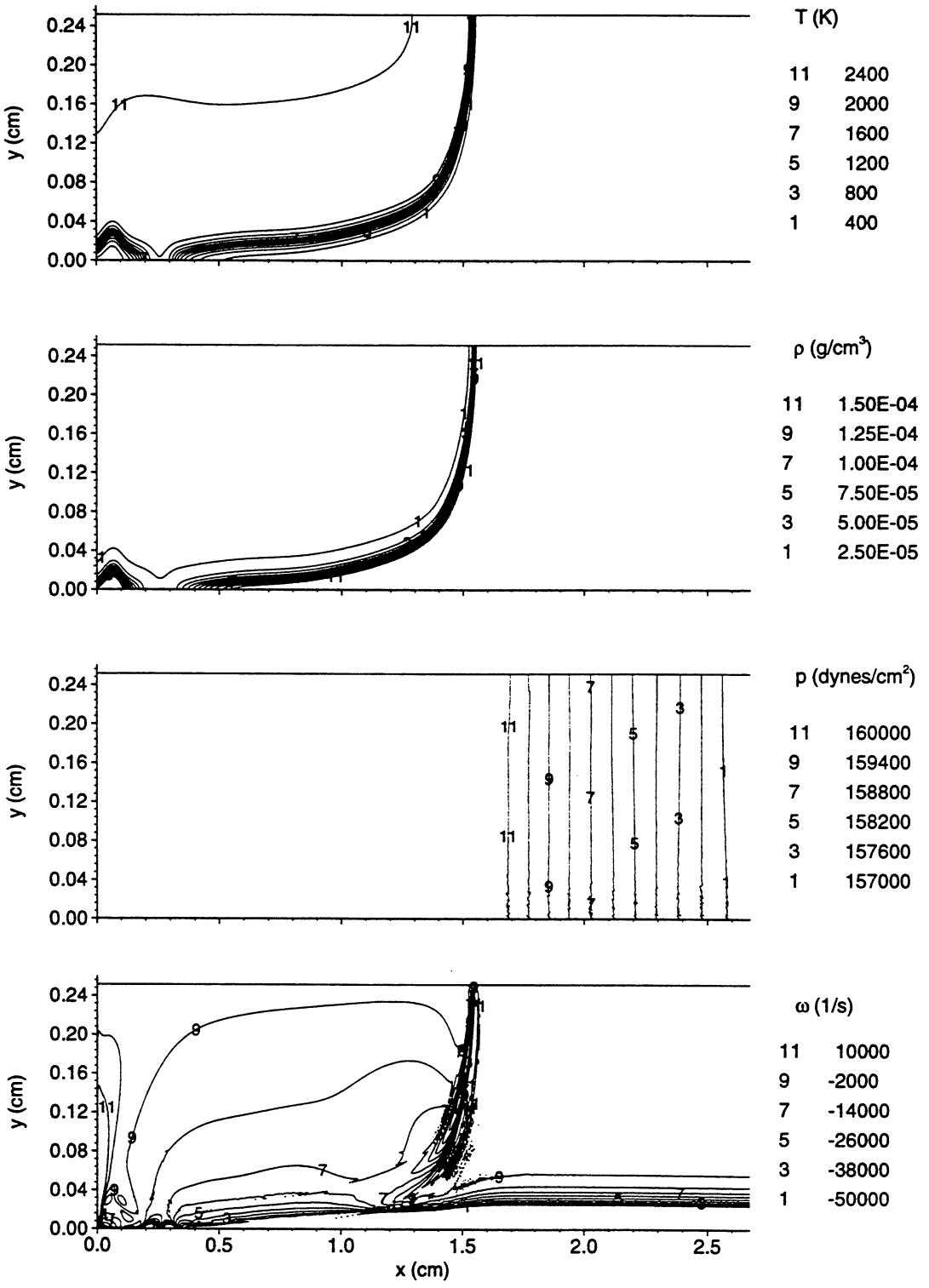

Figure 5.93: Temperature, density, pressure, and vorticity contours, 0.650 ms, AS2.

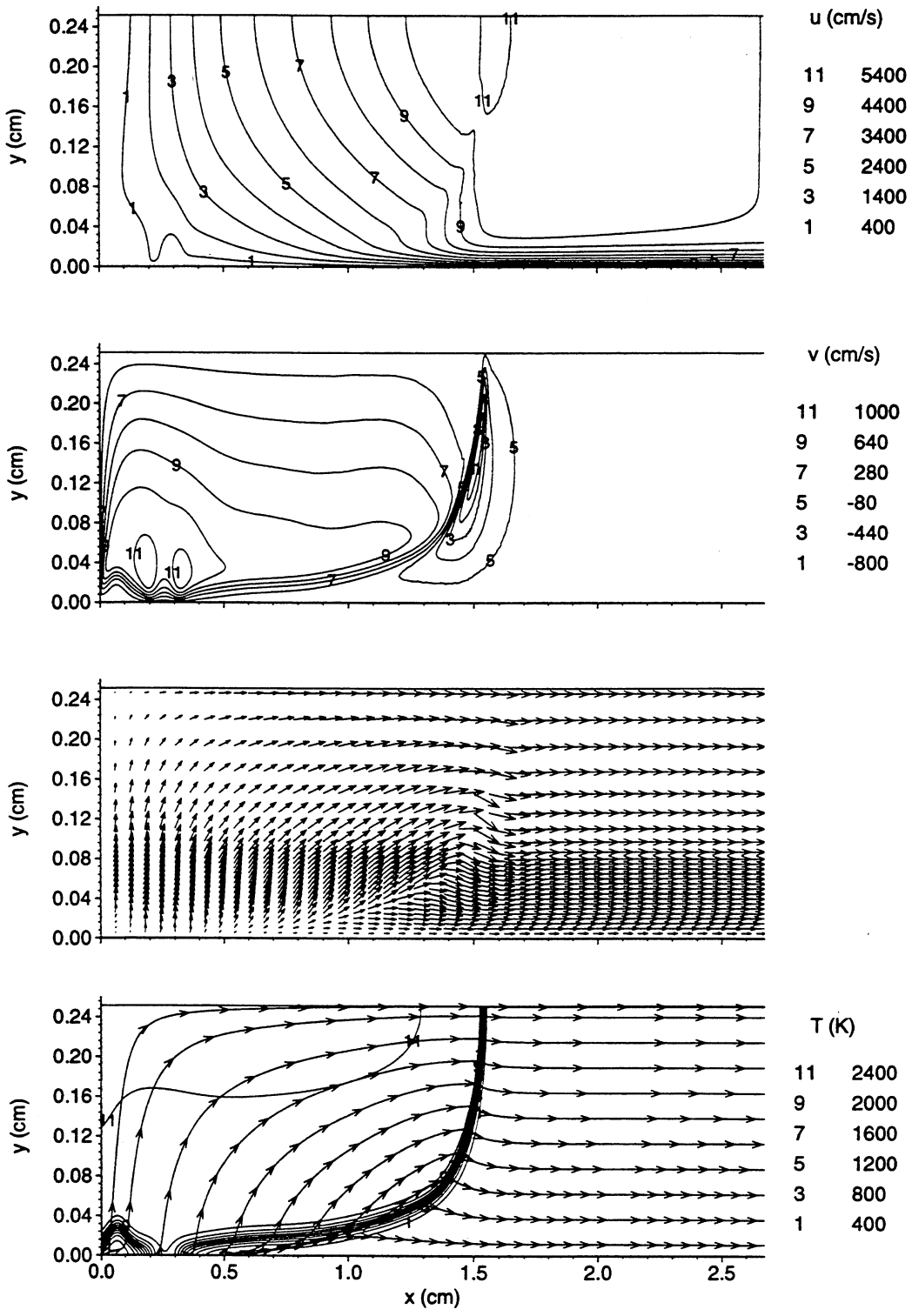

Figure 5.94: Velocity contours, velocity vectors and instantaneous streamlines, 0.650 ms, AS2.

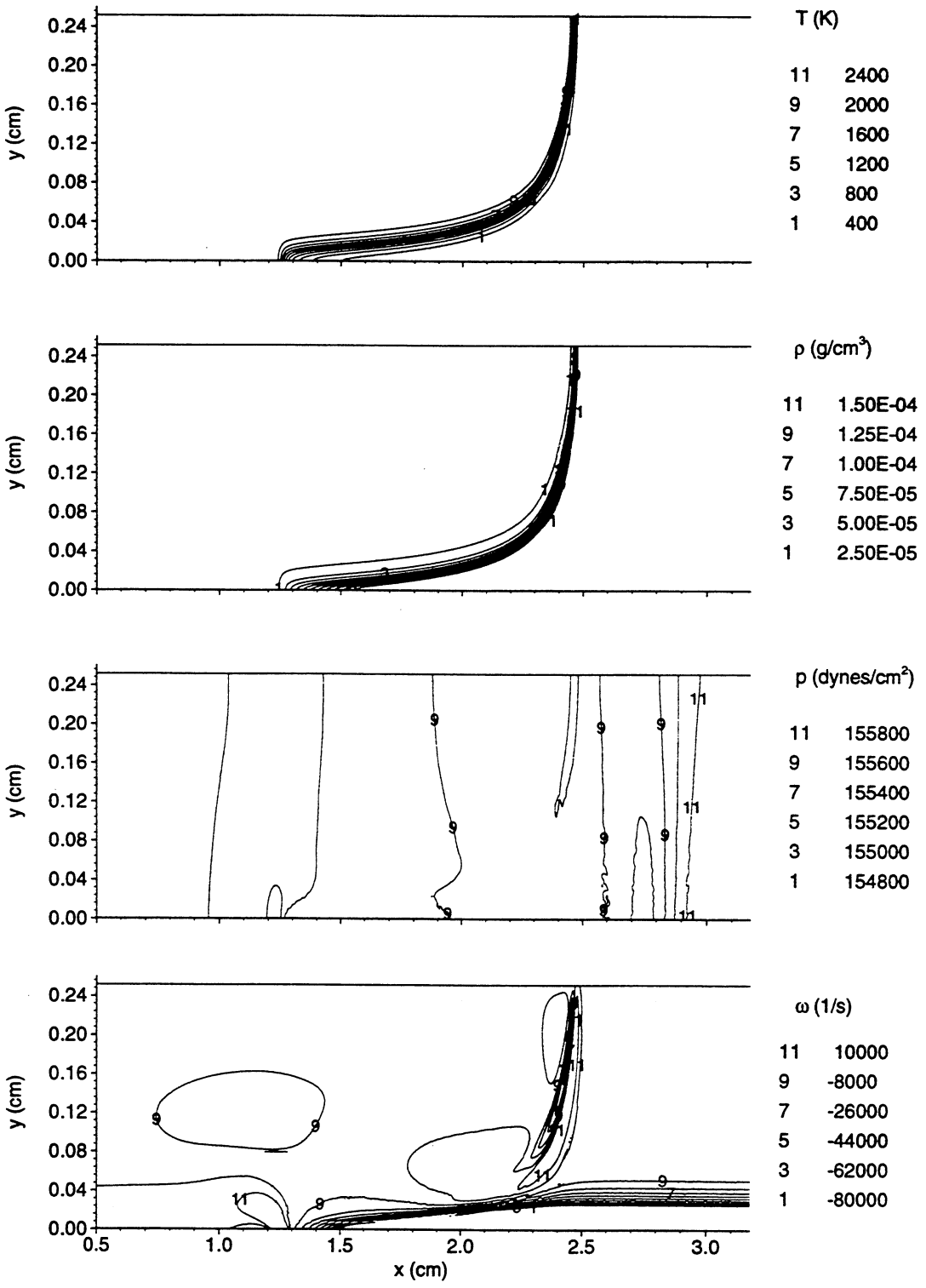

Figure 5.95: Temperature, density, pressure, and vorticity contours, 0.801 ms, AS2.

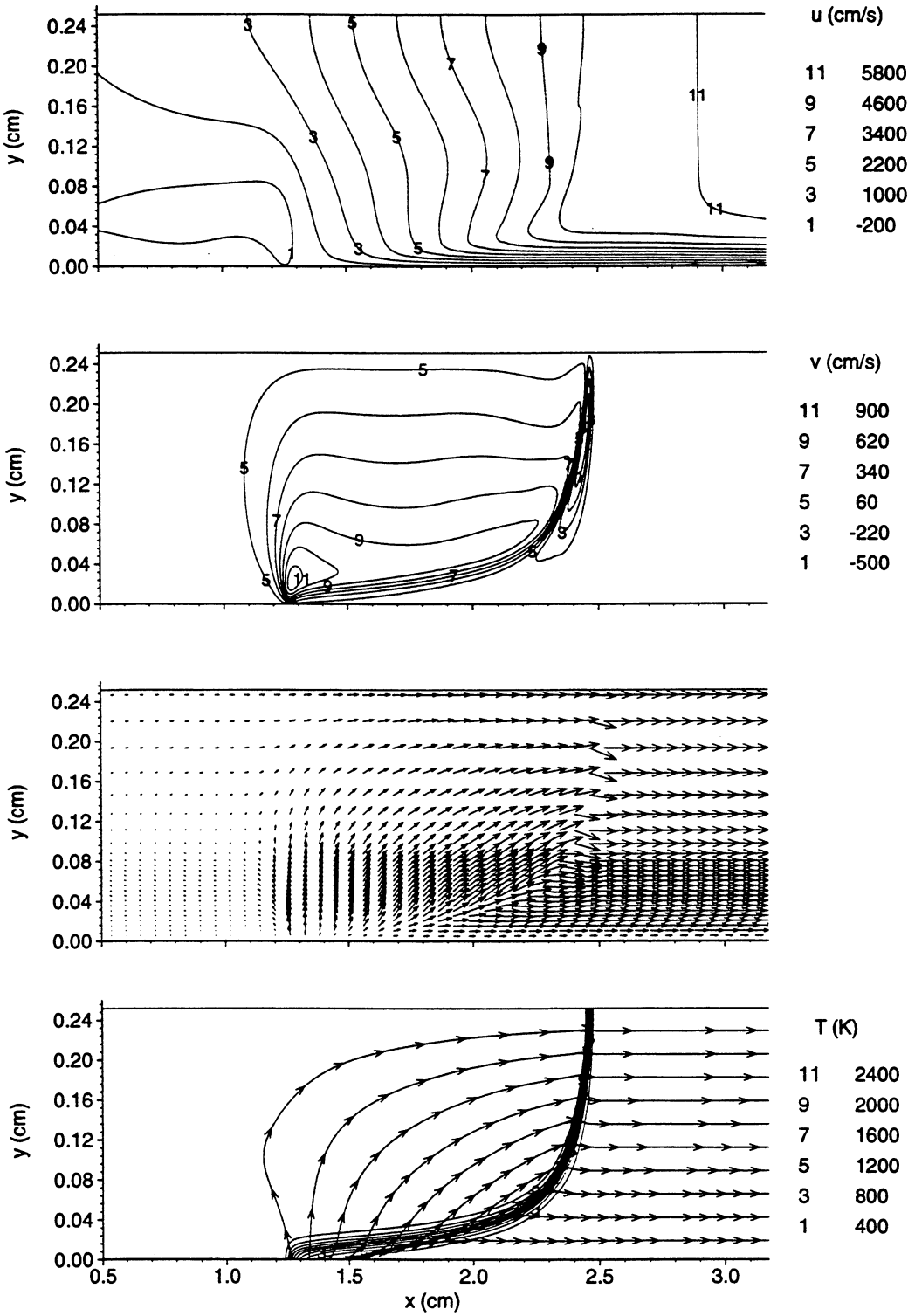

Figure 5.96: Velocity contours, velocity vectors and instantaneous streamlines, 0.801 ms, AS2.

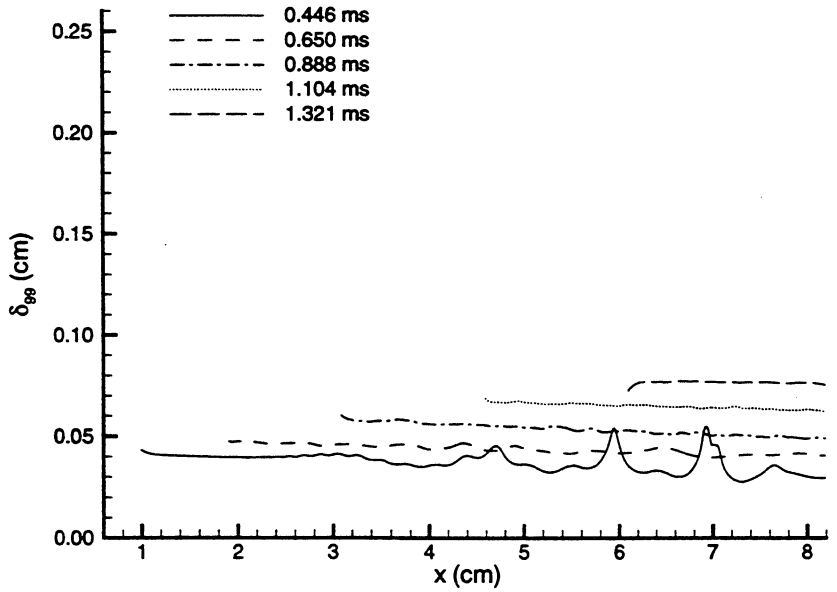

Figure 5.97: Boundary layer thickness, AS2.

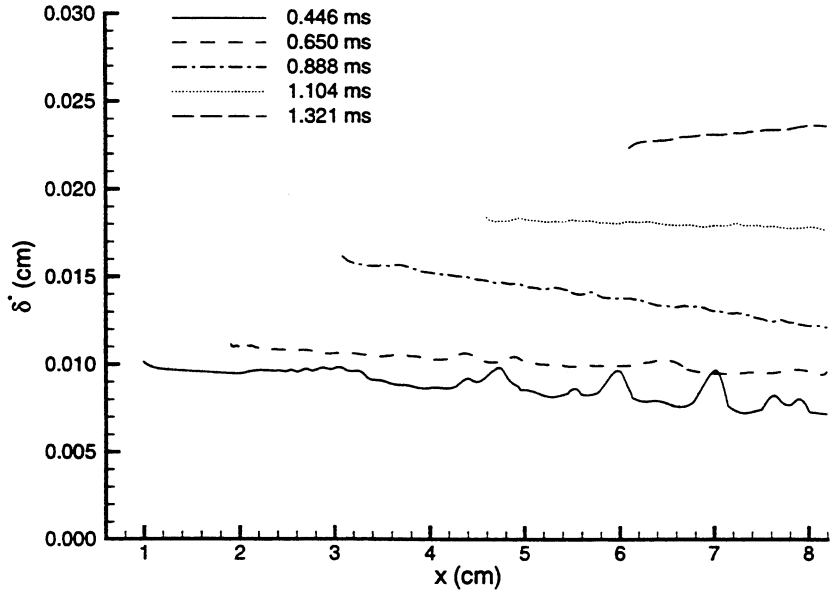

Figure 5.98: Displacement thickness for varying times, AS2.

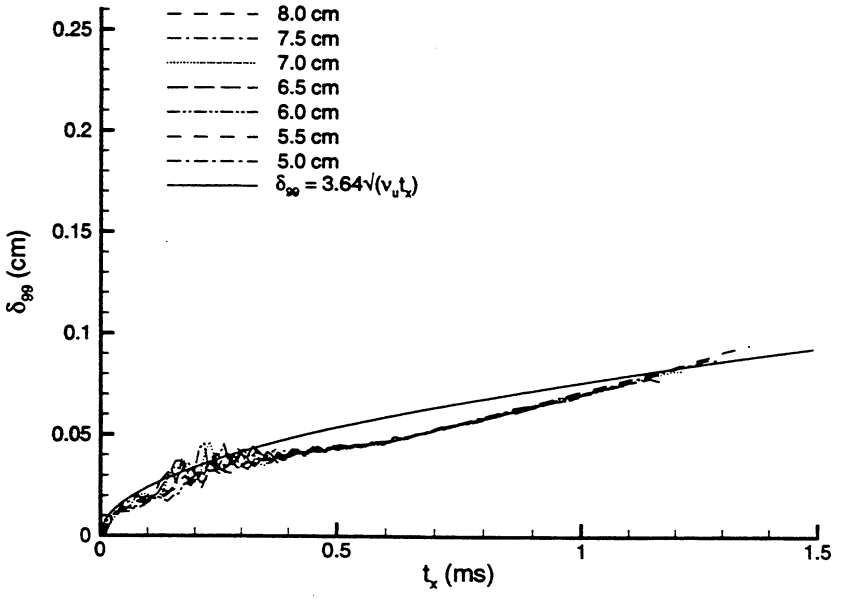

Figure 5.99: Boundary layer thickness at selected channel locations versus local time, AS2.

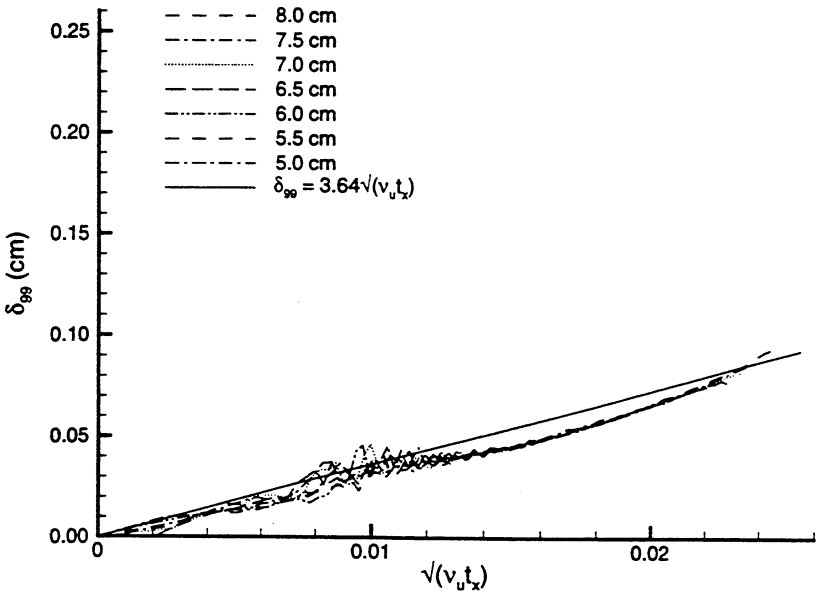

Figure 5.100: Boundary layer thickness at selected channel locations, AS2.

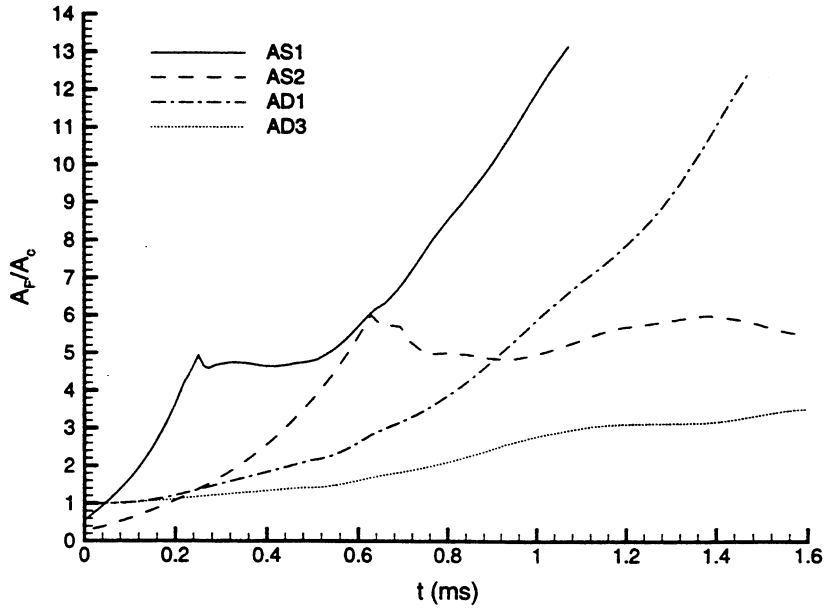

Figure 5.101: Relative flame area ratio comparisons for the spark ignition.

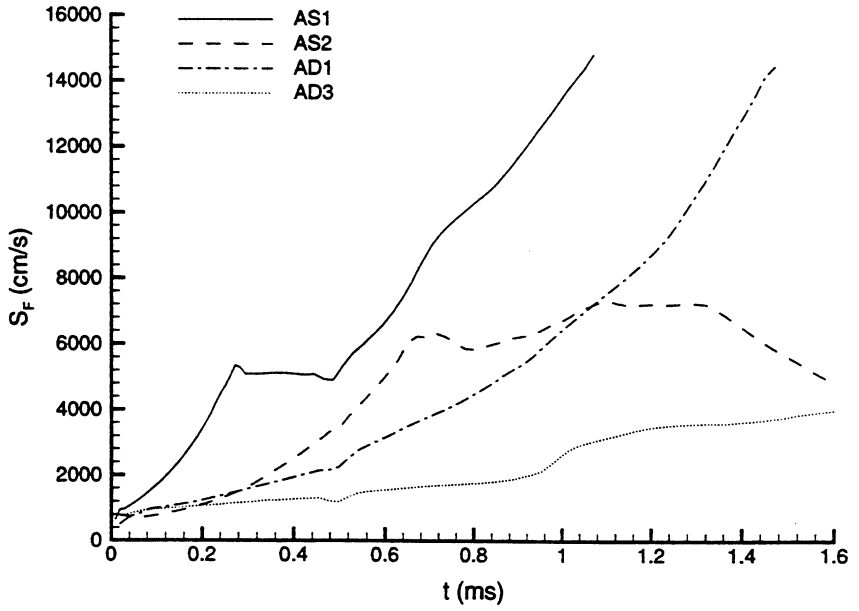

Figure 5.102: Flame speed comparisons for the spark ignition.

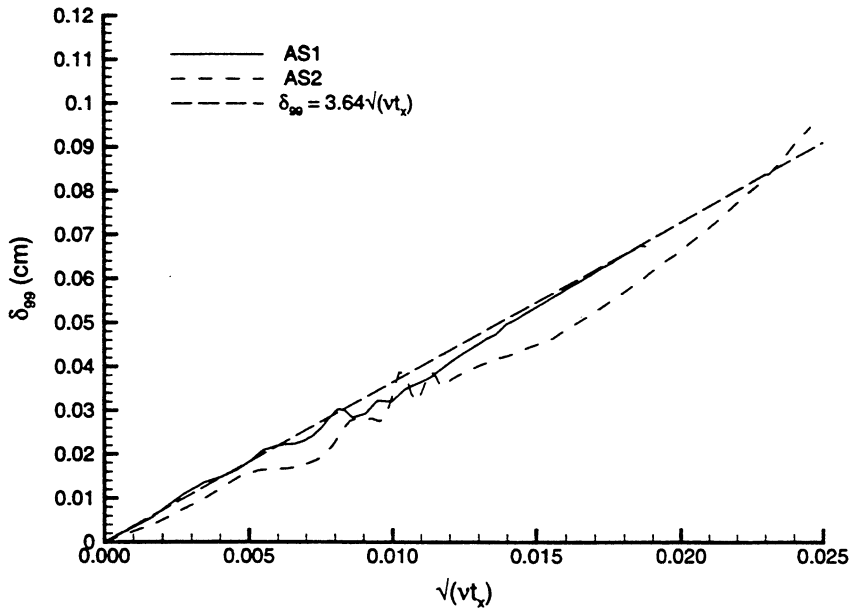

Figure 5.103: Boundary layer growth comparisons for the spark ignition.

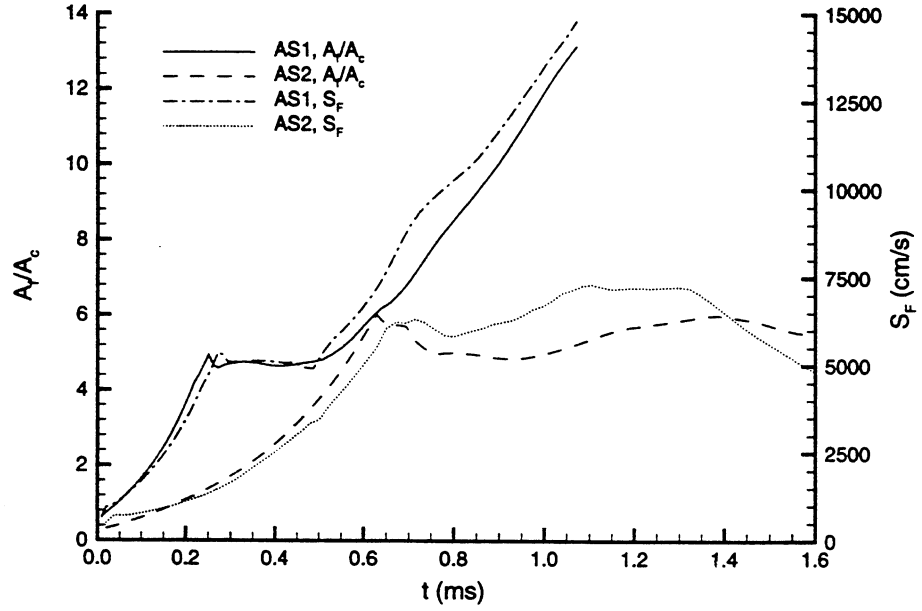

Figure 5.104: Comparison of the relative flame area with the flame speed, spark ignition.

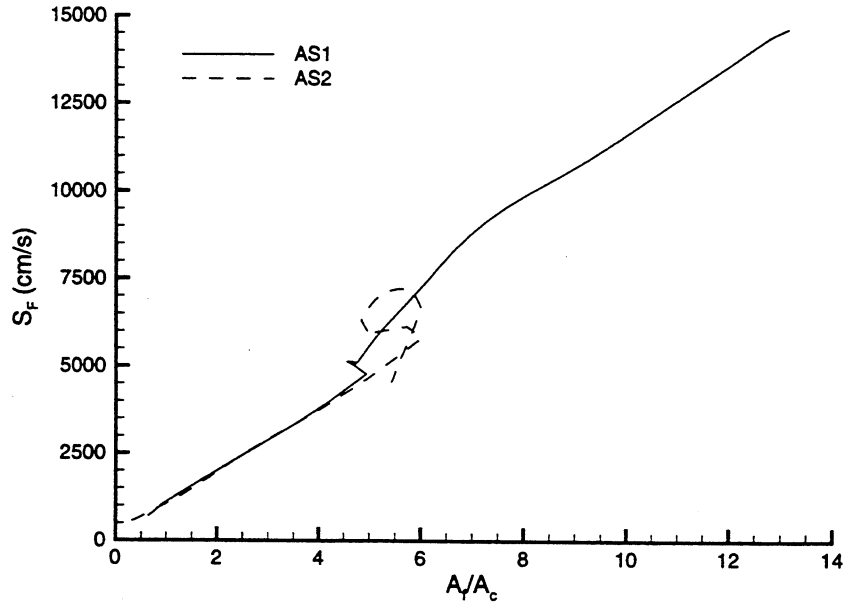

Figure 5.105: Variation of flame speed with area, spark ignition.

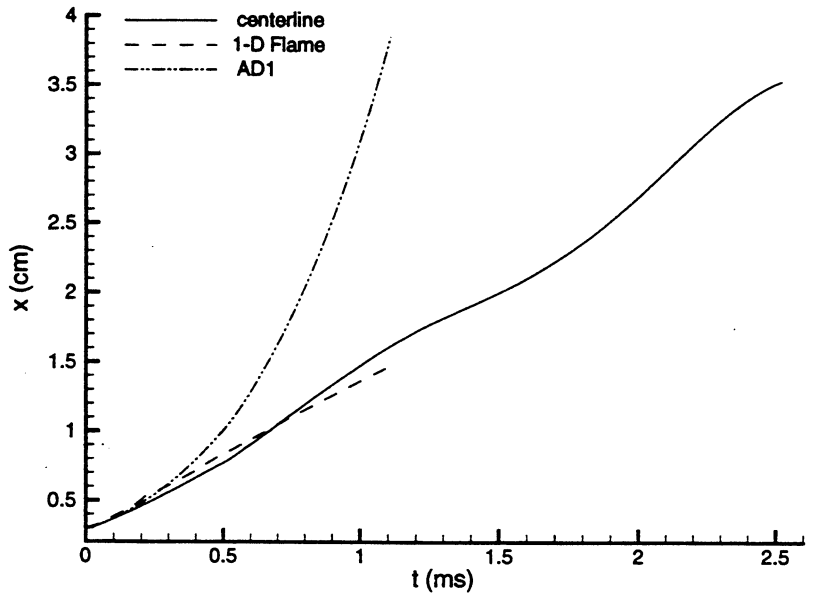

Figure 5.106: Flame position in time for the Isothermal wall case.

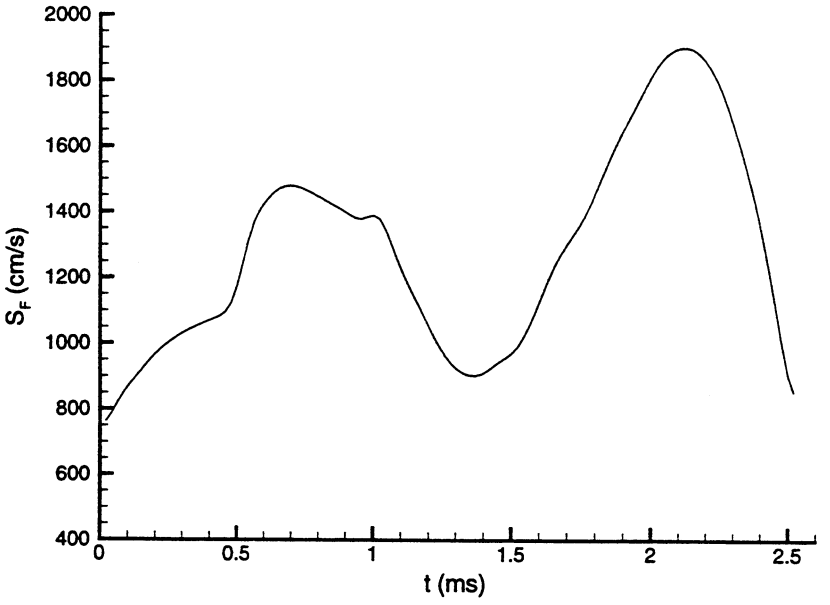

Figure 5.107: Flame speed for the Isothermal wall case.

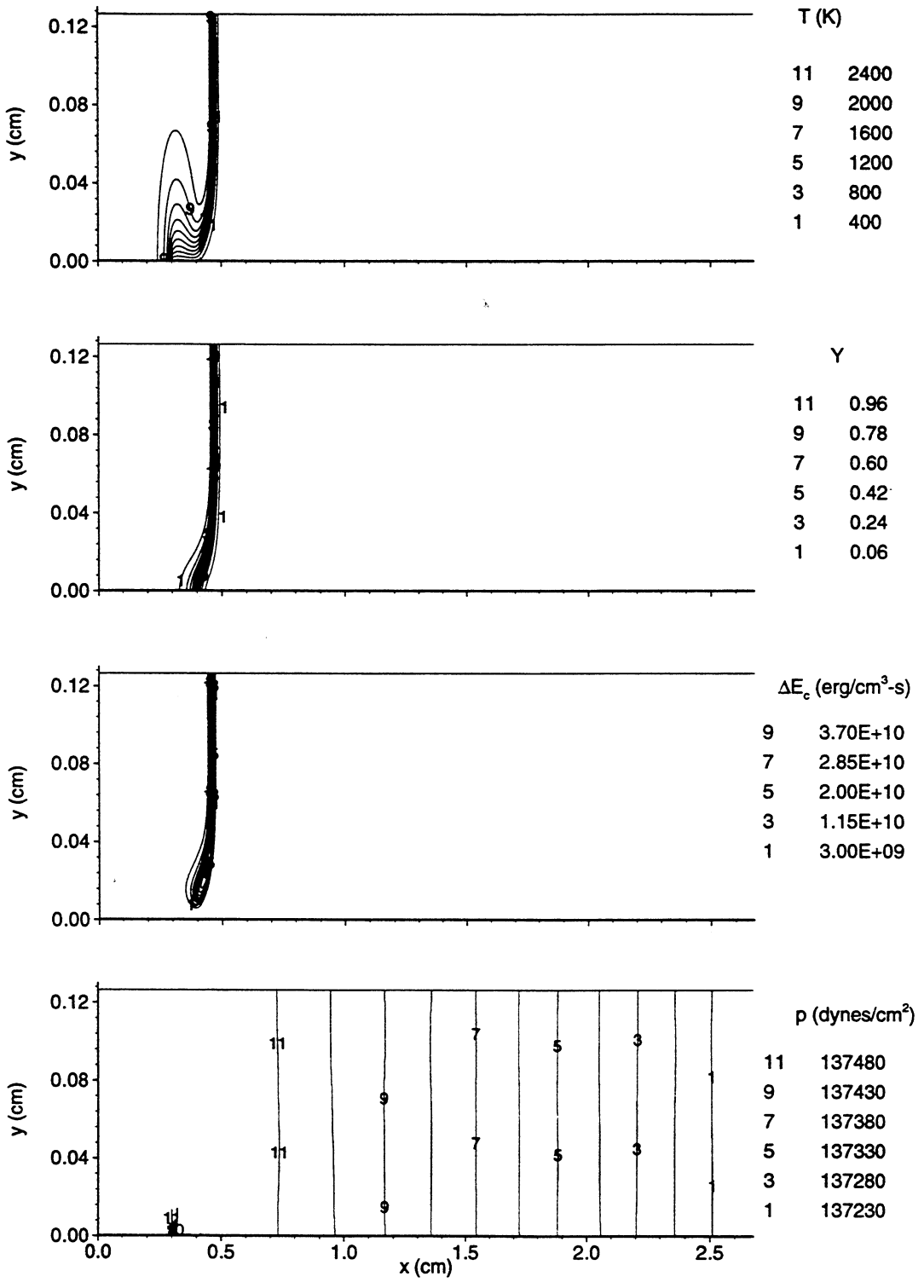

Figure 5.108: Temperature, fuel mass fraction, chemical energy release, and pressure contours, 0.217 ms, ISO.

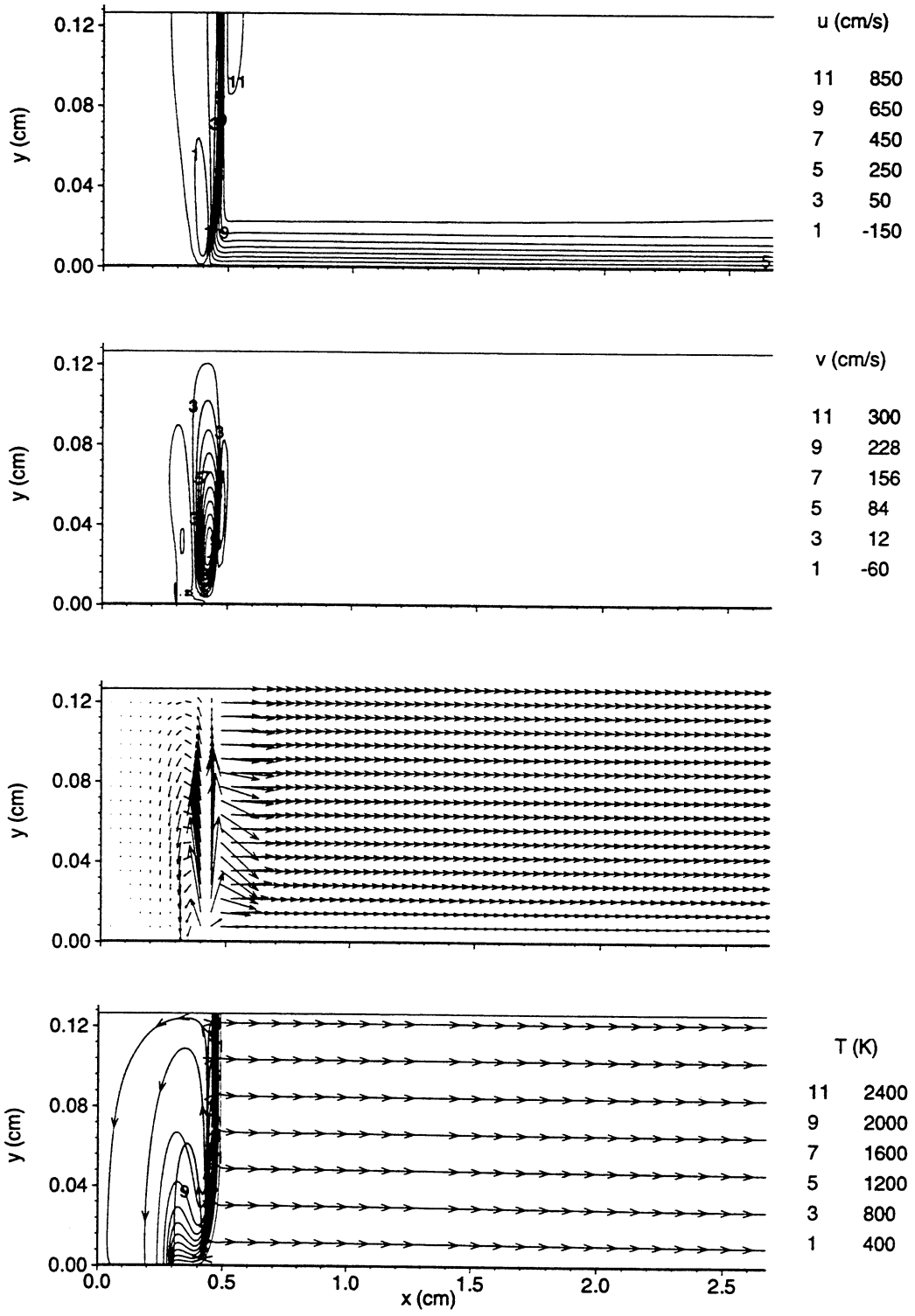

Figure 5.109: Velocity contours, velocity vectors and instantaneous streamlines, 0.217 ms, ISO.

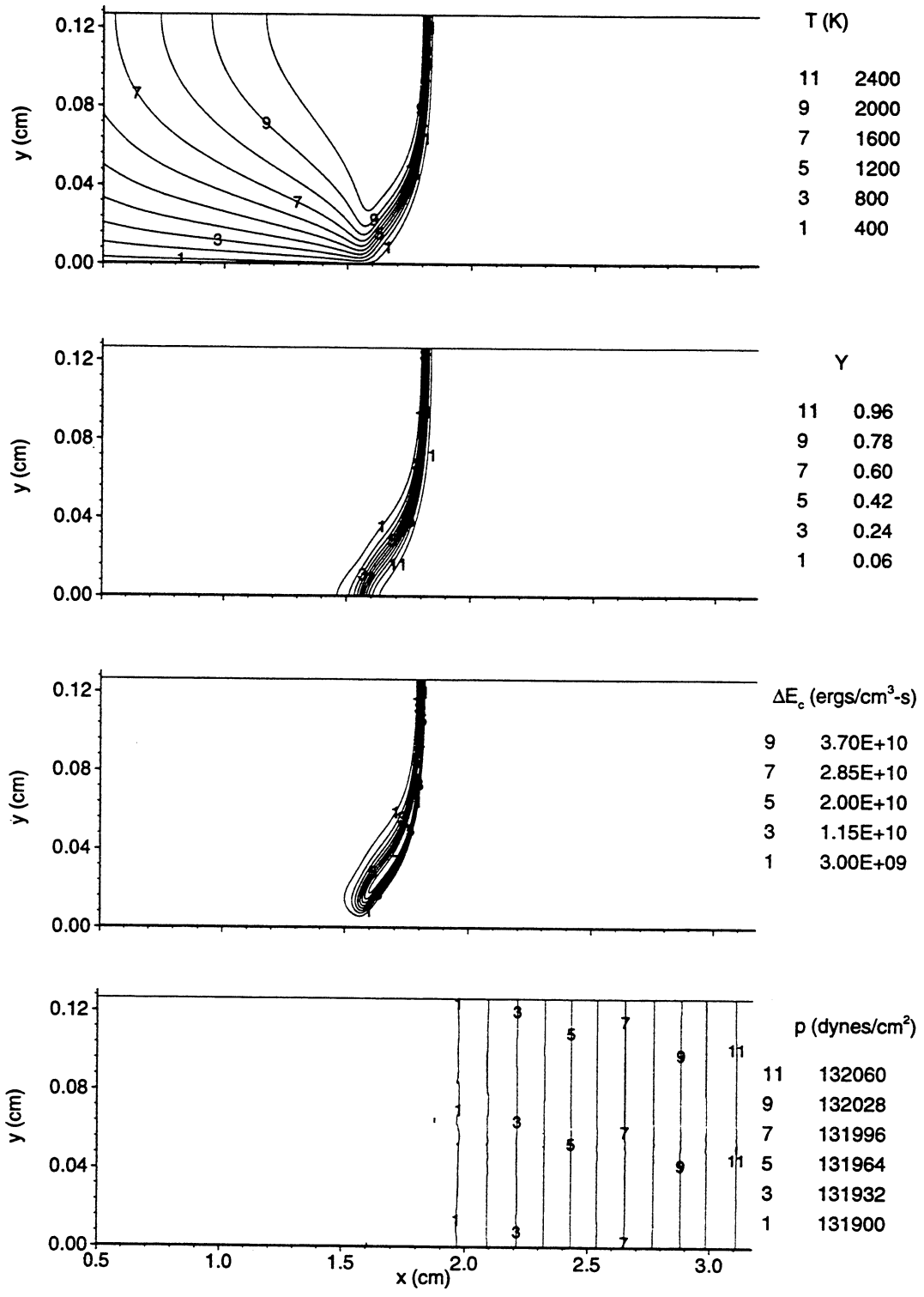

Figure 5.110: Temperature, fuel mass fraction, chemical energy release, and pressure contours, 1.304 ms, ISO.

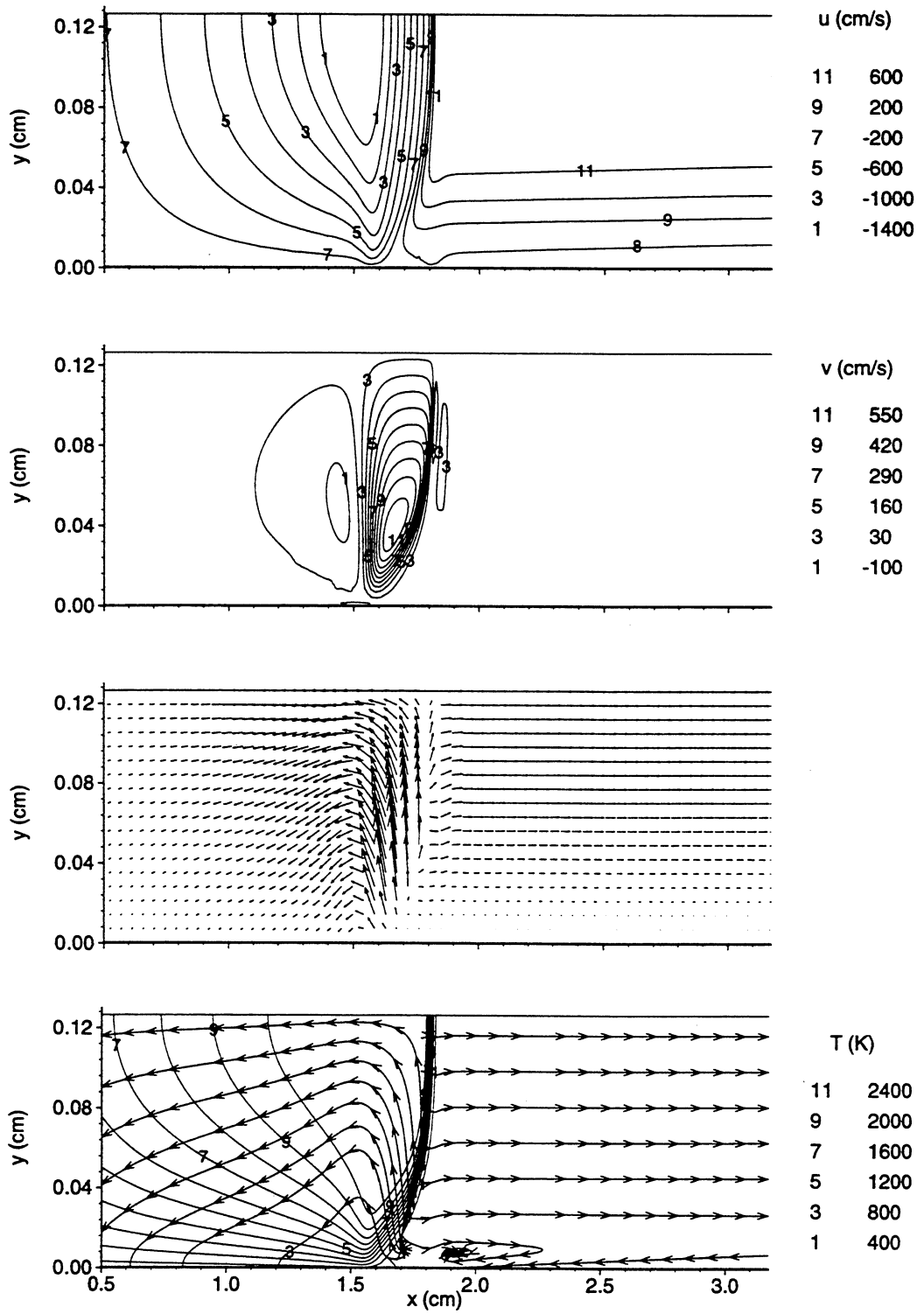

Figure 5.111: Velocity contours, velocity vectors and instantaneous streamlines, 1.304 ms, ISO.

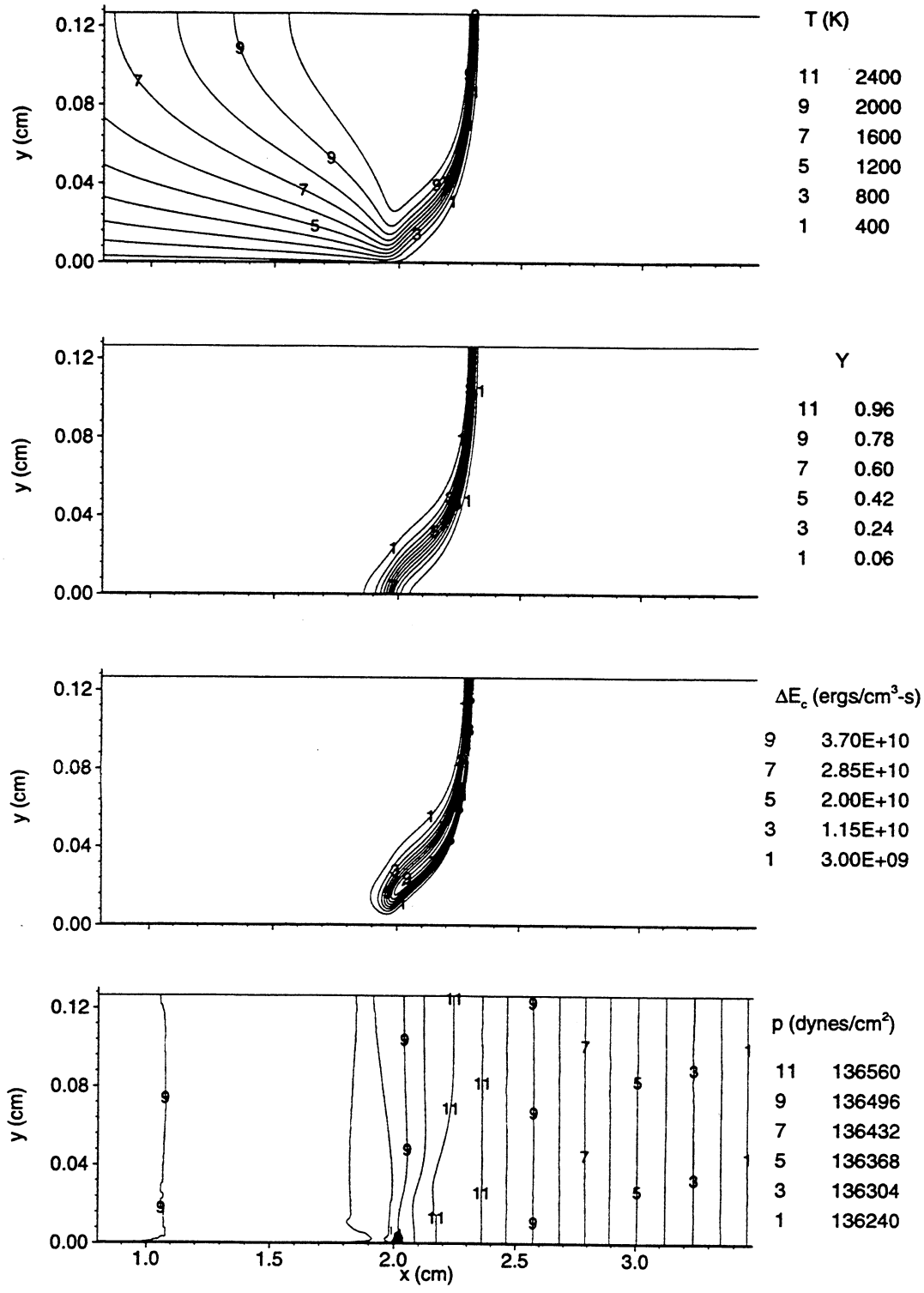

Figure 5.112: Temperature, fuel mass fraction, chemical energy release, and pressure contours, 1.760 ms, ISO.

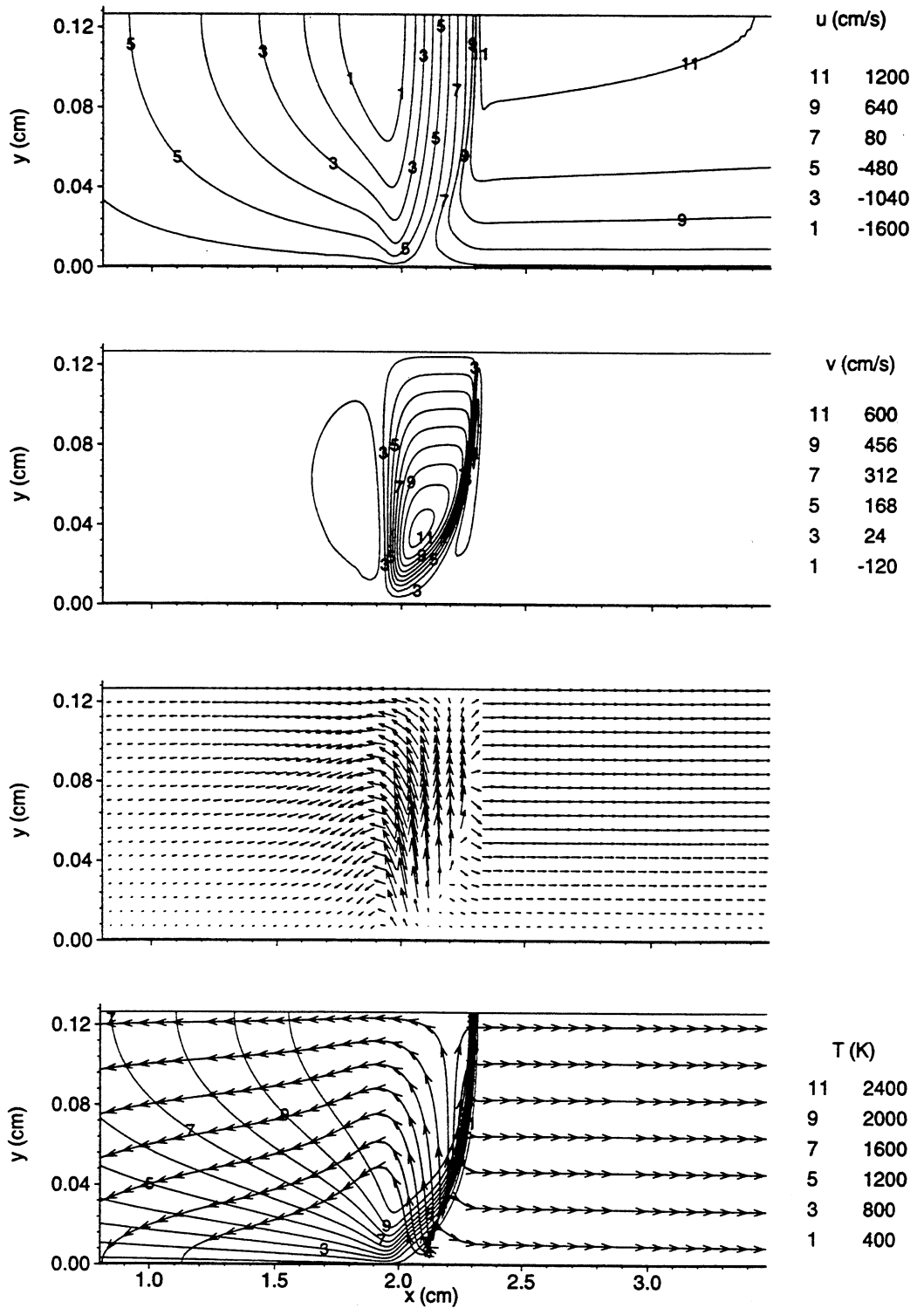

Figure 5.113: Velocity contours, velocity vectors and instantaneous streamlines, 1.760 ms, ISO.

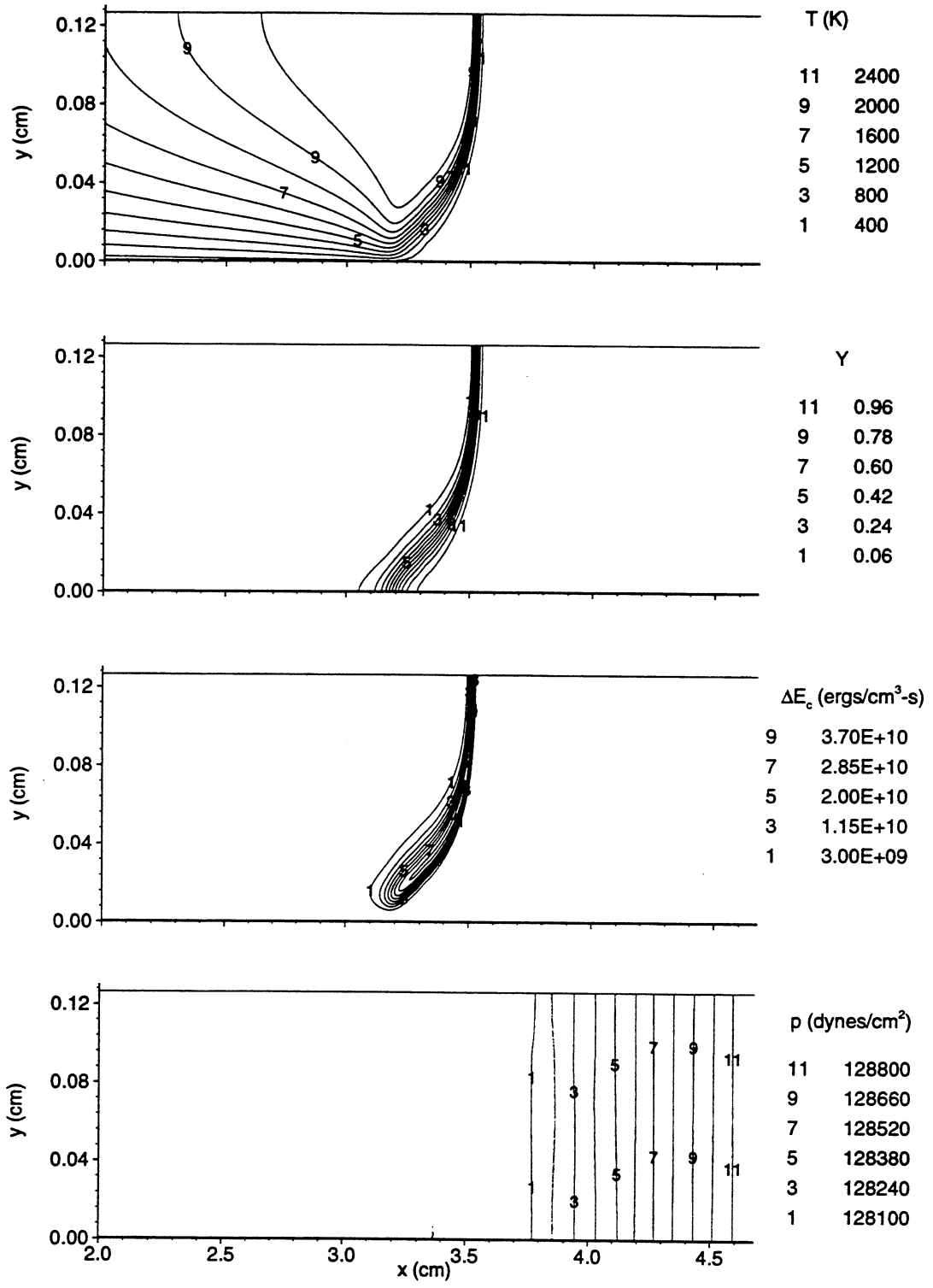

Figure 5.114: Temperature, fuel mass fraction, chemical energy release, and pressure contours, 2.519 ms, ISO.

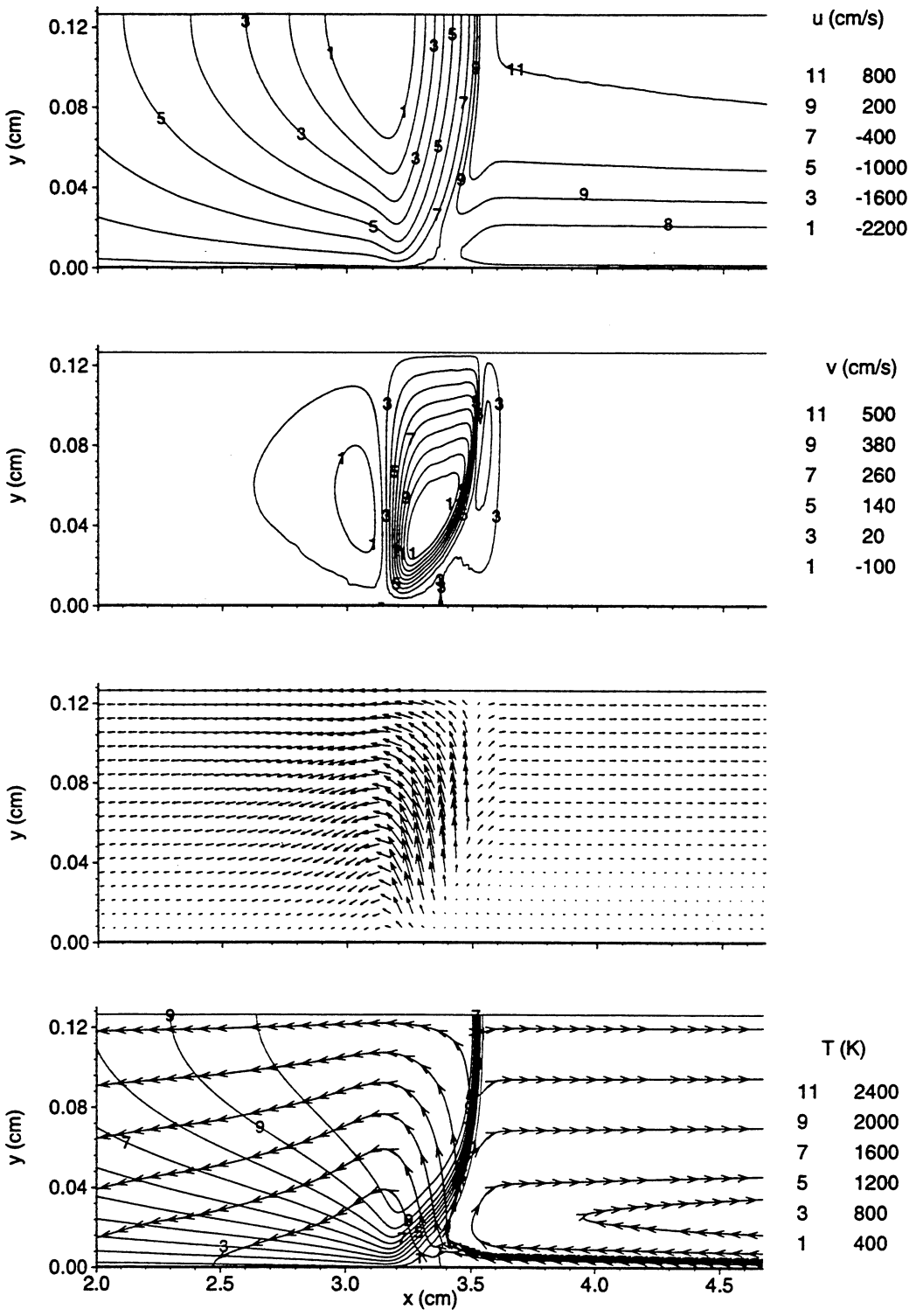

Figure 5.115: Velocity contours, velocity vectors and instantaneous streamlines, 2.519 ms, ISO.

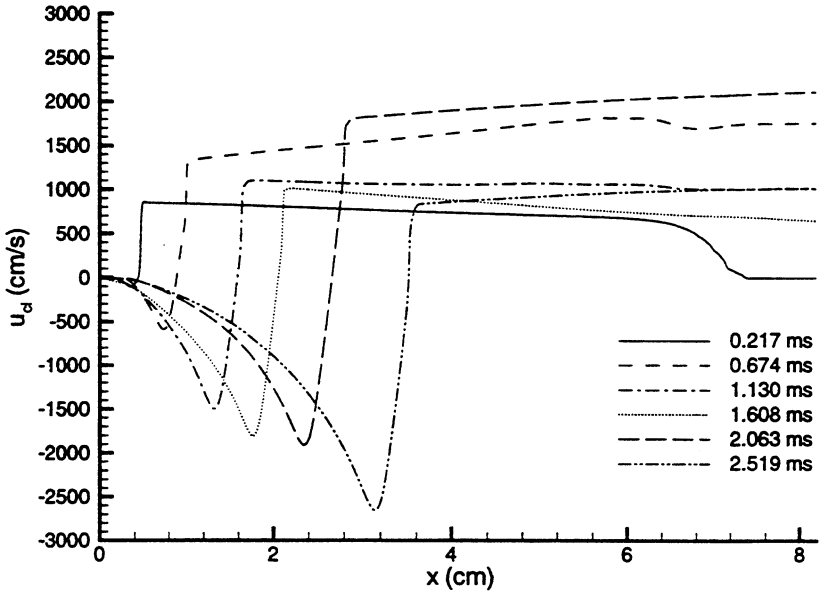

Figure 5.116: Centerline velocity profiles, ISO.

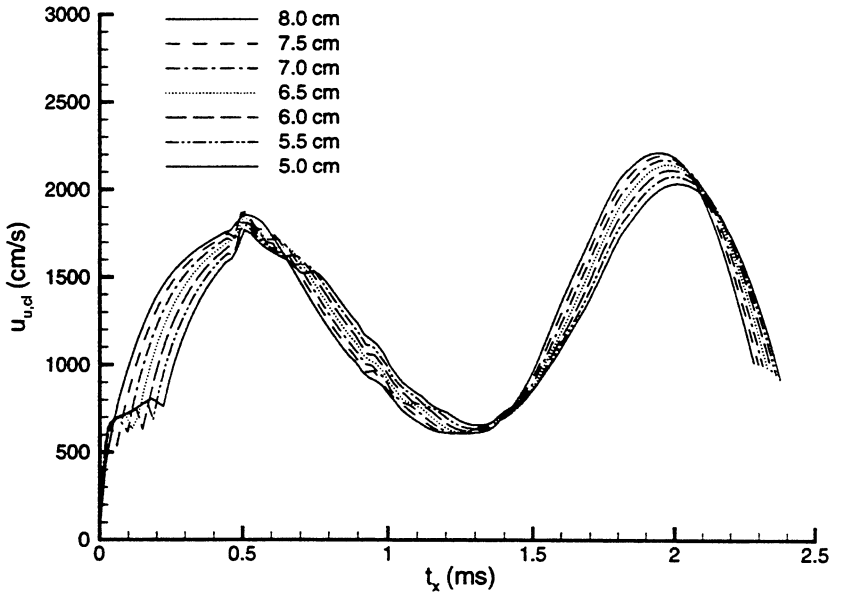

Figure 5.117: Unburned gas velocity at various channel locations, ISO.

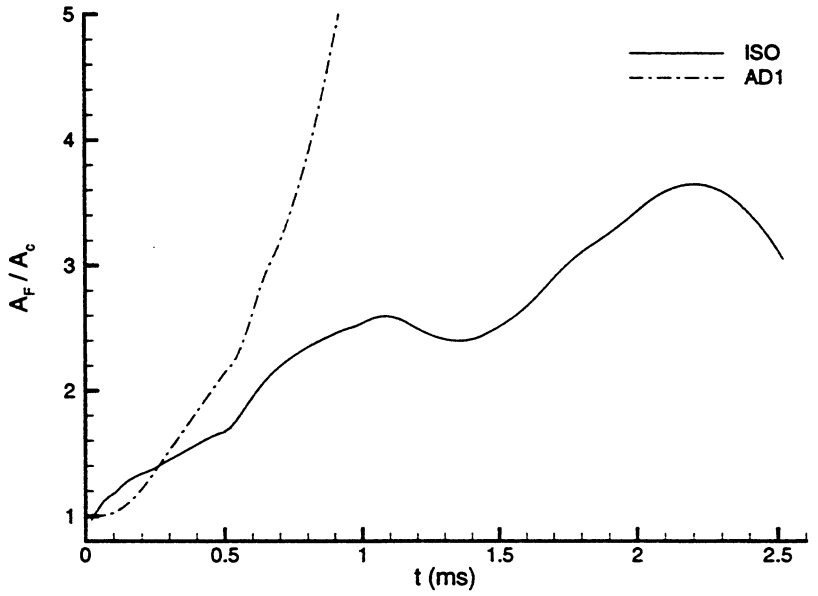

Figure 5.118: Time history of the relative flame area, ISO.

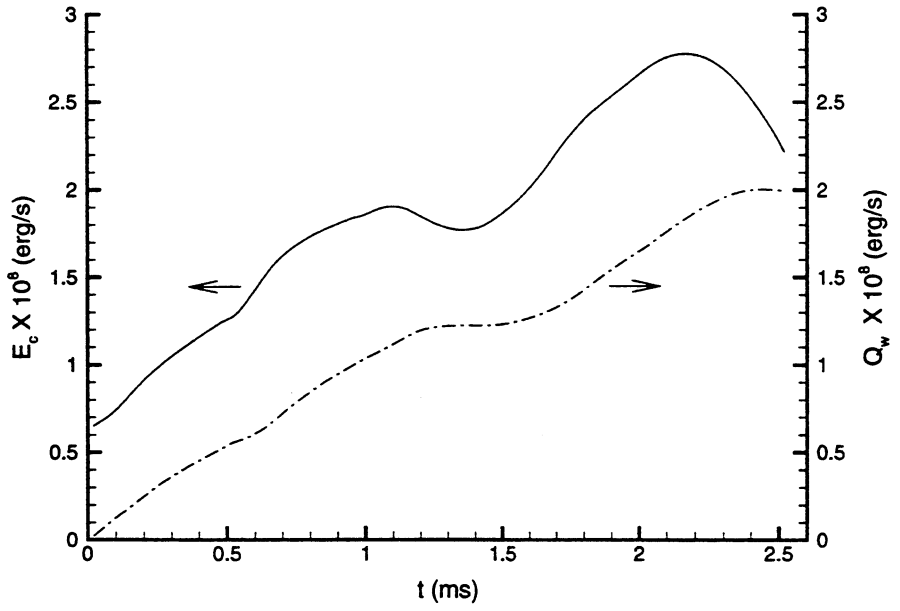

Figure 5.119: Chemical heat addition and thermal extraction in time, ISO.

Chapter 6

Conclusions

The interaction of a laminar flame with its self-generated boundary layer in a rectangular channel was numerically simulated using the two-dimensional, reacting, Navier-Stokes equations. A two species chemistry model was implemented which simulates the stoichiometric reaction of acetylene and air. Calculations were performed to investigate the effects of altering the boundary condition of the wall temperature, the Lewis number, the dynamic viscosity, and the ignition method. The purpose of this study was to examine the fundamental physics of the formation of the boundary layer and the interaction of the flame as it propagates into the boundary layer that its own motion has created.

6.1 Summary of Results

The pressure waves, that are emitted by the flame as it moves down the channel, induce a flow ahead of the flame in the same direction as the flame propagation. This induced flow creates a boundary layer on the channel wall ahead of the flame. The flame then propagates into this boundary layer that was created due to its own motion. These pressure waves are represented in the solution procedure. The compression and expansion waves produced by the flame are the mechanism by which the gas is set into motion. The interaction of the pressure waves with the gas is seen in the boundary layer growth ahead of the flame. Ahead of the initial pressure wave, which moves at the local speed of sound, the gas is unaware of the flame. The boundary layer begins to grow in time starting from the location of the initial pressure wave. This solution represents a direct numerical simulation of the acoustic interactions of the pressure waves created by the flame motion.

The growth of the boundary layer is found to be self-similar in local time. Local time is defined to start at the instant the initial pressure wave generated by the flame reaches that point in the channel. The growth follows the general solution of Stokes' First Problem. With the growth being

self-similar in local time, an analytical theory could be developed to calculate the flame position and speed in a channel. The boundary layer growth caused by the flame could be modeled as Stokes' First Problem with an acceleration term.

The deviation from the classical solution of Stokes' First Problem is due to the flame acceleration. Flames that accelerate at a faster rate show more deviation then flames with a slower acceleration. Increasing the channel height has the effect of slowing the flame, thereby causing better agreement. When the viscosity was increased, the flame accelerated at a faster pace, causing a greater deviation. The reason for the acceleration of the flame is the upwelling at the wall. When the material burns in the flame, the density decreases. The material that burns near the wall is restricted by the boundary layer, which causes a flow blockage. The material that cannot expand ahead of the flame is forced to expand upwards, creating the upwelling. The upwelling turns at the centerline and provides additional momentum to the flame near the centerline. This creates the mushroom shape flame. When the channel height was increased, the upwelling was not dispersed over the entire flame, but acted on a flame region between the wall and the centerline. This created a rearward cusp at the centerline. Since the curved region near the wall grows in time, the upwelling increases, and its effects are dispersed over a greater portion of the flame. This leads to the rearward cusp at the centerline forming and then shrinking in time.

When a simulated spark was used for the flame ignition, the flame propagated at a faster speed. This was due to the flame developing a greater flame front area in a shorter time as compared to the planar ignition cases. The greater the flame front area, relative to the channel height, the more material will be burned, and the more the flame will be accelerated. An interesting feature observed in the case with increased height was the formation of a flame on the end wall of the channel with a similar shape as the flame that propagates down the side wall. When the flame on the end wall reached the side wall a flame remnant formed that became detached from the main flame and eventually burned itself out.

The results for an isothermal wall differed greatly from the results for an adiabatic wall. Since the wall temperature was fixed at the unburned gas temperature, the flame was quenched at the lower wall. Also, since the burned volume behind the flame was cooled by heat transfer to the lower wall, the burned material could expand in both directions. This had the effect of slowing the flame and at times even reversing the propagation direction. When the propagation direction was reversed, an area of reverse flow existed near the lower wall.

6.2 Recommendations for Future Work

The simulations presented in this study represent work done for a two-dimensional laminar flame in a rectangular channel in the absence of a gravitational force. Recommendations for future work include :

- The gravitational term should be included. This would require that the orientation of the channel be specified, either vertical or horizontal. The flame shape and propagation will be altered by the buoyancy effects of the lower density burned gas behind the flame. In a horizontal channel, the buoyancy would require the simulation of the entire channel, the centerline symmetry condition could not be applied.

- A calculation should be performed with a full-chemistry model, such as a methane-air or hydrogen-air model. A full chemistry model would allow the transport and chemical properties, such as the specific heats, to vary over the flame and channel.

- A turbulence model should be included. Turbulent flames propagate at a higher velocity then laminar flames. Also a turbulent boundary layer is thicker and would provide a greater blockage to the gas motion ahead of the flame. An alternate approach to adding an explicit model would be the direct numerical calculation of the turbulence by decreasing the grid size.

Appendix A

Stokes' First Problem with Various Accelerations

Stokes' First Problem was discussed in section 3.2.3 dealing with code validation. The general equation is derived from the x-momentum equation (2.2) with the following assumptions :

- The u velocity is independent of the x direction, $u = u(y,t)$.
- $v = 0$.
- The edge velocity is at most a function of time, $U_e = U_e(t)$.

With these assumptions, the x-momentum equation reduces to

$$\frac{\partial u}{\partial t} = -\frac{1}{\rho}\frac{\partial p}{\partial x} + \nu\frac{\partial^2 u}{\partial y^2} \tag{A.1}$$

The edge velocity, $U_e(t)$, must satisfy the above equation. Substituting the edge velocity into equation A.1 gives

$$\frac{dU_e}{dt} = -\frac{1}{\rho}\frac{\partial p}{\partial x} \tag{A.2}$$

This equation can be used to replace the pressure gradient term with the acceleration of the edge flow, dU_e/dt. The final equation to be solved is

$$\frac{\partial^2 u}{\partial y^2} - \frac{1}{\nu}\frac{\partial u}{\partial t} = -\frac{1}{\nu}\frac{dU_e}{dt} \tag{A.3}$$

with the boundary conditions given by

$$y = 0 \quad : \quad u = 0 \tag{A.4}$$

$$y \to \infty \quad : \quad u \to U_e(t) \tag{A.5}$$

To show that flow with acceleration reduces the boundary layer thickness, three different accelerations will be discussed.

A.1 Zero Acceleration

This case has zero acceleration, giving a constant edge velocity, $U_e(t) = U_e$. This problem is Stokes' First Problem, as discussed in section 3.2.3. Let η be defined as

$$\eta = \frac{y}{2\sqrt{(\nu t)}} \tag{A.6}$$

The solution to this problem is given by Schlichting as[55] as

$$\frac{u(y,t)}{U_e} = 1 - \text{erfc}(\eta) \tag{A.7}$$

where erfc is the complementary error function defined as

$$\text{erfc}(\eta) = 1 - \text{erf}(\eta) \tag{A.8}$$

$$\text{erf}(\eta) = \frac{2}{\sqrt{\pi}} \int_{\eta}^{\infty} exp(-\eta^2) d\eta \tag{A.9}$$

This equation, along with the solutions for the next two sections, is shown in figure A.1.

To obtain the boundary layer thickness, δ_{99}, equation (A.7) is solved for the η where the velocity is 0.99% of the edge value. This gives the boundary layer thickness as

$$\delta_{99} = 3.64\sqrt{(\nu t)} \tag{A.10}$$

A.2 Constant Acceleration

For this case the acceleration is a constant, giving a linear edge velocity profile. Let the acceleration be given by a, so that the edge velocity is given by $U_e(t) = at$. The governing equation (A.3), boundary conditions, and initial conditions are given as

$$\frac{\partial^2 u}{\partial y^2} - \frac{1}{\nu}\frac{\partial u}{\partial t} = -\frac{a}{\nu} \tag{A.11}$$

$$u(y,0) = 0 \tag{A.12}$$

$$u(0,t) = 0 \tag{A.13}$$

$$u(y \to \infty, t) \to at \tag{A.14}$$

To solve the problem, a change of variables is performed.

$$v(y,t) = u(y,t) - at \tag{A.15}$$

Substituting into the above equations gives a new, homogeneous equation to be solved.

$$\frac{\partial^2 v}{\partial y^2} - \frac{1}{\nu}\frac{\partial v}{\partial t} = 0 \tag{A.16}$$

with initial and boundary conditions given by

$$v(y,0) = 0 \tag{A.17}$$

$$v(0,t) = -at \tag{A.18}$$

$$v(y \to \infty, t) \to 0 \tag{A.19}$$

A general solution exists for the problem with the boundary condition at the wall given by

$$v(0,t) = K\phi^{\frac{1}{2}n}, n = -1, 0, 1, 2, ... \tag{A.20}$$

The solution is given by Carslaw and Yeager[69] as

$$v = K\Gamma(\frac{1}{2}n + 1)(4t)^{\frac{1}{2}n} i^n \text{erfc}(\eta) \tag{A.21}$$

where Γ is the gamma function. To complete the solution, the following formula are used to obtain a solution without the complex variable, i.

$$2ni^n\text{erfc}(x) = i^{n-2}\text{erfc}(x) - 2xi^{n-1}\text{erfc}(x) \tag{A.22}$$

$$i^2\text{erfc}(x) = \frac{1}{4}[\text{erfc}(x) - 2xi\text{erfc}(x)] \tag{A.23}$$

$$i\text{erfc}(x) = \frac{1}{\sqrt{\pi}}\exp(-x^2) - x\text{erfc}(x) \tag{A.24}$$

For the problem as stated in equations (A.16 - A.17), $K = -a$ and $n = 2$. The gamma function for $n = 2$ is given by $\Gamma(2) = 1$. Solving the transformed problem and transforming back to the original variable, $u(y,t)$, gives

$$\frac{u(y,t)}{at} = 1 - (1 + 2\eta^2)\text{erfc}(\eta) + \frac{2}{\sqrt{\pi}}\eta\exp(-\eta^2) \tag{A.25}$$

This equation is shown in figure A.1. To obtain the boundary layer thickness, this equation is solved for the η where $u(y,t)/at = 0.99$. This value is $\eta = 1.45$. The boundary layer thickness for the constant acceleration problem is given by

$$\delta_{99} = 2.90\sqrt{\nu t} = (0.797)3.64\sqrt{\nu t} \tag{A.26}$$

This shows that for a constant acceleration, the boundary layer thickness grows slower then for the constant velocity case.

A.3 Linear Acceleration

For this case, the velocity follows a parabolic distribution which gives a linear acceleration. Let the acceleration be given by at, so that the edge velocity is given by $U_e(t) = 0.5at^2$. The governing equation (A.3), boundary conditions, and initial conditions are given as

$$\frac{\partial^2 u}{\partial y^2} - \frac{1}{\nu}\frac{\partial u}{\partial t} = -\frac{at}{\nu} \tag{A.27}$$

$$u(y,0) = 0 \tag{A.28}$$

$$u(0,t) = 0 \tag{A.29}$$

$$u(y \to \infty, t) \to \frac{1}{2}at^2 \tag{A.30}$$

As was done in the previous section, a change of variables is performed.

$$v(y,t) = u(y,t) - \frac{1}{2}at^2 \tag{A.31}$$

Substituting into the above equations gives a new, homogeneous equation to be solved.

$$\frac{\partial^2 v}{\partial y^2} - \frac{1}{\nu}\frac{\partial v}{\partial t} = 0 \tag{A.32}$$

with initial and boundary conditions given by

$$v(y,0) = 0 \tag{A.33}$$

$$v(0,t) = -\frac{1}{2}at^2 \tag{A.34}$$

$$v(y \to \infty, t) \to 0 \tag{A.35}$$

Making use of the general solution given in equation (A.21), $K = -\frac{1}{2}a$, $n = 4$, and the gamma function for $n = 4$ is given by $\Gamma(3) = 2$. Solving the transformed problem and transforming back to the original variable, $u(y,t)$, gives

$$\begin{aligned}\frac{u(y,t)}{\frac{1}{2}at^2} &= 1 - \left[(1+2\eta^2)\mathrm{erfc}(\eta) - \frac{2}{\sqrt{\pi}}\eta\exp(-\eta^2)\right] \\ &+ \frac{4}{3}\eta\left[\frac{1}{\sqrt{\pi}}\exp(-\eta^2) - \eta\mathrm{erfc}(\eta)\right] \\ &- \frac{2}{3}\eta^2\left[(1+2\eta^2)\mathrm{erfc}(\eta) - \frac{2}{\sqrt{\pi}}\eta\exp(-\eta^2)\right]\end{aligned} \tag{A.36}$$

This equation is shown in figure A.1. To obtain the boundary layer thickness, this equation is solved for the η where $u(y,t)/U_e = 0.99$. This value is $\eta = 1.23$. The boundary layer thickness for the constant acceleration problem is given by

$$\delta_{99} = 2.46\sqrt{\nu t} = (0.677)3.64\sqrt{\nu t} \tag{A.37}$$

This shows that for the case of a linearly accelerating edge velocity, the boundary layer grows slower then both the constant and zero acceleration cases.

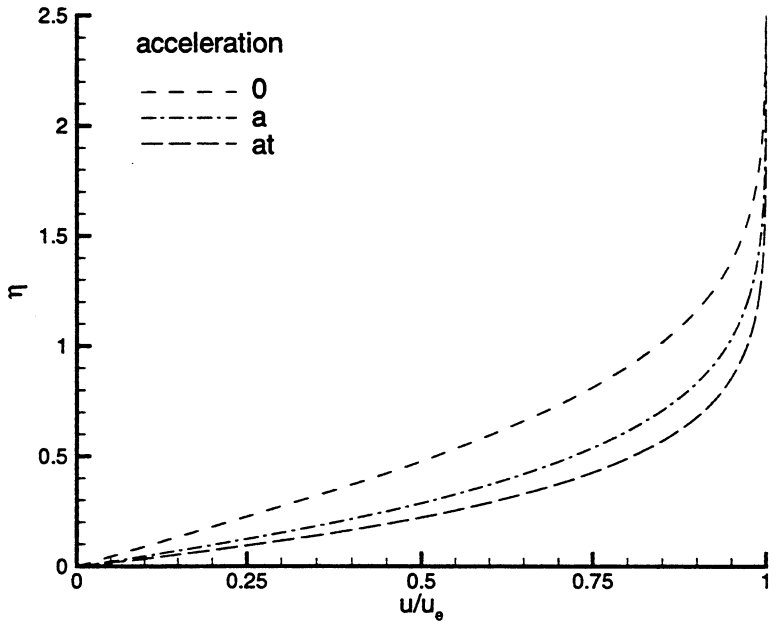

Figure A.1: Velocity profiles with varying edge accelerations

Appendix B

Density and Temperature Variations Due to a Compression Wave

A finite compression wave is defined as a wave where the changes, or perturbations, from the initial conditions may not be small. This is opposed to a weak or acoustic compression wave where the perturbations are assumed to be small so that linear relationships may be developed. When a finite compression wave passes through a point in space, the pressure, density, and temperature all increase. Let the initial condition be given by p_1, T_1, and ρ_1. After the wave has passed by, the new conditions in region 2 are given by a perturbation from the initial conditions.

$$p_2 = p_1 + \Delta p \tag{B.1}$$

$$T_2 = T_1 + \Delta T \tag{B.2}$$

$$\rho_2 = \rho_1 + \Delta \rho \tag{B.3}$$

Assume the wave is isentropic. This allows the conditions in regions 1 and 2 to be related by the isentropic flow relations.

$$\left(\frac{\rho_2}{\rho_1}\right)^{\gamma} = \left(\frac{T_2}{T_1}\right)^{\gamma/\gamma-1)} \tag{B.4}$$

where γ is the ratio of specific heats. Substituting equations (B.2) and (B.3) and reducing gives

$$\left(\frac{\Delta\rho}{\rho_1}+1\right) = \left(\frac{\Delta T}{T_1}+1\right)^{1/(\gamma-1)} \tag{B.5}$$

To relate this result to the relative pressure increase, the equation of state is used. In regions 1 and 2, the equation of state becomes

$$p_1 = \rho_1 R_s T_1 \tag{B.6}$$

$$p_2 = \rho_2 R_s T_2 \tag{B.7}$$

Using equations (B.1 - B.3), the equation in state 2 becomes

$$p_1 + \Delta p = (\rho_1 + \Delta\rho) R_s (T_1 + \Delta T) \tag{B.8}$$

$$p_1 + \Delta p = \rho_1 R_s T_1 + \rho_1 R_s \Delta T + \Delta\rho R_s T_1 + \Delta\rho R_s \Delta T \tag{B.9}$$

Dividing both sides by equation (B.6) and reducing using equation (B.6) gives

$$\frac{\Delta p}{p_1} = \frac{\Delta\rho}{\rho_1} + \frac{\Delta T}{T_1} + \frac{\Delta\rho}{\rho_1}\frac{\Delta T}{T_1} \tag{B.10}$$

This equation provides the relationship between the relative increases of the density and temperature as related to the pressure increase.

B.1 Acoustic Wave

Assume that the ratio of the perturbation to the initial condition is small.

$$\frac{\Delta T}{T_1} \ll 1 \tag{B.11}$$

Using the binomial expansion, neglecting higher order terms, equation (B.5) reduces to

$$\frac{\Delta\rho}{\rho_1} \doteq \left(\frac{1}{\gamma - 1}\right)\left(\frac{\Delta T}{T_1}\right) \tag{B.12}$$

For the present chemistry model, $\gamma = 1.25$ so that the above equation becomes

$$\frac{\Delta\rho}{\rho_1} \doteq 4\left(\frac{\Delta T}{T_1}\right) \tag{B.13}$$

This shows that for a finite compression wave, the relative increase in density is greater then the relative increase in temperature, 4× for the present chemistry model. Assuming that the product of perturbations is small, equation (B.10) becomes

$$\frac{\Delta p}{p_1} \doteq \frac{\Delta\rho}{\rho_1} + \frac{\Delta T}{T_1} \tag{B.14}$$

$$\frac{\Delta p}{p_1} \doteq \frac{\gamma}{\gamma - 1}\frac{\Delta T}{T_1} \tag{B.15}$$

$$\frac{\Delta p}{p_1} \doteq 5\frac{\Delta T}{T_1} \tag{B.16}$$

B.2 Finite Wave

For a finite wave the perturbations need not be small. Solving equation (B.5 for the density variation gives

$$\frac{\Delta\rho}{\rho_1} = \left(\frac{\Delta T}{T_1} + 1\right)^{1/(\gamma-1)} - 1 \tag{B.17}$$

Substituting this relation into the pressure equation gives

$$\frac{\Delta p}{p_1} = \left(\frac{\Delta T}{T_1} + 1\right)^{\gamma/(\gamma-1)} - 1 \tag{B.18}$$

For a given relative increase in the pressure due to a finite wave, the relative increase in the density is greater the the relative increase in the temperature.

Appendix C

Laminar Flame Theory

C.1 Overview

Laminar flame theory provides a means to estimate the flame speed, which is defined as the speed of the flame relative to the flow ahead of it, and the flame thickness. Mallard and LeChatelier[27] developed a model of a flame as shown in Figure C.1. The flame is divided into two region. The first region, Zone I in the figure, is a preheat region. There is no chemical reaction in this region. The unburned material is heated due to thermal conduction up to a temperature T_i, which is assumed to be close to the temperature of the burned material, T_b. In the second region, Zone II in the figure, the material combusts. The flame is stationary with the gas flow coming towards it at the laminar flame speed, S_l.

C.2 Laminar Flame Speed

Zeldovich and Frank-Kamenetskii[60–62] and Semenov[63] developed a laminar flame theory based on the model described above. They solved the species mass conservation equation and the energy conservation equation to determine a formula for the laminar flame speed. The assumptions that they made are :

- One-dimensional ($\frac{\partial}{\partial y} = 0$).
- Steady state ($\frac{\partial}{\partial t} = 0$).
- Viscous stress terms are negligible.

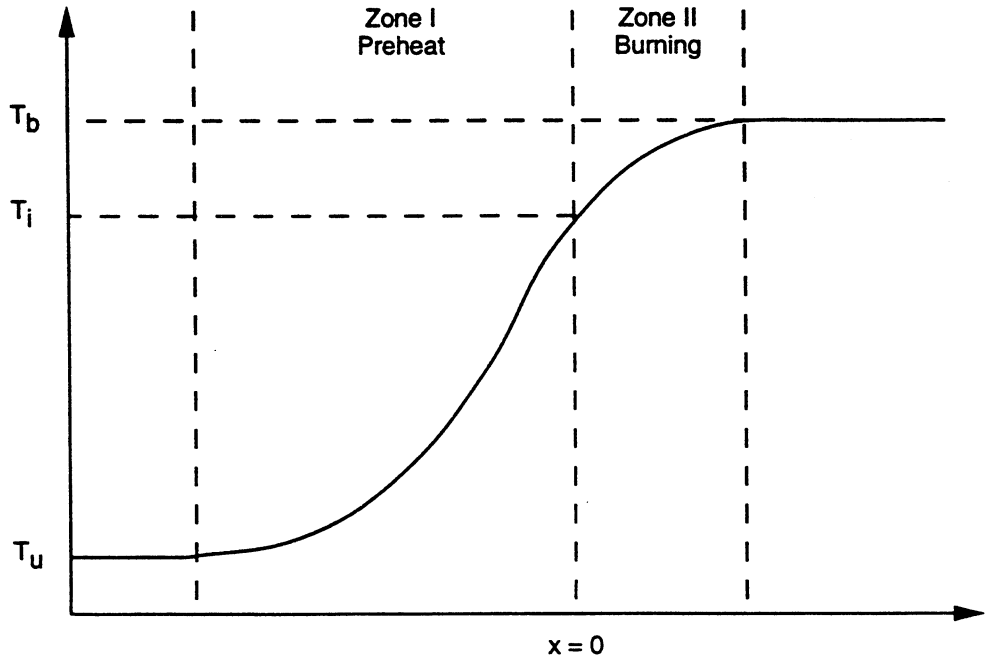

Figure C.1: Temperature profile across a laminar flame

- Constant pressure.
- The number of moles is constant during the reaction.
- The specific heat, c_p, is constant
- The thermal conductivity, k, is constant
- Lewis number is unity. From equation (2.30) this implies that $k/c_p = \rho D$.

With the above assumptions, the global continuity equation, (2.1), can be written as

$$\frac{\partial \rho u}{\partial x} = 0 \Rightarrow \rho u = constant \tag{C.1}$$

This is a statement that the mass flow rate is constant. Applying this equation to the flame model in Figure C.1 gives

$$\rho u = \rho_u S_l \tag{C.2}$$

For a steady, one-dimensional flame, the species continuity equation, (2.5), written in terms of the fuel mass fraction, Y, is given by

$$\rho u \frac{dY}{dx} = \frac{d}{dx}(\rho D \frac{dY}{dx}) + \omega \tag{C.3}$$

where ω is the production rate of fuel. Using equations (2.18) and (2.19), this terms becomes

$$\omega = \rho^2 Y A exp(-T_a/T) \tag{C.4}$$

Transforming this equation using $\phi = Y - Y_u$, equation (C.3) can be written as

$$\rho D \frac{d^2\phi}{dx^2} - \rho u \frac{d\phi}{dx} + \omega = 0 \tag{C.5}$$

The energy equation, (2.4), is written in terms of temperature. For the current chemistry model, this equation becomes

$$(\frac{k}{c_p})\frac{d^2T}{dx^2} - \rho u \frac{dT}{dx} - \frac{\omega q}{c_p} = 0 \tag{C.6}$$

Transforming by $\theta = (c_p/q)(T_u - T)$, this equations becomes

$$(\frac{k}{c_p})\frac{d^2\theta}{dx^2} - \rho u \frac{d\theta}{dx} + \omega = 0 \tag{C.7}$$

The boundary conditions for equations (C.5) and (C.7) are given by

$$x = -\infty \begin{cases} \phi = 0 \\ \theta = 0 \end{cases} \tag{C.8}$$

$$x = +\infty \begin{cases} \phi = -Y_u = -1 \\ \theta = (c_p/q)(T_u - T_b) \end{cases} \tag{C.9}$$

Comparing equations (C.5) and (C.7) and the above boundary conditions, it can be seen that the solutions of the two equations will be the same, $\phi = \theta$, if the boundary conditions at infinity are the same.

$$\begin{aligned} -Y_u &= \frac{c_p}{q}(T_u - T_b) \\ c_p T_b &= c_p T_u + q \end{aligned} \tag{C.10}$$

This condition is satisfied if the flame is adiabatic. To prove this, examine equation (2.33). Setting the x component of heat flux to 0, and integrating over the flame from T_u to T, we get

$$\begin{aligned} q_x = 0 &= -k\frac{dT}{dx} - \rho D q \frac{dY}{dx} \\ -k\int_{T_u}^{T} dT &= \rho D q \int_{Y_u}^{Y} dY \\ c_p T + qY &= c_p T_u + q \end{aligned} \tag{C.11}$$

The left hand side of this equation is evaluated at the burned side, where $T = T_b$, and $Y_b = 0$, to get

$$c_p T_b = c_p T_u + q \tag{C.12}$$

This equation is identical to equation (C.10). Making the assumption that the flame is adiabatic, equation (C.11) can be used in place of equation (C.5). This reduces the system to one differential equation and one algebraic equation.

The solution procedure is to integrate equation (C.6) over the two zones in figure C.1 and match the first derivative at $x = 0$. This ensures that the heat flux is balanced between the two regions. In Zone I there is assumed no reaction, $\omega = 0$.

$$\frac{d^2T}{dx^2} - \left(\frac{\rho u c_p}{k}\right)\frac{dT}{dx} = 0 \tag{C.13}$$

with boundary conditions for this region

$$x = \begin{cases} -\infty, & T = T_u, \quad \frac{dT}{dx} = 0 \\ 0^-, & T = T_i \end{cases} \tag{C.14}$$

Integration this equation from $-\infty$ to 0^- and applying the boundary conditions at $-\infty$ gives

$$\frac{dT}{dx} = \frac{\rho u c_p}{k}(T - T_u) \tag{C.15}$$

This equation for the derivative is evaluated at $x = 0^-$. It is assumed that T_i is very close to T_b, so that $T_i \approx T_b$.

$$\left(\frac{dT}{dx}\right)_{x=0^-} = \frac{\rho u c_p}{k}(T_b - T_u) \tag{C.16}$$

In Zone II, it is assumed that the convective term in equation (C.6) is negligible, since T_i is very close to T_b.

$$\frac{d^2T}{dx^2} + \frac{\omega q}{k} = 0 \tag{C.17}$$

with boundary conditions for this region given by

$$x = \begin{cases} \infty, & T = T_b, \quad \frac{dT}{dx} = 0 \\ 0^+, & T = T_i \end{cases} \tag{C.18}$$

Integrating the above equation from 0^+ to ∞, applying the boundary conditions, and evaluating the result at 0^+ gives

$$\left(\frac{dT}{dx}\right)_{x=0^+} = \sqrt{\frac{2q}{k}I} \tag{C.19}$$

where

$$I = \int_{T_i}^{T_b} \omega dT \approx \int_{T_u}^{T_b} \omega dT \tag{C.20}$$

The lower integration bound can be replaced by T_u since it is assumed that there is no reaction from T_i to T_u.

At $x = 0$ the two derivative equations, (C.16) and (C.19), must be equal to ensure a heat flux balance between the two regions.

$$\frac{\rho u c_p}{k}(T_b - T_u) = \sqrt{\frac{2q}{k}I} \tag{C.21}$$

Solving the above equation for ρu, substituting the result into equation (C.2), and reducing using equation (C.12), gives an equation for the laminar flame speed, S_l as

$$S_l = \sqrt{\left(\frac{k}{\rho_u c_p}\right)\left(\frac{1}{\rho_u}\right)\left(\frac{2}{T_b - T_u}\right)I} \tag{C.22}$$

According to Kuo,[2] this formula doesn't give very accurate results, but it does predict the trends well. One of these trends is that the flame speed is proportional to the square root of the thermal conductivity, $S_l \propto \sqrt{k}$.

C.3 Laminar Flame Thickness

Turns[64] outlines a method from Spalding[65] to calculate the laminar flame thickness, defined by

$$\delta_t = \frac{T_b - T_u}{\left(\frac{dT}{dx}\right)_{max}} \tag{C.23}$$

Spalding[65] assumed that the temperature gradient through the flame was constant, making the temperature profile a straight line. Equation (C.6), the energy equation, is integrated from $-\infty$ to $+\infty$, with the following boundary conditions

$$x = \begin{cases} +\infty, & T = T_b, \quad dT/dx = 0 \\ -\infty, & T = T_u, \quad dT/dx = 0 \end{cases} \tag{C.24}$$

This integration yields

$$\rho u(T_b - T_u) = \frac{q}{c_p}\int_{-\infty}^{+\infty} \omega dx \tag{C.25}$$

Solving equation (C.23) for dx, substituting into the above equation, reducing using equations (C.12) and (C.20), and substituting in for ρu from equation (C.2), gives

$$\rho_u S_l(T_b - T_u) = \delta_t I \tag{C.26}$$

The term I can be removed from this equation by solving equation (C.22) for I and substituting. After reduction, the equation for the laminar flame thickness becomes

$$\delta_t = \frac{2}{S_l}\left(\frac{k}{\rho_u c_p}\right) \tag{C.27}$$

Since the laminar flame speed was shown in the previous section to be proportional to the square root of the thermal conductivity, this equation shows that the thickness is also proportional to the square root of the thermal conductivity, $\delta_t \propto \sqrt{k}$.

C.4 Quenching Distance

Assume that the flame propagates between two parallel plates separated by some distance. The quenching distance, d_q, is defined as the smallest plate separation that will allow the flame to propagate. If the plate distance is set any smaller, the flame will be quenched. The quenching distance can be calculated by equating the heat generated due to the chemical reactions, q_c, to the heat lost at the wall, q_w.[2,64]

Let A_w represent an area of wall surface. The total heat loss to both walls in given by

$$q_w = 2k_w \left(\frac{\partial T}{\partial x}\right)_w A_w \tag{C.28}$$

Let the temperature profile is linear from the wall to the center of the channel. Also assume the the wall temperature, T_w is equal to the unburned gas temperature, T_u. Using the linear temperature profile, the heat loss at the wall can be written as

$$q_w = 2k_w A_w \frac{T_q - T_u}{d_q/2} \tag{C.29}$$

The heat release due to the chemistry is estimated as the average reaction rate over the volume between the plates, times the heat of formation. The reaction rate, I, is given by equation (C.20)

$$q_c = \frac{I}{T_b - T_u} q A_w d_q \tag{C.30}$$

Equations (C.29) and (C.30) are equated and solved for the quenching distance, d_q.

$$d_q^2 = \frac{4k_w(T_q - T_u)(T_b - T_u)}{Iq} \tag{C.31}$$

Solving equation (C.22) for I, and making use of equation (C.27), the reaction rate is given by

$$I = \frac{2k(T_b - T_u)}{c_p \delta_t^2} \tag{C.32}$$

Substituting this result into equation (C.31), and using equation (C.10) for the heat of reaction, q, the quenching distance is calculated as

$$d_q = \delta_t \sqrt{2\left(\frac{k_w}{k}\right)\left(\frac{T_q - T_u}{T_b - T_u}\right)} \tag{C.33}$$

In this equation, T_q is the lowest temperature at which the flame can propagate. Also k is evaluate at the same temperature used in the determination of the laminar flame speed.

Appendix D

General Outline of CMRFAST2D

This Appendix will outline the basics of CMRFAST2D, a Connection Machine, Reacting, FAST, Two-Dimensional code. A flowchart of the code structure is shown in figure D.1.

(i) The initial values of the flowfield properties are defined either from a restart file or from user-defined initial values. The boundary conditions are established and the gridding is defined. The viscous stress terms, heat conduction terms and mass diffusion terms are initialized to zero.

(ii) The timestep is determined as discussed in section 2.5 The total time of the simulation is calculated.

(iii) The viscous stress terms in both the momentum and energy equations are calculated using a second order method.

(iv) The heat conduction terms in the energy equation are calculated using a second order method.

(v) The mass diffusion terms in the species continuity equations and the heat flux due to the mass diffusion in the energy equation are calculated using a second order method.

(vi) The governing equations are integrated in time using the LCPFCT[40] routine as described in section 2.4. The viscous, heat conduction, and mass diffusion terms are used as source terms. The integration technique uses directional splitting to integrate in the x and the y coordinate directions.

(vii) The chemical rate equations are integrated in time, as described in section 2.6.

(viii) This routine updates the values at the boundaries using the characteristic boundary method described in section 2.7. Boundaries can be specified as subsonic outflow, inflow, solid wall, symmetry, or extrapolation (supersonic outflow).

(ix) This routine outputs the flowfield values at selected times. It also generates a restart file at selected times.

(x) If the total time is less then a stop time, the loop continues by determining a new time-step. If the time is greater, a restart file is written and the program ends. This loop criteria can also be based upon an iteration counter.

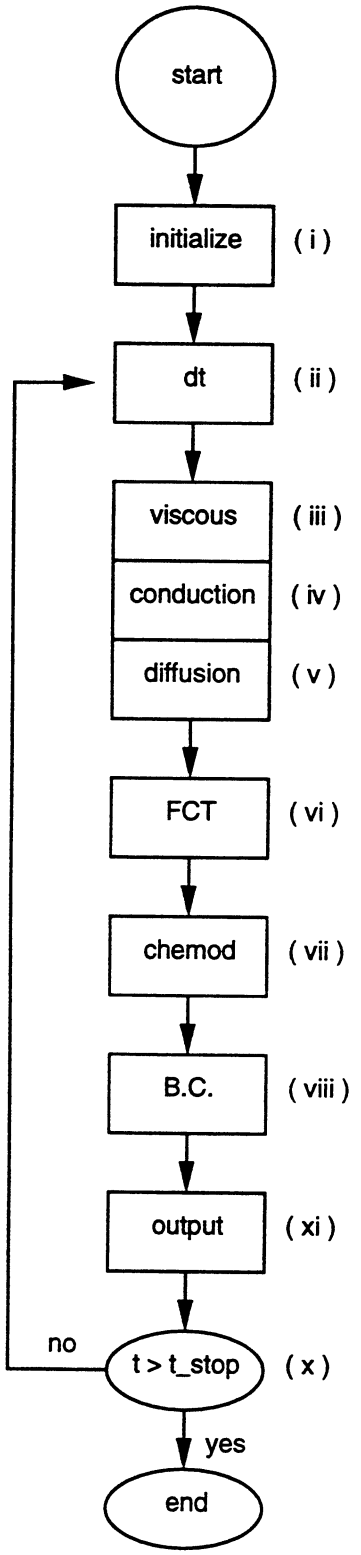

Figure D.1: CMRFAST2D program flowchart.

Bibliography

[1] Chu, B., "On the Generation of Pressure Waves at a Planar Flame Front," in *Fourth Symposium (International) on Combustion*, pp. 603–612, Combustion Institute, 1952.

[2] Kuo, K. K., *Principles of Combustion.* New York: Wiley, 1986.

[3] Lee, J. H. S. and Moen, I. O., "The Mechanism of Transition from Deflagration to Detonation in Vapor Cloud Explosions," *Progress in Energy and Combustion Science*, Vol. 6, 1980, pp. 359–389.

[4] Shepherd, J. E. and Lee, J. H. S., *Major Research Topics in Combustion.* New York: Springer, 1992.

[5] Lewis, B. and von Elbe, G., *Combustion, Flames, and Explosions of Gases.* New York: Academia, 3rd ed., 1987.

[6] Ellis, O. C., "Propagation of a Flame through a Tube From Ignition at One End," *Fuel*, Vol. 7, No. 11, 1928, pp. 502–508.

[7] Schmidt, E. H. W., Steinicke, H., and Neubert, U., "Flame and Schlieren Photographs of Combustion Waves in Tubes," in *Fourth Symposium (International) on Combustion*, pp. 658–667, Combustion Institute, 1952.

[8] Salamandra, G. D., Bazhenova, T. V., and Naboko, I. M., "Formation of Detonation Wave during Combustion of Gas in Combustion Tube," in *Seventh Symposium (International) on Combustion*, pp. 851–857, Combustion Institute, 1959.

[9] Guenoche, H., *Nonsteady Flame Propagation.* New York: Pergamon Press, 1964.

[10] Leyer, J. and Manson, N., "Development of Vibratory Flame Propagation in Short Closed Tubes and Vessels," in *Thirteenth Symposium (International) on Combustion*, pp. 551–557, Combustion Institute, 1970.

[11] Starke, R. and Rothe, P., "An Experimental Investigation of Flame Behavior During Cylindrical Vessel Explosions," *Combustion and Flame*, Vol. 66, 1986, pp. 249–259.

[12] Dunn-Rankin, D., Barr, P. K., and Sawyer, R. F., "Numerical and Experimental Study of "Tulip" Flame Formation in a Closed Vessel," in *Twenty-First Symposium (International) on Combustion*, pp. 1291–1301, Combustion Institute, 1986.

[13] Kooker, D. E., "Transient Laminar Flame Propagation in Confined Premixed Gases: Numerical Predictions," in *Seventeenth Symposium (International) on Combustion*, pp. 1329–1338, Combustion Institute, 1978.

[14] Kooker, D. E., "Numerical Study of a Confined Premixed Laminar Flame: Oscillatory Propagation and Wall Quenching," *Combustion and Flame*, Vol. 49, 1983, pp. 141–149.

[15] Rothman, D. A. and Oppenheim, A. K., "Aerothermodynamic Properties of Stretched Flames in Enclosures," in *Twenty-First Symposium (International) on Combustion*, pp. 1303–1312, Combustion Institute, 1986.

[16] Gonzalez, M., Borghi, R., and Saquab, A., "Interaction of a Flame Front with its Self-Generated Flow in an Enclosure: The "Tulip Flame" Phenomenon," *Combustion and Flame*, Vol. 88, 1992, pp. 201–220.

[17] McGreevy, J. L. and Matalon, M., "Lewis Number Effect on the Propagation of Premixed Flames in Closed Tubes," *Combustion and Flame*, Vol. 91, 1992, pp. 213–225.

[18] N'Konga, B., Fernandez, G., Guillard, H., and Larrouturo, B., "Numerical Investigations of the Tulip Flame Instability - Comparisons with Experimental Results," *Combustion Science and Technology*, Vol. 87, 1992, pp. 69–89.

[19] Matalon, M. and McGreevy, J. L., "The Initial Development of a Tulip Flame," in *Twenty-Fifth Symposium (International) on Combustion*, pp. 1407–1413, Combustion Institute, 1994.

[20] Dold, J. W. and Joulin, G., "An Evolution Equation Modeling Inversion of Tulip Flames," *Combustion and Flame*, Vol. 100, 1995, pp. 450–456.

[21] Gonzalez, M., "Acoustic Instability of a Premixed Flame Propagating in a Tube," *Combustion and Flame*, Vol. 107, 1996, pp. 245–259.

[22] Tien, J. H., "Effects of Flame Stretch on Premixed Flame Propagation on a Closed Tube," *Combustion and Flame*, Vol. 107, 1996, pp. 303–306.

[23] Marra, F. S. and Continillo, G., "Numerical Study of Premixed Laminar Flame Propagation in a Closed Tube with a Full Navier-Stokes Approach," in *Twenty-Sixth Symposium (International) on Combustion*, pp. 907–913, Combustion Institute, 1996.

[24] Darrieus, G. *Journal of Chemical Physics*, Vol. 88, 1944.

[25] Landau, L. *Journal of Experimental and Theoretical Physics*, Vol. 14, 1944.

[26] Zeldovich, Y. B., "Structure and Stability of Steady Laminar Flame at Moderately Large Reynolds Numbers," *Combustion and Flame*, Vol. 40, 1981, pp. 225–234.

[27] Mallard, E. and Le Chatelier, H. L., "Recherches Experimentelles et Theoriques sur la Combustion des Melanges Gazeux Explosifs," *Ann. Mines*, Vol. 4, 1883, pp. 379–568.

[28] Coward, H. F. and Hartwell, F. J., "Studies in the Mechanism of Flame Movement. Part I. The Uniform Movement of Flame in Mixtures of Methane and Air, in Relation to Tube Diameter," *Journal of the Chemical Society*, Vol. 141, 1932, pp. 1996–2004.

[29] Guenoche, H. and Jouy, M., "Changes in the Shape of Flames Propagating in Tubes," in *Fourth Symposium (International) on Combustion*, pp. 403–406, Combustion Institute, 1952.

[30] Gerstein, M., "The Structure of Laminar Flames," in *Fourth Symposium (International) on Combustion*, pp. 35–43, Combustion Institute, 1952.

[31] Singer, J. M. and von Elbe, G., "Flame Propagation in Cylindrical Tubes Near the Quenching Limit," in *Sixth Symposium (International) on Combustion*, pp. 127–130, Combustion Institute, 1956.

[32] Markstein, G. H., "Instability Phenomena in Combustion Waves," in *Fourth Symposium (International) on Combustion*, pp. 44–59, Combustion Institute, 1952.

[33] Lee, S. T. and Tsai, C. H., "Numerical Investigation of Steady Laminar Flame Propagation in a Circular Tube," *Combustion and Flame*, Vol. 99, 1994, pp. 484–490.

[34] Hackert, C. L., Ellzey, J. L., and Ezekoye, O. A., "Effects of Thermal Boundary Conditions on Flame Shape and Quenching in Ducts," *Combustion and Flame*, Vol. 112, 1998, pp. 73–84.

[35] Anderson, J. D. Jr., *Hypersonic and High Temperature Gas Dynamics*. New York: McGraw-Hill Book Co., 1989.

[36] Kee, R. J., Dixon-Lewis, G., Warnatz, J., Coltrin, M. E., and Miller, J. A., "A Fortran Computer Code Package for the Evaluation of Gas-Phase Multi-Component Transport Properties," Sandia National Laboratories, SAND-86-8246, 1986.

[37] Khokhlov, A. M., Oran, E. S., Chtchelkanova, A. Y., and Wheeler, J. C., "The Interaction of a Shock with a Sinusoidally Perturbed Flame," *Combustion and Flame*, Vol. 117, No. 1, 1999.

[38] Weber, J. W., Jr., *The Efficient Simulation of Gas Detonation Physics on a Massively Parallel Connection Machine*. PhD thesis, University of Maryland at College Park, 1994.

[39] Bird, B. R., Stewart, W. E., and Lightfoot, E. N., *Transport Phenomena*. New York: John Wiley & Sons, Inc., 1960.

[40] Boris, J., Landsberg, A., Oran, E. S., and Gardner, J., "A Flux Corrected Transport Algorithm for Solving Generalized Continuity Equations," Naval Research Laboratory, NRL/MR/6410-93-7192, 1993.

[41] Boris, J. P. and Book, D. L., "Solutions of the Continuity Equation by the Method of Flux-Corrected Transport," *Methods in Computational Physics*, Vol. 16, 1976, pp. 85–129.

[42] Hoffman, K. A., *Computational Fluid Dynamics for Engineers*. Austin, Texas: Engineering Education System, 1989.

[43] Pointsot, T. and Lele, S., "Boundary Conditions for Direct Simulation of Compressible Viscous Flows," *Journal of Computational Physics*, Vol. 101, 1992, pp. 104–129.

[44] Thompson, K. W., "Time Dependent Boundary Conditions for Hyperbolic Systems," *Journal of Computational Physics*, Vol. 68, 1987, pp. 1–24.

[45] Thompson, K. W., "Time Dependent Boundary Conditions for Hyperbolic Systems, II," *Journal of Computational Physics*, Vol. 89, 1990, pp. 439–461.

[46] Saint-Martian-Tillet, X. N. and Oran, E. S., "Boundary Conditions for FCT Based Solutions of the Navier-Stokes Equations," Naval Research Laboratory, Internal Report, 1996.

[47] Grumet, A. A., *The Efeects of Surface Catalysis on the Hypersonic Shock Wave / Boundary Layer Interaction.* PhD thesis, University of Maryland at College Park, 1994.

[48] Ruby, D. H. and Strikwerda, J. C., "A Nonreflecting Outflow Boundary Condition for Subsonic Navier-Stokes Calculations," *Journal of Computational Physics*, Vol. 36, 1980, pp. 55–70.

[49] Weber, Y. S., *The Numerical Simulation of the Reflected Shock-Boundary Layer Interaction in High Performance Shock Tubes.* PhD thesis, University of Maryland at College Park, 1994.

[50] Piana, J. private communication, 1996.

[51] Nguyen, T. X., Saint-Martin-Tillet, X. N., and Oran, E. S., "Interactions of Vortical Structures in a Ribbed Channel," AIAA Paper No. 97–0434, Jan. 1997.

[52] Oran, E. S. and Boris, J. P., *Numerical Simulation of Reactive Flow.* New York: Elsevier, 1987.

[53] White, F. M., *Viscous Fluid Flow.* New York: McGraw-Hill Book Co., 2nd ed., 1991.

[54] Hildebrand, F. B., *Advanced Calculus for Applications.* News Jersey: Prentice-Hall, Inc., 2nd ed., 1976.

[55] Schlichting, H., *Boundary-Layer Theory.* New York: McGraw-Hill Book Co., 6th ed., 1968.

[56] Anderson, J. D. Jr., *Modern Compressible Flow with Historical Perspective.* New York: McGraw-Hill Book Co., 2nd ed., 1990.

[57] Glassman, I., *Combustion.* New York: Academic Press, 3rd ed., 1996.

[58] Williams, F. A., *Principles of Combustion.* California: The Benjamin / Cummings Publishing Company, Inc., 1985.

[59] Kanury, A. M., *Introduction to Combustion Phenomena (for Fire, Incineration, Pollution, and Energy Applications).* New York: Gordon and Breach Science Publishers, 1982.

[60] Zeldovich, Y. B. and Frank-Kamenetskii, D. A., "K Teorii Ravnomernogo Rasprostraneniya Plameni (On the Theory of Uniform Flame Propagation)," *Dokl. AN SSSR*, Vol. 19, 1938, p. 693.

[61] Zeldovich, Y. B. and Frank-Kamenetskii, D. A., "Teorii Teplovoga Rasprostraneniya Plameni (The Theory of Thermal Flame Propagation)," *Zhurnal Fizicheskoi Khimii*, Vol. 12, 1938, p. 100.

[62] Zeldovich, Y. B., "Theory of Flame Propagation," NACA TM-1282, 1951.

[63] Zeldovich, Y. B. and Semenov, N. N. *Journal of Experimental and Theoretical Physics, USSR*, Vol. 10, 1940, p. 1116.

[64] Turns, S. R., *An Introduction to Combustion, Concepts and Applications.* New York: McGraw-Hill Book Co., 1996.

[65] Spalding, D. B., *Combustion and Mass Transfer.* New York: Pergamon, 1979.

[66] Thomas, G. private communication, 1997.

[67] Zeldovich, Y. B., Barenblatt, G. I., Librovich, V. B., and Makhviladz, G. M., *The Mathematical Theory of Combustion and Explosion.* New York: Consultants bureau, 1985.

[68] James, M. L., Smith, G. M., and Wolford, J. C., *Applied Numerical Methods for Digital Computation.* New York: Harper and Row, 3rd ed., 1985.

[69] Carslaw, H. S. and Yeager, J. C., *Conduction of Heat in Solids.* London: Oxford University Press, 2nd ed., 1959.

REPORT DOCUMENTATION PAGE

Form Approved
OMB No. 0704-0188

1. AGENCY USE ONLY (*Leave blank*)	2. REPORT DATE	3. REPORT TYPE AND DATES COVERED
	September 1999	Final Contractor Report

4. TITLE AND SUBTITLE

The Interactions of a Flame and Its Self-Induced Boundary Layer

5. FUNDING NUMBERS

WU–538–17–10–00
C–78082–F

6. AUTHOR(S)

James D. Ott, Elaine S. Oran, and John D. Anderson

7. PERFORMING ORGANIZATION NAME(S) AND ADDRESS(ES)

Naval Research Laboratory
Washington, DC

8. PERFORMING ORGANIZATION REPORT NUMBER

E–11923

9. SPONSORING/MONITORING AGENCY NAME(S) AND ADDRESS(ES)

National Aeronautics and Space Administration
John H. Glenn Research Center at Lewis Field
Cleveland, Ohio 44135–3191

10. SPONSORING/MONITORING AGENCY REPORT NUMBER

NASA CR—1999-209401

11. SUPPLEMENTARY NOTES

James D. Ott and Elaine S. Oran, Laboratory for Computational Physics and Fluid Dynamics, Naval Research Laboratory, Washington, DC; and John D. Anderson, Department of Aerospace Engineering, University of Maryland, College Park, Maryland. Project Manager, J.D. Holdeman, Turbomachinery and Propulsion Systems Division, NASA Glenn Research Center, organization code 5830, (216) 433–5846.

12a. DISTRIBUTION/AVAILABILITY STATEMENT

Unclassified - Unlimited
Subject Category: 07 Distribution: Nonstandard

This publication is available from the NASA Center for AeroSpace Information, (301) 621–0390.

12b. DISTRIBUTION CODE

13. ABSTRACT ***(Maximum 200 words)***

The interaction of a laminar flame with its self-generated boundary layer in a rectangular channel was numerically simulated using the two-dimensional, reacting, Navier-Stokes equations. A two species chemistry model was implemented which simulates the stoichiometric reaction of acetylene and air. Calculations were performed to investigate the effects of altering the boundary condition of the wall temperature, the Lewis number, the dynamic viscosity, and the ignition method. The purpose of this study was to examine the fundamental physics of the formation of the boundary layer and the interaction of the flame as it propagates into the boundary layer that its own motion has created.

14. SUBJECT TERMS

Fluid mechanics combustion; Droplet; Strain; Boundary layer; Flame

15. NUMBER OF PAGES

193

16. PRICE CODE

A09

17. SECURITY CLASSIFICATION OF REPORT	18. SECURITY CLASSIFICATION OF THIS PAGE	19. SECURITY CLASSIFICATION OF ABSTRACT	20. LIMITATION OF ABSTRACT
Unclassified	Unclassified	Unclassified	